### FINAL TECHNICAL REPORT

### OFFICE OF NAVAL RESEARCH

GRANT N00014-97-1-0109

## Multidimensional Structure of Wall Bounded Turbulence-Continuation

RONALD J. ADRIAN
University of Illinois
Department of Theoretical and Applied Mechanics
216 Talbot Laboratory
104 South Wright Street
Urbana, Illinois 61801

December 22, 1998

Approved for prints releases

Distribution Unitarities

19990104 01

## REPORT DOCUMENTATION PAGE

Form Approved OMB No. 0704-0188

Public reporting burden for this collection of information is estimated to average 1 hour per response, including the time for reviewing instructions, searching existing data sources,

collection of information, including suggestions for red Davis Highway, Suite 1204, Arlington, VA 22202-4302	ucing this burden to Washington Headquarter 2, and to the Office of Management and Budg	Services, Directorate for Information Project	nation Operations and Reports, 1215 Jefferson 1 (0704-0188), Washington, DC 20503
1. AGENCY USE ONLY (Leeve blank)	2. REPORT DATE 11/03/98	3. REPORT TYPE AND	
MILE AND SUBTITLE MILE AND SUBTITLE MILE AND SUBTITLE			5. FUNDING NUMBERS
Bounded Turbules			G: N00014-97-1-0109
Christopher David Tom	kins and Ronald J.	Adrian,	
Thesis Director, Profe	essor and P.I.		
7. PERFORMING ORGANIZATION NAMES(S) Department of Theoret: The University of Ill: 216 Talbot Lab, 104 S. Urbana, IL 61801	ical & Applied Mechinois at Urbana-Cha . Wright Street		8. PERFORMING ORGANIZATION REPORT NUMBER
9. SPONSORING / MONITORING AGENCY NAMES(S) AND ADDRESS(ES)			10. SPONSORING / MONITORING
Office of Naval Research Regional Office Chicago 536 S. Clark Street, Room 208			AGENCY REPORT NUMBER
Chicago, IL 60605-1588			
Tomkins, C.D., Adrian, R.J., Balachandar, S., 1998, "The Structure of Vortex Packets in Wall Turbulence", AIAA Paper No.98-2962, 29th AIAA Fluid Dynamics Conference, Albuquerque, NM, June 15-18, 1998.			
a. DISTRIBUTION / AVAILABILITY STATEMEN	NT .		12. DISTRIBUTION CODE
13 APSTRACT (Maximum 200			
13. ABSTRACT (Maximum 200 words)			

#### Abstract

Broad goals of the work were to study the structure of the turbulent wall layer using modern particle image velocimetry techniques to measure instantaneous velocity fields, and to interpret the structure. Earlier work (C. D. Meinhart, Ph.D. Thesis, Univ. Illinois, 1994) supported by ONR had suggested that low momentum regions are created in wall turbulence by the alignment of hairpin vortices, but the field of view of this work was not wide enough to see entire groups of vortices and the patterns in which they formed. Experiments were conducted in boundary layer using wide-angle PIV measurements that gave views of structure that had not been attainable before. They show that the hairpins definitely occur in packets that grow more or less linearly at an angle of 12+/- 6 degrees with respect to the wall. Packets containg up to 12 hairpins were observed.

turbulence, boundary layer, fluid flow			15. NUMBER OF PAGES 390	
			16. PRICE CODE	
17. SECURITY CLASSIFICATION OF REPORT unclassified	18. SECURITY CLASSIFICATION OF THIS PAGE unclassified	19. SECURITY CLASSIFICATION OF ABSTRACT unclassified	20. LIMITATION OF ABSTRACT	

## FINAL TECHNICAL REPORT

## OFFICE OF NAVAL RESEARCH

GRANT N00014-97-1-0109

# Multidimensional Structure of Wall Bounded Turbulence-Continuation

RONALD J. ADRIAN
University of Illinois
Department of Theoretical and Applied Mechanics
216 Talbot Laboratory
104 South Wright Street
Urbana, Illinois 61801

December 22, 1998

# TABLE OF CONTENTS

Cl	HAP	TER	Page
1	Intr	oduction	1
	1.1	Motivation	. 1
	1.2	Hairpin Vortices in the Turbulent Boundary Layer	. 2
	1.3	Recent Advances in Understanding Hairpin Vortices	
		1.3.1 Unresolved Issues	
	1.4	The Present Work	. 4
2	Bac	kground of Turbulent Boundary Layers	5
	2.1	Introduction	
	2.2	Early Investigations	. 5
	2.3	Flow-Visualization Investigations	. 6
	2.4	Hot-Wire/Conditional Sampling Investigations	
		2.4.1 Pre-conditional sampling	. 8
		2.4.2 Intermittancy Sampling	. 9
		2.4.3 Quadrant Detection	. 9
		2.4.4 VITA Sampling	. 10
		2.4.5 Linear Stochastic Estimation	
	2.5	Numerical Simulation	. 11
	2.6	Turbulent Boundary Layer Models	. 11
	2.7	Recent work: Observations of Zones	. 13
3	Par	ticle Image Velocimetry: Background and Present Details	15
	3.1	Pulsed Light Velocimetry	
		3.1.1 Introduction	
		3.1.2 Particle Image Velocimetry	. 15
	3.2	Particle Imaging	. 16
	3.3	Interrogation	. 18
	3.4	Sources of Error	. 20
4	Exp	perimental Procedure	. 21
	$4.1^{-}$		
		4.1.1 Lasers and light-sheet forming optics	
		4.1.1.1 Lasers	
		4.1.1.2 Laser Timing	
		4.1.1.3 Light-sheet forming optics	

		4.1.2 Low-turbulence Windtunnel	24
		4.1.2.1 Test Section	25
		4.1.2.2 Windtunnel Performance and Instrumentation	26
		4.1.3 Image Recording	27
		4.1.3.1 Camera and Film	
		4.1.3.2 Camera focusing	28
		4.1.3.3 Film development	
	4.2	Interrogation	
		4.2.1 Hardware	
		4.2.2 Software	
	4.3	Vector Cleanup	
		4.3.1 Cleanvec Software	
		4.3.2 Cleanup Procedure	
	4.4	Data Storage and Manipulation	
5	Bou	ndary Layer Flow Statistics	38
	5.1	Documentation of Data	. 38
		5.1.1 Data Overview	. 38
		5.1.2 Flow Conditions	
		5.1.3 Boundary Layer Parameters	
		5.1.4 Resolution of Principle Data Set	
	5.2	Comparison with Previous Results	
		5.2.1 Mean Horizontal Velocity Profiles	
		5.2.2 RMS Velocity Profiles	
		5.2.3 Statistical Sampling Uncertainty	
	5.3	Effect of Trip Location	. 47
6	A 200	lysis of Instantaneous Data Fields	40
U	6.1	Interpreting two-dimensional planar velocity measurements	
	0.1	6.1.1 Convection Velocity	
		6.1.2 Random two-dimensional measurements of a three-dimensional phenomeno	
	6.2	Uniform Momentum Zones	
	0.2	6.2.1 Introduction to Zones	
		6.2.2 The Role of Hairpin Vortices	
		6.2.3 Autogeneration by Hairpin Vortices	
	6.3	Large-scale patterns in the boundary layer	
	0.0	6.3.1 High Reynolds No. Large-scale Patterns	
		6.3.1.1 Sawtooth	
		6.3.1.2 Long Uninterrupted Growth	
		6.3.1.3 Half-Diamond	
		6.3.1.4 Constant Height Layer	
		6.3.2 Low Reynolds No. Large-scale Patterns	
		6.3.2.1 Sawtooth	
		6.3.2.2 Long Uninterrupted Growth	
		6.3.2.3 Half-Diamond	
	C A	Observations of Out-of-Plane Motion	74

	6.5	Analysis of Zone Growth Angles
7	Con	lusions, Conjectures, and Recommendations
	7.1	Conclusions
	7.2	Conjectures
	7.3	Recommendations
$\mathbf{A}$	PPE	DIX 83
A	Velo	ity Vector Plots
$\mathbf{R}$	EFEI	ENCES 381

# LIST OF FIGURES

Figure	P	age
3.1	Schematic Diagram of PIV Setup: Particles in object plane are illuminated by a laser light sheet and the scattered light exposes film in the image plane	16
3.2	Schematic diagram of interrogation: Film is back illuminated with light, then individual interrogation spot is digitized by camera and autocorrelated by computer	
	individual interrogation spot is digitaled by carnera and advocorrelated by computer	10
4.1	Diagram of light-sheet forming optics: top and side view. Beams are combined,	
	formed into sheets, and reflected upwards into the test section	
4.2	Diagram of Windtunnel Test Section	
4.3	Schematic diagram of camera setup	
4.4	Organization of Data Files	30
5.1	Streamwise variation in the momentum thickness $\theta$ with linear curve fit	41
5.2	Comparison of Mean Velocity Profiles with data from Meinhart (1994)– plotted	
	with inner variables	43
5.3	Comparison of Mean Velocity Profiles with data from Meinhart (1994) – plotted	40
E 1	with outer variables	
$5.4 \\ 5.5$	Horizontal RMS Velocity Profiles—scaled with inner variables	
5.6	Vertical RMS Velocity Profiles—scaled with inner variables	
5.7	Vertical RMS Velocity Profiles—scaled with outer variables	
5.8	Low Reynolds Number Velocity Profiles with Different Trip Locations	
	•	
6.1	(a) Inclined shear layers (hairpin vortices) aligned in the streamwise direction	
	over $3\delta$ — high Reynolds No. case. (b) Hairpin vortices aligned in the streamwise	
<i>c</i> 0	direction over $2.5\delta$ — low Reynolds No. case	52
6.2	Low Reynolds No. data containing hairpin vortex signatures consistent with computational results showing autogeneration of hairpin-like vortices	55
6.3	Large-Scale Patterns in High Reynolds No. Flows.	
6.4	Example of high Reynolds No. sawtooth pattern—zone region enlarged to reveal	50
0.1	three hairpin vortex signatures aligning in the streamwise direction	58
6.5	Example of high Reynolds No. sawtooth pattern	
6.6	Enlarged regions of sawtooth pattern: (a) Hairpin vortex signatures aligned	
	streamwise composing low-speed region. (b) HVS/Inclined shear layers aligned	
	streamwise composing near-wall low-speed region	61

6.7	Example of a long uninterrupted growth pattern. The enlarged area reveals Zone	
	II hairpin vortex signatures and Zone I inclined shear layers	63
6.8	Example of a half-diamond pattern	65
6.9	Enlarged regions of a half-diamond pattern: (a) Two trains of hairpin vortex	
	signatures, one nested within another. (b) The border of a low and high speed	
	region marked with transverse vortices	66
6.10	Example of a relatively constant height layer	68
6.11	Enlarged regions of a constant height layer pattern. (a) Transverse vortices	
	marking the border between low and high speed fluid. (b) Inclined shear layers	
	align in the streamwise direction near the wall	70
6.12	Example of a low Reynolds No. sawtooth-like pattern	72
6.13	Example of a long uninterrupted growth large-scale pattern in a low Reynolds	
	No. flow. Enlarged region reveals two sets of vortices contributing to Zones I and	
	II respectively	73
6.14	Example of half-diamond large-scale pattern for low Reynolds No. flow. Enlarged	
	area reveals inclined shear layers aligned streamwise near the wall	75
6.15	Out of Plane Motion Interrupting a Low Speed Near-wall Layer	77
6.16	Probability density function of growth angles from wall for low speed uniform	
	momentum zones.	78

# LIST OF TABLES

Table	Page	
4.1	Interrogation Hardware Parameters. Note the LN case has two values of $\theta$ based on two trip locations	ı
4.2	Interrogation Software Parameters. Note "Particle Image Diameter" is not the	
4.0	actual image diameter but an interrogation parameter	
4.3	Discrete weighting function w used in Vector Interpolation	
5.1	Summary of PIV Images Acquired and Flow Conditions. <sup>1</sup> Atmospheric pressure was assumed to be $101.3kPa$ . Maximum error in $Re_{\theta}$ due to variation in local pressure is estimated to be $\pm 1.8\%$	)
5.2	Boundary Layer Flow Parameters	
5.3	Resolution of the Interrogation Images	
6.1	Frequency of Occurrence of Large-scale Patterns in High Reynolds No. Data.  The patterns are not mutually exclusive	,
0.0	•	
6.2	Frequency of Occurrence of Large-scale Patterns in Low Reynolds No. Data 71	

### CHAPTER 1

#### Introduction

Recent experimental results (Meinhart and Adrian 1997) [29] and computational results (Zhou et al. 1997) [45] have provided a new outlook on the turbulent boundary layer, particularly concerning the role of hairpin-like vortices. The experimental results are two-component particle image velocimetry (PIV) measurements in the x-y plane with streamwise field of view  $\approx 1.5\delta$ . The data reveals uniform U-momentum zones of fluid often composed of packets of hairpin-like vortices. The computational results introduce the concept of hairpin vortex autogeneration, where given an existing vortex additional vortices can form both up and downstream. The present work is an experimental PIV study of the turbulent boundary layer. U and V velocity components were measured in the x-y plane over a streamwise field of view of  $\approx 3\delta$ . Approximately 50 realizations were performed at each of two Reynolds numbers:  $Re\theta = 1015$  and 7705. The experiment aims to confirm observations of uniform momentum zones and vortex packets, and provide insight into the nature, extent, and large-scale behavior of these structures.

#### 1.1 Motivation

The turbulent boundary layer is important in numerous engineering problems. Applications range from air flow over a car or airplane to liquid flow over a heat exchanger. The fundamental mechanisms of heat and momentum transfer in all applications are controlled by the dynamics of the turbulent boundary layer. Understanding the fundamentals of this flow will improve modeling and control in these practical applications.

## 1.2 Hairpin Vortices in the Turbulent Boundary Layer

This investigation focuses on the nature of coherent structures within the boundary layer. No universal definition of a coherent structures exists at this time, but Robinson (1991) [38] offers the following general definition: A three-dimensional region of the flow over which at least one fundamental flow variable (velocity component, density, temperature, etc.) exhibits significant correlation with itself or with another variable over a range of space and/or time that is significantly larger than the smallest scales of the flow. The concept that such structures exist and play a fundamental role in turbulence production and dissipation has been studied for around 40 years. Within the past 15 years or so, a base of evidence has accumulated that suggests one particular structure plays a crucial role in boundary layer dynamics: the horseshoe or hairpin-like vortex.

The existence of hairpin-like vortices was suggested by Theodorson (1952) [40]. Theodorson's model consisted of a horseshoe shape vortex extending upwards from the wall inclined at an angle downstream. As the vortex head grows from the wall and the legs remain attached the vortex shape changes, to become more hairpin-shaped. Hence the term "hairpin-like vortex". In this work, this term describes all vortices of this fundamental type regardless of aspect ratio or size.

These vortices were most clearly viewed in the boundary layer in a landmark experiment by Head and Bandyopadhyay (1981) [18]. They used flow visualization with a light sheet inclined  $45^{o}$  downstream to view horseshoe or hairpin shaped structures inclined at the same angle. These vortices appeared to dominate the boundary layer up to  $Re_{\theta} = 10,000$ . These results are consistent with those made by Falco in 1977 [14] and others since 1981.

Turbulent boundary layer models have also reflected these results, beginning with Perry and Chong (1982) [33] who suggested the boundary layer consists of a forest of  $\Lambda$ -shaped vortices originating from the wall. This model was extended in 1986 by Perry et al. [34] who propose that the spectral Kolmogoroff region is created by detached isotropic eddies surrounding the attached  $\Lambda$ -shaped vortices. Recently, Perry and Marusic (1995) [35] further adapted this model to incorporate a second set of vortices, unattached from the wall, also  $\Lambda$ -shaped but with a wide variety of orientations.

These efforts have been crucial in the discovery of hairpin-like vortices in the boundary layer, and important in understanding the role that these vortices play in the flow. However, recent work with direct numerical simulation and planar measurement techniques has offered significant advances in this area.

## 1.3 Recent Advances in Understanding Hairpin Vortices

Meinhart and Adrian (1995, 1997) [28] [29] used particle image velocimetry (PIV) to measure U and V velocity components in the x-y plane of a boundary layer with a field of view of  $1.5\delta$  streamwise. They observed velocity vector patterns that would exist if the measurement volume were to slice down the center of a hairpin-like vortex. These vector patterns often align in the streamwise direction, and the authors concluded these "vortex packets" play an important role in the flow.

Each hairpin-like vortex induces flow upwards and backwards between its legs as it convects downstream, so a packet of these vortices along the wall would create a long streak of low speed fluid with an "ejection" behind each vortex. The authors believed these vortex packets may create the "low-speed streaks" and "bursting" process often observed in the boundary layer, as in Kline et al. (1967) [24]. Indeed, hot-wire like signals extracted from the PIV data compare well with "hot-wire burst signatures" from established results such as Luchik and Tiederman (1987) [26].

Additionally, Meinhart and Adrian observed large, time-varying zones of uniform U-momentum fluid in the flow. These zones are bordered by thin shear layers in which spanwise vorticity exists in concentrated regions. The authors classify a low-speed zone growing from the wall as Zone I, and a faster moving uniform momentum region above this a Zone II. These zones appear to contain the vortex packets described earlier, which induce the observed low-speed fluid along the wall.

Zhou et al. (1997) [45] used computations to show that given an existing large "primary" hairpin-like vortex, additional smaller "secondary" hairpins can be induced both upstream and downstream from the original vortex. This result is believed to explain the observations of vortex packets in the experimental work. Indeed, the measurements included examples of smaller vortices existing upstream of larger ones, consistent with the computational results.

#### 1.3.1 Unresolved Issues

The recent experimental results have provided a new outlook on the turbulent boundary layer, and greatly improved understanding of the role of the hairpin vortex in the flow. However, many issues are unclear, particularly those considering larger regions of the flow, wider than the streamwise field of view of  $1.5\delta$  in these photographs. The present experiment is an effort to make these large-scale issues, described below, clearer.

#### 1.4 The Present Work

Film particle image velocimetry was used to measure U and V velocity components in the x-y plane of a turbulent boundary layer. In the principle data set the streamwise field of view was  $3\delta$ , roughly twice that of the previous results. Tests were conducted at two Reynolds numbers,  $Re_{\theta} = 1015$  and 7705, to compare with the lowest and highest  $Re_{\theta}$  of Meinhart and Adrian (1997) [29]. Approximately 50 realizations were interrogated at each Reynolds No.

This wide field of view data set makes it possible to confirm several interesting results from the earlier work and investigate several important unresolved issues. The data confirms the existence of uniform momentum zones growing from the wall often composed of packets of hairpin-like vortices, as in Meinhart and Adrian (1997), and allows observation of the streamwise extent, wall-normal extent, and growth angle of these zones. The data can also be interpreted to improve understanding of the role of the hairpin vortex in the flow. Examples exist in the data providing fresh evidence supporting the computational results concerning hairpin autogeneration discussed in Section 1.3.2: existence of smaller hairpin vortices both upstream and downstream of a larger "primary" hairpin. The wide view results also provide insight on zone interaction. This includes Zone I/Zone II behavior in the near-wall region, and the interaction of large-scale outer structures with zones both near the wall and approaching the outer part of the boundary layer.

### CHAPTER 2

## Background of Turbulent Boundary Layers

### 2.1 Introduction

A great deal of work has been done on coherent structures over the past 30 years or so, creating an enormous amount of literature. This chapter will focus on only those papers that have made the most significant contributions relevant to this topic. For a thorough discussion of turbulent boundary layer background the reader is referred to a review article by Robinson (1990). [38]

It is worth noting that the majority of turbulent boundary layer research to this point has been performed on low-Reynolds number flows ( $Re_{\theta} < 3000$ ), and there is a general consensus [7] that the major Reynolds no. effects occur below this level. (This is often relevant in flow-visualization experiments which are difficult to conduct for high-Reynolds no. flows). Thus, the Reynolds number should be considered in the interpretation of any results.

## 2.2 Early Investigations

Interest in the concept of coherent structures was brought about by a handful of works in the 1950's. Klebanoff (1954) [23] showed that the vast majority of turbulent kinetic-energy production in a boundary layer occurs in the near-wall region, suggesting that organized motions exist in the inner layer. In the same year, Corrsin and Kistler [13] investigated the intermittent nature of the turbulent/non-turbulent interface of a boundary layer. Grant (1958) [16] performed extensive measurements of the two-point velocity correlation function. He found a

significant value of the streamwise velocity correlation  $R_{11}(\mathbf{r},0,0)$  even with large streamwise separation near the wall, indicating a streamwise coherence in this region.

### 2.3 Flow-Visualization Investigations

There were a host of flow-visualization experiments performed in the late 1960's and early 1970's. The first ground-breaking investigation combined flow-visualization by dye-injection with hot-wire anemometry (Kline et al. 1967) [24]. The visual studies made apparent well-organized spatially and temporally dependent motions in the near-wall region, which led to the formation of low-speed streaks. The authors describe a process in which the streaks slowly "lift-up", and then undergo sudden oscillation, bursting, and ejection. This process was believed to play a "dominant" role in the production of new turbulence.

Corino and Brodkey (1969) [12] used a high-speed video camera moving with the flow to observe a process similar to that described by Kline et al. Corino and Brodkey focused on the ejection of fluid from the wall, a three-dimensional disturbance which occurs randomly with respect to time and position. The intensity and frequency of these ejections was found to be a measurable function of mean flow parameters. They did not observe oscillation directly, but believed this process could be accounted for by a sequence of ejections.

Further investigation of the near-wall region was performed by Kim et al. (1971) [22]. As in Kline et al. they combined hot-wire techniques with visual studies, using hydrogen bubbles for qualitative and quantitative results. Kim et al. focused on the area  $y^+ < 100$  and showed that in this region essentially all turbulence production occurs during a process they call "bursting". This process consists of three stages:

- 1. Lifting of low-speed streaks from the wall.
- 2. Growth of oscillatory motion within the streak.
- 3. Breakup of the oscillatory motion into more random motions.

The data suggests but does not prove the oscillatory growth stage is associated with energy transfer from the mean flow to the fluctuations.

Similar visual techniques were also applied to the outer region. Nychas et al. (1973) [31] used a high-speed camera moving with the flow to view solid particles in water. They described

a sequence of events which produced transverse vorticity in the outer region. The first event was a deceleration of the streamwise velocity extending from the wall to the outer region. A second concurrent event was an acceleration of the upstream streamwise velocity, also extending the height of the layer. The faster moving fluid displaced the slower fluid, and moreso in the outer region than the inner, such that an instability occurred between the regions. This instability led to the formation of a large-scale transverse vortex convecting at slightly less than the mean velocity.

In 1978 Praturi and Brodkey [37] used a stereoscopic camera moving with the flow to view three-dimensional aspects of the boundary layer. Two of their conclusions differ from previous results. First, the events in the outer region of the flow initiate the action in the wall region, so that bulges are not composed of inner vortices but outer region transverse vortices. Second, vortex motions in the wall region result from interaction between high-speed free-stream fluid and the region of retarded fluid trapped between the free-stream and the wall. These points contrast with the idea that the vast majority of turbulence production comes from the inner region.

Falco (1977) [14] investigated the outer region using methods similar to that of the Stanford group— i. e. hot-wire anemometers for quantitative measurements and oil-droplet fog injection for flow visualization measurements. Falco's results indicate that two families of motions exist:

- "Typical eddies": These are highly coherent three-dimensional structures which are strongly
  Reynolds number dependent. A wall-normal and streamwise "slice" of a typical eddy reveals a crescent shape, and a wall-normal and stream-normal "slice" reveals a mushroom
  shape.
- "Large scale motions": These are defined by the existence of smoke free regions extending deep into the layer on the upstream and downstream sides of the bulge.

However, hot-wire results obtained in the outer region showed great variation among large-scale motions. Motions with typical eddies would produce significant Reynolds stress, but sometimes large smoke filled regions would pass without a significant uv signal. Finally, Falco noted that when typical eddies are observed at the upstream boundary of large scale motions (the "backs" of bulges) they produce the largest fluctuations in the u, v, and uv signals. Falco also proposes a model discussed in a later section.

Perhaps the most enlightening flow visualization study was performed by Head and Bandyopadhyay (1981) [18]. They also used oil smoke for flow visualization and hot-wire for quantitative measurements, but inclined their light sheet at 45° upstream and downstream. The
light sheet revealed horseshoe or hairpin shaped vortical structures inclined at a characteristic
angle of approximately 45° to the wall which appeared to dominate the boundary layer up to  $Re_{\theta} = 10,000$ . These structures scaled with wall variables  $(u_{\tau}$  and  $\nu$ ) in their cross-stream
dimensions, while their length was only limited by the depth of the layer. Thus, their aspect
ratio is highly Reynolds number dependent and at roughly  $Re_{\theta} < 500$  the large motions appear to consist of individual vortex loops or a few such loops interacting. At higher Reynolds
numbers,  $Re_{\theta} > 2000$ , the large-scale structures appear to consist of random groups of these
elongated vortices, and the large structures do not appear to be remarkably coherent. At
high Reynolds number,  $Re_{\theta} > 10,000$ , a small portion of the vortices remained coherent and
these become incredibly elongated. Head and Bandyopadhyay also noted occasional evidence
of hairpins forming in a regular sequence, such that their tips lie on a line which is angled at
approximately 20° from the wall.

## 2.4 Hot-Wire/Conditional Sampling Investigations

In the 1970's and 1980's conditional sampling of velocity with hot-wire anemometers was commonly used to investigate turbulent bulges and the bursting process near the wall. Typically, researchers would devise a criterion to capture the velocity field for a given event but often had difficulty positively identifying events while avoiding detection for non-events.

## 2.4.1 Pre-conditional sampling

The outer region was studied by Townsend (1970) [41] with the primary focus on entrainment of non-turbulent fluid into the turbulent region. Townsend develops the model of a "double-roller eddy", which consists of two quasi-streamwise vortices inclined at an angle to the wall. This model is described to be responsible for the entrainment process, a continuous deformation and folding of the turbulent interface.

### 2.4.2 Intermittancy Sampling

Kovasznay et al. (1970) [25] conditionally sampled using an intermittancy function:

$$I(x,y,z,t) = \left\{ egin{array}{ll} 1 & ext{for turbulent flow} \\ 0 & ext{for non-turbulent flow} \end{array} 
ight.$$

Manipulating this function allowed them to sample at the backs and fronts of bulges. They identified the superlayer (turbulent/non-turbulent interface) as a highly corrugated surface, and the turbulent bulges as strongly three-dimensional. They describe the outer flow "riding" over the bulges, up on the backs and down on the fronts.

A similar technique was employed by Hedley and Keffer in 1974 [20] to study intermittancy in the outer region. The authors envisioned a picture of entrainment in which the non-turbulent fluid sweeps over back of a turbulent eddy and strains the superlayer. Gradient changes through this layer are sharp, and if a separation of the free stream fluid takes place a wake region develops on the leading edge of the bulge, thus entraining irrotational fluid into the turbulent layer.

Murlis et al. (1982) [30] combined intermittancy sampling with flow visualization and compared their results with those of earlier authors including Falco (1977) and Head and Bandy-opadhyay (1981). Murlis et al. found evidence supporting the idea that hairpin vortex "typical eddies" scale on the viscous length  $\nu/u_{\tau}$ . However, they also found evidence suggesting that at high Reynolds numbers ( $Re_{\theta} > 5000$ ) the shape of the superlayer is controlled by the classical "large eddies" and not by the inner length scales.

#### 2.4.3 Quadrant Detection

Wallace et al. (1972) [44] introduced quadrant decomposition as a means of classifying the instantaneous product signal uv. The classification was based on the sign of the product components u and v, each group being averaged to compute its contribution to the Reynolds stress  $-\rho \overline{uv}$ . Two groups appeared to give large contributions: negative-u/positive-v motion (Q2), which can be associated with an ejection-type event, and positive-u/negative-v motion (Q4), which can be associated with a sweep-type event. The authors determined that in the near-wall region, these two classifications created a stress considerably greater than the net Reynolds stress.

In 1977, Wallace et al. [43] used a short-time temporal average (TPAV) to define the fluctuating streamwise velocity u. The authors developed a pattern recognition scheme using this fluctuating velocity, based on a characteristic gradual deceleration followed by a sharp acceleration. The u-signal patterns were associated with coherent structures observed visually, and the v-signal was found to be approximately 180° out-of-phase with the u-signal.

### 2.4.4 VITA Sampling

Variable-interval time-averaging (VITA) has also been used in determining a conditional sampling event. The VITA of a quantity  $Q(x_i, t)$  is given by

$$Q(x_i, t, T) = \frac{1}{T} \int_{t - \frac{1}{2}T}^{t + \frac{1}{2}T} Q(x_i, s) ds$$
 (2.1)

Blackwelder and Kaplan (1976) [8] used the VITA average and a wall-normal rake of hotwire probes to conditionally sample in the near-wall region. The authors found an interface between low- and high-speed fluid that was inclined towards the wall and associated this with the bursting process. The vertical extent of the structure scaled with inner variables, while the frequency of occurrence scaled with outer variables.

Chen and Blackwelder (1987) [10] used the intermittancy function and the VITA average in conditionally sampling a boundary layer with temperature contamination. Upon heating the wall they measured a sharp temperature front, which in the outer region corresponded to the backs of turbulent bulges. The warmer (wall) fluid was inside the bulges and the cooler fluid was associated with the non-turbulent region between the bulges.

Brown and Thomas (1977) [9] searched for coherent structures with an array of hot-wire probes and a wall shear stress probe. They correlated the streamwise velocity u with the wall shear stress  $\tau_w$ . Using Taylor's hypothesis in computing the correlation they found structures inclined to the wall at approximately 18° with a streamwise length of order  $2\delta$ .

#### 2.4.5 Linear Stochastic Estimation

Adrian (1977) [2] introduced stochastic estimation as a means of estimating conditional averages without conditionally sampling data. The linear stochastic estimate of a conditionally averaged quantity  $y_i$  given event  $\underline{E}$  is given by

$$\langle y_i \mid \underline{E} \rangle = A_{ij} E_j \tag{2.2}$$

The coefficients  $A_{ij}$  are determined by minimizing the mean square error of the estimate. This technique also permits variation of conditional events through algebraic manipulation.

Guezennec (1989) [17] applied stochastic estimation to a turbulent boundary layer. In particular, linear estimation of conditional averages of Q2 and Q4 events agreed very well with conventional ensemble averages.

### 2.5 Numerical Simulation

With the advent of supercomputers numerical simulation has become a valuable technique for understanding turbulence through Large-eddy simulation (LES) and Direct numerical simulation (DNS). LES involves simulating the large scales of the flow while modeling the smaller scales. This allows simulation for higher Reynolds numbers. DNS involves simulation of the smallest scales of the flow, and thus computation of numerous turbulent quantities. However, DNS is limited to low Reynolds number flows because of the vast computing resources required. Spalart (1988) [39] directly simulated a low Reynolds number turbulent boundary layer. He determined that in the range  $225 < Re_{\theta} < 1410$ , certain flow parameters near the wall do not collapse with inner variables ( $\nu$  and  $u_{\tau}$ ).

## 2.6 Turbulent Boundary Layer Models

Coherent structures have been investigated in turbulent boundary layers for several decades. Over the years various authors have developed models based on the accumulation of data in the field.

Kovasznay et al. (1970) [25] proposed a model for the development of turbulent bulges in the outer region. The authors envisioned a burst of fluid moving outward from the wall region, having both a momentum deficit and angular momentum with respect to its new environment. They compare the flow around this low-speed lump of fluid to the flow around a sphere, with a turbulent wake developing in the downstream direction. The lump gradually loses its momentum deficit and becomes the so-called turbulent bulge.

Falco (1977) [14] proposed a model consisting of typical eddies and large scale motions. The model was based on a large-scale turbulent motion slightly inclined to the flow, with a saddle-point at its upper back (between the non-turbulent fluid and the back of the motion).

Large-scale motions align in the streamwise direction, each containing several typical eddies along its back. The model accounts for the seemingly contradictory observation that the average frequency of outer region bursts scales on outer variables, while the extent of the burst scales on inner variables.

More recently, Perry and Chong (1982) [33] developed a model showing the boundary layer as a forest of  $\Lambda$ -type vortices originating from the wall. A hierarchy of eddy scales must exist to give a logarithmic mean velocity profile with constant Reynolds shear stress as the distance from the wall grows, and two possible mechanisms for this are described:

- A vortex-pairing process, which assumes vortices pair to create a discrete system of hierarchies where the scales go in a geometrical progression with a factor of 2. However, the authors note that pairing of two Λ-vortices to create one Λ-vortex with double the circulation appears to be inconsistent with conservation of kinetic energy.
- 2. A growing-eddy process in which the vortex continuously draws vorticity from the wall. The circulation increases in proportion with its scale, and its shape is preserved. The likelihood of survival must diminish with scale to give the appropriate distribution. However, the authors point out here that "there is no obvious mechanism based on the Biot-Savart law for this continuous roll-up with a 'self-preserving-shape' eddy, nor has its existence been definitely established."

Perry et al. (1986) [34] extended the above model to consider the outer region in the flow and a Kolmogoroff spectral region. The authors show that if the p.d.f. of hierarchy lengthscales has an inverse-power-law form, then the logarithmic law of the wall is satisfied and an inverse-power-law spectral region exists for the fluctuating velocity components parallel to the wall. They propose that the Kolmogoroff region is created by detached isotropic fine-scale eddies which surround the attached  $\Lambda$ -vortices and are responsible for most of the turbulent energy dissipation.

Perry and Marusic (1995) [35] further adapted this model to incorporate a second set of vortices. This was necessary in order to obtain correct quantitative results for all components of the Reynolds stresses. Two types of eddies are considered: type A, which are interpreted to give "wall structure" and type B, which are interpreted to give "wake structure". A variety of shapes were considered for type A vortices, including the Λ-type and a simple Π shape,

all of which gave poor quantitative results when analyzed without the second set of vortices. Type B eddies considered were  $\Lambda$ -shaped, but not attached to the wall and widely varying in orientation. Incorporating these vortices into the model gave much better agreement between measured and predicted Reynolds stresses.

## 2.7 Recent work: Observations of Zones

More recently, particle image velocimetry (PIV) experiments have given new insight into vortical structures in turbulent boundary layers. There is evidence of internal layers, or zones, composed of vortices which grow from the wall inside the boundary layer. Urushihara et al. (1993) [42] observed this type of flowfield in pipe flow. Vector plots revealed inner and outer layers existing with a distinctive interface, often marked with shear  $(\partial u/\partial y)$ , described as a "wavy boundary" dividing the high-speed flow from the low-speed flow.

Meinhart and Adrian (1995, 1997) [28] [29] used PIV to investigate instantaneous turbulent boundary layer structure. The authors observed the existence of large, time-varying, irregularly shaped zones with nearly constant streamwise momentum. The data also revealed that these zones are bounded by thin "viscous-inertial" shear layers in which spanwise vorticity is clumped into concentrated vortical regions. A low-speed layer-like zone growing along the wall is classified as Zone I, and a second faster moving layer-like zone above this is classified as Zone II. Zone I is composed of inclined hairpin-like or cane-like structures, and Zone II extends from the top of Zone I to a random height that may reach  $0.6\delta$ . The region containing Zones I and II is associated with the log layer. The data also suggests that turbulent bulges are associated with zones located further away from the wall.

Meinhart and Adrian also observed that the inclined structures contained in Zone I often line up in the streamwise direction. The authors note that although this might be due to "vortex roll-up of viscous shear layers due to classical instability", flow visualization suggests the process is more complex. Horseshoe vortices can be created by a high-speed flow over a low-speed region. In turn, these vortices induce low-speed fluid between their legs, which interacts with relatively high-speed fluid upstream to create another horseshoe or arch-like vortex. In this way a "train" of vortices can be created— this is intuitively appealing, and more importantly has been shown via the direct numerical simulation of Zhou et al. [45] Thus, this hairpin train

induces a long streamwise region of low-speed fluid, which appears as Zone I in an instantaneous planar measurement of the boundary layer.

### CHAPTER 3

# Particle Image Velocimetry: Background and Present Details

## 3.1 Pulsed Light Velocimetry

#### 3.1.1 Introduction

Pulsed light velocimetry techniques estimate the velocity of a fluid by observing the locations of marker images at two or more times. The velocity is estimated using the definition

$$\mathbf{u}(\mathbf{x},t) = \frac{\Delta \mathbf{x}(\mathbf{x},t)}{\Delta t} \tag{3.1}$$

where  $\Delta \mathbf{x}$  is the displacement of the marker located at  $\mathbf{x}$  at time t, over a time interval  $\Delta t$  (Adrian 1991) [5]. Particle locations are recorded optically by pulses of light that freeze the marker images on a medium such as photographic film, a video array detector, or holographic film.

## 3.1.2 Particle Image Velocimetry

In this experiment, planar particle image velocimetry was used with optical recording on photographic film. A schematic diagram of such a setup is shown in Figure 3.1. There are three primary modes of operation of this system, as described in [5]:

 Laser Speckle Mode— here the concentration of particles is so high that the particle images overlap in the image plane, and a "laser speckle" pattern forms from interference between particle images. The velocity is calculated from the displacement of these laser speckle patterns.

- 2. Particle Tracking Mode— here the concentration of particles is so low that individual particle images can be tracked when subject to multiple exposure or streak exposure. The image tracks are short relative to the mean spacing between the particles so that individual particles are easily identified and their displacement measured.
- 3. High-Image Density PIV Mode— this mode occurs when the concentration of particles lies between the above two extremes. Each interrogation spot contains many images, but not so many as to create a speckle pattern, so that the displacement of groups of images is measured.

The last mode was used in this work.

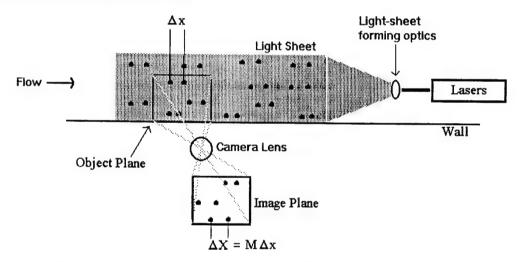


Figure 3.1 Schematic Diagram of PIV Setup: Particles in object plane are illuminated by a laser light sheet and the scattered light exposes film in the image plane

## 3.2 Particle Imaging

The images appearing on the recording medium depend on a great number of factors, including the thickness of the light sheet,  $\Delta z$ , the lens magnification, M, the wavelength of the pulsed light,  $\lambda$ , and the f-number of the camera lens,  $f^{\#}$  (Keane and Adrian 1990) [21]. In the following section several important parameters and their dependence on the above variables will be discussed.

The magnification of the photograph depends on z, and the image-plane displacement of a small object-plane particle displacement is given by

$$\Delta \mathbf{X} = M(0)(\Delta x \hat{\mathbf{x}} + \Delta y \hat{\mathbf{y}}) + M(0) \frac{(x \hat{\mathbf{x}} + y \hat{\mathbf{y}})}{d_o} \Delta z$$
(3.2)

where M(0) is the magnification at z = 0,  $d_o$  is the object distance of the system, and the coordinates are centered on the camera axis [5]. The second term in the equation arises from perspective displacement, in which motion in the x and/or y directions is perceived in the image plane due to z directional motion in the object plane.

The diameter of the particle image is a function of the particle diameter  $d_p$ , the magnification, and the point response function of the lens (the lens response to an infinitely small image) [5]. For a lens limited only by diffraction this point response function is an Airy function (Goodman 1968) [15] with diameter

$$d_s = 2.44(1+M)f^{\#}\lambda \tag{3.3}$$

This point response can be convolved with the geometric particle image  $Md_p$  to estimate the image diameter (Adrian and Yao 1985) [6] as

$$d_{\tau} = (M^2 d_p^2 + d_s^2)^{1/2} \tag{3.4}$$

In this experiment the point response function was approximately  $d_s = 15 \mu \text{m}$ , the particles were nominally 1-2  $\mu \text{m}$  oil droplets, and the magnification was approximately 0.4. Thus, with  $Md_p < 1 \mu \text{m}$ , the particle image size is nearly independent of particle diameter.

The film exposure created by a particle, however, is strongly dependent on its diameter. Adrian and Yao [6] used Mie's scattering theory for homogeneous spherical particles to calculate scattering into a lens whose center is at 90° to the illuminating beam. For an  $f^{\#} \approx 8$ , a 2  $\mu$ m particle can have roughly an order of magnitude greater exposure than a 1  $\mu$ m particle. Nonetheless, a 1  $\mu$ m particle may still scatter enough light to satisfactorily expose the film—this depends on, among other things, laser power and the quantity m, the ratio of the refractive index of the particle  $n_p$  to the refractive index of the fluid n. For this experiment, using oil particles in air,  $m \approx 1.5$  [6]. This is a relatively large value, creating relatively strong scattering.

The particle imaging equations apply when the particle is within the depth of focus of the lens, given by Offutt (1995) [32] and expressed in [5] as

$$\delta z = 4(1 + M^{-1})^2 f^{\#^2} \lambda \tag{3.5}$$

For this experiment the depth of focus is estimated to be  $\delta z = 1.6$ mm. The light sheet thickness at the focal waist was measured (using burn paper) to be 0.25 mm, and the sheet thickness at the wall and in the free stream were calculated geometrically to be 0.36 mm. Thus the light sheet could be completely contained within the depth of focus. A thin light sheet also yields greater light intensity for a given laser power, and minimizes perspective error in the image plane displacement. The minimum light sheet thickness (at the diffraction limited waist) can also be determined by

$$d_w = \frac{2.44\lambda f}{D_{e^{-2}}} (3.6)$$

where  $D_{e^{-2}}$  is the thickness of a collimated Gaussian laser beam [19]. The velocity is estimated from the collection of particle images by the interrogation process.

## 3.3 Interrogation

The photographs in this work were interrogated using the autocorrelation of the intensity in each interrogation spot. A schematic of the interrogation apparatus is shown in Figure 3.2.

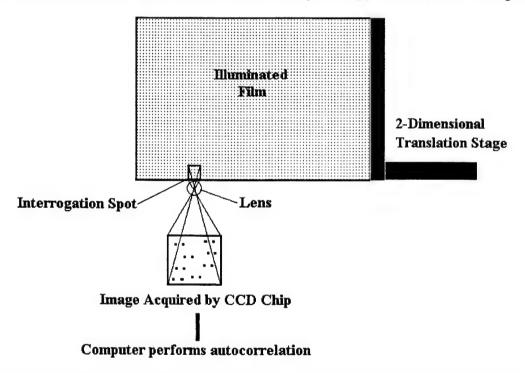


Figure 3.2 Schematic diagram of interrogation: Film is back illuminated with light, then individual interrogation spot is digitized by camera and autocorrelated by computer

The autocorrelation was performed using 2-D spatial correlation of direct images. Given the interrogating beam has intensity  $I_I$  and the photograph has an intensity transmissivity  $\tau(\mathbf{X})$ , the transmitted intensity of an interrogation spot centered at  $\mathbf{X}_I$  is [3]:

$$I(\mathbf{X}) = I_I(\mathbf{X} - \mathbf{X}_I)\tau(\mathbf{X}) \tag{3.7}$$

Then the autocorrelation of this transmitted intensity is given by the following spatial average estimator:

$$\hat{R}(\mathbf{s}) = \int I(\mathbf{X})I(\mathbf{X} + \mathbf{s})d\mathbf{X}$$
 (3.8)

where the vector s is the two-dimensional separation. This autocorrelation signal can be decomposed into 5 components, as in Adrian (1988) [4]:

$$R(s) = R_C(s) + R_P(s) + R_D^+(s) + R_D^-(s) + R_F(s)$$
(3.9)

These terms represent the following parts of the signal, as discussed in [4] and Meinhart (1994) [27]:

- $R_C(\mathbf{s})$  is the background component.
- $R_P(\mathbf{s})$  is the pedestal component, or the self-correlation peak, arising from images correlating with themselves.
- $R_D^+(\mathbf{s})$  and  $R_D^-(\mathbf{s})$  are the positive and negative displacement peaks due to images correlating with their appropriate particle pairs.
- $R_F(s)$  is the fluctuating component, arising from random correlation of non-paired particle images.

The velocity is determined by estimating the centroid of the tallest non-self-correlation peak in the correlation plane, which will correspond to  $R_P(s)$  given a good measurement. If this displacement is  $\mu_{D^+}$  the velocity is estimated from [5]:

$$\mu_1 = \frac{\mu_{D^+}}{M\Delta t} \tag{3.10}$$

Guidelines for optimizing results using double-pulsed auto-correlation have been developed with theoretical analysis and numerical simulations. Keane and Adrian (1990) [21] give the following approximate criteria:

1. 
$$N_I > 10 - 20$$

2. 
$$(u^2 + v^2)^{1/2} \Delta t < \frac{1}{4} d_I / M$$

3. 
$$w\Delta t < \frac{1}{4}\Delta z_o$$

4. 
$$\frac{|\Delta \mathbf{u}|}{\mathbf{u}} < 0.2$$

where  $|\Delta \mathbf{u}|$  is the velocity variation over the measuring volume due to local gradients. Adhering to this criteria, one may make valid measurement in over 90% of the interrogation spots. The specifics of the interrogation in this experiment are given in the following chapter.

#### 3.4 Sources of Error

One consequence of the double-pulsed autocorrelation method is that the estimated velocity signal is biased against high-velocity particles within a given interrogation spot. This is because these particles are less likely to have images from both pulses within the interrogation region due to the larger separation, and are thus less likely to contribute accurately to the correlation. This phenomenon, known as velocity bias [5] only comes into play when a significant velocity gradient exists over the interrogation region, and can be minimized by maintaining a high number of particles in the interrogation spot.

The uncertainty in separation depends upon the algorithm used to compute the image positions and the image diameter  $d_{\tau}$ . Adrian (1986) [3] assumes the uncertainty is proportional to image diameter so that

$$\sigma_{\Delta X} = c d_{\tau} \tag{3.11}$$

where c is a number that depends on the accuracy of image location. If one can neglect errors in timing, which is the case in this work, then the accuracy of velocity (expressed as a fraction of  $u_{max}$ ) becomes [3]:

$$\frac{\sigma_u}{u_{max}} = c \frac{d_\tau}{\Delta \mathbf{x}_{max}} \tag{3.12}$$

Thus, high accuracy requires small particle size relative to particle displacement.

### CHAPTER 4

## **Experimental Procedure**

The experimental procedure consisted of three basic phases. The first phase was the acquisition of PIV photographs. This required focusing laser light sheets into a seeded boundary layer wind tunnel, storing double-pulsed particle images with a film camera, and developing the film. The second phase involved interrogating the developed negatives to produce raw velocity data. The final phase consisted of the "cleanup" of these raw velocity data files, and subsequent analysis of the cleaned velocity data.

## 4.1 Experimental Apparatus

#### 4.1.1 Lasers and light-sheet forming optics

#### 4.1.1.1 Lasers

The lasers used in this experiment were two Continuum Surelite II Nd:YAG lasers which produce light at  $\lambda = 532$  nm while pulsing at a maximum rate of 10 Hz. The lasers produce approximately 200 mJ per pulse (@  $\lambda = 532$  nm) with a pulse width around 5 ns.

Within the laser housing, two laser cavities produce infrared beams ( $\lambda = 1064$  nm) which are combined with a beam-splitting polarizer. One laser, hereafter referred to as "PIV1", lases directly into the polarizer. The other laser, hereafter referred to as "PIV2", reflects from two precision-adjustable high-energy mirrors, and then meets the polarizer. These two mirrors allow for relative adjustment of the two beams, and thus alignment of the light sheets. Once the beams are combined they enter a frequency doubling crystal, from which emerges the observed green light. The beams then reflect from two additional precision-adjustable high-energy mirrors—

these mirrors allow for the positioning of both lasers. Typically, the PIV1 beam must be set using the second set of mirrors, and then PIV2 can be adjusted to match it using the first set of mirrors.

#### 4.1.1.2 Laser Timing

The lasers are timed using a Stanford Research Systems, Inc. four channel digital delay/pulse generator, Model DG535. The timing box is accurate to less than a nanosecond, and contains an internal timebase which was set to match the recommended laser operating frequency of 10 Hz. Channel A and Channel B triggered the flashlamp and Q-switch, respectively, of PIV1. Likewise, Channels C and D triggered the flashlamp and Q-switch, respectively, of PIV2. The Q-switch delay time for both lasers is 190  $\mu$ s, so the timing equations entered in the delay menu were simply the following:

- $A = T_o$  (internal time base).
- $B = A + 190 \mu s$ .
- $C = A + \Delta t$  ( $\Delta t$  is the time between pulses).
- D = C + 190  $\mu$ s.

The equations would take a slightly different form if the Q-switch delay times were not the same for the two lasers.

#### 4.1.1.3 Light-sheet forming optics

Upon emerging from the laser housing the beams enter the light-sheet forming optics, which are set with the lasers on a Newport optical table. A diagram of the light-sheet forming optics is shown in Figure 4.1. A top view is given on the left side of the figure, and a side view on the right. The optics consist of several components:

- Negative Horizontal Cylindrical Lenses (L1, L3, L4)— these spread the beam out into a sheet.
- 2. Positive Vertical Cylindrical Lens (L2)— this focuses the beam to thin the sheet, so that the thinnest point is in the middle of the boundary layer.

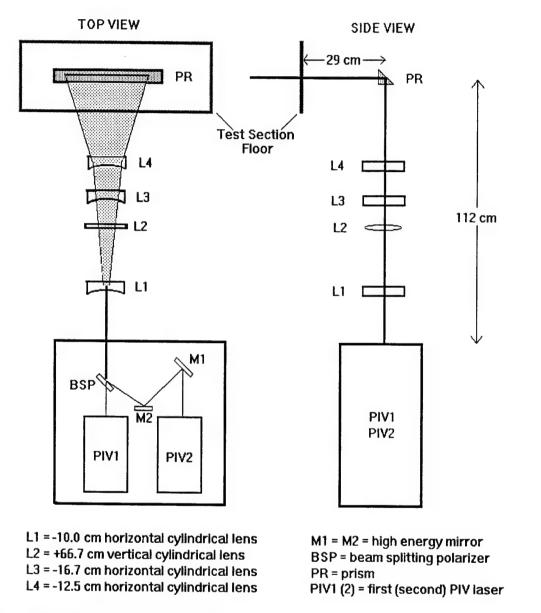


Figure 4.1 Diagram of light-sheet forming optics: top and side view. Beams are combined, formed into sheets, and reflected upwards into the test section.

3. Prism (PR)— this reflects the light sheet 90° so that it becomes vertical and passes through the test section floor.

For the main data set, the light sheet has spread to 25 cm when it meets the test section floor, and continues through the fluid until it reaches the test section ceiling where it is absorbed with black cloth. Data sets with this light sheet are referred to as "wide" because of the relatively wide field of view. Additional data sets were taken with a light sheet of 19 cm— these are referred to as "narrow" because of the slightly smaller field of view.

The center of both light sheets was located at x = 5.31 m from the leading edge of the plate. As discussed in Chapter 3, the thickness of the focal waist (the thinnest part) of the light sheet was measured to be around 0.25 mm, located at a y-location of approximately 4 cm. The light sheet spread to a greater thickness at the wall and the free stream, where based on a geometric calculation from the focusing lens the thickness was approximated as 0.36 mm (assuming a beam width of 6 mm).

The light sheet was aligned in the following manner. A string was placed at the ceiling of the test section in the streamwise direction, suspended at each end in the very middle (spanwise) of the tunnel. A second string was placed underneath the test section, again aligned in the streamwise direction. The light sheet was considered vertical and streamwise when it i)struck the lower string completely and ii)struck the upper string completely when the lower one was removed. The verticality was double checked by placing a T-square on the test section floor. The z-location and the streamwise orientation of the light sheet were doubled checked with a ruler on the test section floor.

#### 4.1.2 Low-turbulence Windtunnel

The flow facility was a low-turbulence windtunnel manufactured by *Engineering Laboratory Designs*. A thorough description of the windtunnel design, operation, and performance is given in Meinhart (1994) [27], and will not be repeated here. However, a general description of the tunnel will be given with features relevant to this experiment.

The wind tunnel is an open circuit Eiffel type. Air is drawn in through an elliptical inlet and travels through a series of screens and honeycomb to minimize inlet turbulence [27]. The air then enters a contraction, where it is accelerated into the test section. The flow rate is

controlled with the fan speed (electronically) and fan blade pitch (pneumatically). The test section flow speed ranges from about 0.65 m/s to 30 m/s.

#### 4.1.2.1 Test Section

The test section is constructed of aluminum, Plexiglas and float glass [27]. It is 609.6 cm long to allow for growth of the boundary layer, and 91.4 cm wide. This width is roughly ten times greater than the height of the thickest boundary layer studied in this experiment in order to minimize side effects. The height of the section is 45.7 cm, but can be lowered to adjust the pressure gradient as desired. The pressure is measured with static pressure taps placed every 30.5 cm streamwise on the boundary layer plate. A diagram of the test section is shown in Figure 4.2. The boundary layer plate consists of two aluminum frames, each fitted with a float

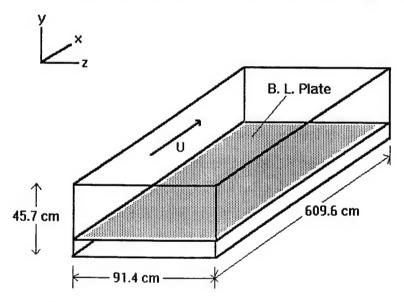


Figure 4.2 Diagram of Windtunnel Test Section

glass piece with dimensions 1.27 cm thick x 61.0 cm wide x 274.3 cm long. The leading edge of the boundary layer plate was machined into an elliptical shape, preventing flow separation. Measurements were taken over the 2nd float glass piece, from x = 517 cm to x = 541 cm (x = 0 at the leading edge). A 4.7 mm diameter rod was placed flat on the test section to trip the boundary layer. The trip was located at x = 152 cm in the LW case and at x = 11 cm in the HW case.

There is a slight downward lip at the front of this glass where it meets the aluminum housing, at x = 320 cm. This lip is located 209 cm upstream of the *center* of the light sheets, and is  $0.14 \pm 0.02$  mm in height, which is 3 percent of the boundary layer trip height. As a measure of caution two simple calculations have been made to determine if the lip might shed vortices.

First, the height of the trip was measured in terms of inner units for the smallest turbulent length scale, and it was determined that  $h^+ \approx 3.5$ . This is less than the roughness required effect the flow according to conventional wisdom.

Secondly, a "Vortex Shedding" Reynolds number based on the analysis of Acarlar and Smith (1987) [1] was calculated. The authors studied vortex shedding from a hemisphere in a laminar boundary layer, defining a Reynolds number  $Re_R = \hat{u}R/\nu$ , where  $\hat{u}$  is the velocity jump across the hemisphere and R is the radius of the hemisphere. They found regular shedding is initiated at  $Re_R \approx 120$ . In the calculations for the lip the radius R was substituted with the lip height h. The velocity jump across the lip was calculated by assuming a linear profile near the wall and estimating dU/dy from the wall friction velocity  $u_{\tau}$ . The highest value of  $Re_R$  determined was 14, only about one-tenth of that estimated by Acarlar and Smith to initiate regular vortex shedding. Based on the above calculations and the absence in the data of some height at which vortices predominantly exist (as might be expected if the lip were regularly shedding them), it was determined the lip does not significantly effect the flow.

#### 4.1.2.2 Windtunnel Performance and Instrumentation

The windtunnel performance has been evaluated in Meinhart (1994) [27]. He estimated the free-stream turbulence intensity throughout a cross section at x = 65 cm to be 0.16%.

As mentioned above, the windtunnel contains 23 static pressure taps for determination of the streamwise pressure gradient. The pressure taps are attached to a Scanivalve W2 fluid switch wafer which allows for measurement of any given tap with a Validyne DP103 wet-wet differential pressure transducer [27]. The pressure transducer signal is then read with a Validyne model CD23 converter digital transducer indicator which digitally displays the pressure in inches of water. This system is accurate to 0.00025 inches  $H_20$ . Scanning through the series of pressure taps and adjusting the test section ceiling ensured a zero-pressure gradient boundary layer.

The flow was seeded using a nozzle-based olive oil atomizer [27] designed to create large amounts of particles, nominally 1-2  $\mu$ m. Due to entrainment in the boundary layer, a large inlet

area must be seeded in order to ensure a uniform density of particles in the measurement area. This was achieved by dividing the seeded flow into 11 nozzles, the outflow of which was mixed with a box fan. The box fan did not significantly effect the freestream turbulence intensity.

The windtunnel freestream speed was measured with a pitot tube. For the low Reynolds number case the highly accurate pressure transducer discussed earlier was used, while for the high Reynolds number case a manometer was used.

#### 4.1.3 Image Recording

#### 4.1.3.1 Camera and Film

The scattered light from particles in the light sheet was recorded with a large format camera. The camera consisted of a shutter, lens, and film plate mounted on two parallel rods. The lens plane and image plane location could be adjusted along the rods, and the height of these planes could be adjusted along vertical rods. A schematic diagram of the camera setup is shown in Figure 4.3. The camera was modified from its original design. A traverser and micrometer were

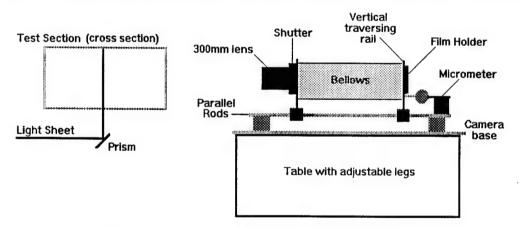


Figure 4.3 Schematic diagram of camera setup.

added to allow for fine adjustment of the image distance, and the table was adapted to allow for rotation of the camera around the vertical axis. These features made fine focusing possible.

The lens is a Carl Zeiss S-Tessar 5.6/300 lens, and the shutter a Copal No. 7. The shutter was set to open for approximately one-tenth of a second, which matched the length between laser flashes. Thus, although the shutter is not timed in coordination with the lasers, nearly every exposure recorded one and only one set of particle images. The shutter aperture was slightly closed to give an  $f^{\#} \approx 8$ . Although this slightly reduced the amount of scattered light

collected by the lens, it slightly increased the depth of focus to ensure all areas of the light sheet were in good focus.

The recording medium was Kodak TMAX-400 4 x 5 inch (102 mm x 127 mm) film. This offers 125 lines/mm resolution and thus stores a great deal of information.

#### 4.1.3.2 Camera focusing

The focusing procedure was critical in achieving clear particle images and thus good results in the autocorrelation. The camera was placed in very rough focus using the desired magnification  $(M = d_i/d_o)$  of the system and the thin lens equation,

$$\frac{1}{f} = \frac{1}{d_i} + \frac{1}{d_o} \tag{4.1}$$

where  $d_i$  and  $d_o$  are the image and object distances respectively, measured from the principal planes of the lens. Rough focus is achieved by placing an object in the light sheet location, and ensuring the camera is at the proper angle, height, and distance.

Fine focus is achieved using the light sheet itself as a target. The test section of the windtunnel is blocked off at either end, and the volume filled with olive oil particles. Frosted glass is placed in the image plane of the camera, so that particle images appear on the glass when the lasers fire. In order to place the particles in focus three adjustments can be made:

- 1. The image plane is translated along the parallel rods to change the image distance with the micrometer.
- 2. The camera itself is rotated about the vertical using set screws located on the table.
- 3. The table surface is rotated by changing the leg height at the front and back.

Proper focusing requires systematic iteration of these steps. The particles are viewed on the frosted glass using an Edscorp 50:1 magnifier, which is earlier set to focus on the inside of the glass. The ultimate test, however, is development of the film and inspection of the particle images.

The optical distances used in this camera focusing were based on a desired magnification, which in turn was calculated from a desired field of view. However, because of the many adjustments during the focusing process, the true magnification is determined by capturing an

image of a ruler when the camera is completely focused and fixed. For the wide field of view data set, this magnification is  $M=0.411\pm0.002$ . For the narrow field of view data set, the value is  $M=0.419\pm0.002$  (The entire width of the film was not used). The magnifications were calculated using both the entire width of the photo and the middle third only, and each method gave similar results, indicating the magnification did not change significantly over the photo area.

#### 4.1.3.3 Film development

The film was developed using a simple 3-step process with freshly mixed chemicals. Film was first placed in TMAX developer for 6.5 minutes, then Kodak indicator stop bath for 30 seconds, and finally Kodak rapid fixer for 5 minutes. The film was agitated according to chemical specifications. The developed film was washed for roughly 25 minutes, and hung to dry. The resulting negatives were interrogated directly.

# 4.2 Interrogation

#### 4.2.1 Hardware

The interrogation procedure involves back illuminating the negative with incoherent (white) light and using the traverser to scan the entire interrogation area spot-by-spot with the CCD camera (as shown in Figure 3.2). The film is placed in a double sided glass slot and illuminated with light from a Fiber-Lite Model 190 Fiber Optic Illuminator, powered by a Staco Energy Productions Co. Power Source Type L1010. This power source can be adjusted to give maximum contrast between the particle images and the background.

The glass slot is moved in discrete two-dimensional increments with two Aerotech Unidex1 Motion Controllers. The film is focused onto a CIDTEC CD 2250 CCD camera with a 10:1 magnifier. Spacers of 35 mm were placed between the magnifier and the camera, which provided the desired field of view while eliminating distortion on the edges of the image. The camera has an array of 512 x 512 pixels, and its field of view was 1.863 mm in both directions. Thus, with an interrogation spot of 256 x 256 pixels, the film interrogation spot size was 0.932 mm. The field of view of the CCD camera was measured by performing a series of interrogations on an image with known particle displacement, and comparing the measured displacement with

the known displacement—this is the calibration process. The calibration area used was a region of a film labeled "PIV CALIBRATION FILM" and dated "11/21/89". The region contained 500 particle images with 0.25 mm displacement at a 45° angle. Thus with a photographic magnification of M=0.41, a film interrogation spot size of 0.932 mm corresponds to 2.27 mm in the fluid. For each interrogation spot, the actual autocorrelation is performed digitally by a *Dell* 386 PC equipped with an FFT board. A listing of several interrogation hardware parameters is given in Table 4.1 for three cases. Note each case is identified as Case (L or H) (W or N)— this denotes (Low or High Reynolds number) and (Wide or Narrow field of view). Thus Case LW is low Reynolds number, wide field of view. A complete listing of interrogation software parameters is given in Table 4.2.

Parameter	LW Case	HW Case	LN Case
$Re_{ heta}$	1015	7705	954, 1325
Video Camera Field of View	1.863 mm	1.863 mm	1.863 mm
Interr. Spot Size	0.932  mm	$0.932 \mathrm{\ mm}$	0.932 mm
Number of Vectors	19440	18792	13680
Photo Magnification	0.41	0.41	0.42
x-distance in fluid	$24.3~\mathrm{cm}$	$24.3~\mathrm{cm}$	$16.5~\mathrm{cm}$

**Table 4.1** Interrogation Hardware Parameters. Note the LN case has two values of  $\theta$  based on two trip locations.

Before interrogation, the camera must be aligned with the film so that the boundary layer wall lies just beneath the first row of interrogation spots. This is achieved by adjusting the angle of the glass slot so that the wall is parallel with the horizontal traverser, and setting the (0,0) home location on the wall.

#### 4.2.2 Software

The interrogation software used was the *TSI* Model 6001 PIV Analysis System Version 3.6. A description of this system can be found in the software manual and in the "manual supplement" located in the interrogation system desk. The relevant interrogation parameters in the software are given in Table 4.2.

All software interrogation parameters were either fixed by the system or chosen to give the best results. The camera field of view is made small enough to give good resolution, but large enough so that a good number of particle pairs are in each interrogation spot, and thus a high

Menu	Parameter	Setting
System Configuration	Number of Pixels	512 x 512
< S >	Pixel Size ( $\mu$ m)	15 x 15
Interrogation Setup	Pixel Resolution	256
< I >	Interrogations per frame	Multiple
< I >	Int. Spot Overlap	50%
< I >	Starting Location (mm)	0, 0
$\langle I \rangle$	Ending Location (mm)	40, 100 (hw)
$\langle I \rangle$	Ending Location (mm)	42, 100 (lw)
< I >	Ending Location (mm)	42, 70 (ln)
< I >	Peak Search Zone	Right
Interrogation Hardware	Particle Image Diameter $(\mu m)$	30
$\langle H \rangle$	Central Peak Diameter (µm)	75
< H >	Photo Magnification (wide view)	0.41
< H >	Photo Magnification (narrow view)	0.42
< H >	Image Shift	0
< H >	Delta t, Low Re $(\mu s)$	300
< H >	Delta t, High Re (µs)	44
< H >	Camera Field of View (mm)	1.863 x 1.863
< H >	Interrogation Spot Size (mm)	$0.932 \times 0.932$
< H >	Columns to Exclude	5
Calibration	Particle Image Diameter $(\mu m)$	20
< C >	Displacement (mm)	0.25
< C >	Number of Calibrations	10
Data File Management	Family Name	lw, hw, or ln
< D >	< D > Path	

**Table 4.2** Interrogation Software Parameters. Note "Particle Image Diameter" is not the actual image diameter but an interrogation parameter.

percentage of vectors are valid. The  $\Delta t$ 's were chosen so as to give a free stream displacement of about 1/4 of the interrogation spot size, as discussed in the autocorrelation background section. The calibration is performed by interrogating a photo with known particle size and displacement—this calculates the camera field of view (and interrogation spot size).

The interrogation for each wide view picture took approximately 7 hours, and approximately 5 hours for each narrow view realization. Upon completion, the raw velocity data was stored in a data file on the PC. For each vector, the raw file contained an x and y location and the u and v velocity components for the first, second and third highest displacement peaks in the autocorrelation plane. The additional velocity choices may be used later in the vector cleanup.

Prasad et al. (1992) [36] distinguished two types of errors in PIV interrogations. The first, mean bias errors, arise when the pixel size approaches the particle image diameter ( $\frac{d_{\tau}}{d_{pix}} < 4$ ). This occurs during the calculation of the peak location in the autocorrelation plane. In this experiment, the particle image diameter was directly measured to be  $d_{\tau} \approx 30 \mu \text{m}$ , while the pixel size was calculated to be  $d_{pix} = 3.5 \mu \text{m}$ . Thus, the ratio  $\frac{d_{\tau}}{d_{pix}}$  is greater than 8 and mean bias error is not significant.

The second type of errors discussed, random errors, are due to imperfections in the particle images, film grain and electronic noise, the peak location method, and the interrogation technique. For the auto-correlation technique, using centroiding for peak location, Prasad et al. calculate the random error to be 0.07  $d_{\tau}$ . Thus, the random error is approximately 2.1  $\mu$ m on the film, which corresponds to about 5  $\mu$ m in the fluid. This displacement error gives a velocity error of approximately 1% of the free stream velocity.

## 4.3 Vector Cleanup

### 4.3.1 Cleanvec Software

Cleanvec software is an interactive post-interrogation program written by Carl Meinhart (for a detailed description see [27]) that runs on Silicon Graphics workstations. Cleanvec can run in two modes: automatic, which performs a specific set of commands on an entire vector plot, and manual, which performs user entered commands on a vector-by-vector basis. Automatic mode was used here because of the large number of vectors in each plot.

Raw files from the TSI-6001 system were transferred to the Silicon Graphics machine 'i.tam.uiuc.edu', and were slightly modified in order to be read in by Cleanvec. This modification involved removing some preliminary lines in the file and removing certain characters from each column. A very brief script program was written to do this, and it is stored on 'i' in the /usr/people/ctomk/tools directory as "process". A description of how to use this is given in the TSI-6001 manual supplement. Once files had been processed, they were read into Cleanvec in the default format.

#### 4.3.2 Cleanup Procedure

The following procedure was used for the cleanup of all vector plots. It assumes the raw data file has been read into Cleanvec (**bold face** indicates a Cleanvec command).

- Set Mean Velocity: This sets the velocity component(s) which is averaged in the calculated statistics— this was set to U.
- 2. Set Average Type: This sets the direction(s) in which the above velocity component is averaged—this was set to x, so that the u-component of the flow is averaged in the x-direction and subtracted off from each row of data. For viewing the cleaned vector data a choice of x and y averaging is best, but it is appropriate to search for erroneous vectors having subtracted out the mean velocity profile (x-average).
- 3. **Zoom**: This command was used to move and size the vector plot to fill the screen area and choose a vector length which allowed for easy viewing of the vectors.
- 4. Edit Vectors—Tolerance: In the Edit Vectors menu, the Tolerance choice allows for removal of vectors based on a global tolerance test. This requires each vector to be within a specified number of standard deviations from the mean, calculated in the way discussed above. A value of 4.0 was set for both the u and v velocity components. The Toggle Show Tolerance command was selected to view which vectors would be removed under this criterion, and the Enforce Tolerance command was used to remove these vectors. Cleanvec then recalculates the mean and standard deviation, and highlights vectors which would be removed if the tolerance were enforced again. Thus, the enforcement is iterated until i) no "bad" vectors remained or ii) a group of apparently good vectors would be removed if the tolerance were enforced. This usually took three or four enforcement iterations.
- 5. Edit Vectors— Magnitude Difference: This choice allows for removal of vectors based on a local magnitude difference test. The magnitude difference is a measure of the difference between a given velocity vector and the mean at its location. It is defined by

$$MagDiff = \sqrt{\frac{(u - u_{ave})^2}{u_{rms}^2} + \frac{(v - v_{ave})^2}{v_{rms}^2}}$$
(4.2)

where u and v are the velocity components of the given vector and  $u_{ave}$  and  $v_{ave}$  are the average neighborhood velocity components. The magnitude difference of the vector in question is required to be within a user-specified number Md of the median magnitude difference of the surrounding vectors. The operator may enter two values of Md to break the vectors into three groups—accept, remove, or questionable. In this procedure, both values were set to Md = 2.0, which simply breaks the data into accept or remove groups. The Toggle Show Mag. Diff. command was used to highlight which vectors would be removed, and the Enforce Mag. Diff. command used to remove them. The statistics were recalculated and the vectors outside of the specified magnitude difference range again highlighted. As with the tolerance, this normally required 3 or 4 enforcement iterations.

- 6. Edit Vectors—Replace with Alternatives: This option replaces removed vectors with the 2nd or 3rd peak choices from the autocorrelation plane. The user specifies a u and v tolerance, and if an alternative choice is within this tolerance Cleanvec will replace the removed vector with the alternative one. If more than one alternative are within the user specified tolerance, Cleanvec selects the one with lowest magnitude difference. Tolerance settings of 3.5 were chosen for both u and v velocity components, which is more restrictive than the tolerance given earlier because we are no longer working with first choices.
- 7. Edit Vectors— Magnitude Difference: Cleanvec has recalculated the statistics with the replaced vectors, so it is necessary to perform further iterations of magnitude difference (using 2.0 for both entered values of Md) until outlying vectors are completely removed.
- 8. Edit Vectors— Tolerance: Final iterations of the tolerance removal are performed with values of 4.0 for both the u and v velocity components.
- 9. Fill Vectors: This command allows the user to interpolate for a removed velocity vector based on surrounding vectors. It requires an input parameter IP between zero and one, which is a measure of the percentage of neighboring vectors present required to interpolate in a given vector location. The actual measure of neighboring vectors present is calculated for each vector location X in question using the discrete weighting function w given in Table 4.3 and normalizing.

0	0	1	0	0
0	2	4	2	0
1	4	X	4	1
0	2	4	2	0
0	0	1	0	0

Table 4.3 Discrete weighting function w used in Vector Interpolation.

For this experiment an input parameter value of IP = 0.7 (70%) was used. If the required neighborhood vectors are present, the interpolated velocity vector is then calculated using the following convolution:

$$\mathbf{u}(\mathbf{x}') = \int \mathbf{w}_{\mathbf{n}}(\mathbf{x} - \mathbf{x}')\mathbf{u}(\mathbf{x})d\mathbf{x}$$
 (4.3)

where  $\mathbf{w_n}$ , the weighting function, is the function  $\mathbf{w}$  in Figure 4.3 normalized.

- 10. Save to Raw File: The cleaned vector plot is saved to its raw file, although the original can always be retrieved using the Reset Vector Field command.
- 11. Smooth the Data: The data is smoothed by convolving the vector field with a Gaussian kernel given by:

$$G(\mathbf{x} - \mathbf{x}') = \exp(-\frac{(\mathbf{x} - \mathbf{x}')^2}{\mathbf{x}_k^2})$$
(4.4)

where  $\mathbf{x}_k$  is the size of the kernel defined in grid spacing units. The low Reynolds No. data are smoothed with a kernel size of  $\mathbf{x}_k = 0.7$ , while the high Reynolds No. data are smoothed with a kernel size of  $\mathbf{x}_k = 0.8$ . The process of smoothing saves the data to a *smooth* format file, where it can be manipulated further using *short* format programs discussed below.

# 4.4 Data Storage and Manipulation

A series of *short* format programs (also written by Carl Meinhart) exist which calculate a variety of statistics of the data. *Smooth* format files are converted to *short* format using the "smooth2short" program, and then the smooth files are deleted. The resulting set of short files can then be manipulated using the *short* format programs.

In this analysis, two sets of short files were created for each wide view Reynolds number. The principle data sets were created using a smoothing kernel of 0.7 for the low and 0.8 for the high, as discussed above. In addition, two more data sets were created using a kernel of 1.5. These short files were used in creating U- and V-contour plots, as they eliminate noise in the contours without significantly altering the fundamental contour shapes. The lower kernel data sets are stored as "lw.sh[001-052]" and "hw.sh[001-051]", while the higher kernel smoother data sets are stored as "lw.sht[001-052]" and "hw.sht[001-051]". All statistics, unless otherwise specified, are calculated using the low kernel files.

The low Reynolds No. narrow view data is broken down into two groups, labeled "lna" and "lnb". The third letter denotes trip location, which was altered keeping all other variables constant. Only one set of short files were created for each of these data sets, using a kernel of 0.8. These short files are labeled "lna.sh[001-010]" and "lnb.sh[001-010]".

The organization of the entire set of data stored on 'i' is shown in Figure 4.4. The directories

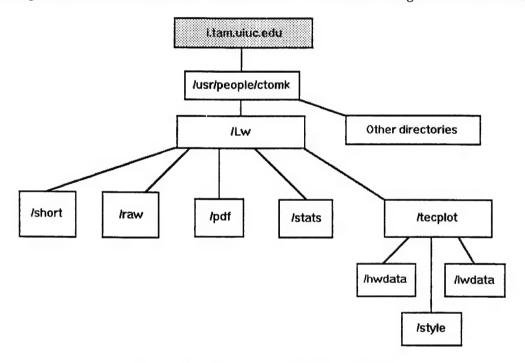


Figure 4.4 Organization of Data Files

contain the information listed below:

- /short: The short directory contains every short file—the lw.sh\*\*\*, lw.sht\*\*\*, hw.sh\*\*\*, hw.sht\*\*\*, lna.sh\*\*\*, and lnb.sh\*\*\* data sets.
- /raw: The raw directory contains all the raw data— the lw.r\*\*\*, hw.r\*\*\*, lna.r\*\*\*, and lnb.r\*\*\* data all of which is compressed using "gzip".

- /pdf: The pdf directory contains pdfs of u-velocity for all lw files, and 2 additional pdfs based on all lw files combined (2 different bin sizes).
- /stats: The stats directory contains data files of mean and/or ensemble statistics for both Reynolds numbers, including many tecplot-format versions (denoted by \*.plt).
- /tecplot: The tecplot directory contains three directories— hwdata, lwdata and style. The two data directories contain tecplot-format files of velocity vectors (computed from both types of short files), vorticity, and instantaneous Reynolds stress. *U* and *V*-Contour plots can be created from the velocity data. The style directory contains tecplot stylesheets for plotting numerous statistical quantities from the tecplot datasets. This directory also contains several macros— brief tecplot programs which perform a series of operations on a given data set, to convert it to some desired plotting format.

Each of these directories also contains a "README" file which explains its contents in greater detail.

## CHAPTER 5

## **Boundary Layer Flow Statistics**

## 5.1 Documentation of Data

#### 5.1.1 Data Overview

The U- and V-velocity components in the x-y plane of a zero-pressure gradient boundary layer were measured over two fields of view— 25 cm and 16.5 cm streamwise. The wider view experiments were conducted at two Reynolds numbers,  $Re_{\theta} = 1015$  and 7705. These cases are hereafter referred to as "LW" and "HW" denoting (Low or High Reynolds number) Wide view data, and are the data on which the principle analysis and conclusions of this thesis are based.

Additional low Reynolds number data was acquired with the 16.5 cm field of view using two different trip locations. These cases are referred to as "LNA" and "LNB"— Low Reynolds number Narrow view data where the third character denotes trip location (listed in Table 5.1). Each trip location corresponds to a different momentum thickness  $\theta$ , so although both data sets had the same free stream velocity they had different  $Re_{\theta}$  of 954 and 1325, respectively.

A second set of high Reynolds number data was also obtained with the 16.5 cm field of view, but these were not interrogated. All of the negatives acquired are listed in Table 5.1. Note that the coding system used for the film was different from that used in the thesis. A description of the resolution of the interrogated data is given later in this chapter.

#### 5.1.2 Flow Conditions

For the principle data set (LW and HW), the flow conditions are listed in Table 5.1. The free stream velocity was calculated by x-averaging the uppermost row of ensemble averaged

Images Acquired					
Film Code	Case 1A	Case 1B	Case 2	Case 3	Case 4
Thesis Code	LNA	LNB	none	LW	HW
Short Format File Code	lna.sh***	lnb.sh***	none	lw.sh***	hw.sh***
$Re_{ heta}$	1325	954	N/A	1015	7705
Number of Pictures	53	10	11	52	51
Number Interrogated	10	10	0	52	51
Illuminated Field of View (cm)	16.5	16.5	16.5	24.3	24.3
Magnification	0.42	0.42	0.42	0.41	0.41
Flow Conditions					
Free Stream Velocity, $U_{\infty}$ (m/sec)	1.79	1.77	N/A	1.77	11.39
Temperature, $T$ ( ${}^{o}C$ )	N/A	N/A	N/A	22	22
Kinematic Viscosity <sup>1</sup> , $\nu$ (m/s <sup>2</sup> )	N/A	N/A	N/A	$1.54 \times 10^{-5}$	$1.54 \times 10^{-5}$
Light Sheet Center x-location (m)	5.31	5.31	5.31	5.31	5.31
(measured from leading edge)					
Trip Location (from leading edge)	12 cm	152 cm	N/A	$152~\mathrm{cm}$	11 cm
Fan Speed (Hz)	5.7	5.7	34.2	5.7	34.2
Pitot Tube $\Delta P$ (inches $H_20$ )	0.0062	0.0062	0.29	0.0062	0.29

**Table 5.1** Summary of PIV Images Acquired and Flow Conditions. <sup>1</sup>Atmospheric pressure was assumed to be 101.3kPa. Maximum error in  $Re_{\theta}$  due to variation in local pressure is estimated to be  $\pm 1.8\%$ .

PIV data. The temperature was measured with a thermometer near the wind tunnel, and the viscosity was calculated with this temperature assuming atmospheric pressure. The trip in all cases was a 4.7 mm diameter cylindrical rod, laid flat on the test section floor spanning its full z-dimension. The trip location was adjusted to match that of Meinhart (1994) [27] for both the low and high Reynolds number cases. The fan speed was measured from a digital display on the fan motor once the velocity was set. The pressure drop was calculated based on a desired free stream velocity, and measured in a pitot tube with the manometers discussed in Chapter 4.

#### 5.1.3 Boundary Layer Parameters

The two Reynolds numbers were chosen to allow for comparison with the data of Meinhart (1994). The low  $Re_{\theta}$  is near the DNS boundary layer computations of Spalart (1988) [39], and the high  $Re_{\theta}$  data is above the range where Reynolds No. effects are strong. The trip locations were adjusted to match those of Meinhart as mentioned in Section 5.1.2— this yields similar Reynolds numbers given similar free stream velocities. The boundary layer flow parameters for

Parameter	LW Case	CDM Case 1	HW Case	CDM Case 3
$Re_{\theta}$	1015	930	7705	6845
$Re_{\delta}$	8743	7719	61863	55164
$U_{\infty}$ (m/s)	1.77	1.60	11.39	10.88
$\delta$ (mm)	76.2	75.7	83.1	78.0
$\theta$ (mm)	8.84	9.1	10.35	9.71
$\delta^*$ (mm)	12.3	_	14.4	_
$u_{ au}$ (m/s)	0.086	0.074	0.41	0.40
y* (mm)	0.179	0.213	0.0375	0.039
$\delta^+$	426	355	2216	2000
$H(\delta^*/\theta)$	1.391	_	1.391	_
$\delta/\theta$	0.116	0.120	0.125	0.124

Table 5.2 Boundary Layer Flow Parameters

this experiment are given in Table 5.2, along with the comparable data of Meinhart (referred to in the table as CDM).

The momentum thickness  $\theta$  and displacement thickness  $\delta^*$  (and thus the shape factor H) are calculated by numerically integrating the boundary layer profile U(y). The boundary layer thickness  $\delta$  is calculated using the .99 criterion— however, due to the very large slope of the profile near  $y = \delta$ , this quantity is not determined accurately.

The wall friction velocity,  $u_{\tau}$ , is calculated using the velocity profiles with the Clauser chart method (1956) [11]. This method fits the data to the logarithmic law of the wall,

$$u^{+} = 2.44 \log(y^{+}) + 5.1 \tag{5.1}$$

and estimates  $u_{\tau}$  to within an error of 4% [27]. The quantities  $y^*$  and  $\delta^+$  are then calculated based on  $u_{\tau}$ .

This estimation of the wall friction velocity was doubled checked using the streamwise variation of the momentum thickness,  $d\theta/dx$ . Ensemble-averaged data was divided into 8 streamwise segments each of which were x-averaged to obtain a velocity profile U(y). The momentum thickness was calculated for each of these profiles, and is plotted as a function of x for both Reynolds numbers in Figure 5.1. A linear fit to the data estimates  $d\theta/dx = 0.00242$  for the LW case, and  $d\theta/dx = 0.00215$  for the HW case. With the skin friction coefficient  $C_f = 2d\theta/dx$  for a zero-pressure gradient boundary layer and using the definition of  $C_f = 2\tau_w/\rho U_\infty^2$ , one may solve for  $\tau_w/\rho$ . Then the friction velocity is easily given by  $u_\tau = (\frac{\tau_w}{\rho})^{1/2}$ . Using this approach  $u_\tau$  is estimated to be  $0.087 \pm 0.098$  m/s for the LW case and  $0.528 \pm 0.339$  for the

HW case. These estimates of  $u_{\tau}$  are consistent with the estimates using the Clauser chart method within their uncertainty. The uncertainties were calculated by separating the data into four streamwise groups and measuring  $d\theta/dx$  between these groups.  $u_{\tau}$  was estimated for each  $d\theta/dx$ , and the mean and standard deviation were calculated from this set. The uncertainty given is *one* standard deviation.

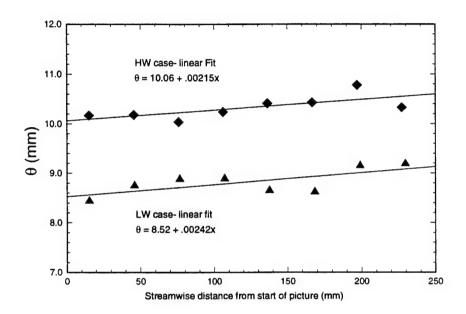


Figure 5.1 Streamwise variation in the momentum thickness  $\theta$  with linear curve fit.

#### 5.1.4 Resolution of Principle Data Set

Given these flow parameters, one may compute the resolution of the interrogated data using both inner and outer flow variables. This is shown for the principle data set in Table 5.3.

The LW data set had slightly more vectors than the HW set because the interrogation was continued further into the free stream. The estimated  $\Delta x$  and  $\Delta y$  values are based on 50% overlap between interrogation spots, and the estimated  $\Delta z$  is based on the geometric light sheet thickness of 0.36 mm. The  $y_{min}^+$  value for the LW case is greater than half the interrogation spot size because the interrogation began approximately 6.3  $y^+$  units from the wall (which has been accounted for in the statistics).

	LW Case	HW Case
Number of Vectors	19440	18792
$\Delta x^+$	6.3	30
$\Delta y^+$	6.3	30
$\Delta z^+$	2.0	9.6
$y_{min}^+$	12.6	30
$y_{min}/\delta$	0.030	0.014
$x_{max}/\delta$	3.17	2.93
$y_{max}/\delta$	1.34	1.17

Table 5.3 Resolution of the Interrogation Images

## 5.2 Comparison with Previous Results

The two wide view data sets have been compared with equivalent data from Meinhart (1994) [27]. Mean U-velocity profiles and u and v RMS velocity profiles are given below.

### 5.2.1 Mean Horizontal Velocity Profiles

Mean Horizontal velocity profiles for the current work and that of Meinhart (1994) are shown on the following page, plotted in both inner (Figure 5.2) and outer (Figure 5.3) variables. In the former, the velocity U has been normalized in each case with the wall friction velocity  $u_{\tau}$ , and the normal distance from the wall y has been normalized with the viscous length scale  $y^*$ . Figure 5.2 also shows the logarithmic law of the wall for comparison—this is plotted to a  $y^+$  of greater than 1000 although it is not valid there. There is good agreement between the data for each Reynolds number. In the latter (outer variables) case, the velocity U has been normalized by the free stream velocity  $U_{\infty}$ , and the normal distance from the wall y has been normalized by the boundary layer thickness  $\delta$ . Again, there is good agreement between the data for each Reynolds number.

The profiles were calculated by ensemble averaging over all realizations and then averaging in the streamwise direction to obtain U(y). The boundary layer grows approximately 3.6% over the width of the photograph, and there was no correction for this.

#### 5.2.2 RMS Velocity Profiles

Horizontal and vertical RMS velocity profiles are also calculated and plotted with comparable data from Meinhart (1994). The horizontal RMS profiles are plotted with inner variables

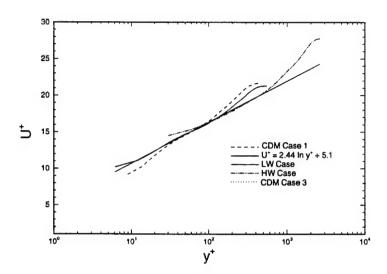


Figure 5.2 Comparison of Mean Velocity Profiles with data from Meinhart (1994)– plotted with inner variables

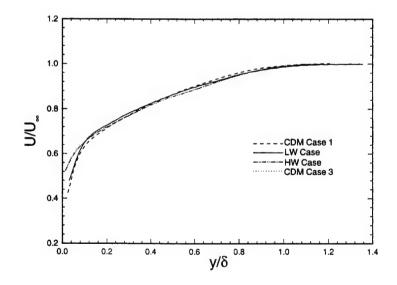


Figure 5.3 Comparison of Mean Velocity Profiles with data from Meinhart (1994)– plotted with outer variables

in Figure 5.4, where  $\sigma_u$  is normalized with  $u_\tau$  and y is normalized with  $y^*$ . There is reasonably good agreement with each Reynolds number, although the high speed cases show a difference as they approach the wall. This may be due to the existence of sharp velocity gradients which bias data estimated using autocorrelation more severely than data estimated using cross-correlation (as in Meinhart). The difference may also be due to sampling uncertainty, as discussed in the following section. The horizontal RMS profiles are plotted again in Figure 5.5, where  $\sigma_u$  is again normalized with  $u_\tau$  but y is normalized with  $\delta$ . These plots show reasonable agreement between each of the Reynolds numbers to beyond the boundary layer edge, though again with differences near the wall. Differences outside the near-wall region may be attributed to sampling uncertainty.

Vertical RMS profiles are plotted in inner variables in Figure 5.6. Here  $\sigma_v$  is scaled with  $u_{\tau}$  and y is scaled with  $y^*$ . Figure 5.7 also shows the quantity  $\sigma_v/u_{\tau}$ , but scales y with  $\delta$  revealing the profile to  $y/\delta > 1$ . The data agree reasonably well for the vertical RMS profiles also, although near the wall (Figure 5.6) the high Reynolds number data shows consistent differences of up to 20% and there are differences of roughly 10% throughout the layer. Again these can be attributed to a lack of statistical samples.

## 5.2.3 Statistical Sampling Uncertainty

Although recording images with film has clear advantages in resolution, it has the disadvantage of being more time-consuming than many digital alternatives such as a CCD camera. Thus, the number of statistical samples is limited. For estimating first and second order time-averaged turbulent boundary layer velocity statistics to within an accuracy of  $\pm 3\%$ , it is suggested that one should average continuously for  $1000~U_{\infty}/\delta$  [27]. If a vector plot covers  $3\delta$  and if Taylor's frozen field hypothesis can be applied over this length, then the number of photographs required is about 300. This is at least 6 times the number in this experiment. Thus, significant errors can be expected in these velocity statistics, particularly second-order quantities. The data of Meinhart (1994) has similar sampling error so the observed differences in RMS statistics do not necessarily represent any fundamental difference in the data.

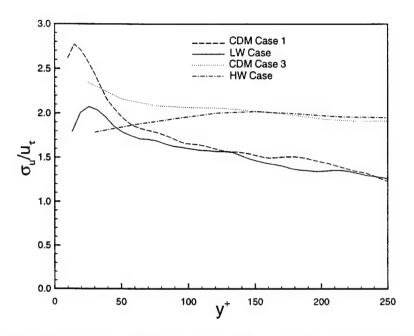


Figure 5.4 Horizontal RMS Velocity Profiles- scaled with inner variables

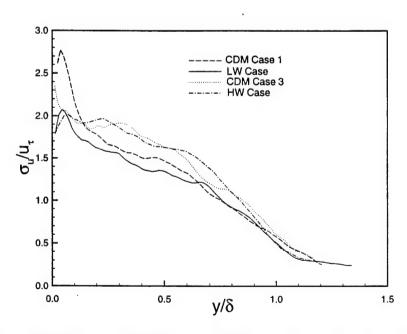


Figure 5.5 Horizontal RMS Velocity Profiles- scaled with outer variables

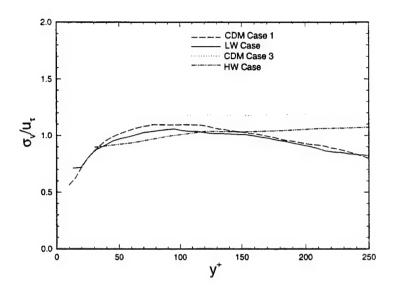


Figure 5.6 Vertical RMS Velocity Profiles- scaled with inner variables

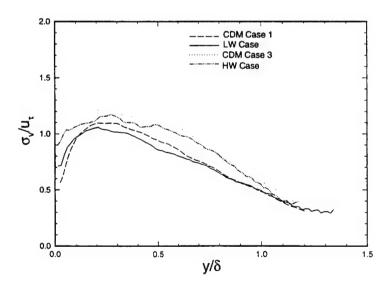


Figure 5.7 Vertical RMS Velocity Profiles- scaled with outer variables

## 5.3 Effect of Trip Location

A secondary test was performed during this experiment to obtain a qualitative understanding of the effect of trip location on the boundary layer. This was considered for low Reynolds number, narrow view data, in which the only variable changed was the trip location (LNA and LNB cases). Ten pictures were interrogated for each location, and the horizontal mean velocity profiles are shown in Figure 5.8. Also listed are the momentum thickness, free stream velocity, and  $Re_{\theta}$ .

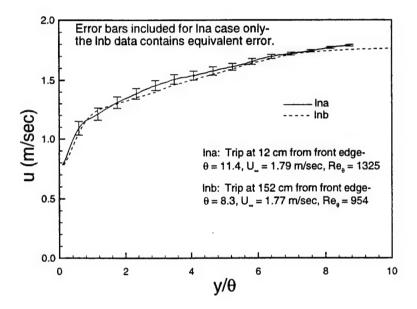


Figure 5.8 Low Reynolds Number Velocity Profiles with Different Trip Locations

The error bars are shown for only the lna case, although roughly equal error exists for the lnb case. The error shown is  $\pm 2\sigma$ , where  $\sigma = \sigma_u/(N_{eff})^{1/2}$ . Here  $\sigma_u$  is the RMS streamwise velocity and  $N_{eff}$  is the effective number of samples, about 30 (3 per realization). The wall-normal coordinate is normalized with momentum thickness, and the two profiles agree to within error out to  $y/\theta \approx 8$ .

Qualitatively, the upstream trip has the expected effect that the turbulence has more time to develop and the boundary layer flow is more retarded by the time it meets the test section. Thus the momentum thickness is greater for the early trip location, which of course produces a higher  $Re_{\theta}$ . The free stream velocity is also slightly higher for this case, perhaps due to conservation of mass given the greater momentum deficit in the layer. Thus the effective "leading edge"

appears to be moved as the trip is moved. However, it is important to remember that these results are based on only about 30 independent samples, roughly two orders of magnitude less than that required for accurate statistics.

## CHAPTER 6

# Analysis of Instantaneous Data Fields

In this chapter, instantaneous data fields are presented for both high and low Reynolds numbers (cases LW and HW). All plots are scaled with outer variables  $\delta$  and  $U_{\infty}$ , and are given primarily as examples of concepts discussed in the text. Subtracted convection velocities are chosen to make structures of interest most clear and are listed on each plot. Every realization for these cases is plotted in the Appendix with three different convection velocities:  $U_c = 0.85U_{\infty}$ , constant over the entire plot to reveal inner and outer structures,  $U_c = 0.65U_{\infty}$ , constant over the entire plot to reveal structures, and  $U_c = \text{Reynolds}$  averaged velocity (U and V velocities averaged in the x-direction).

# 6.1 Interpreting two-dimensional planar velocity measurements

## 6.1.1 Convection Velocity

In this experiment the U-component of velocity is always positive, shown as left to right on the vector plots, and the mean U-velocity is roughly an order of magnitude greater than fluctuations in the U or V component. Thus, viewing the data in this form reveals only thousands of vectors pointing approximately in the same direction with slightly varying magnitudes. This type of presentation makes it next to impossible to observe structures in the flow. Thus, a convection velocity (denoted  $U_c$  and held constant over each realization in this chapter) is subtracted from each picture. The resulting plot shows vector direction relative to this convection velocity, as in Figure 6.1. Vectors pointing to the right represent fluid moving faster than this velocity, and vectors pointing to the left represent fluid moving slower than this velocity. Whiter regions contain relatively short vectors, so this fluid is close in speed to the convection velocity.

# 6.1.2 Random two-dimensional measurements of a three-dimensional phenomenon

All of the realizations in this experiment contain two-dimensional velocity data in a plane of a three-dimensional boundary layer. Thus, when interpreting the data one must consider the following effects:

- Because only two velocity components are measured, the velocity vectors presented here
  are effectively the projection of the actual velocity vectors onto the streamwise/wallnormal plane. This makes out-of-plane motion difficult to detect.
- 2. Because the components are measured in a plane, any structures observed in the data represent a 2-D "slice" through a 3-D structure, which may or may not be oriented in the streamwise direction.
- 3. Because the sampling location in the spanwise direction is random, vector patterns of the same fluid phenomenon may vary greatly. Thus, two vector plots of similar structures may appear either identical, roughly similar, or completely different depending on their z measurement position.

Specifically for this work, measurement of a hairpin-like vortex may produce a variety of velocity vector patterns. If the vortex is oriented in the streamwise direction and the measurement volume slices through its head and between its legs, one would expect the resulting vector plot to contain three characteristic patterns: 1) A prograde spanwise vortex representing the head, 2) a Q2 event associated with the counter-rotating legs pumping up low-speed fluid from below, and 3) an inclined shear layer resulting from interaction between upstream fluid and the Q2 event. The angle of inclination of the shear layer is characteristically in the range 30-50 degrees. In viewing the velocity plots these are the characteristic vector patterns that represent hairpin-like vortices, and a region with this pattern is labeled a "Hairpin Vortex Signature", or HVS. Clear examples of such patterns are given in Figure 6.1(b).

## 6.2 Uniform Momentum Zones

#### 6.2.1 Introduction to Zones

Uniform *U*-momentum zones were discovered to exist in the turbulent boundary layer by Meinhart and Adrian (1995) [28]. Zones were primarily classified into two groups: Zone I, consisting of inclined structures close to the wall, and Zone II, located directly above the wall zone and roughly coincidental with the logarithmic layer. Meinhart and Adrian (1997) [29] then showed these zones are composed of packets of hairpin-like vortices which align in the streamwise direction. They also proposed that as a given Zone I grows, a new zone forms beneath it— and in time the new zone becomes Zone I and the previous Zone I becomes Zone II.

These experimental results are supported by the computational work of Zhou et al. (1997) [45] who showed that given an existing hairpin vortex, additional hairpin vortices may form both upstream and downstream of the original "primary" vortex. The data of Meinhart and Adrian (1997) is consistent with this, providing examples of vortices forming upstream behind an existing larger vortex.

This data has provided a great deal of insight into the boundary layer, particularly through the concepts discussed above. However, the streamwise field of view (in this case, about  $1.5\delta$ ) limits understanding of structures or groups of structures extending beyond this range, and vortex packets or zones appear to do so. The current experiment was designed to provide information about these concepts over a field of view of about  $3\delta$ , and thus shed light on the extent, nature, and interaction mechanisms of these zones and vortex packets.

## 6.2.2 The Role of Hairpin Vortices

The current experiment provides evidence consistent with the data of Meinhart (1994) [27] that hairpin-like vortices play a dominant role in boundary layer structure. Uniform momentum zones extending from the wall at some characteristic angle between 5 and 30 degrees are apparent in 27 out of 50 realizations in the HW case and 37 out of 49 realizations in the LW case. These zones are shown to contain hairpin vortex signatures (HVS), often aligned in the streamwise direction representing a vortex packet in the fluid.

Figure 6.1(a) gives an example of this for the high Reynolds number case, with the convection

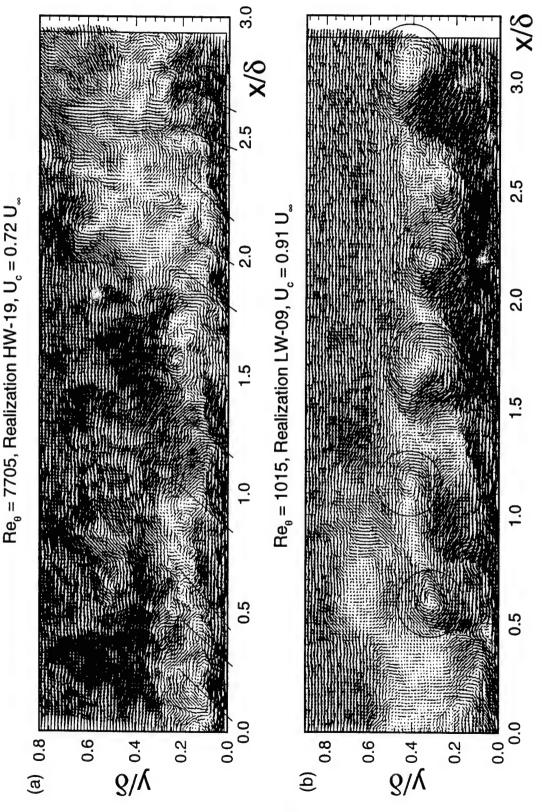


Figure 6.1 (a) Inclined shear layers (hairpin vortices) aligned in the streamwise direction over 36— high Reynolds No. case. (b) Hairpin vortices aligned in the streamwise direction over 2.56— low Reynolds No. case.

velocity chosen to illuminate the near-wall region. Here, approximately 10 inclined shear layers, marked with straight lines, are evident. These shear layers are interpreted to represent inclined hairpin-like vortices, whose legs are moving near-wall fluid outwards to create the observed shear layer. The heads are not apparent on many of the structures, which may be due to one or more of the following reasons:

- 1. The convection velocity  $U_c$  was chosen to highlight the shear layers and obscures the transverse vorticity in the heads.
- 2. The resolution is not fine enough to capture a vortex head at this young stage of growth.
- 3. In this near-wall region, the heads of some vortices are not properly developed yet.
- 4. Random sampling in the spanwise direction (as mentioned earlier) in some way captures the Q2 event without capturing significant spanwise vorticity.

It is noteworthy that near-wall vortices exist over nearly the full  $3\delta$  of the photographic field of view. Most realizations do not show such a long series of vortex signatures, but almost all HW realizations show near-wall inclined shear layers as seen here.

Figure 6.1(b) gives a similar example for the low Reynolds number case. Here 5 larger hairpin vortex signatures are observed aligned in the streamwise direction. Each contains the characteristic spanwise vorticity of the head, circled in the figure, and inclined shear layer/Q2 event behind and beneath the head. These are interpreted as a hairpin vortex packet in the fluid, extending about  $2.5\delta$  streamwise.

These two realizations also provide insight into the differences between these two boundary layers. As may be seen in several later examples, the low speed case is dominated by relatively few larger vortices, while the more turbulent high speed case contains a greater number of smaller vortices.

# 6.2.3 Autogeneration by Hairpin Vortices

As mentioned earlier, the computational work of Zhou et al. (1997) provided the interesting result that given an existing "primary" vortex, additional vortices could form both upstream and downstream of this initial vortex. In the upstream case the computations indicate that this autogeneration occurs when a hairpin-like vortex begins to form from the legs of the

primary vortex as quasi-spanwise vorticity bridges the gap between the legs. In the downstream case, the computations indicate autogeneration occurs when counter-rotating legs are induced downstream, and these legs then form a hairpin-like vortex by a similar process.

The data of Meinhart (1994) is consistent with these results, providing examples of smaller vortices forming upstream behind a larger vortex. The current work is also consistent with the computational results, and includes examples of vortex packets similar to those in Meinhart and Adrian (1997). Additionally, there are examples in which vortices form both upstream and downstream of a larger vortex, as seen in the computational work. Two examples of this are shown in Figure 6.2. These are low Reynolds number cases, which again contain larger (more easily seen) vortices relative to the high Reynolds number flows and are closer to the Reynolds number of the computations. Figure 6.2(a) shows several hairpin vortex signatures aligned in the streamwise direction. In particular, three large signatures in close proximity have been identified, with circles marking the heads and lines marking the inclined shear layers of the HVS. These have been labeled "U", "P", and "D", for upstream, primary, and downstream vortices respectively. Figure 6.2(b) has been labeled in the same way. In both realizations, these three HVS are interpreted as hairpin vortices whose relative size and location is remarkably consistent with vortices in the computations discussed above, and thus support the concept of autogeneration.

Although one or more smaller vortices forming upstream of a larger vortex is very common in the data, a vortex located immediately downstream is less so. It has been observed in the following low Reynolds number realizations: 2, 5, 7, 11, 28, 32, 45, and 50. However, if one searches the data for these patterns, it is important to remember that the majority of these can be seen by choosing a convection velocity which reveals events in the near-wall region.

It should be noted, however, that because the present work contains no time-evolution information, it does not directly prove that the large central vortex generated the other two. The data is, however, notably consistent with the computational results. One may also note in Figure 6.2(a) three inclined shear layers upstream of the labeled vortices, marked with straight lines.

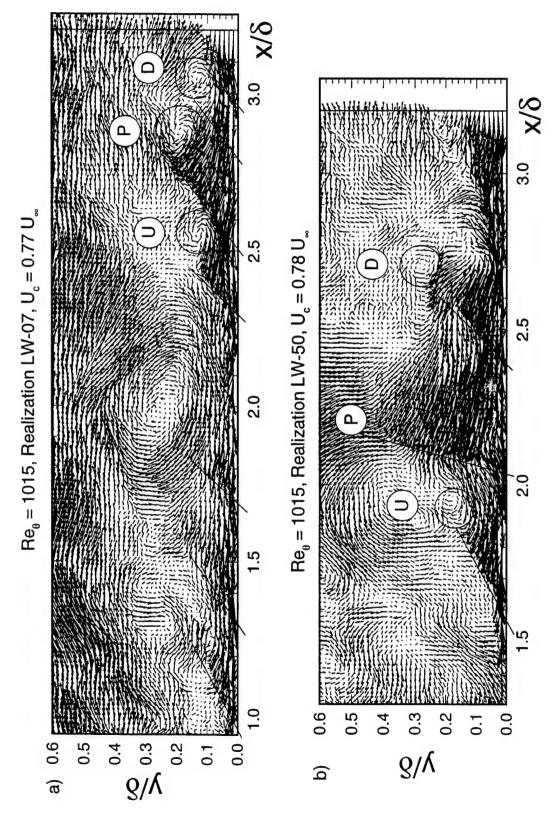


Figure 6.2 Low Reynolds No. data containing hairpin vortex signatures consistent with computational results showing autogeneration of hairpin-like vortices.

# 6.3 Large-scale patterns in the boundary layer

One of the principle objectives of this work is to learn about the interaction, growth, and extent of vortex packets and/or zones. The wide field of view made clear a variety of large-scale patterns in the flow containing one or more packets of vortices. The patterns appear due to the existence of zones of uniform momentum fluid which take on a roughly uniform shading on the vector plot, and contrast with other zones present. These patterns are most clear in the high Reynolds number flows, where large numbers of vortices group together and individual aberrations do not significantly effect the overall pattern. In the low Reynolds number flows, the zones are dominated by individual vortices and are less regular. Thus, four patterns have been identified based on the high Reynolds number data, and a schematic diagram of each is given in Figure 6.3 (where shaded regions represent low-speed fluid along the wall).

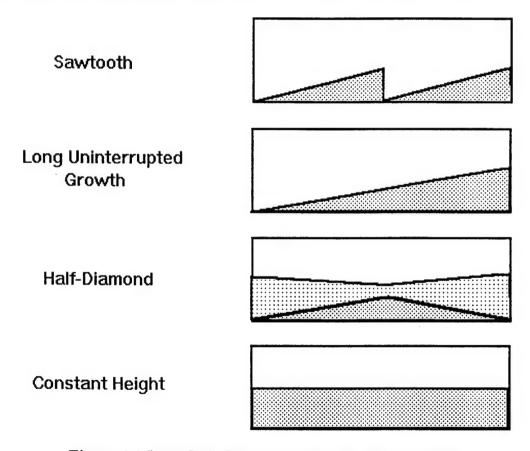


Figure 6.3 Large-Scale Patterns in High Reynolds No. Flows.

Large-scale Pattern	Number of Realizations	Percentage of Total
Sawtooth	5	10
Long Uninterrupted Growth	13	26
Half-Diamond	17	34
Constant Height Layer	10	20
Total No. Examined	50	100

Table 6.1 Frequency of Occurrence of Large-scale Patterns in High Reynolds No. Data. The patterns are not mutually exclusive.

## 6.3.1 High Reynolds No. Large-scale Patterns

Patterns selected were observed in a relatively large number of realizations (considered in light of how restrictive the pattern criterion is). The number of occurrences of each pattern is given in Table 6.1, and a complete listing of selected realizations is given in each discussion section.

#### 6.3.1.1 Sawtooth

The sawtooth pattern is formed when a zone of low-speed fluid along the wall grows at a characteristic angle for some distance, and another zone of the same length begins roughly where the first zone ends, creating a sawtooth-shaped region of low-speed fluid. Specifically, the criterion requires each zone grow at an angle between 5 and 25 degrees, extending  $1-1.5\delta$  streamwise, and the second zone must start where the first one ends. This pattern is observed in the following HW realizations: 2, 9, 16, 42, and 48.

An example of this pattern is shown in Figure 6.4. The lower picture shows the full streamwise field of view of the photograph and extends up to one  $\delta$  in y. A schematic sawtooth (shown on the right of the figure) is overlayed on the plot, and matches up very well with the pattern in the data. The zones grow at a characteristic angle of about  $18^o$ , and extend about  $1.5\delta$ , in keeping with the criteria given earlier.

The upper picture shows a region "blown up" from the lower picture, with a different convection velocity subtracted off. It shows three HVS defining the border of the zone and the fluid above it. These signatures are interpreted as a hairpin vortex packet, aligned streamwise and inducing a region of low-speed fluid between their legs. The first zone appears to end at about  $x = 1.3\delta$  from the start of the photograph, where the next zone begins. Transverse

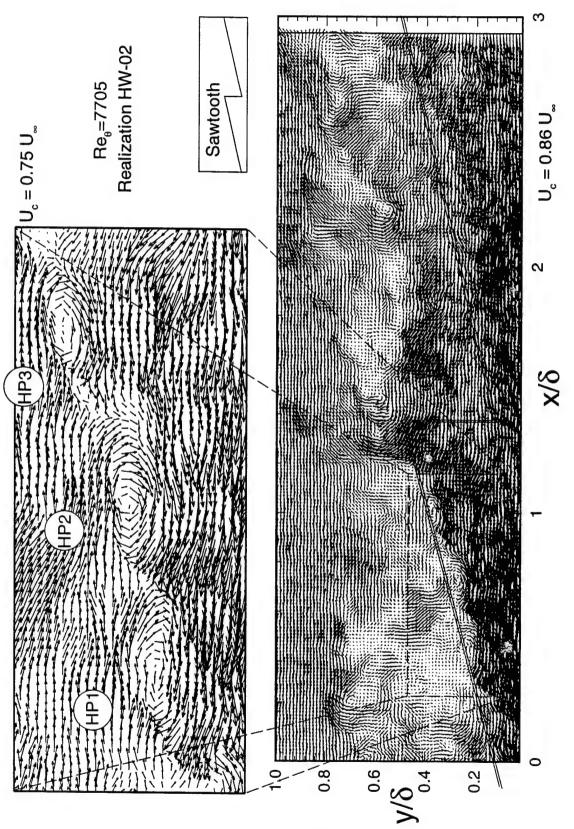


Figure 6.4 Example of high Reynolds No. sawtooth pattern—zone region enlarged to reveal three hairpin vortex signatures aligning in the streamwise direction.

vortices are not evident in the second zone. The abrupt ending of the first zone may be due to an interruption from the outer region of the layer or out-of-plane motion. It may also result from the natural zone evolution—vortices form and align streamwise, move away from the wall, and the zone ends abruptly downstream of the first vortex in the packet.

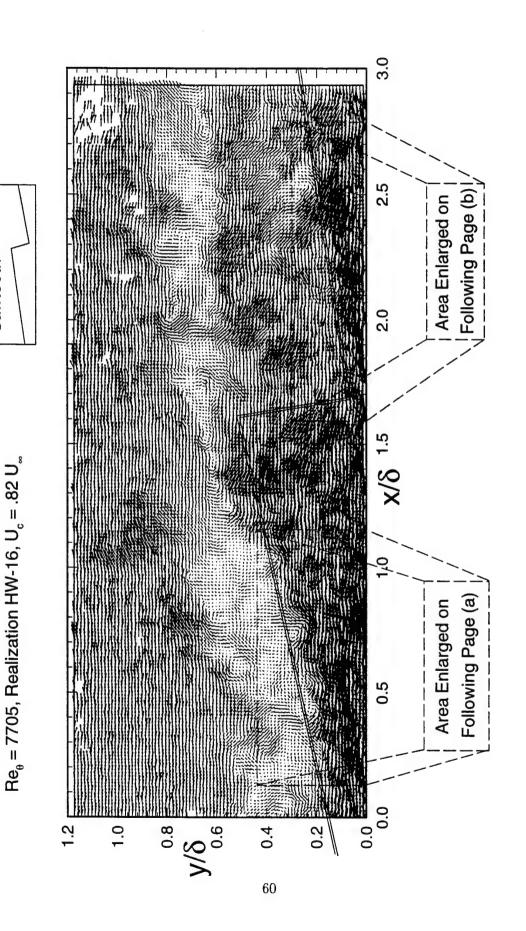
Another example of the sawtooth is shown in Figure 6.5. Again the criteria for this pattern can be seen, with a layer growing at a characteristic angle for about  $1.5\delta$ , ending abruptly, and another similar layer starting growth at this point. A slightly different schematic of the sawtooth has been included in the figure and is overlayed on the data. In this realization the second layer does not extend as far from the wall as the first, likely because it has not developed as much. Sections of both low speed regions have been enlarged in Figure 6.6 with convection velocities chosen to reveal near-wall structures.

The upstream zone is shown in Figure 6.6(a). The vector plot clearly shows four HVS with rotating heads and associated inclined shear layers, labeled A, B, C, and D. A fifth vortex, labeled E, is also apparent. These HVS represent hairpin vortices, which induce the low speed region beneath them. This zone appears to be more developed than its downstream counterpart, as the vortices have grown further from the wall and the heads are clearly seen.

The downstream zone is shown in Figure 6.6(b). This plot shows a series of HVS or inclined shear layers, labeled F through K. These are interpreted as hairpin-like vortices in various stages of development, such that vortex heads are apparent on some (H, I, J, K) but not others (F, G), for reasons discussed in Section 6.2.2. This is also an example (at high Reynolds number) of hairpins arranging themselves both upstream and downstream of a larger vortex. In this interpretation, J is the primary vortex, K the downstream vortex, and F through I the upstream vortices. However, whether these vortices were autogenerated from J or created by some other means, the underlying mechanisms behind these patterns seem quite clear. This sawtooth pattern results from low speed regions developing and arranging in a certain way, and these low speed regions or zones often contain packets of hairpin-like vortices.

#### 6.3.1.2 Long Uninterrupted Growth

A "long uninterrupted growth" pattern occurs when a low-speed region begins near the wall and grows outwards with relatively uniform U-momentum to reach the outer section of the boundary layer. Specifically, the region must grow at a characteristic angle of between 5



Sawtooth

Figure 6.5 Example of high Reynolds No. sawtooth pattern.

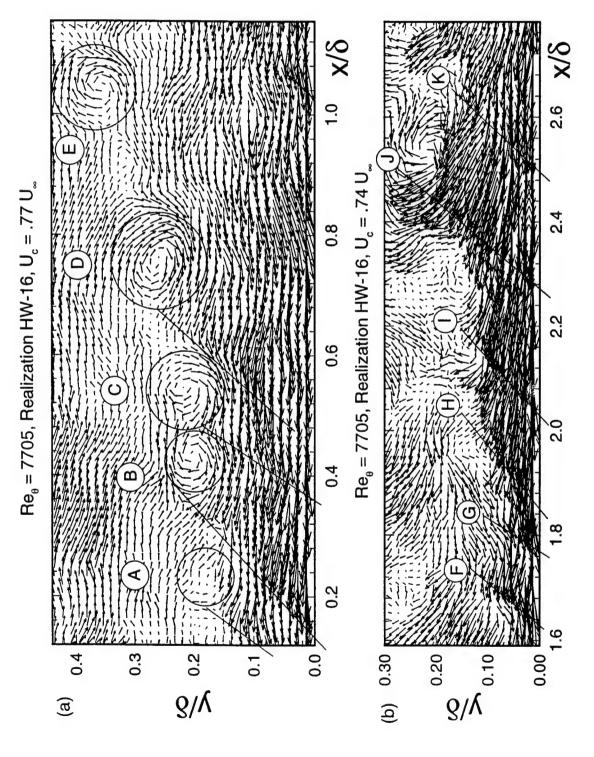


Figure 6.6 Enlarged regions of sawtooth pattern: (a) Hairpin vortex signatures aligned streamwise composing low-speed region. (b) HVS/Inclined shear layers aligned streamwise composing near-wall low-speed region.

and 30 degrees, and extend for over  $1.5\delta$  streamwise. The following HW realizations satisfy this criteria: 4, 9, 10, 13, 20, 23, 31, 32, 34, 43, 44, 47, and 48. Note that HW-09 and HW-48 also satisfy the criteria for a sawtooth pattern.

An example of this pattern is given in Figure 6.7. The upper picture shows the full field of view of the photograph in x and  $\delta$  in y. The low-speed region growing from the wall extends the full  $3\delta$  of the measurement volume. A schematic of the pattern is included in the upper right of the figure, and overlayed on the data for clarity. The low speed region extends remarkably far from the wall, to  $y/\delta \approx 0.8$ , but not many vortices are obvious for  $y/\delta > 0.4$ . This outer low speed region may have evolved through continual outward growth of the near-wall zone with eventual interaction with the outer region, causing breakup and diffusion of the outer lower speed vortices while retarding the outer flow. A large portion of the vector field is enlarged in the lower picture, marked by the dotted lines.

This picture makes several groups of structures apparent. A group of five HVS exist slightly away from the wall, marking the border of the low speed region at a height of about  $0.3\delta$ . These are labeled A through E. The heads of the vortices have been circled, and the associated Q2 events (and inclined shear layers) are present though not as obvious because of the convection velocity chosen. These HVS are interpreted as Zone II hairpin vortices, which induce the relatively low-speed flow in the region of the long uninterrupted growth that they occupy.

A second group of HVS/inclined shear layers exists beneath this group—these are labeled F through K. These vortices are interpreted as Zone I near-wall structures, associated with the Zone II above them. Six inclined shear layers are apparent, and they have aligned in the streamwise direction and nested within the Zone II hairpin packet (assuming these vortices grow self-similarly the Zone II hairpins will be wider as well as higher than the Zone I packet). It is also feasible, however, that the vortices F through K are not inherently associated with the vortices A through E, but these two groups happened to arrange in this way as the photo was taken. This may be the case if the Zone II structures are moving faster than the Zone I structures, such that they might interact with the vortices L, M, and N (discussed below) at some later time.

The third group of HVS/inclined shear layers exists upstream of the previous two, and are labeled L, M, and N. These are interpreted as an additional group of Zone I structures, which may or may not be independent of the structures F through K. These appear to be slightly

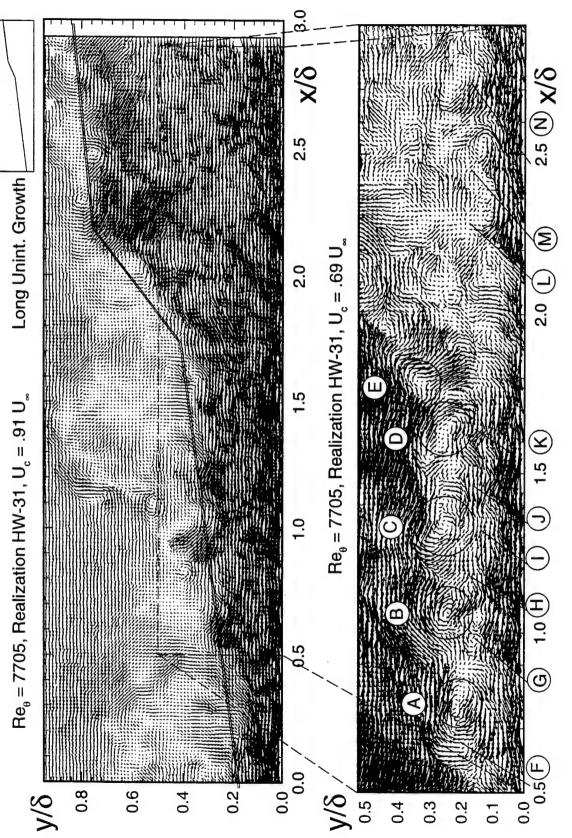


Figure 6.7 Example of a long uninterrupted growth pattern. The enlarged area reveals Zone II hairpin vortex signatures and Zone I inclined shear layers.

more developed than the downstream Zone I, so that the spanwise vorticity representing the heads of the vortices can be seen.

#### 6.3.1.3 Half-Diamond

A half-diamond pattern is somewhat more general than the previous large-scale patterns, and is described by the following criteria. There must exist a demarcation between a high and low speed region that is inclined from the wall at 5 to 30 degrees and then declined towards the wall at roughly the same angle (such that would form in the near-wall region by a packet of hairpins, the largest and strongest in the center with the hairpins growing steadily smaller and weaker with distance from the center up or downstream). Also considered are demarcations with the decline upstream and the incline downstream at similar characteristic angles. Both types of half-diamond patterns are shown in Figure 6.3. The following HW realizations satisfy the above criteria: 3, 7, 12, 13, 14, 17, 20, 27, 32, 33, 35, 36, 37, 38, 39, 46, and 49.

An example of the half-diamond pattern is given in Figure 6.8. This plot extends  $3\delta$  streamwise and  $\delta$  wall-normal. The convection velocity is chosen to reveal structures in the near-wall region and just above. A lower half-diamond pattern grows near the wall, and returns to the wall after about  $2\delta$  streamwise, while an upper half-diamond pattern descends to the lower pattern's apex and then ascends to about  $0.6\delta$ . As in the other figures a schematic of the pattern is included in the upper right and overlayed on the plot. It is likely coincidence that the high and low points, respectively, of the two half-diamond regions appear to have the exact same x-location, for the reason that the regions appear to have different velocities. Nonetheless, these regions appear to interact within the flow at this instant in time and probably continue to do so as they move downstream.

Two regions, marked by dotted lines, are enlarged in Figure 6.9. The area where the two half-diamond patterns meet is enlarged with a different convection velocity in Figure 6.9(a). This plot shows a series of five HVS, labeled A through E. The heads have been circled, and the associated inclined shear layers are present although not as obvious again because of the chosen convection velocity. These HVS are interpreted as a train of hairpin vortices comprising a Zone II region. Below these are a second train of four inclined shear layers, marked with straight lines, which have been labeled F through I. These are interpreted as a Zone I set of hairpin vortices, again nested within the Zone II vortices as seen in Figure 6.7. It appears from

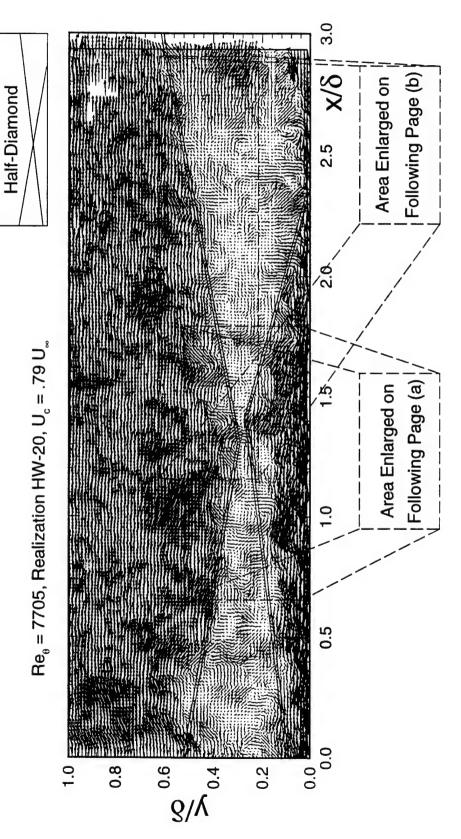


Figure 6.8 Example of a half-diamond pattern.

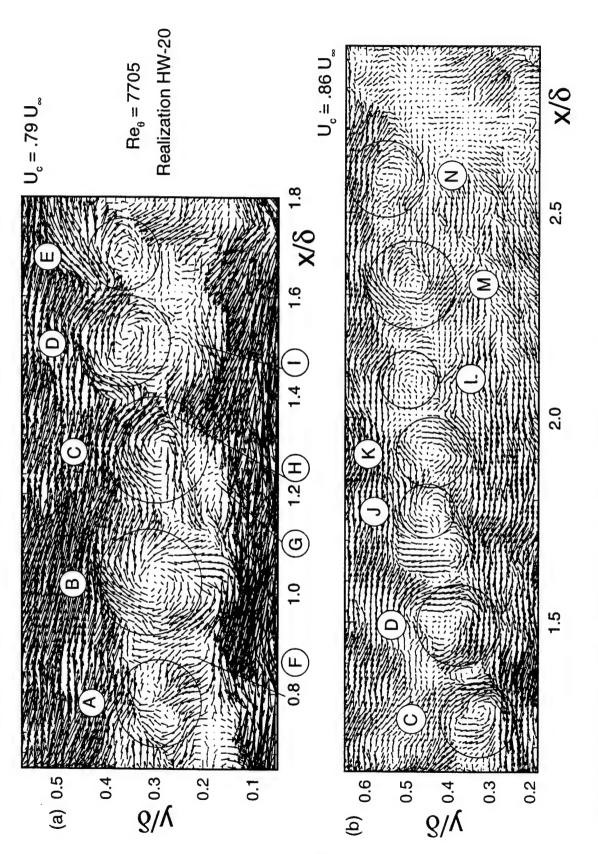


Figure 6.9 Enlarged regions of a half-diamond pattern: (a) Two trains of hairpin vortex signatures, one nested within another. (b) The border of a low and high speed region marked with transverse vortices.

the data that the upper half-diamond pattern, the Zone II region, and the lower half-diamond pattern (Zone I) all have slightly different velocities, and thus may not remain in such close proximity as the flow evolves.

The interface of the upper half-diamond region and the lower speed fluid below it is enlarged in Figure 6.9(b). Here seven transverse vortices are clear. Vortices C and D are also shown in part (a) of the figure, and are believed to be hairpin-like structures. Vortex E is not clear in this plot because of the convection velocity. The structures J through N may well be hairpin-like vortices, but it can only be stated with confidence that they represent spanwise vortices. These structures mark the border of the upper half-diamond with the region of uniform momentum fluid below it to the upstream side. These vortices (and the region below them) may be an aged Zone II which has remained undisrupted, and grown to the outer region of the boundary layer.

Thus, like previous large-scale patterns discussed, the half-diamond pattern is composed of several regions of uniform momentum fluid, which often contain packets of hairpin-like vortices.

### 6.3.1.4 Constant Height Layer

A constant height layer pattern occurs when a region of low speed fluid exists over a significant length with relatively constant thickness. Specifically, a demarcation between low and high speed regions must exist of length  $2\delta$  whose distance from the wall remains within a range of  $\delta/4$  over its length. The following HW realizations satisfy this criteria: 13, 14, 15, 27, 30, 33, 41, 46, 47, and 50.

An example of this pattern is given in Figure 6.10. This figure shows the entire width of the photograph in x and extends to nearly  $1.2\delta$  in y. The actual boundary layer thickness appears to be significantly less than the quantity  $\delta$  over the entire streamwise field of view. Again a simple diagram of the pattern has been included in the figure and overlayed on the vector plot. Because the free stream remains unperturbed down to a height of about  $0.4\delta$ , it effectively borders the internal layer over this streamwise distance. Thus, the layer itself seems to suffer no perturbations from the outer region, but maintains a very slow rate of growth. The conditions under which these zones grow and which variables effect the rate of growth are not well understood.

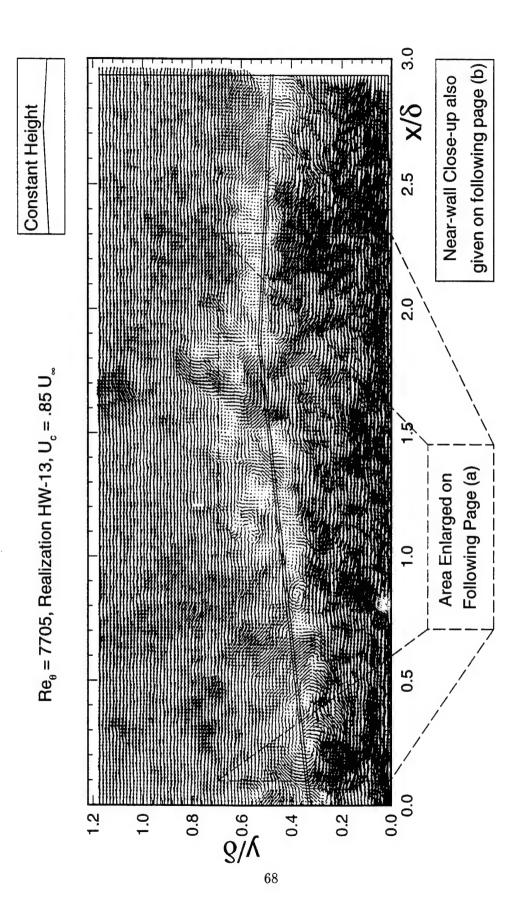


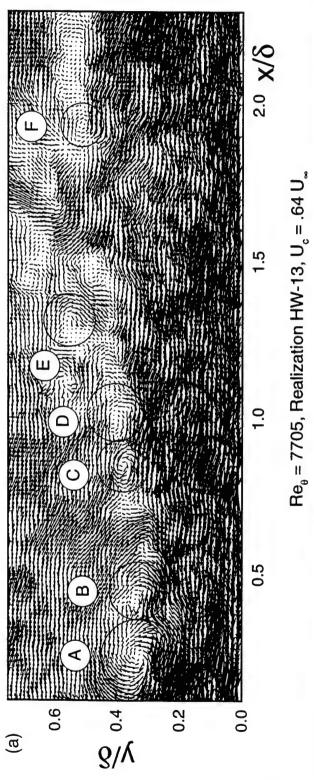
Figure 6.10 Example of a relatively constant height layer.

Two regions of this realization have been enlarged using different convection velocities. The area enclosed by dotted lines is shown in Figure 6.11(a). Six structures can be seen in the vector plot on the low speed/high speed fluid border. These are labeled A through F. Rotating patterns are clear in all six— however, the Q2 event associated with this rotation in a classic HVS is only clear on structures A, B, and D (although small Q2 events are present on structures C and F also). But whether these are hairpin-like vortices, or simply transverse vortices, they mark the boundary above the low speed fluid, and may indeed help to create this momentum deficit through induction. These vortices may also comprise a Zone II region, particularly A through E. This interpretation of the data is discussed further in light of the lower plot (b).

Figure 6.11(b) shows the entire streamwise view of the photograph with a convection velocity chosen to reveal structures in the near-wall region. Twelve inclined shear layers exist near the wall, and are marked with straight lines in the plot. These structures are interpreted to represent hairpin-like vortices, likely in the developing stage where the heads cannot be resolved. The remainder of the constant height layer is seen as white in this plot, and appears to have a uniform velocity. The faster moving fluid above this is also clearly seen. The inclined shear layers appear to represent an extended Zone I along the wall, comprised of multiple packets of hairpin-like structures not growing significantly in height with distance downstream. The fluid above them, then, may be interpreted as a Zone II region, as discussed above, although HVS are not obvious in this reference frame. This data seems to support this interpretation in the region  $0-1.5\delta$  from the start of the photograph, although further downstream the issue is not so clear. Regardless, this relatively constant height layer is yet another large-scale pattern identified based on an arrangement of uniform momentum regions, and these regions are shown to contain packets of vortices.

Thus, each of the four identified high Reynolds number large-scale patterns exist through the development and arrangement of uniform U-momentum zones. These zones are often seen to contain several PIV hairpin vortex signatures aligned in the streamwise direction, which represent a hairpin vortex packet in the fluid. Again, it is important to remember the effects of sampling a three-dimensional phenomenon randomly with an essentially two-dimensional measurement volume, and these effects are apparent in the variety of vector patterns possible from the measurement of a hairpin-like vortex.





70

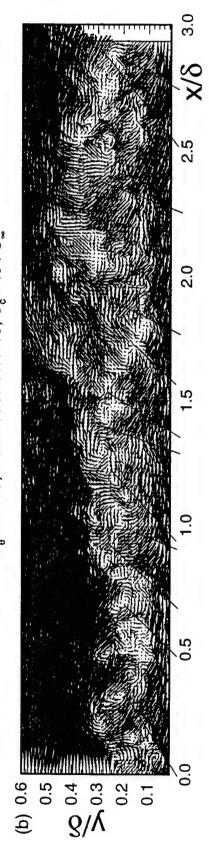


Figure 6.11 Enlarged regions of a constant height layer pattern. (a) Transverse vortices marking the border between low and high speed fluid. (b) Inclined shear layers align in the streamwise direction near the wall.

Large-scale Pattern	Number of Realizations	Percentage of Total
Sawtooth	3	6
Long Uninterrupted Growth	5	10
Half-Diamond	14	29
Total No. Examined	49	100

Table 6.2 Frequency of Occurrence of Large-scale Patterns in Low Reynolds No. Data.

### 6.3.2 Low Reynolds No. Large-scale Patterns

The large scale patterns previously identified were based solely on observations of the high Reynolds number data. Nonetheless, similar patterns to those seen above exist in the LW data, and three such examples are presented here. The patterns and frequency of occurrence in this data set are summarized in Table 6.2.

#### 6.3.2.1 Sawtooth

An example of a sawtooth pattern in the low Reynolds number data set is given in Figure 6.12. The plot reveals over  $3\delta$  streamwise and over  $1.3\delta$  wall-normal. As in the HW case, a schematic of the pattern is given on the figure and overlayed on the plot. The low-speed fluid near the wall clearly takes on a sawtooth-like pattern, although the hairpin vortex signatures one would expect to see in the HW case are not present. A few vortex-like vector patterns exist near the upstream layer, but these do not appear to define a zone. Nonetheless, the low speed regions grow at the characteristic angle seen on the high Reynolds No. plots.

This plot also reveals a highly corrugated superlayer typical of the low Reynolds No. boundary layer, including a turbulent inrush plunging down to about  $0.4\delta$ . Again, this corrugation is a result of the larger vortices present in the low Reynolds No. boundary layer.

### 6.3.2.2 Long Uninterrupted Growth

Figure 6.13 gives an example of a low Reynolds No. long uninterrupted growth large-scale pattern. The upper picture gives the full streamwise field of view of the photograph, and overlays a schematic pattern for clarity. A low-speed region near the wall can be seen growing in discreet stages. Two hairpin vortex signatures are clear in the upper level of the growth, labeled A and B. These are interpreted as low Reynolds No. Zone II vortices, and likely contribute strongly to the momentum deficit of the region below them. Similar vortices in the lower level of the

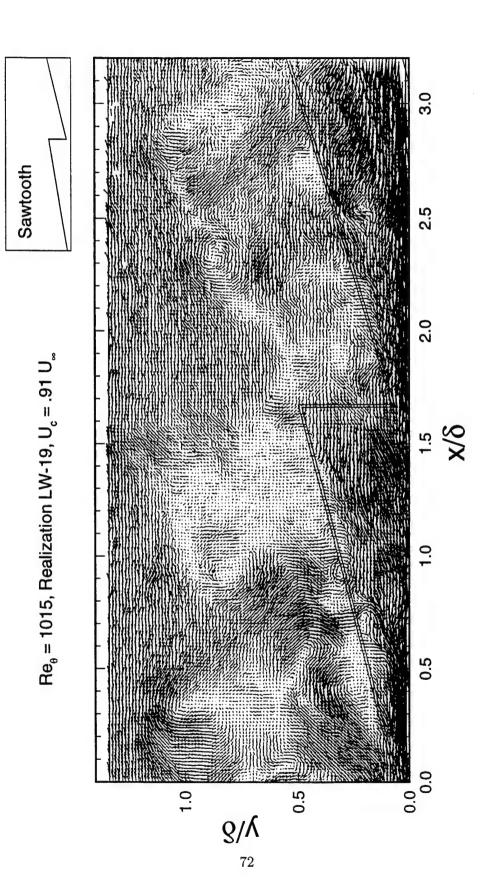


Figure 6.12 Example of a low Reynolds No. sawtooth-like pattern.

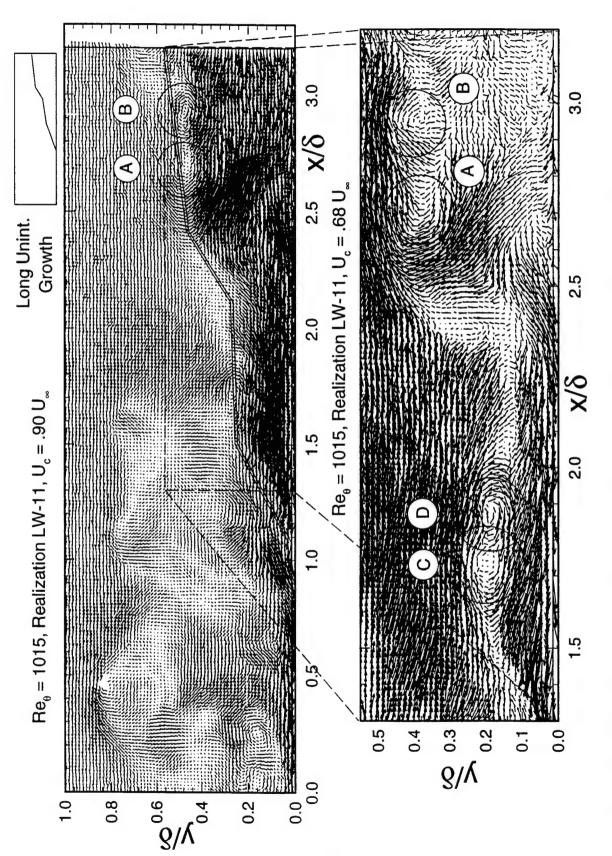


Figure 6.13 Example of a long uninterrupted growth large-scale pattern in a low Reynolds No. flow. Enlarged region reveals two sets of vortices contributing to Zones I and II respectively

growth are not clear in this plot, but the enlarged region at the bottom of the figure makes these obvious.

Two vortex signatures, labeled C and D, are clear in this reference frame. These are interpreted as hairpin-like vortices comprising a Zone I region near the wall. A region with severe momentum deficit about  $0.5\delta$  in length is induced beneath them. These vortices combine with the Zone II vortices to create a low speed region fitting the criteria for a long uninterrupted growth pattern.

It is *possible* that the vortices C and D are in the process of pairing, one mechanism by which they may grow. This is feasible because the two strong vortices are in such close proximity and the region of retarded flow between their legs is so long. The actual pairing process has not yet been observed in a turbulent boundary layer, however.

#### 6.3.2.3 Half-Diamond

The final low Reynolds No. example of a HW large-scale pattern is the half-diamond, given in Figure 6.14. The upper picture extends over  $3\delta$  in x and  $\delta$  in y, and is overlayed with a schematic of the pattern. Six vortex signatures are present, labeled A through F. These are not necessarily hairpin-like vortices, but appear to have transverse vorticity, and exist on the border of these diamond-shaped regions. The large numbers of HVS and Zone I/II structuring seen in the high Reynolds number example is not apparent in this flow, but again the low speed region grows near the characteristic angle seen in the more turbulent case.

The enlarged region is included to reveal four near-wall structures. Inclined shear layers G, H, I, and J are marked with straight lines and are aligned streamwise within the half-diamond pattern. This is quite like the HW case, although the large circulating vortices in the white area above these structures emphasize the different nature of the low Reynolds number boundary layer.

# 6.4 Observations of Out-of-Plane Motion

In addition to the previously mentioned large-scale patterns, observations of the data revealed another event of interest appearing in a significant number of realizations. This event is the disruption of a low speed streak with out of plane motion of greater *U*-velocity. A set

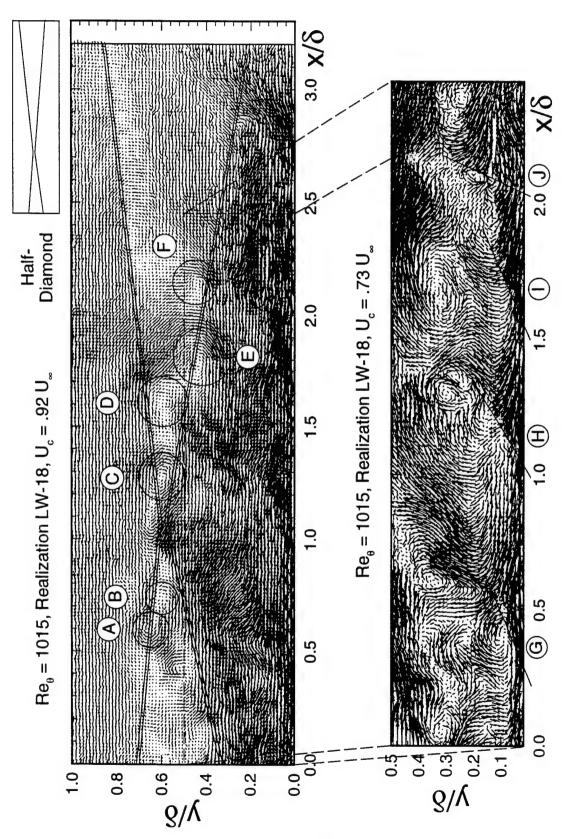


Figure 6.14 Example of half-diamond large-scale pattern for low Reynolds No. flow. Enlarged area reveals inclined shear layers aligned streamwise near the wall

of criteria was created for this event, as follows: a near-wall ( $\approx 0.2\delta$ ) low speed layer of length  $1.5\delta$  or more streamwise must exist, within which appears a relatively high speed source, sink, or other vector pattern which represents out of plane motion. The following high Reynolds No. realizations satisfy this criteria: 7, 8, 12, 15, 16, 18, 20, 30, 34, 36, 37, 38, 39, and 42. The out of plane motion in almost all of these cases may be seen most clearly with a convection velocity highlighting the near-wall area.

An example of this out of plane motion is given in Figure 6.15. This figure shows the full streamwise field of view in x and the full interrogated height in y. The low speed streak is marked with a series of straight lines, and the area of perceived out of plane motion is circled.

This fluid is moving faster than the low speed region, so it is likely that it originated further from the wall, and because it appears to have a significant out of plane component it probably originated at some different z-location. If this is the case, this event could be described as a three-dimensional sweep type of motion. (Note: It is also possible (though less likely) that it originated at the same y-location, if there existed a low speed streak extending in x with limited z-dimension and higher speed fluid alongside it with significant W-velocity). So this event is an example of a highly three-dimensional motion in the near-wall region probably originating in the outer region and disrupting a lengthy streamwise low speed streak, and it occurs in 28% of realizations.

# 6.5 Analysis of Zone Growth Angles

Low speed regions growing from the wall are observed on almost every high Reynolds No. vector plot, and sometimes multiple regions exist on the same plot. These zones seem to grow at characteristic angles from the wall. This range of angles has been estimated as 5 to 30 degrees, but in the interest of quantifying this variable a probability density function of zone angles has been constructed.

This pdf includes the angle of every zone of uniform momentum fluid growing from the wall in the HW data set which extends  $0.5\delta$  or greater in the streamwise direction, and is given in Figure 6.16. The modal value of the plot is approximately 11 degrees. This is different from the angle of about 18–20 degrees seen in several plots given as examples, but the angle also seems to be a function of layer size and age. So well-developed zones which are more likely to be used

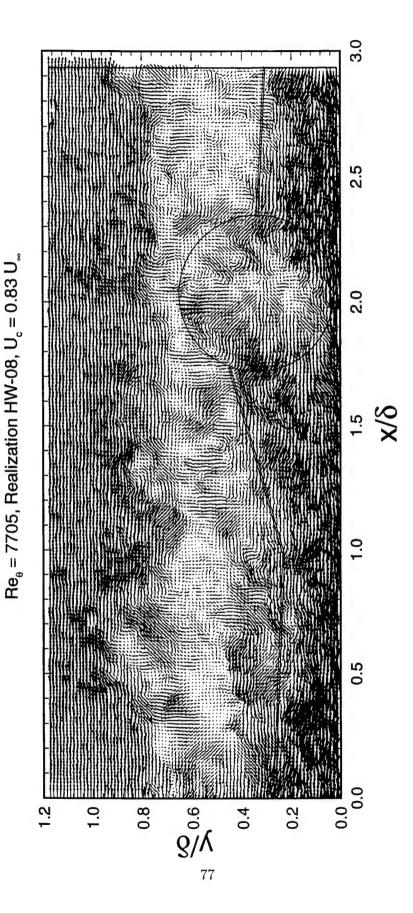


Figure 6.15 Out of Plane Motion Interrupting a Low Speed Near-wall Layer

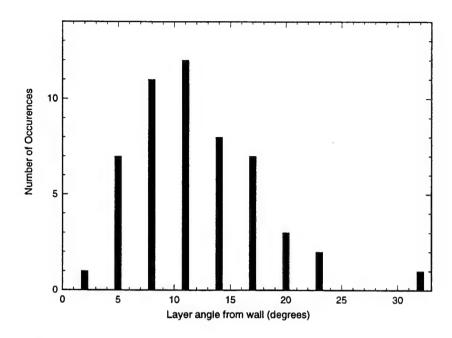


Figure 6.16 Probability density function of growth angles from wall for low speed uniform momentum zones.

as an example are also more likely to have a greater angle. Note that the angle of 18–20 degrees in several examples is very consistent with the work of Head and Bandyopadhyay (1981) [18] and Brown and Thomas (1977) [9]. The former observed hairpins lining up such that the tips formed an angle of 20°, and the latter used hot-wire correlations to measure structures inclined from the wall at 18°. The range of zone angles estimated earlier is now clear from Figure 6.16—almost all angles are between 4 and 24 degrees.

# CHAPTER 7

# Conclusions, Conjectures, and Recommendations

Particle Image Velocimetry was used to measure the U and V velocity components in the x-y plane of a turbulent boundary layer. A streamwise field of view of  $3\delta$  was measured at  $Re_{\theta}$  = 1015 and 7705. Approximately 50 realizations were performed at each Reynolds number. The following conclusions, conjectures, and recommendations are offered based on this experiment.

## 7.1 Conclusions

- 1. The data confirms several observations from the results of Meinhart and Adrian (1997), particularly the existence of uniform U-momentum zones of fluid, often containing packets of hairpin-like vortices aligned in the streamwise direction. These zones grow from the wall at characteristic angles, typically between 4 and 24 degrees. Zone-like internal layers have been observed extending up to  $3\delta$  in the streamwise direction and out to  $\approx \delta$  in the wall-normal direction.
- 2. The data provides evidence supporting the concept of hairpin vortex autogeneration described in Zhou et al. (1997). In particular, smaller hairpin vortices have been observed both upstream and downstream of a larger hairpin vortex. This observation is consistent with the computational results. If this interpretation of the data is correct, a larger central "primary" vortex can generate smaller neighboring "secondary" vortices.
- 3. In the high Reynolds No. data, these uniform momentum zones and/or hairpin vortex packets interact to form large-scale patterns in the flowfield. Four particular patterns have been identified, listed here with the percentage of realizations in which the pattern

appears: sawtooth (10%), long uninterrupted growth (26%), half-diamond (34%), and constant height layer (20%). Examples in each pattern reveal hairpin-like vortices aligning into packets in the streamwise direction.

4. In this range, Reynolds number has a significant effect on the nature of the turbulent boundary layer. For  $Re_{\theta} \approx 1000$ , the boundary layer is dominated by a fewer number of larger structures. These structures often grow to the outer region of the layer and create a highly corrugated superlayer. For  $Re_{\theta} \approx 7700$ , the boundary layer is dominated by a greater number of smaller vortices with smaller interspacing. These structures form packets which may grow to the outer region of the layer, creating a less corrugated superlayer.

# 7.2 Conjectures

1. The dynamics of the turbulent boundary layer are obviously extremely complex, but the most fundamental mechanisms of large-scale zone/vortex packet growth and interaction may be as simple as the following. Assume that vortex packets form in some way near the wall. This may or may not be a result of autogeneration, and the packets may develop at a characteristic angle or be parallel to the wall. The vortices in the packet grow self-similarly as they convect downstream, so that the shape of the packet does not change significantly. Then the large-scale patterns may exist simply because packets independently grow until they border and eventually overlap one another.

Thus, if one packet forms behind another, both growing at a characteristic angle from the wall, aligned roughly streamwise with spacing of  $1 - 1.5\delta$ , at some time downstream this gives the appearance of a sawtooth pattern. If a given packet, again growing at this characteristic angle from the wall, is quite long and by chance isolated from other packets or disruptions, it produces a long uninterrupted growth pattern. If a given packet, formed so that the vortices are equal in height, is quite long and again temporarily isolated from disruptions, a constant height layer appears. Finally, if packets form at a variety of angles (both towards and away from the wall) and grow to interact with each other, one of an endless variety of half-diamond shaped patterns may appear.

In all cases, packets will likely exist until they are disrupted by an external influence. This includes growth into another zone, disruption by a sweep-type motion, interaction with the faster moving fluid in the outer region of the layer, or any similar phenomenon. Upon disruption, individual vortices may exist and diffuse for some time thereafter.

The formation of packets may be random, but it is likely not entirely random. For example, packets may be more inclined to form behind another downstream packet because of the low speed streak induced between its legs.

- 2. Concerning the formation of vortex packets: Because of the consistently close spacing of hairpin vortices in the data, autogeneration is an appealing concept, particularly in light of the computational results. Even if the "primary" vortex in a group is created because the conditions are favorable for such a process, the existence of this vortex would likely make conditions even more favorable for generation of another.
- 3. If the growth rate of vortices is relatively constant, one may draw a relation between the shape of a packet or zone and the way in which it was created. Two types of packets are commonly observed: i) those growing at an angle between 8 and 20 degrees, and ii) those whose distance from the wall is roughly constant. Certainly packets of other descriptions exist, but these are two common cases. The former may be an example of a "primary" vortex existing and others being generated behind it at a later time, thus creating the angle defined by the vortex head heights. In this interpretation the range of angles of the packets would be related to the range of times it takes for a "secondary" hairpin to form behind an existing hairpin. The latter may be an example of hairpins being created at the same time and at different locations, and evolving together.
- 4. One final statement can be made in conclusion concerning the nature of the turbulent boundary layer. The data reveals the boundary layer is dominated by vortices, as seen in previous experiments, but it also reveals uniform momentum regions over the extent of the layer. Thus, in some ways the boundary layer is more discrete than continuous in nature, and thinking of it solely in terms of the mean velocity profile and deviations from that profile is misleading. It is better represented in terms of a discrete collection of chunks of roughly uniform momentum fluid interacting to create the velocity profile when averaged.

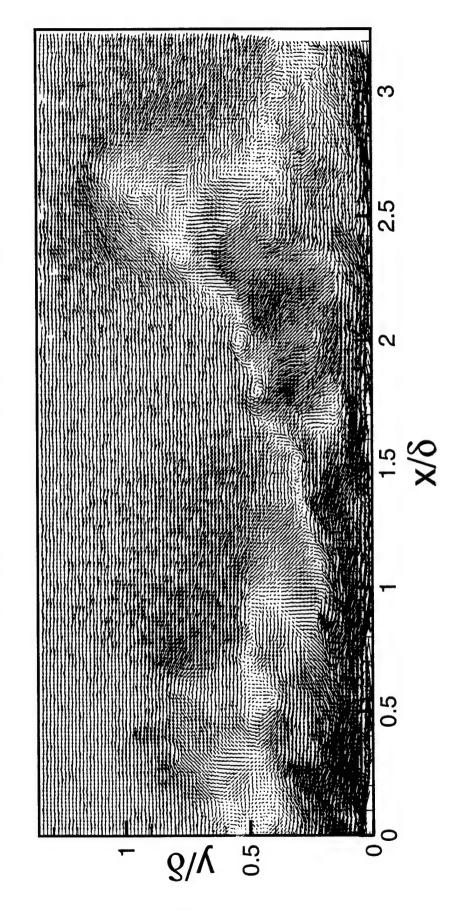
# 7.3 Recommendations

- 1. One of the limitations of two-component PIV is the difficulty in determining out-of-plane motion. A researcher may be able to identify large source or sink regions, but more subtle observations cannot be made with any certainty. Thus, stereo PIV yielding the third velocity component would provide valuable information when interpreting vector plots, and potentially provide great insight into the boundary layer.
- 2. Another limitation in this experiment is the inability to determine the time evolution of the structures in the flow. This information is crucial in understanding how structures grow and interact. Thus, a similar wide field of view experiment with images acquired some appropriate time interval apart may improve understanding of the boundary layer. A related experiment, with separate images acquired at two streamwise locations with an appropriate time delay, would provide similar insight. These time-evolution techniques may also be employed with intentional shedding of vortices to investigate their interaction mechanisms.

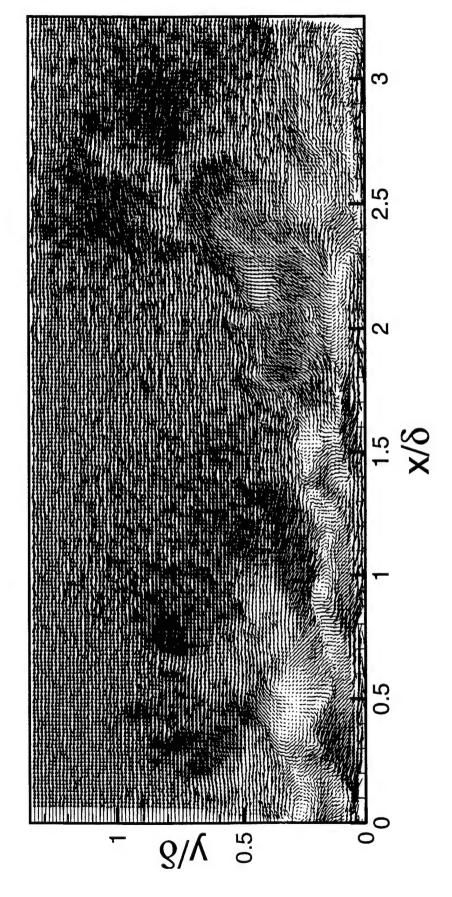
# APPENDIX A

Velocity Vector Plots

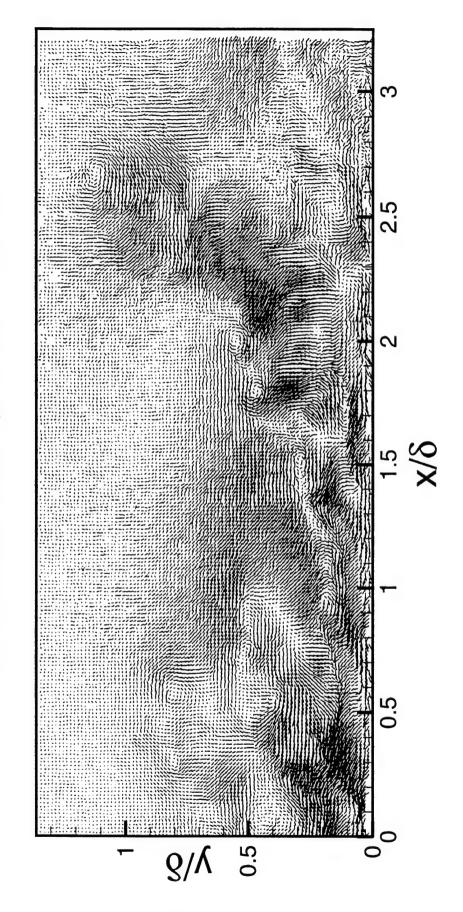
Realization LW-01,  $U_c = 0.85 U_{\odot}$ 



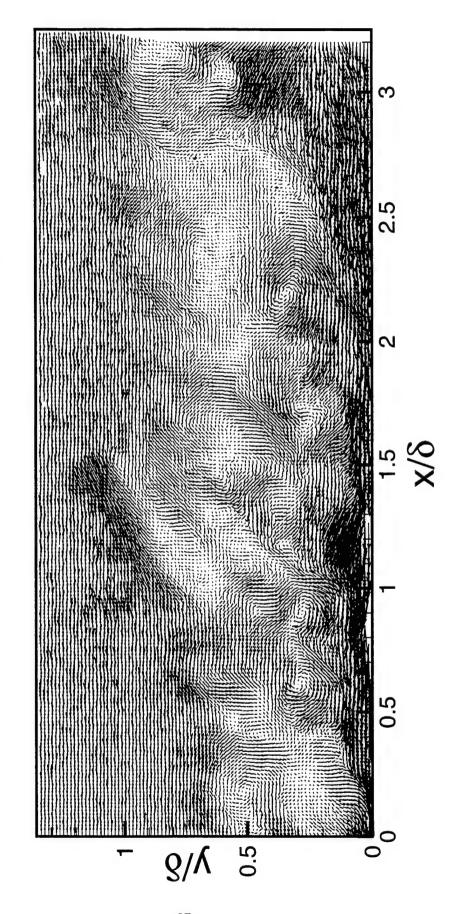
Realization LW-01,  $U_c = 0.65 U_{\odot}$ 



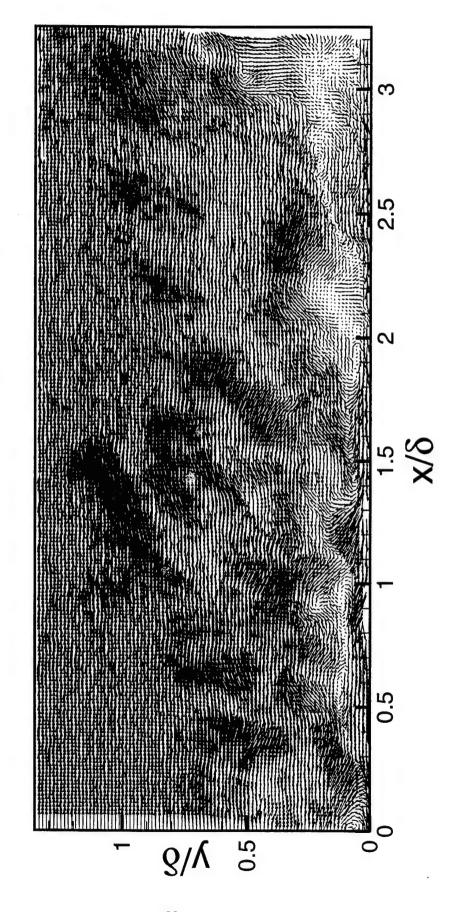
Realization LW-01, Reynolds Fluctuations



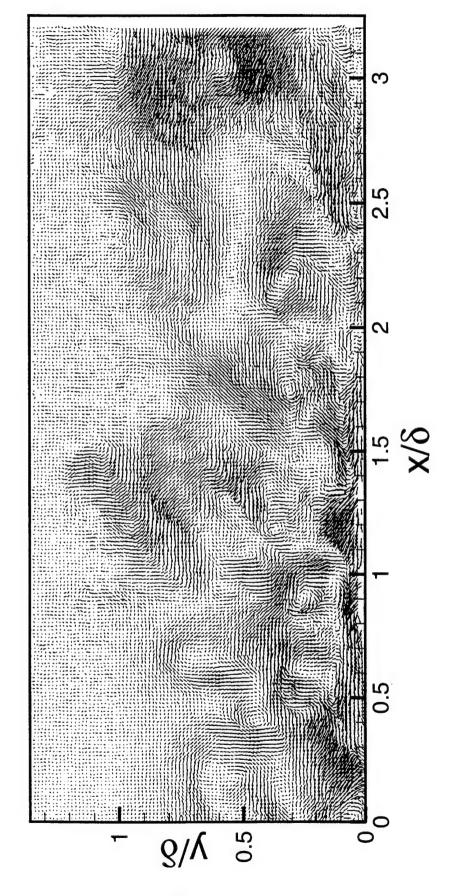
Realization LW-02,  $U_c = 0.85 U_{\odot}$ 



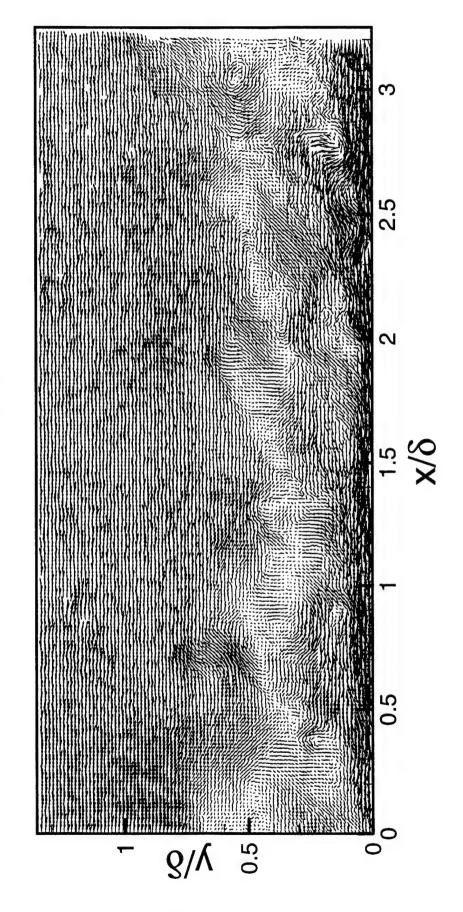
Realization LW-02,  $U_c = 0.65 U_{\odot}$ 



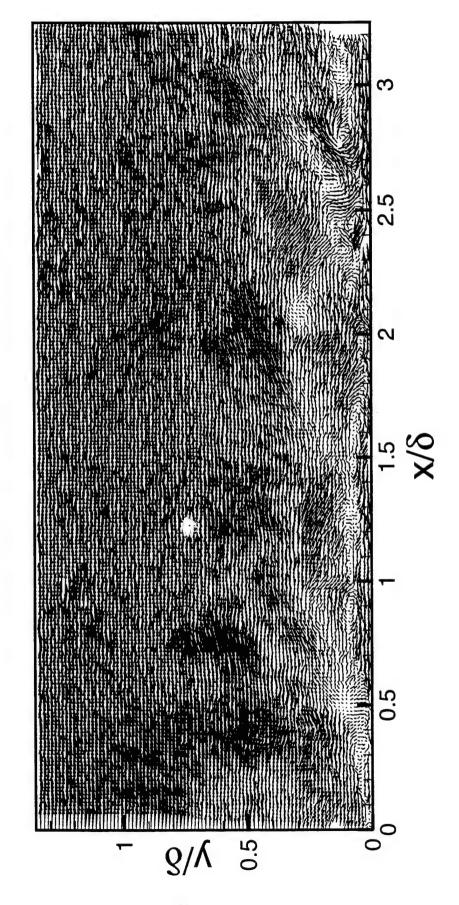
Realization LW-02, Reynolds Fluctuations



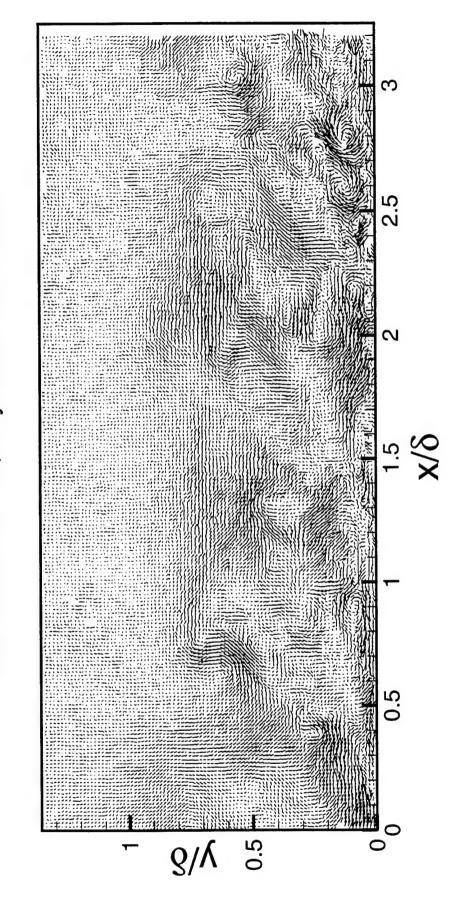
Realization LW-03,  $U_c = 0.85 U_{\odot}$ 



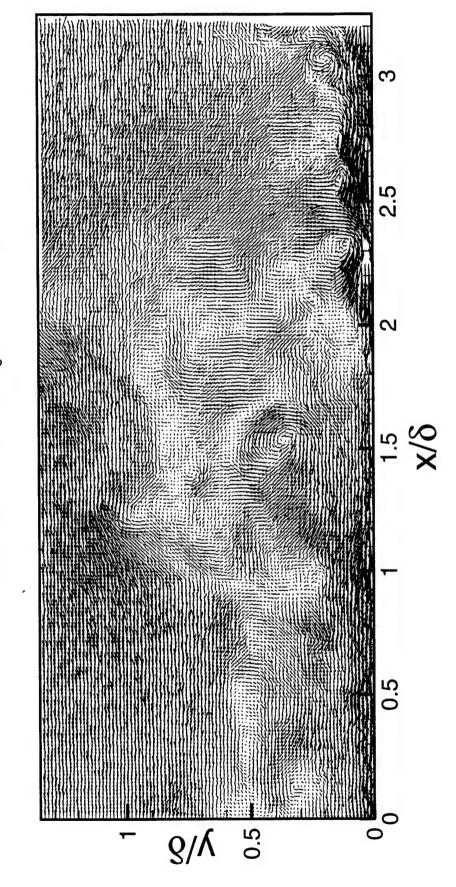
Realization LW-03,  $U_c = 0.65 U_{\odot}$ 



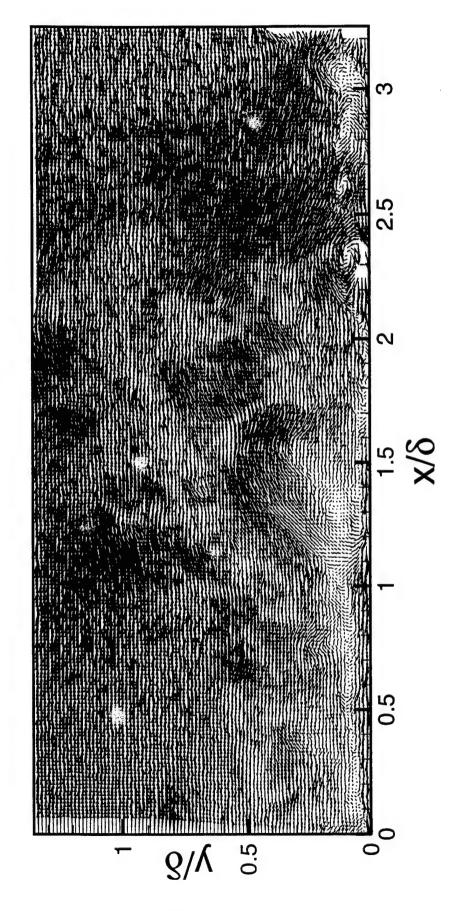
Realization LW-03, Reynolds Fluctuations



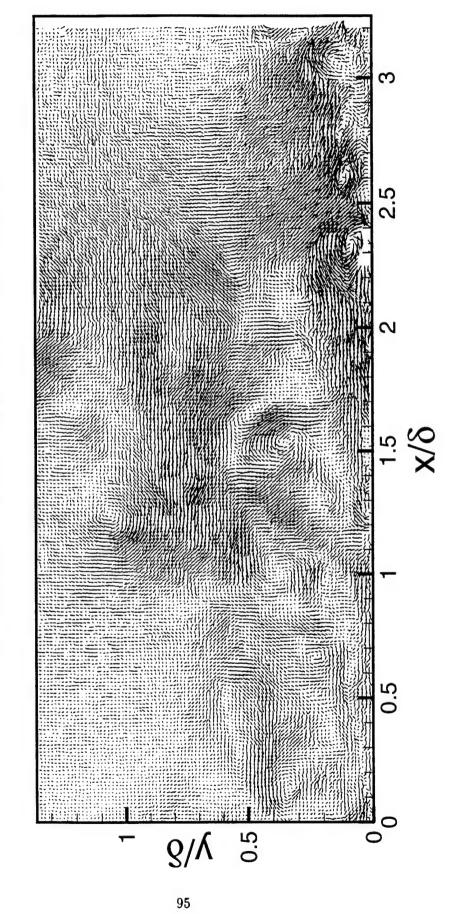
Realization LW-04,  $U_c = 0.85 U_s$ 



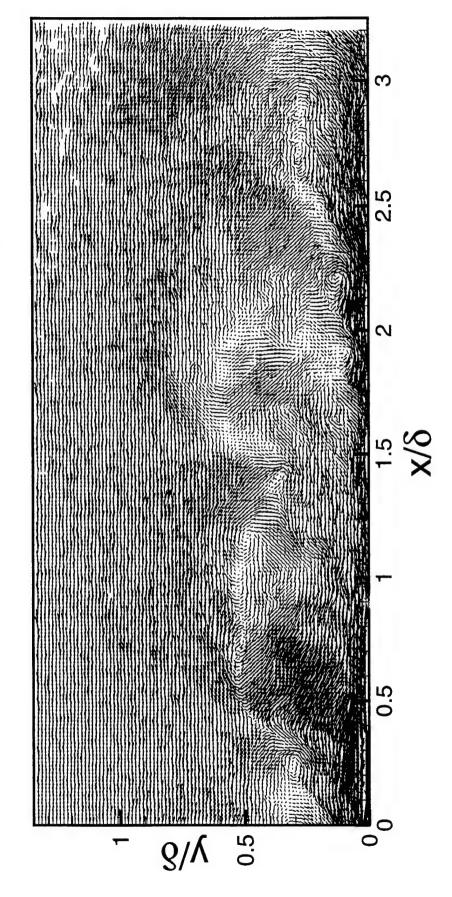
Realization LW-04,  $U_c = 0.65 U_{\odot}$ 



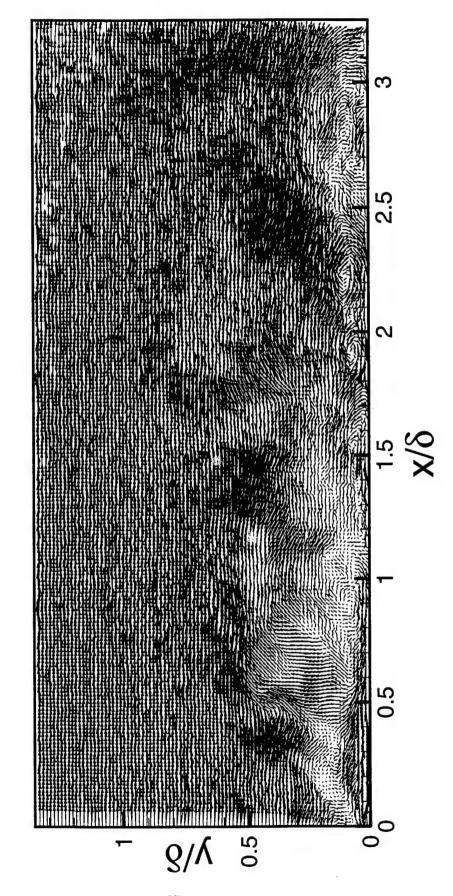
Realization LW-04, Reynolds Fluctuations



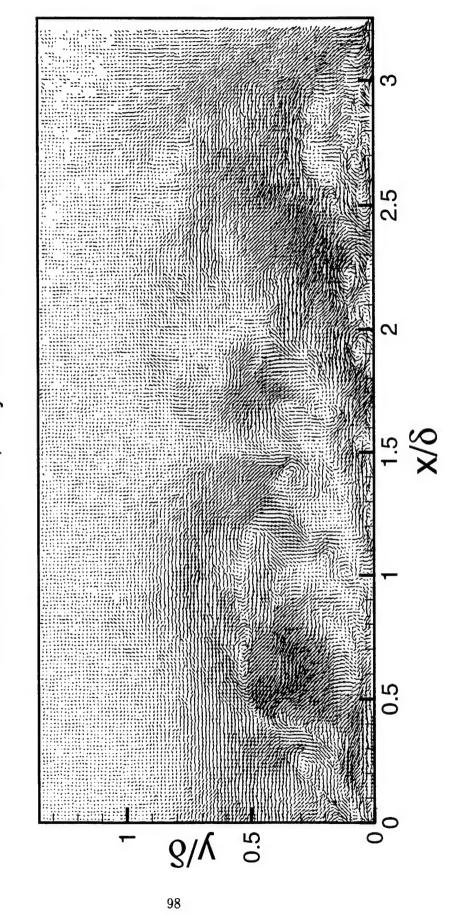
Realization LW-05,  $U_c = 0.85 U_{\odot}$ 



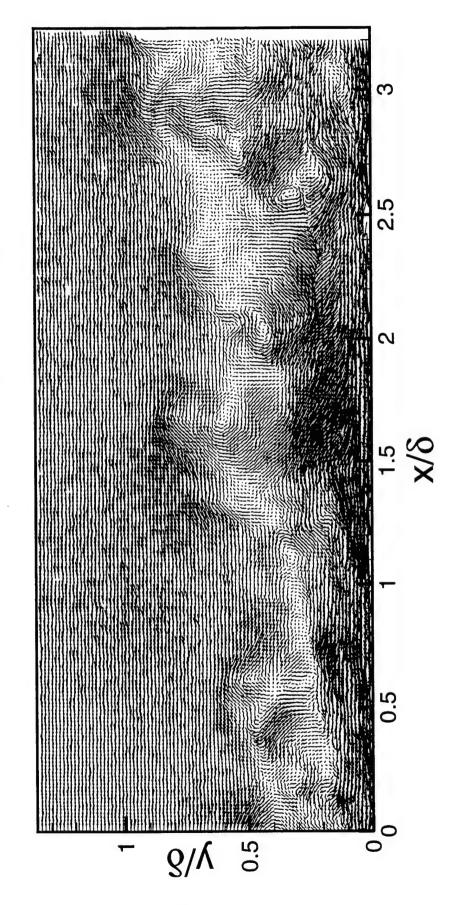
Realization LW-05,  $U_c = 0.65 U_{\odot}$ 



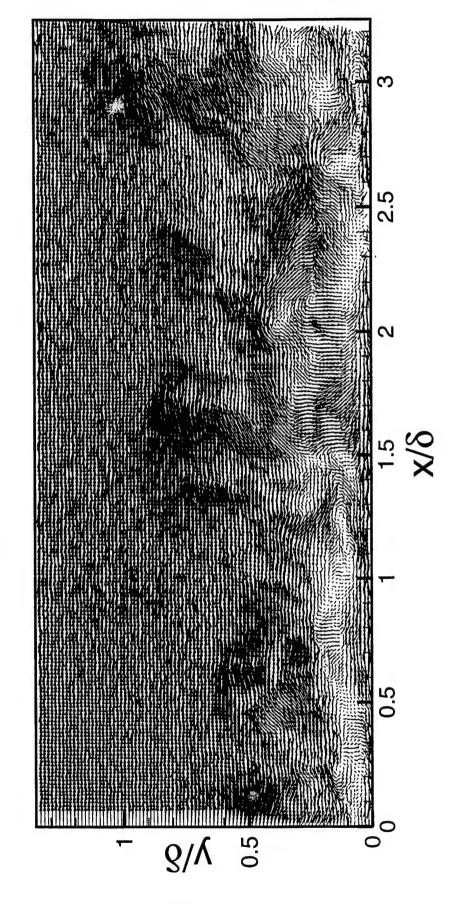
Realization LW-05, Reynolds Fluctuations



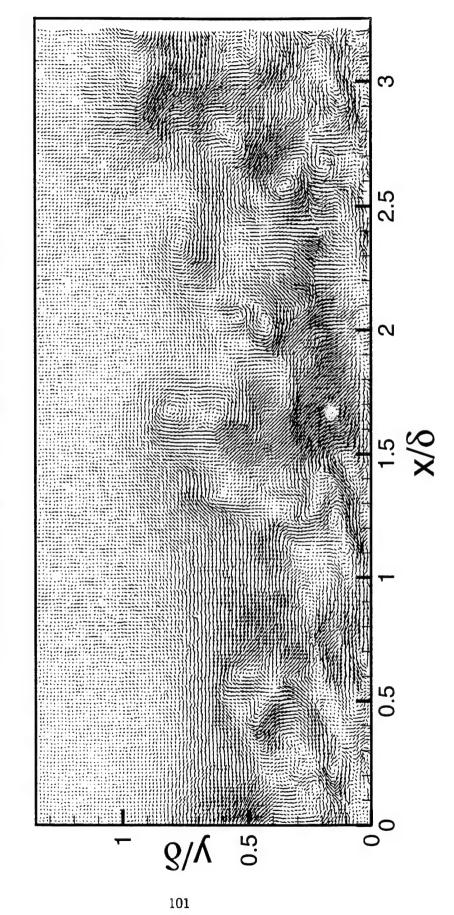
Realization LW-06,  $U_c = 0.85 U_{\odot}$ 



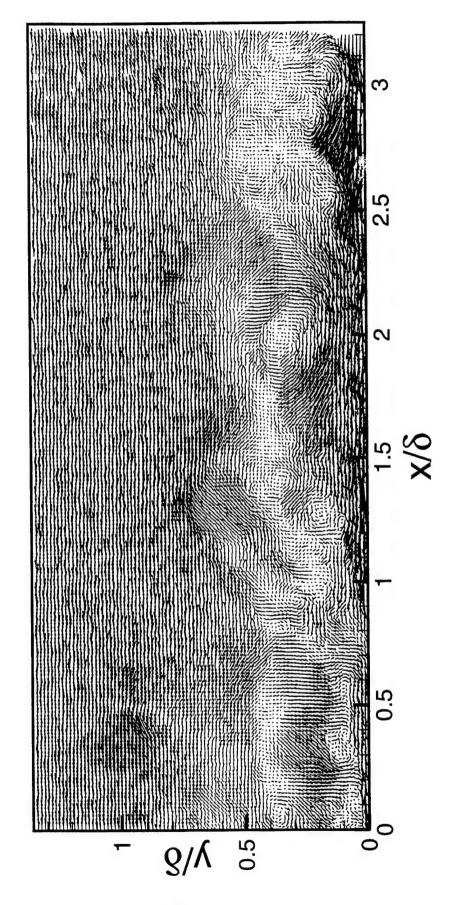
Realization LW-06,  $U_c = 0.65 U_{\odot}$ 



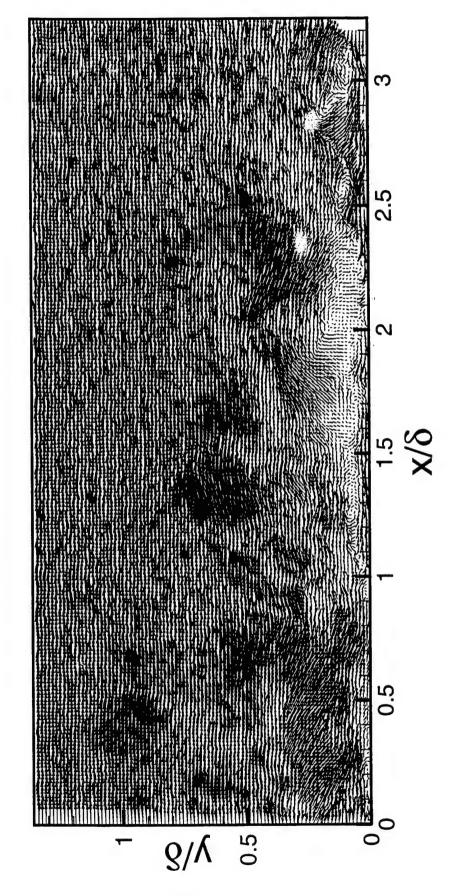
Realization LW-06, Reynolds Fluctuations



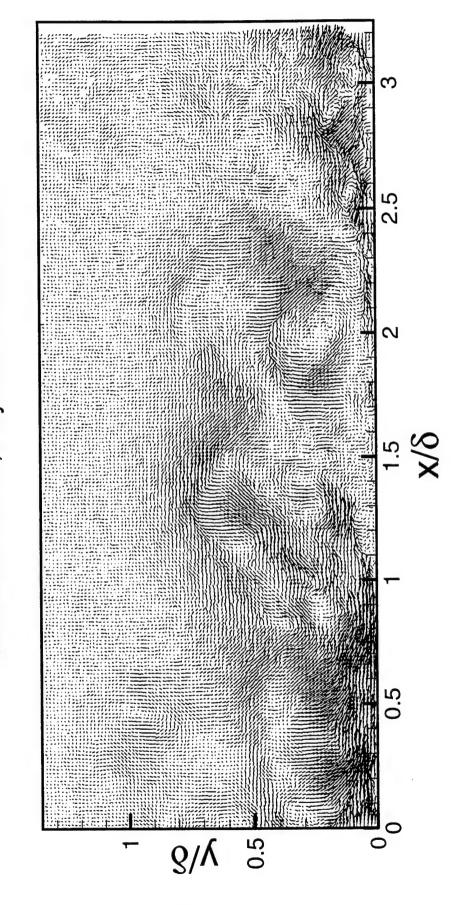
Realization LW-07,  $U_c = 0.85 U_{\odot}$ 



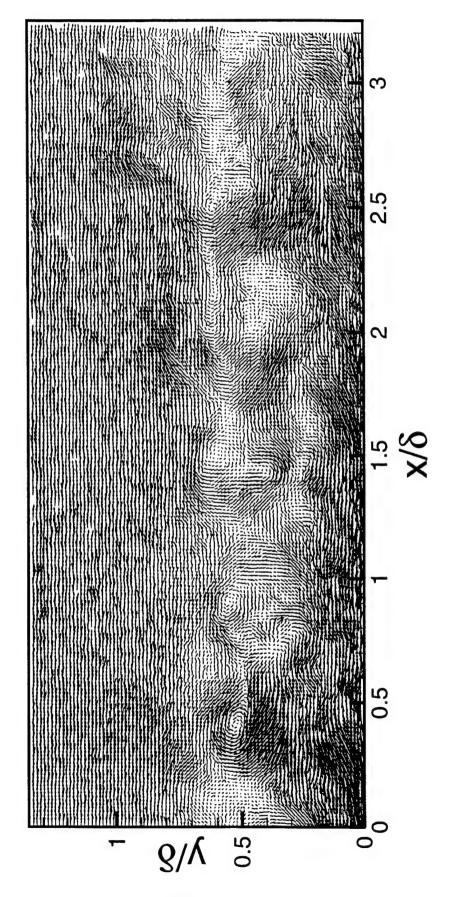
Realization LW-07,  $U_c = 0.65 U_{\odot}$ 



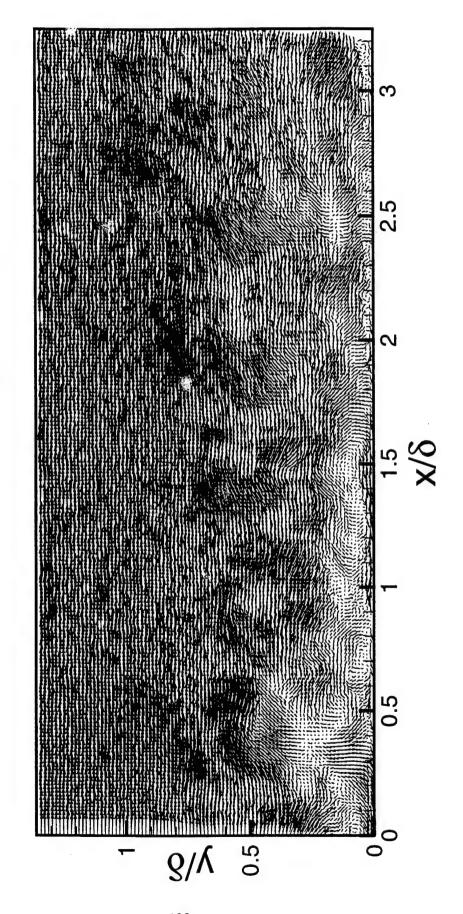
Realization LW-07, Reynolds Fluctuations



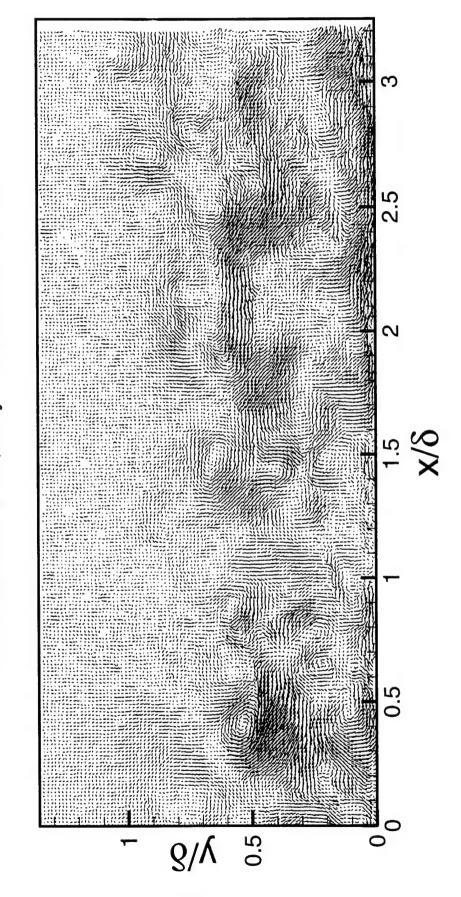
Realization LW-08,  $U_c = 0.85 U_{\odot}$ 



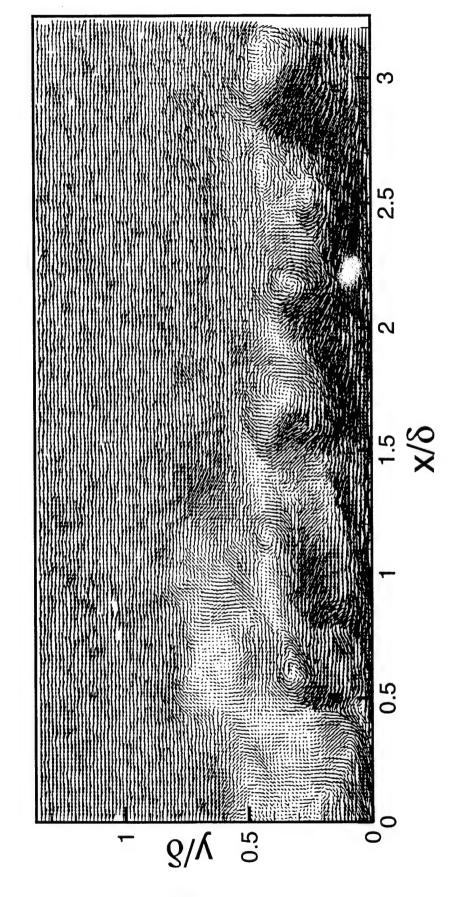
Realization LW-08,  $U_c = 0.65 U_{\odot}$ 



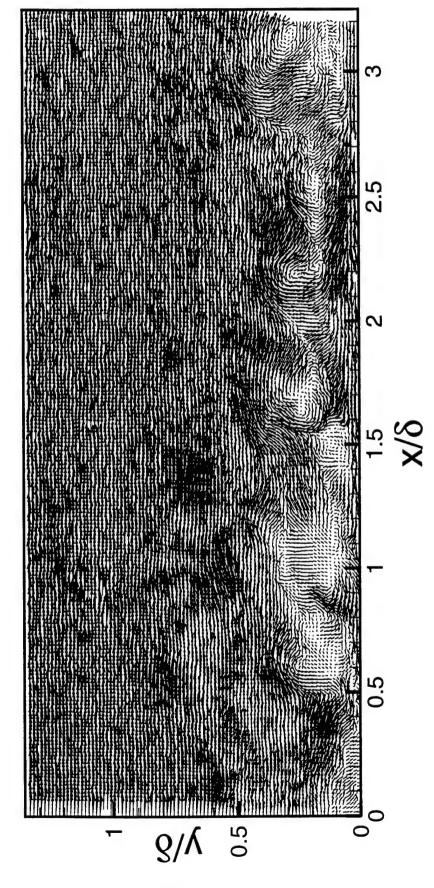
Realization LW-08, Reynolds Fluctuations



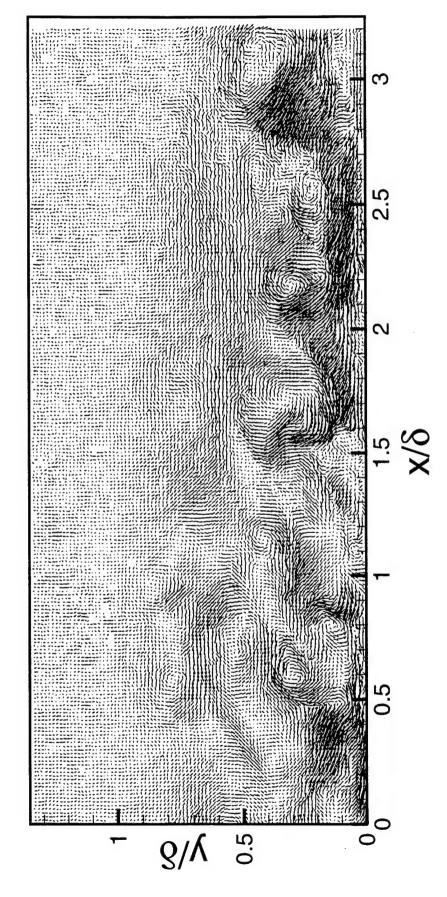
Realization LW-09,  $U_c = 0.85 U_{\odot}$ 



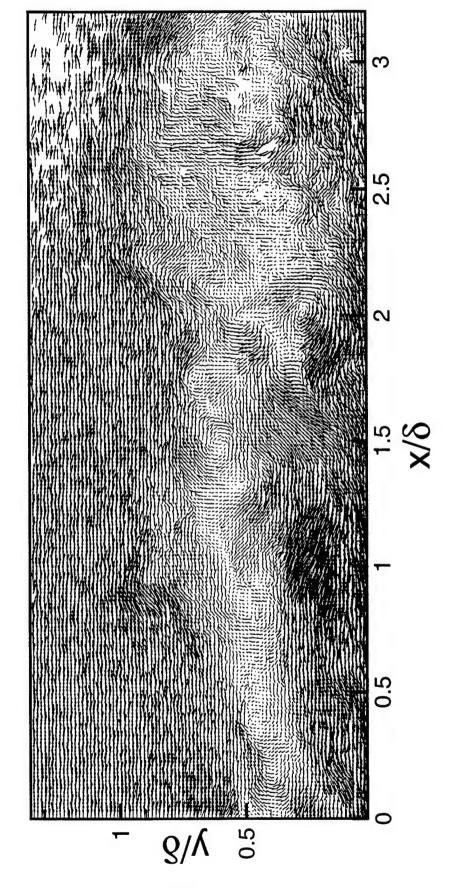
Realization LW-09,  $U_c = 0.65 U_{\odot}$ 



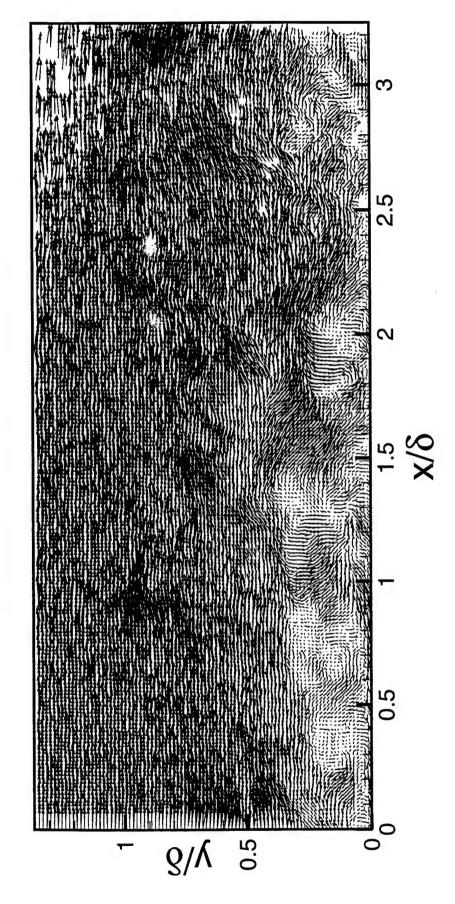
Realization LW-09, Reynolds Fluctuations



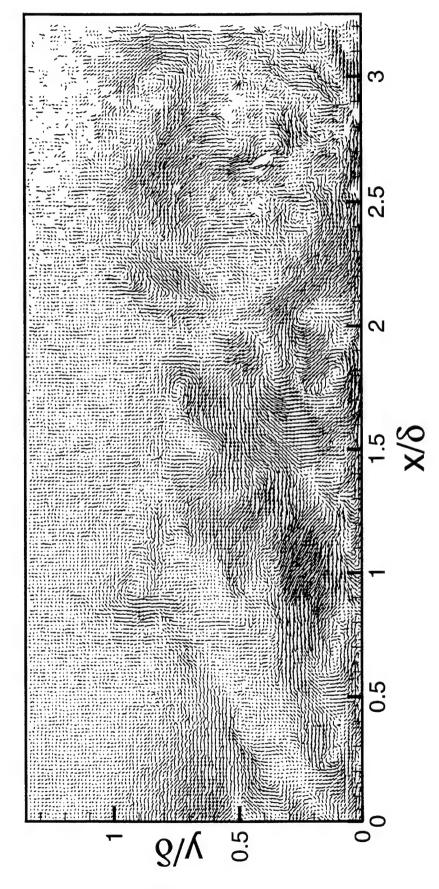
Realization LW-10,  $U_c = 0.85 U_{\odot}$ 



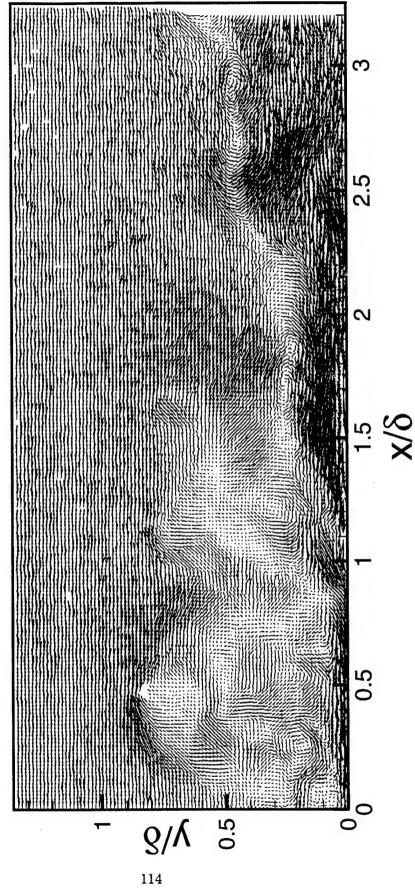
Realization LW-10,  $U_c = 0.65 U_{\odot}$ 



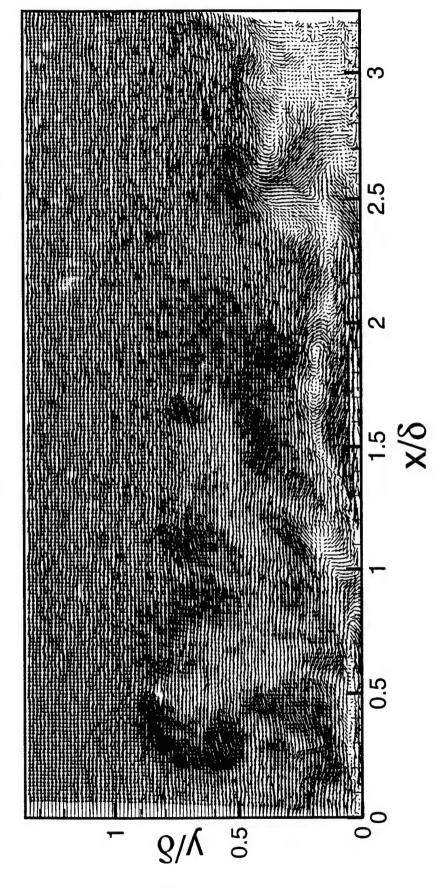
Realization LW-10, Reynolds Fluctuations



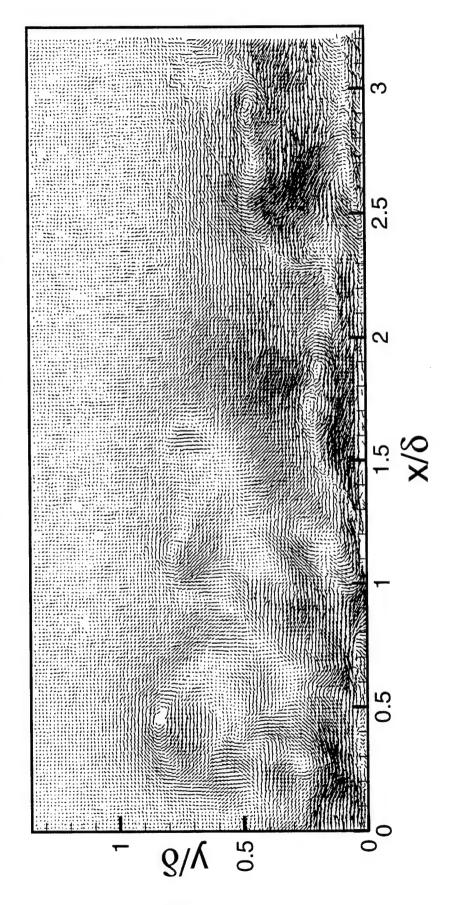
Realization LW-11,  $U_c = 0.85 U_{\odot}$ 



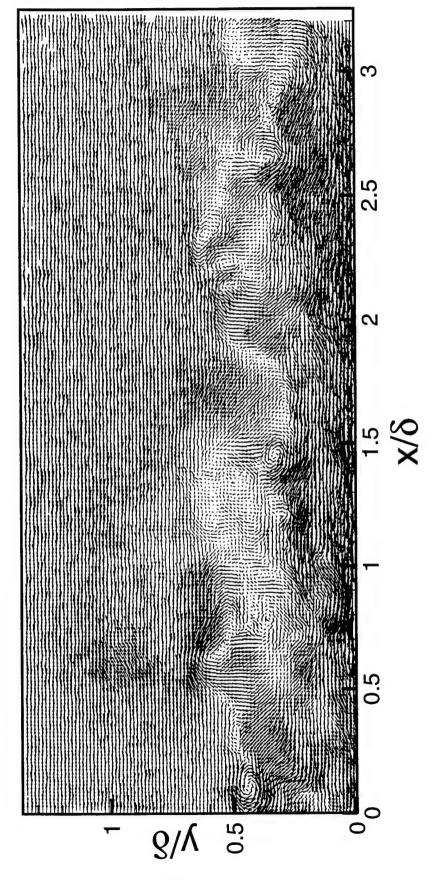
Realization LW-11,  $U_c = 0.65 U_{\odot}$ 



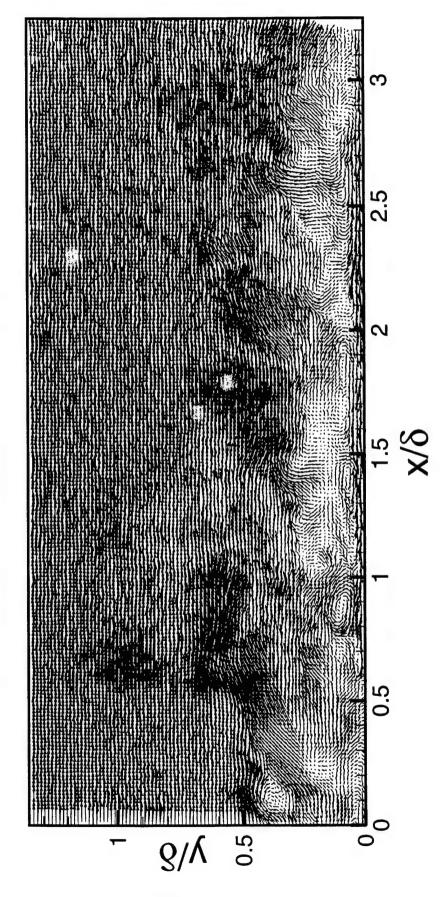
Realization LW-11, Reynolds Fluctuations



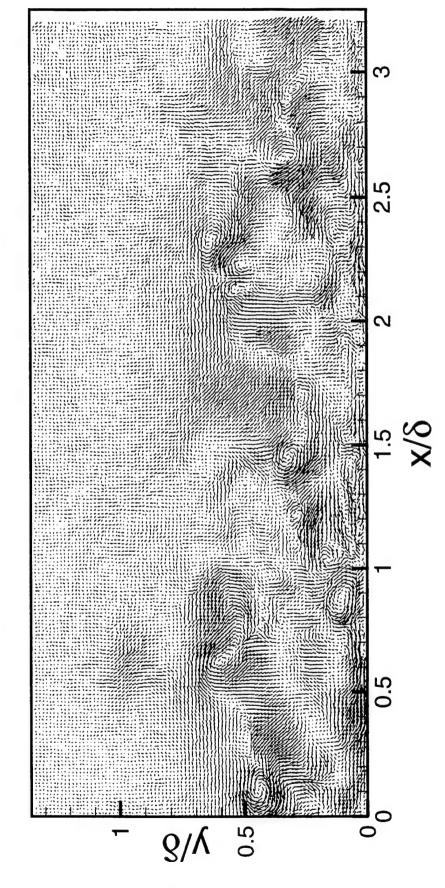
Realization LW-12,  $U_c = 0.85 U_{\odot}$ 



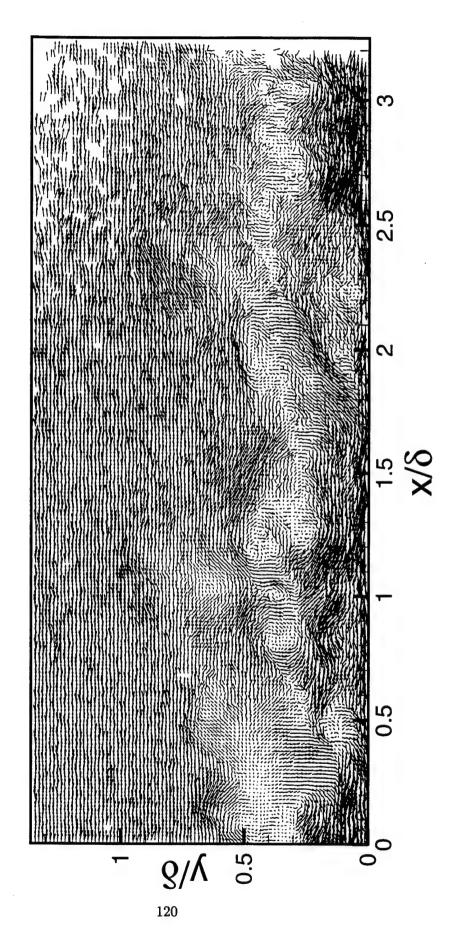
Realization LW-12,  $U_c = 0.65 U_{\odot}$ 



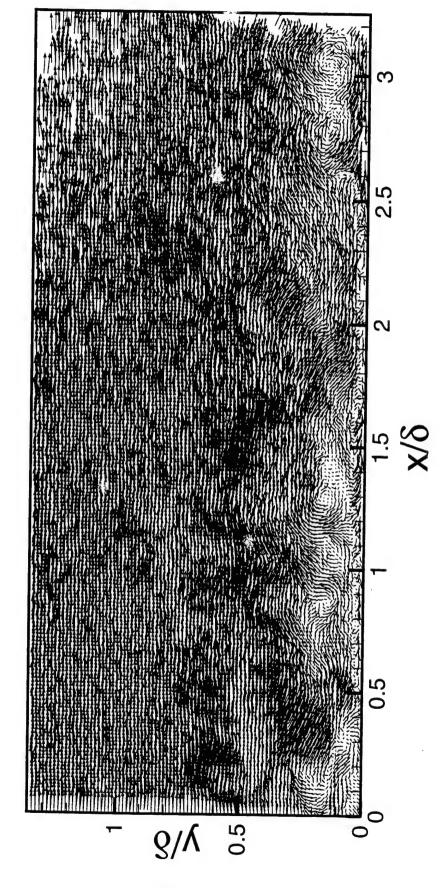
Realization LW-12, Reynolds Fluctuations



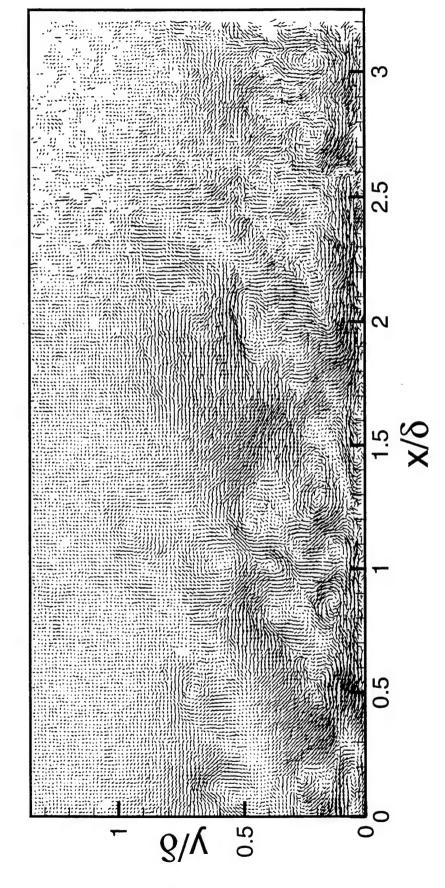
Realization LW-13,  $U_c = 0.85 U_{\odot}$ 



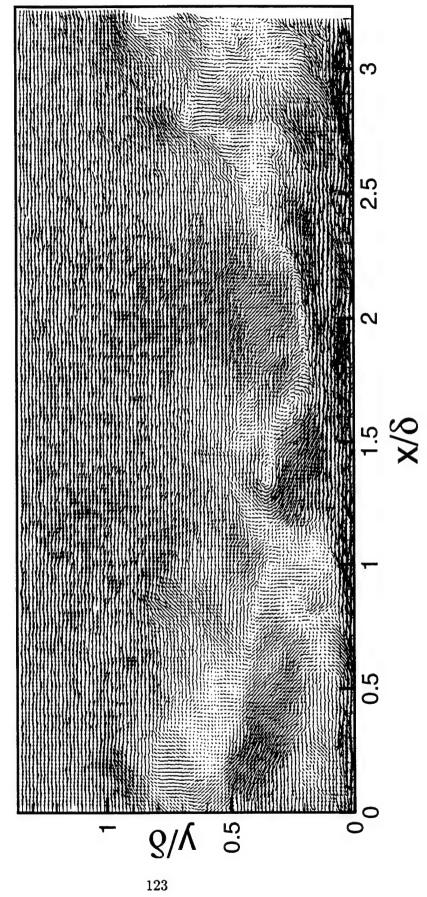
Realization LW-13,  $U_c = 0.65 U_{\odot}$ 



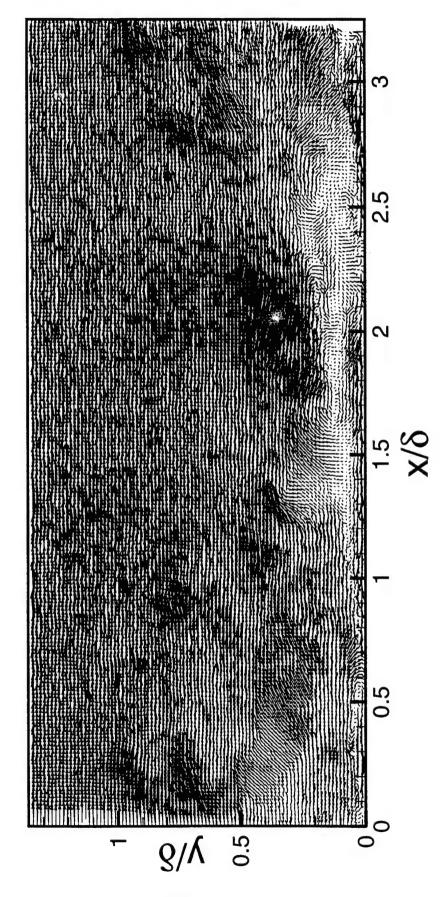
Realization LW-13, Reynolds Fluctuations



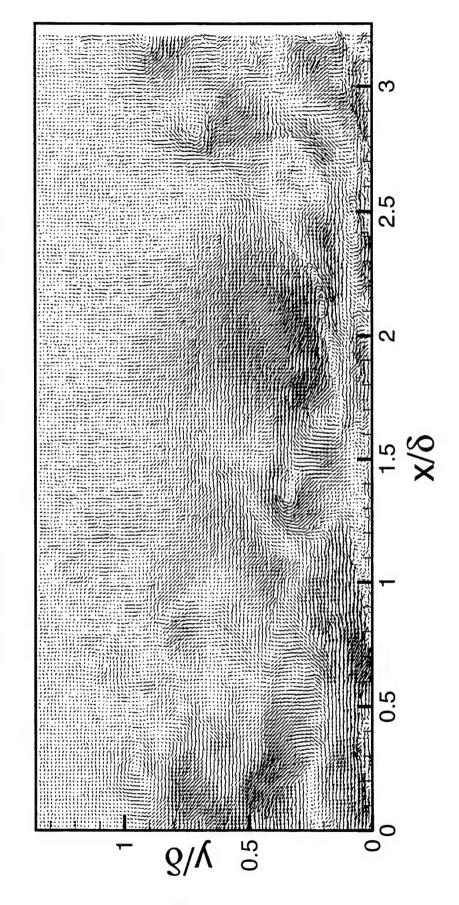
Realization LW-14,  $U_c = 0.85 U_{\odot}$ 



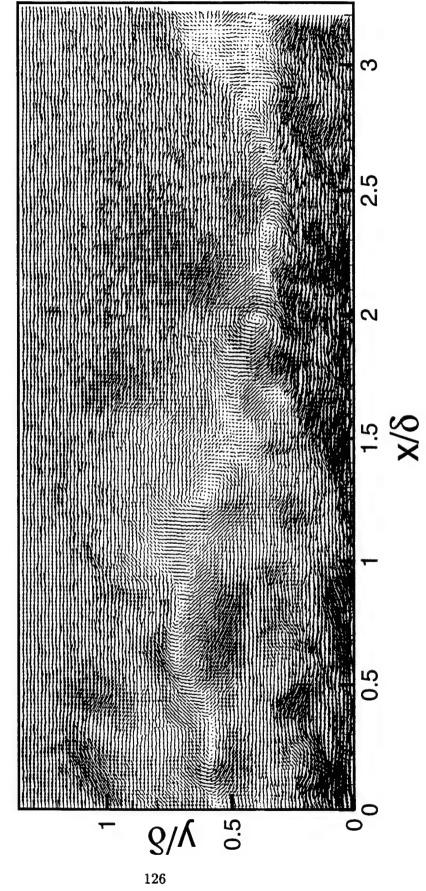
Realization LW-14,  $U_c = 0.65 U_{\odot}$ 



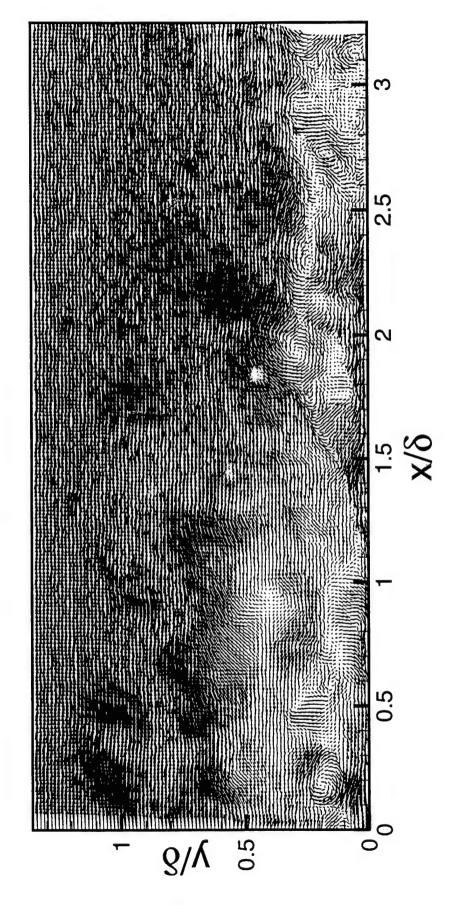
Realization LW-14, Reynolds Fluctuations



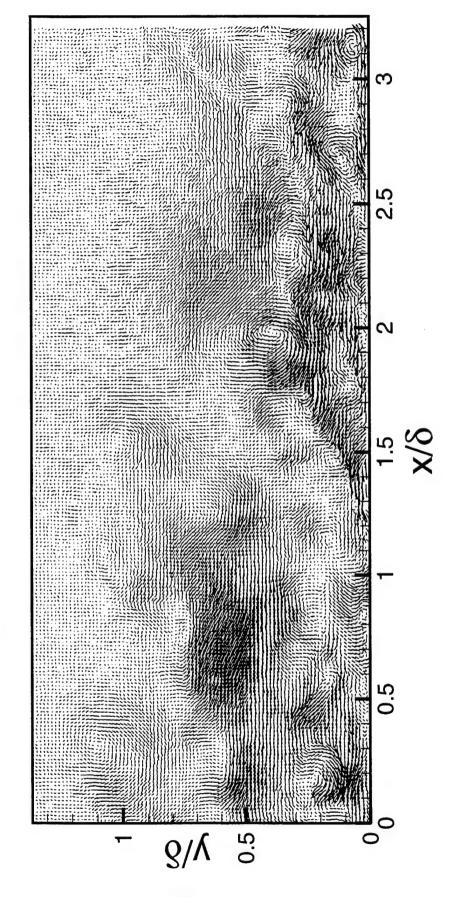
Realization LW-15,  $U_c = 0.85 U_{\odot}$ 



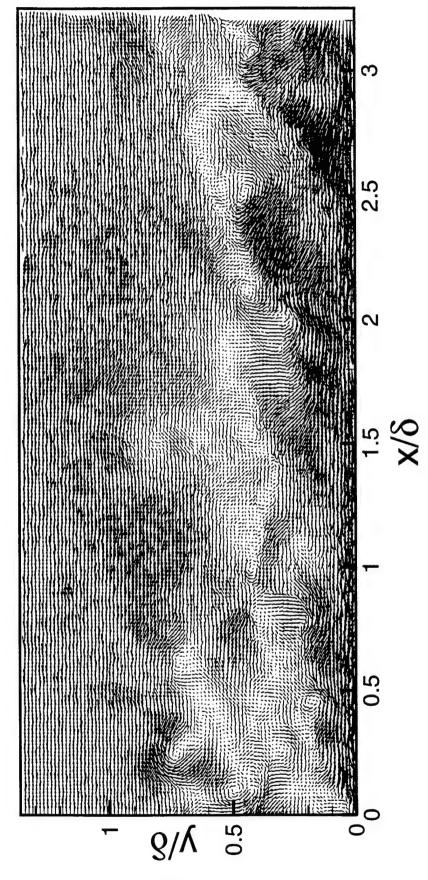
Realization LW-15,  $U_c = 0.65 U_{\odot}$ 



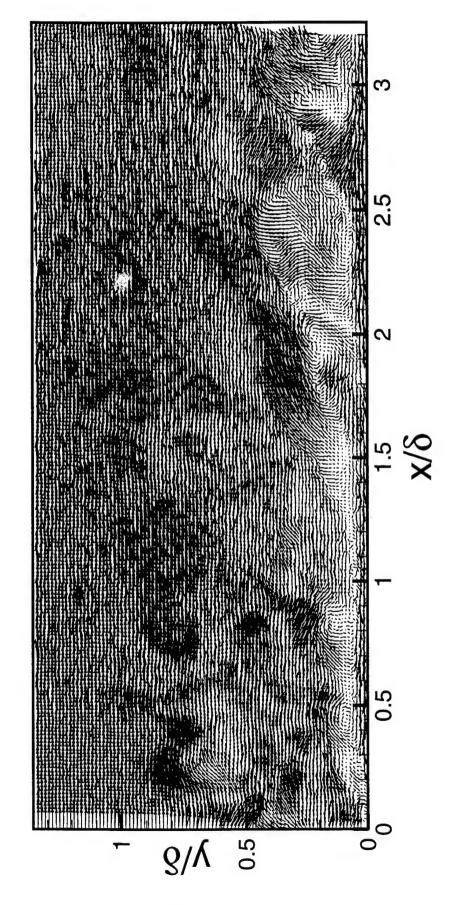
Realization LW-15, Reynolds Fluctuations



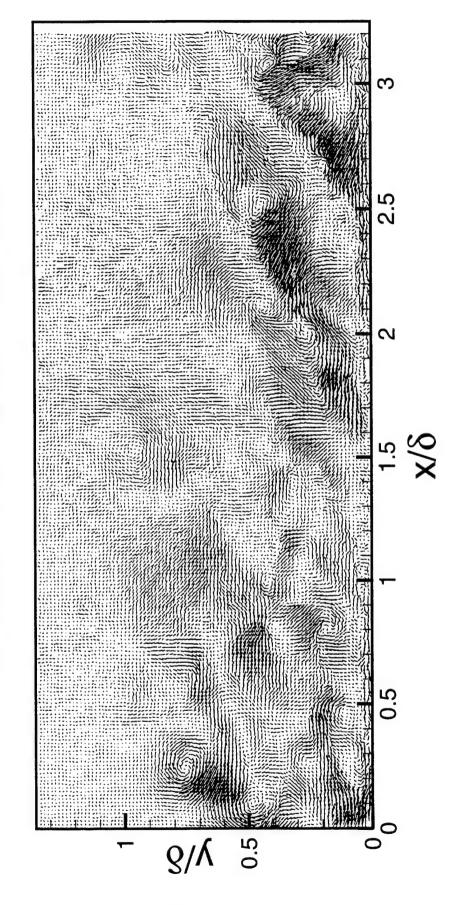
Realization LW-16,  $U_c = 0.85 U_{\odot}$ 



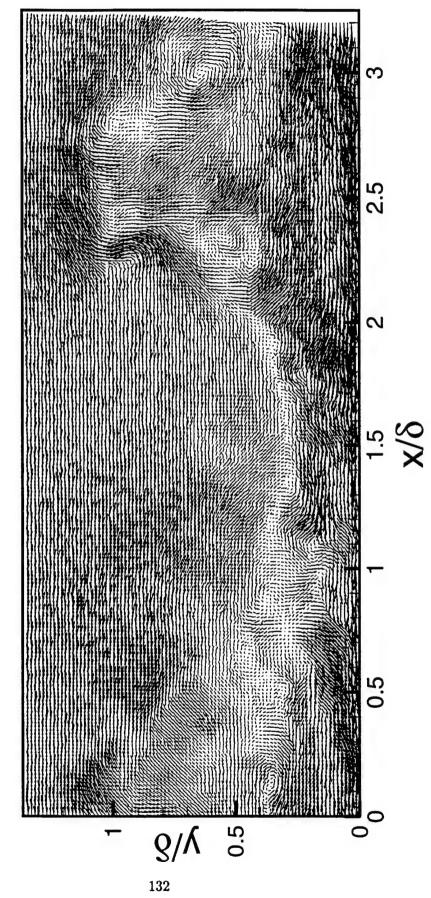
Realization LW-16,  $U_c = 0.65 U_{\odot}$ 



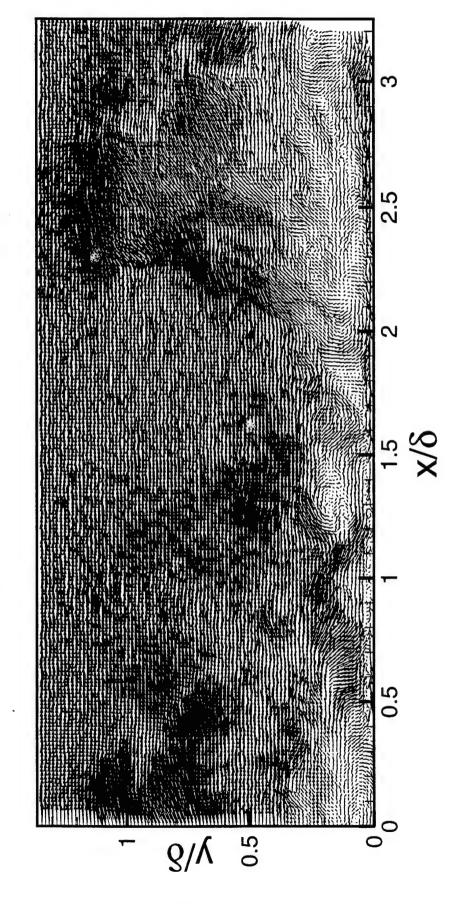
Realization LW-16, Reynolds Fluctuations



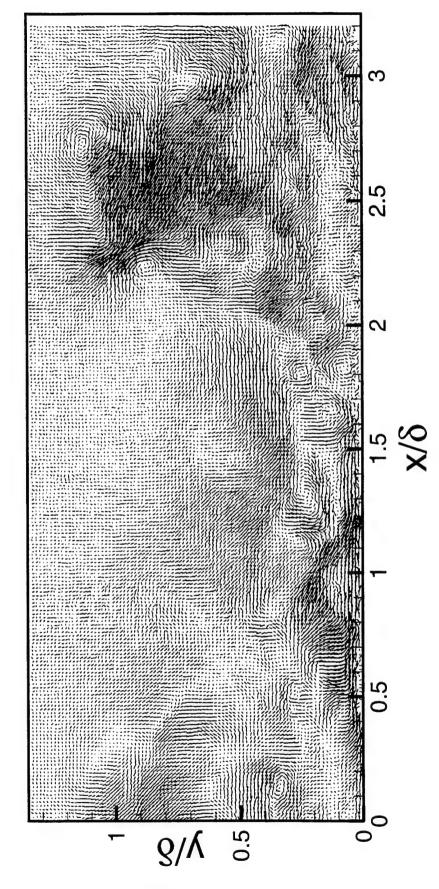
Realization LW-17,  $U_c = 0.85 U_{\odot}$ 



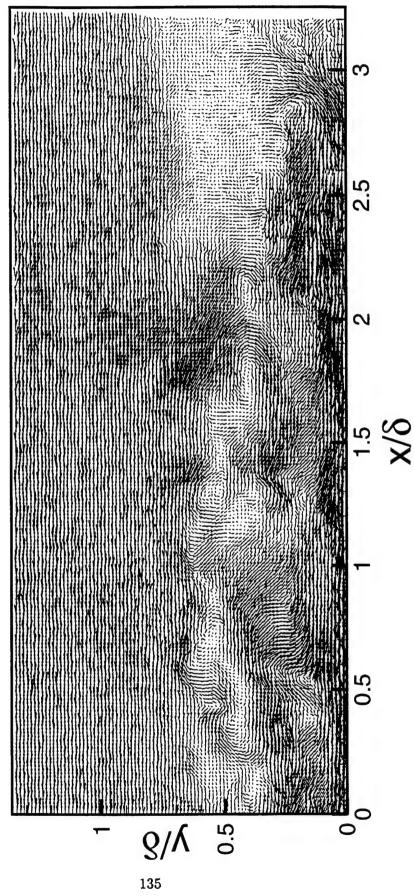
Realization LW-17,  $U_c = 0.65 U_{\odot}$ 



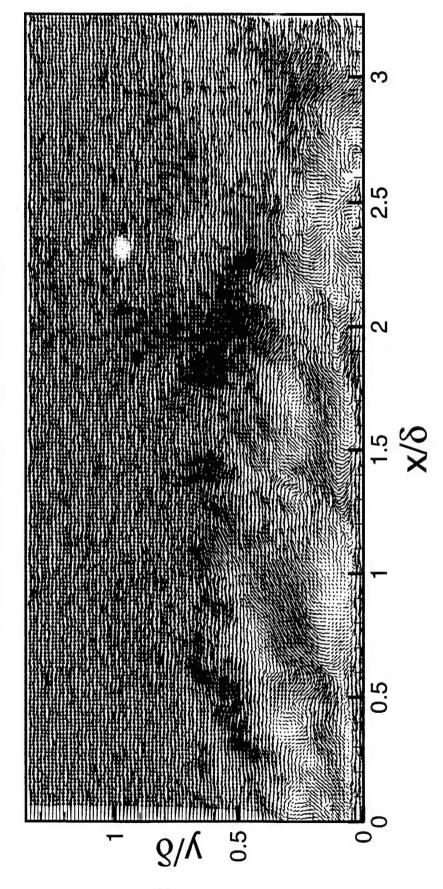
Realization LW-17, Reynolds Fluctuations



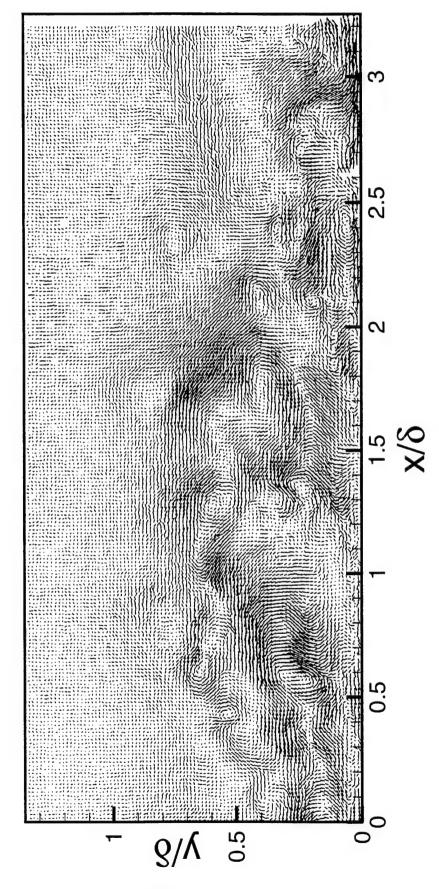
Realization LW-18,  $U_c = 0.85 U_{\odot}$ 



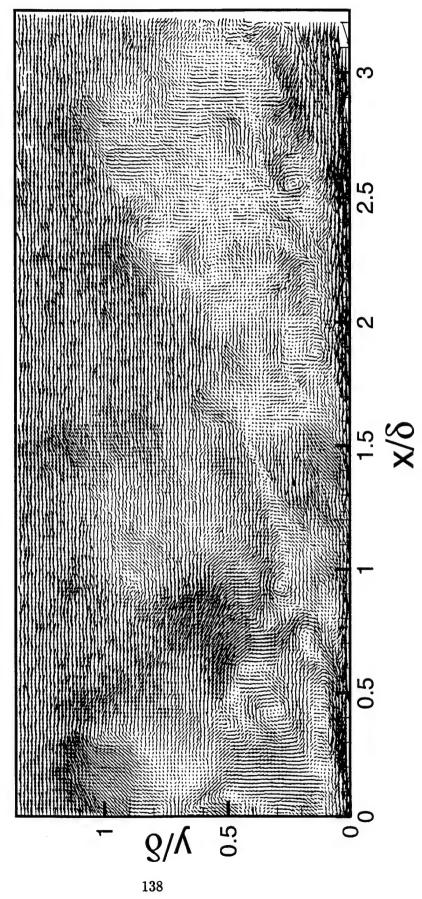
Realization LW-18,  $U_c = 0.65 U_{\odot}$ 



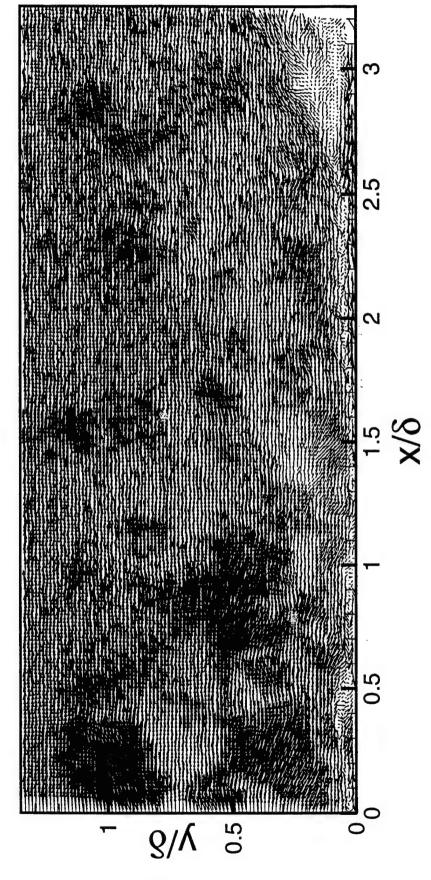
Realization LW-18, Reynolds Fluctuations



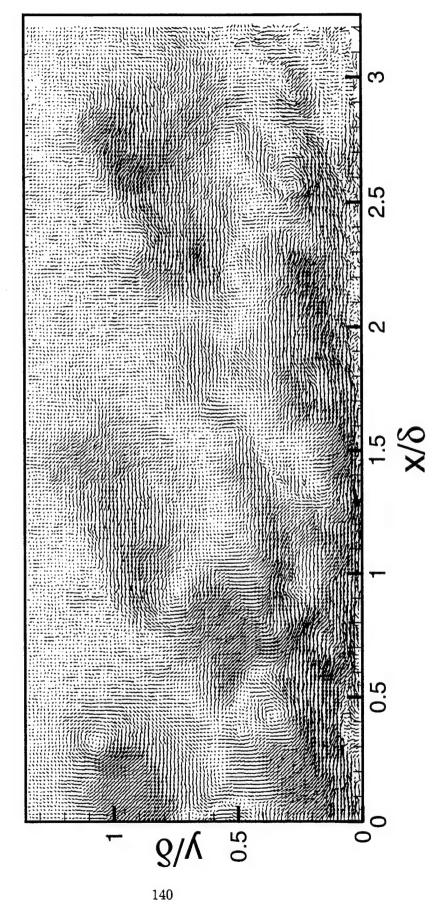
Realization LW-19,  $U_c = 0.85 U_{\odot}$ 



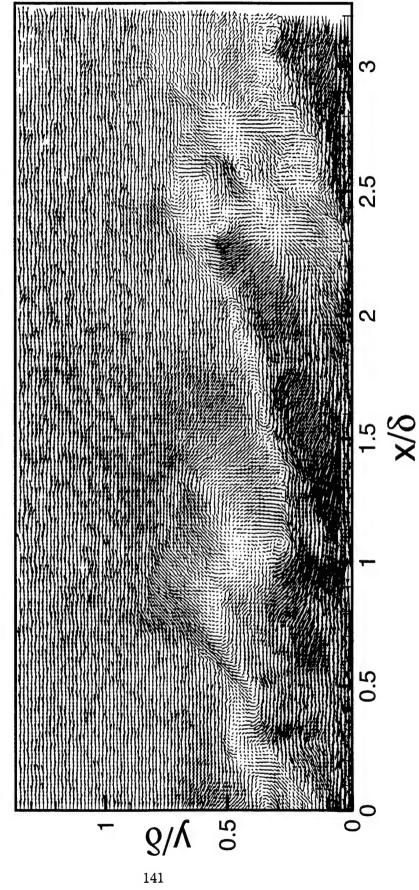
Realization LW-19,  $U_c = 0.65 U_{\odot}$ 



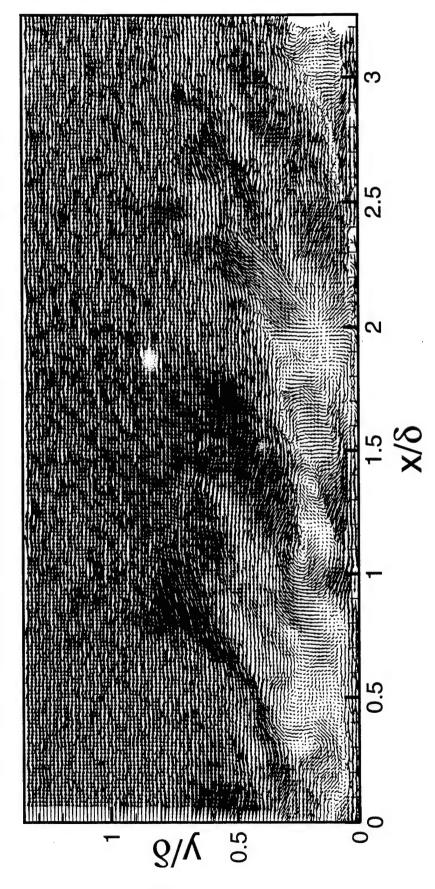
Realization LW-19, Reynolds Fluctuations



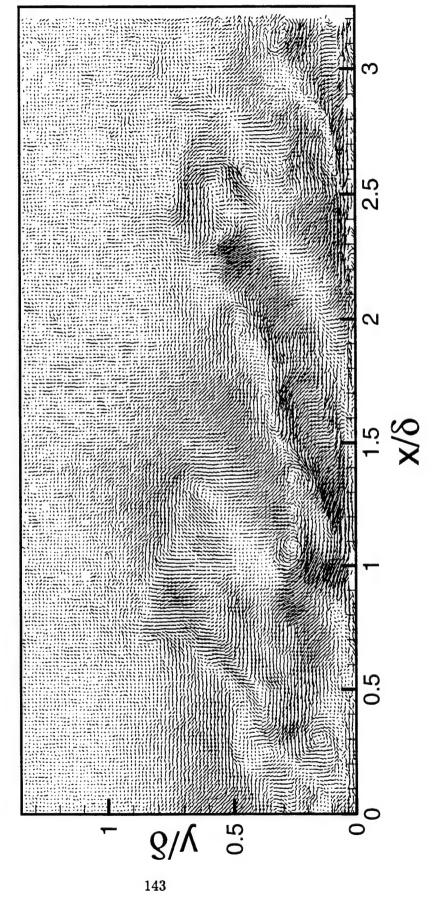
Realization LW-20,  $U_c = 0.85 U_{\odot}$ 



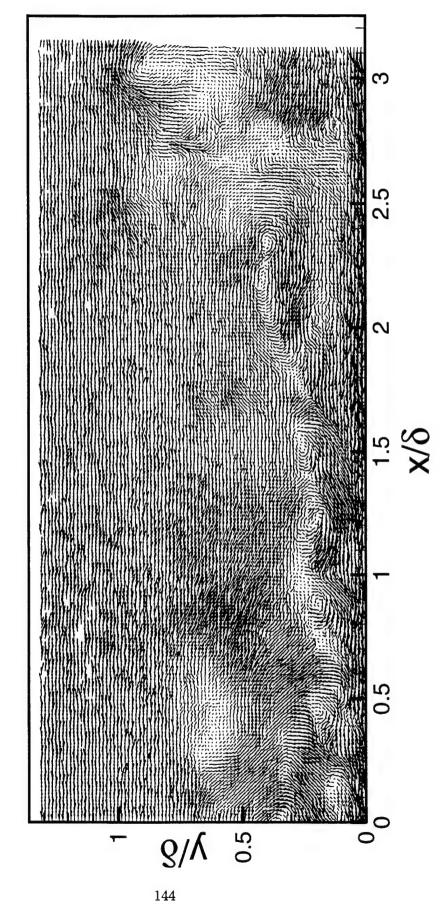
Realization LW-20,  $U_c = 0.65 U_{\odot}$ 



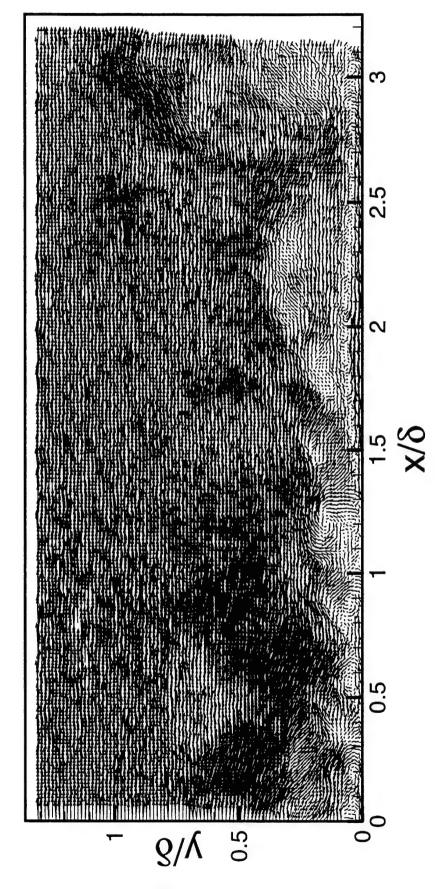
Realization LW-20, Reynolds Fluctuations



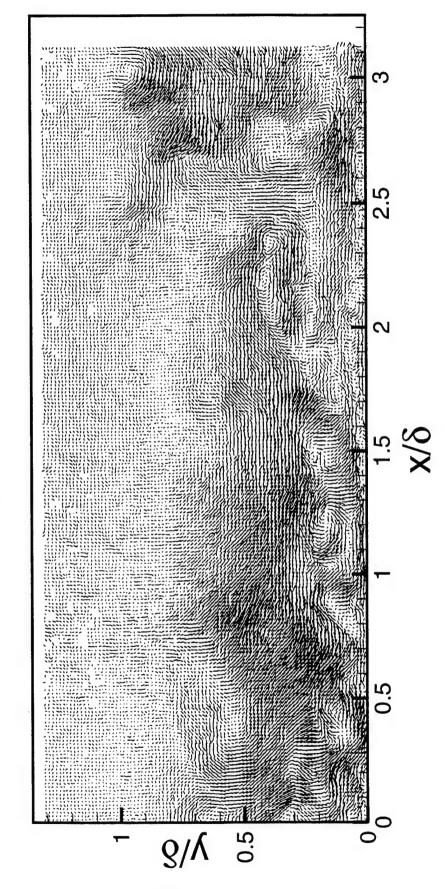
Realization LW-21,  $U_c = 0.85 U_{\odot}$ 



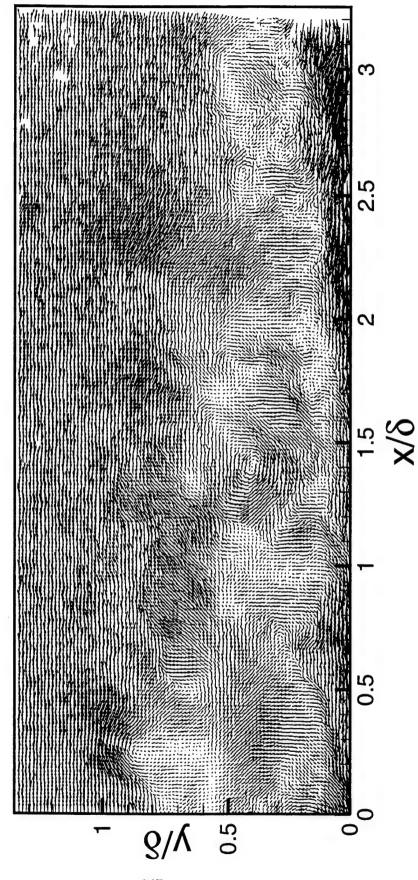
Realization LW-21,  $U_c = 0.65 U_{\odot}$ 



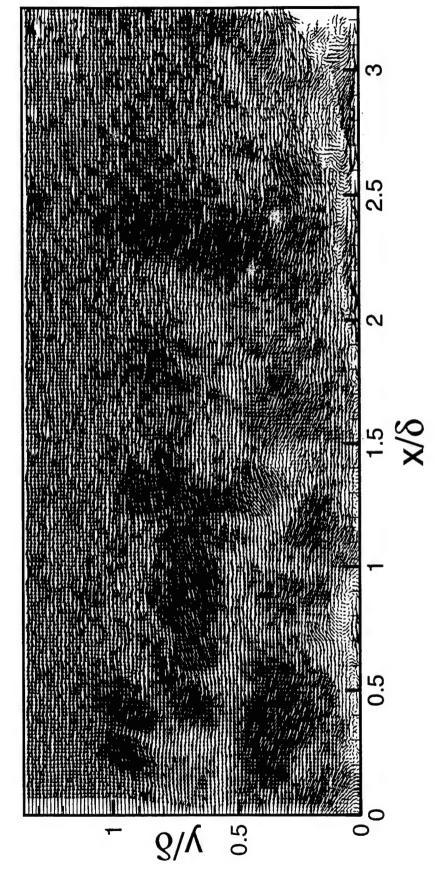
Realization LW-21, Reynolds Fluctuations



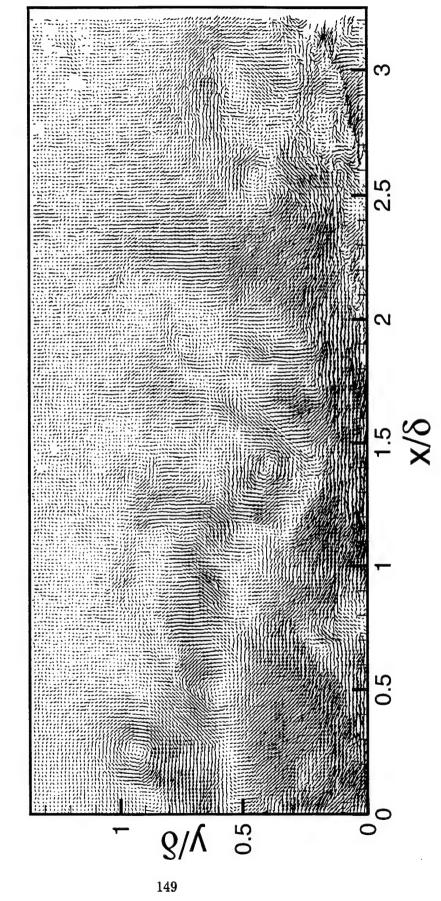
Realization LW-22,  $U_c = 0.85 U_{\odot}$ 



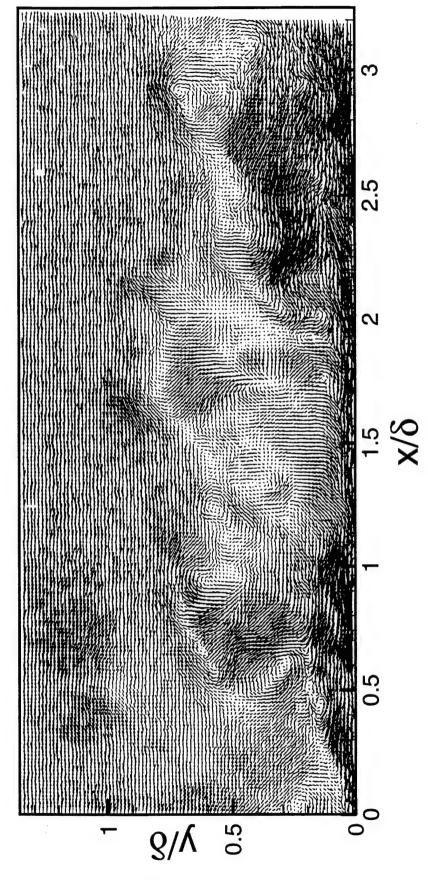
Realization LW-22,  $U_c = 0.65 U_{\odot}$ 



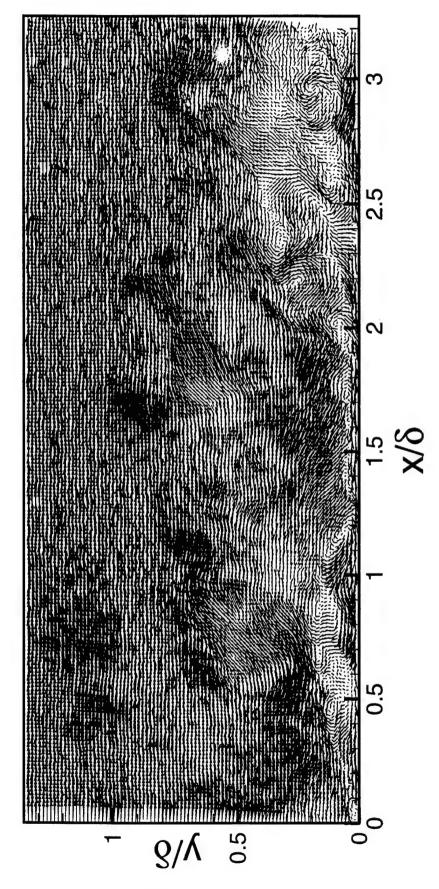
Realization LW-22, Reynolds Fluctuations



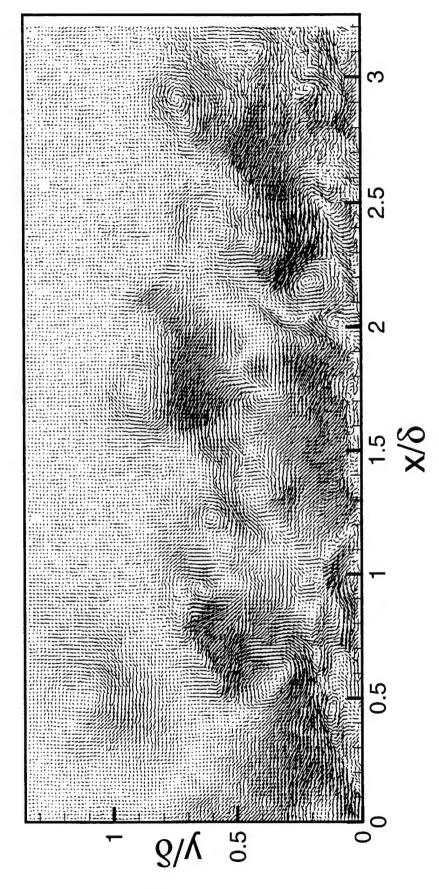
Realization LW-23,  $U_c = 0.85 U_{\odot}$ 



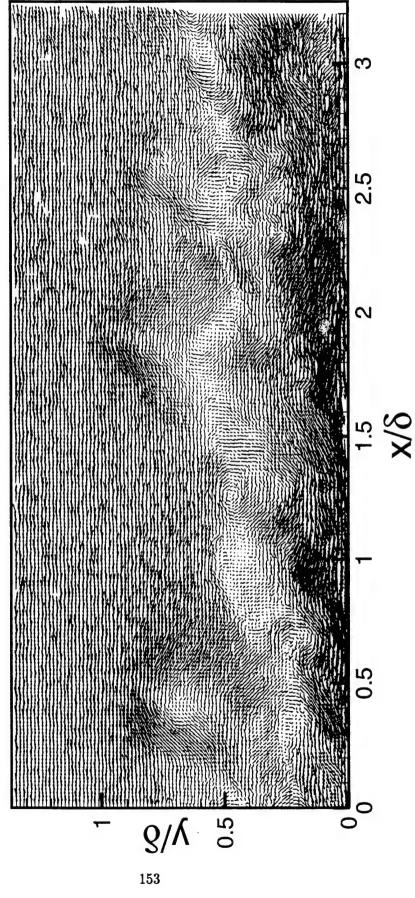
Realization LW-23,  $U_c = 0.65 U_{\odot}$ 



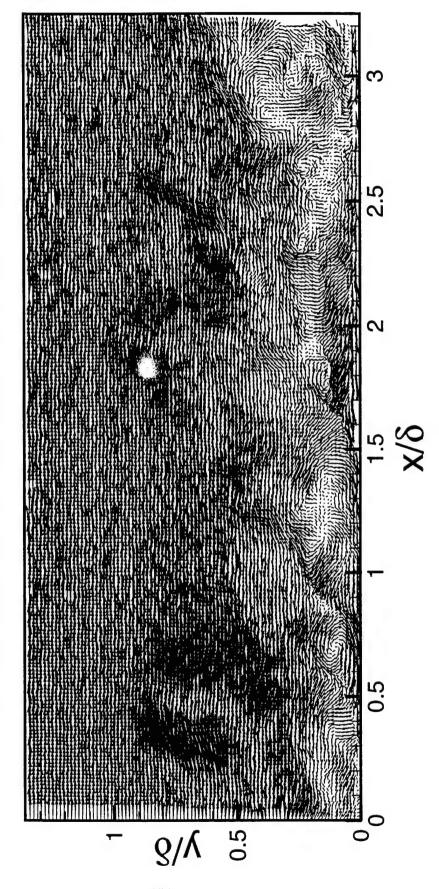
Realization LW-23, Reynolds Fluctuations



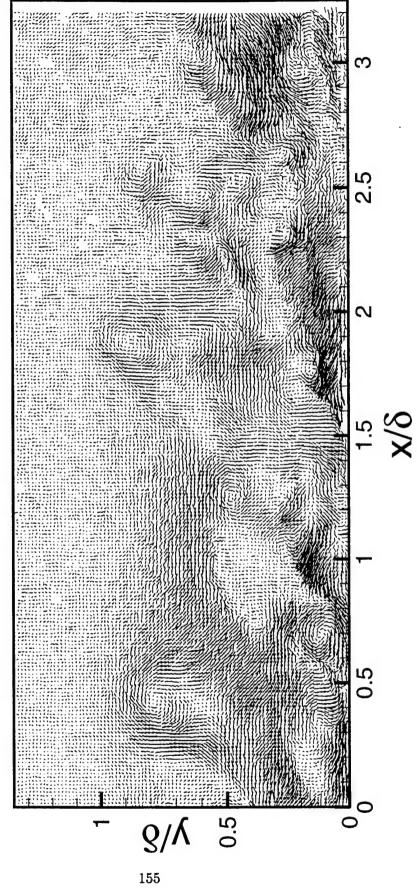
Realization LW-24,  $U_c = 0.85 U_{\odot}$ 



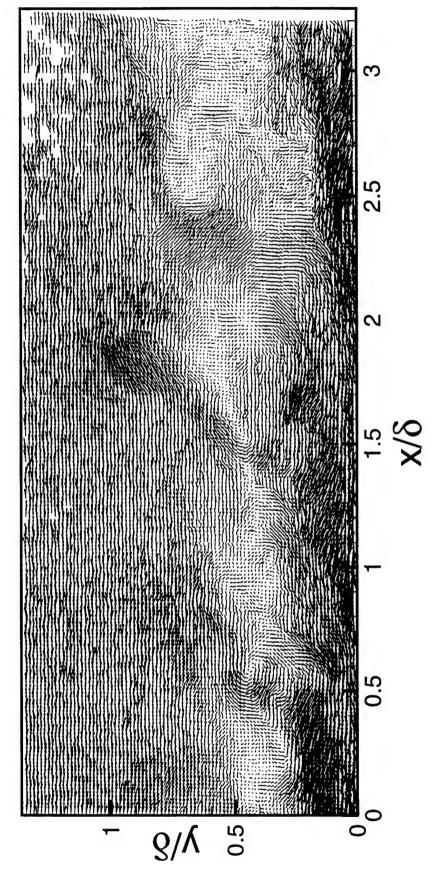
Realization LW-24,  $U_c = 0.65 U_{\odot}$ 



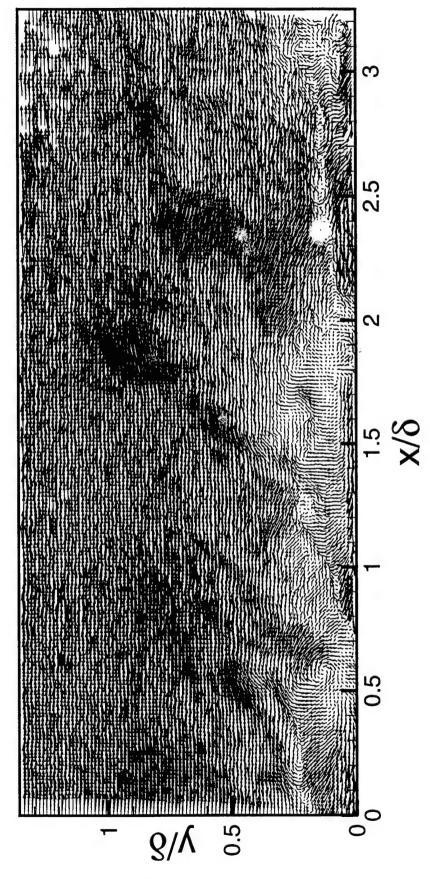
Realization LW-24, Reynolds Fluctuations



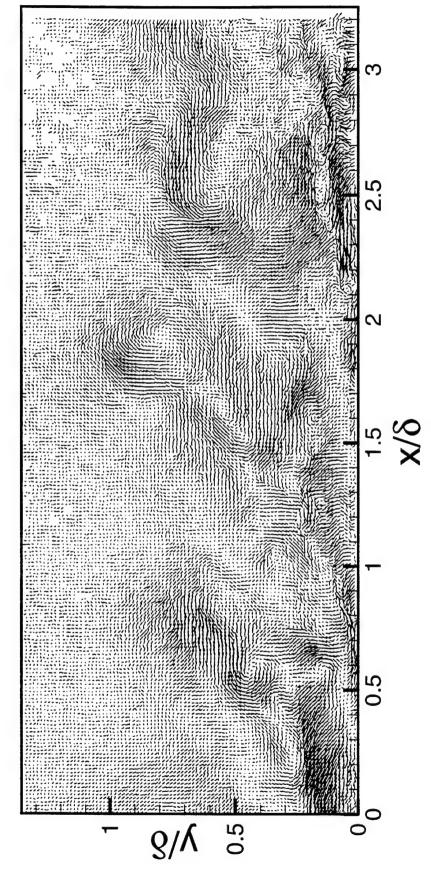
Realization LW-25,  $U_c = 0.85 U_{\odot}$ 



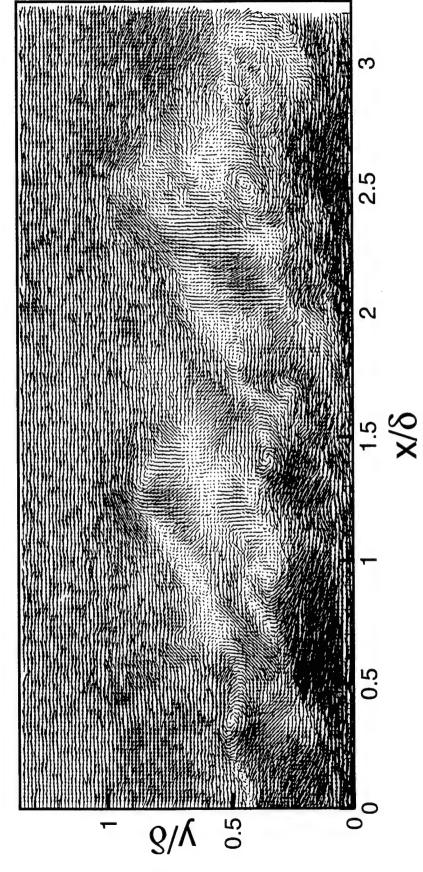
Realization LW-25,  $U_c = 0.65 U_{\odot}$ 



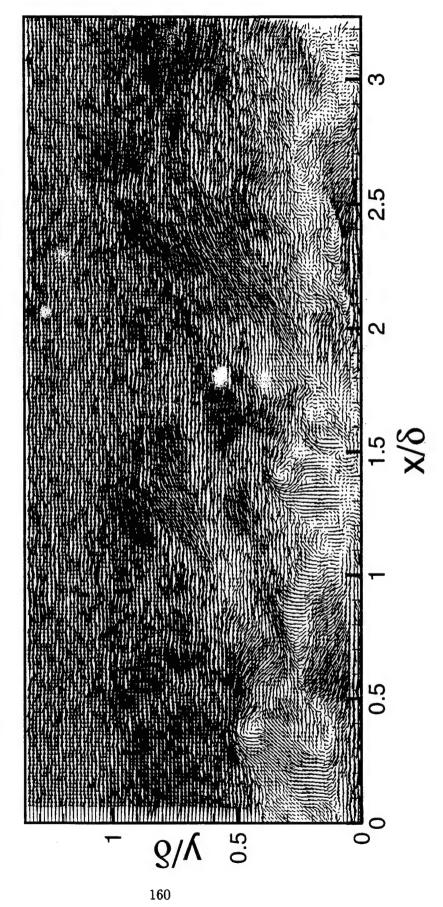
Realization LW-25, Reynolds Fluctuations



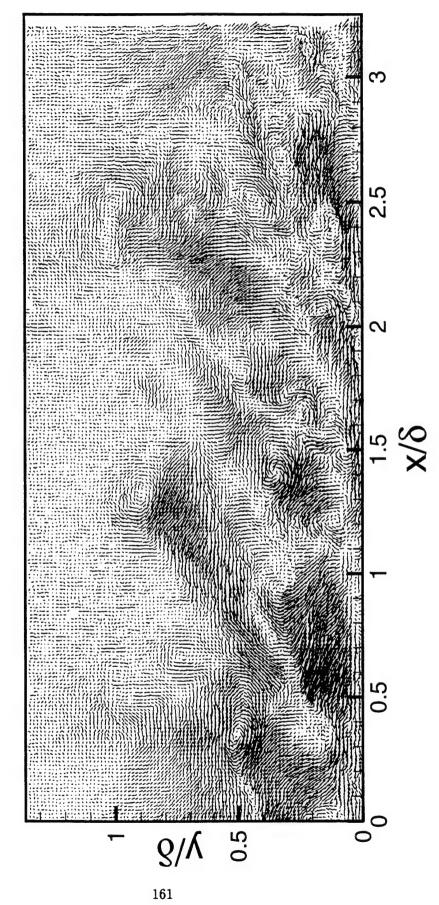
Realization LW-26,  $U_c = 0.85 U_{\odot}$ 



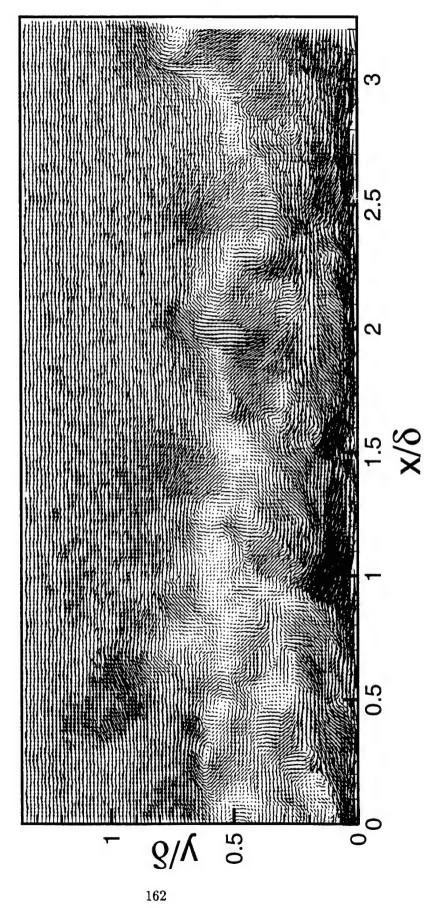
Realization LW-26,  $U_c = 0.65 U_{\odot}$ 



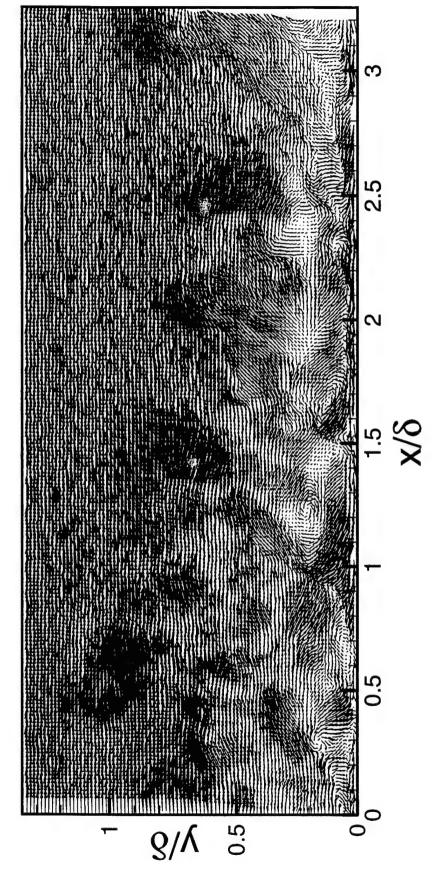
Realization LW-26, Reynolds Fluctuations



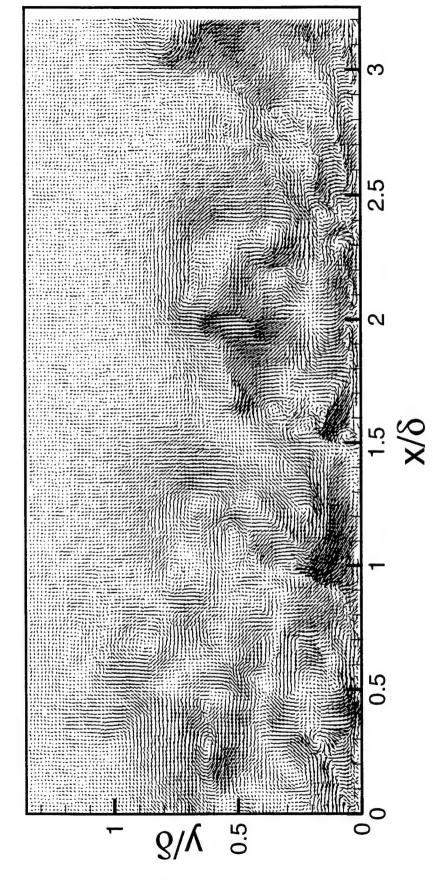
Realization LW-28,  $U_c = 0.85 U_{\odot}$ 



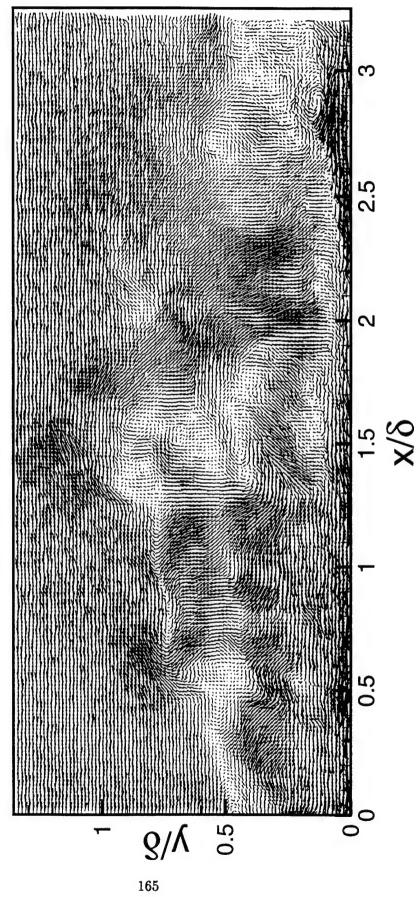
Realization LW-28,  $U_c = 0.65 U_{\odot}$ 



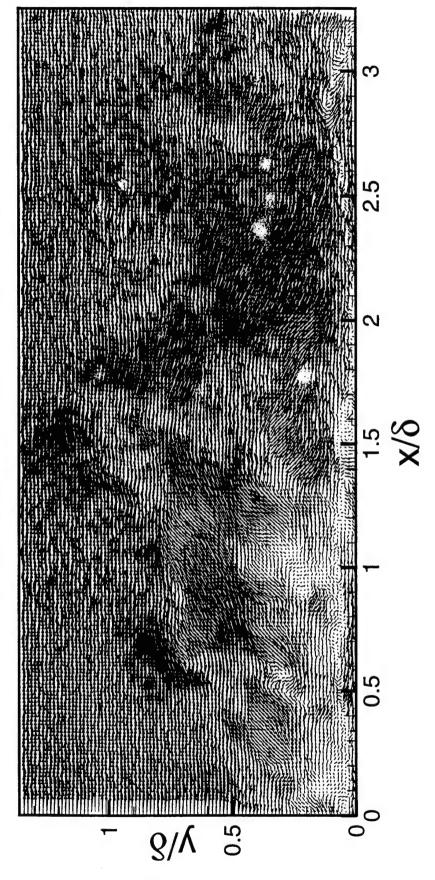
Realization LW-28, Reynolds Fluctuations



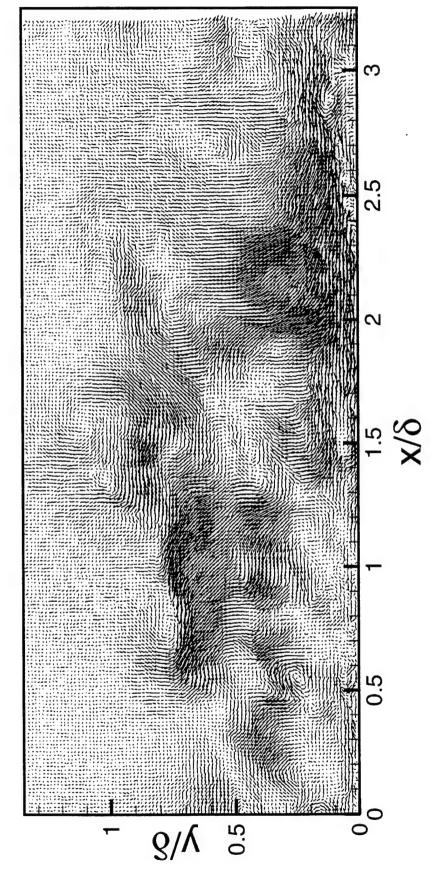
Realization LW-29,  $U_c = 0.85 U_{\odot}$ 



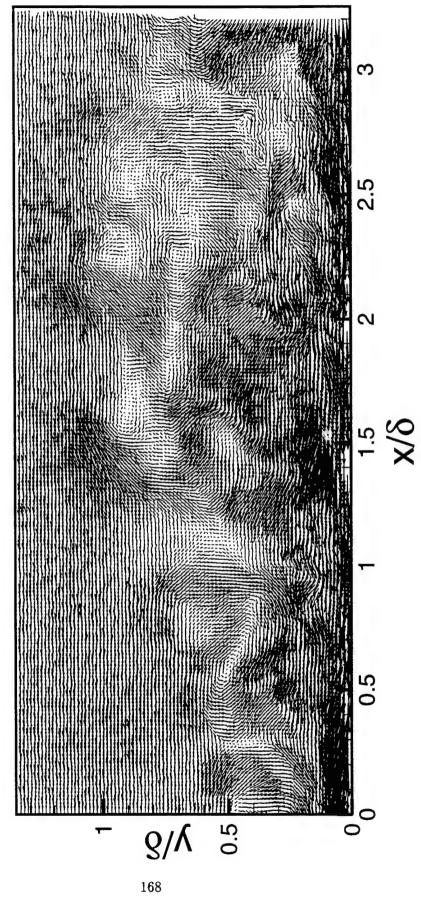
Realization LW-29,  $U_c = 0.65 U_{\odot}$ 



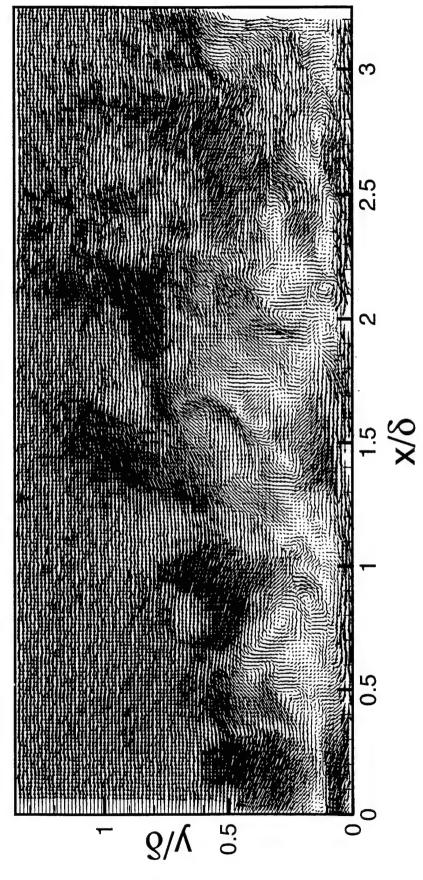
Realization LW-29, Reynolds Fluctuations



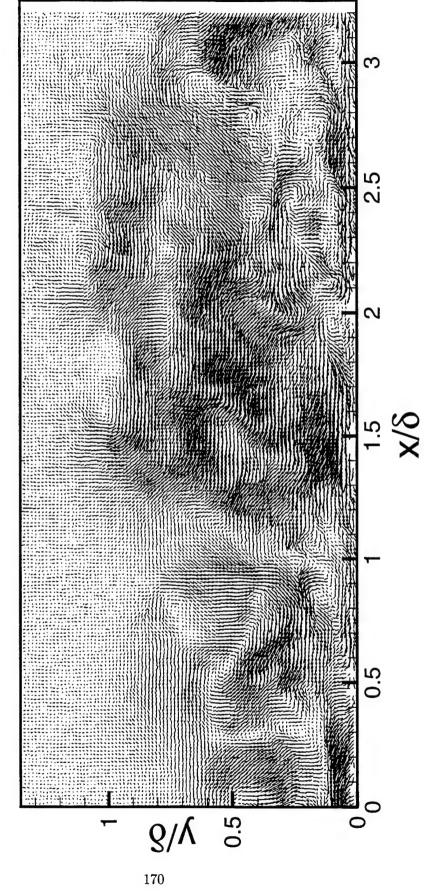
Realization LW-30,  $U_c = 0.85 U_{\odot}$ 



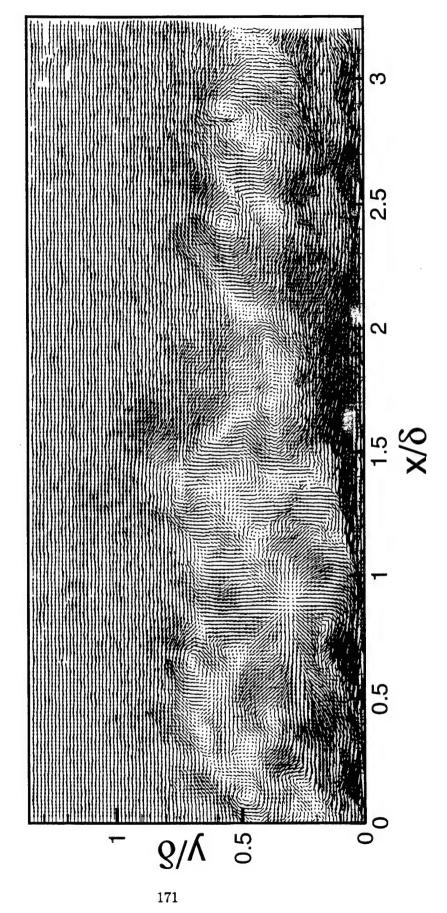
Realization LW-30,  $U_c = 0.65 U_{\odot}$ 



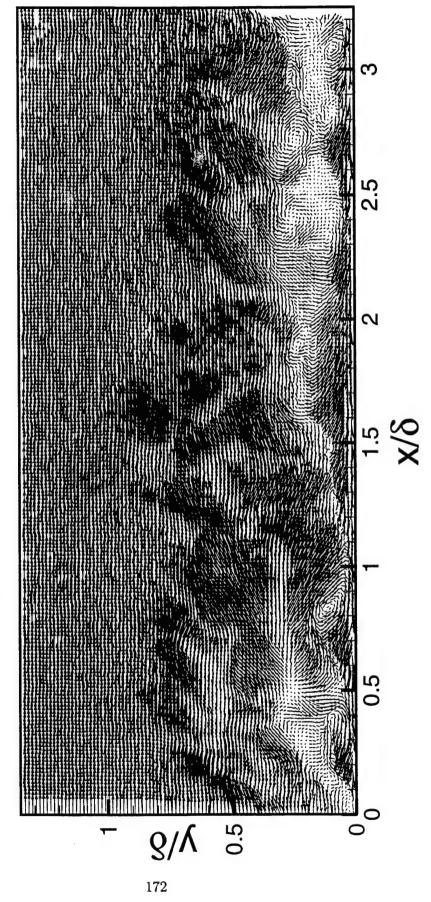
Realization LW-30, Reynolds Fluctuations



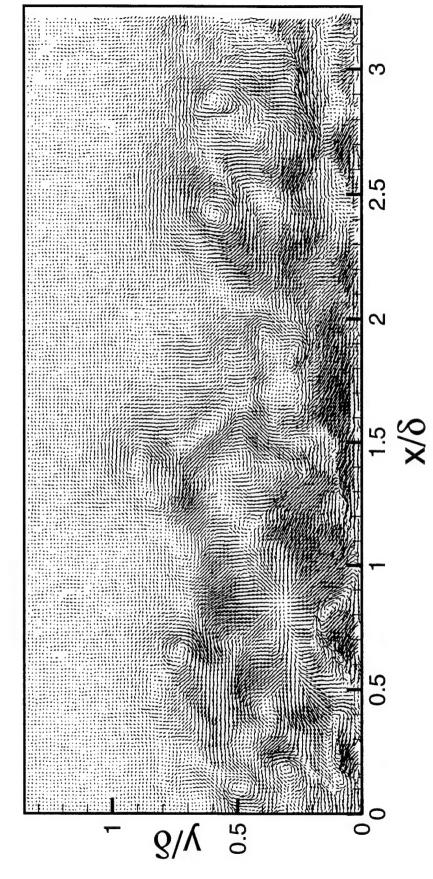
Realization LW-32,  $U_c = 0.85 U_{\odot}$ 



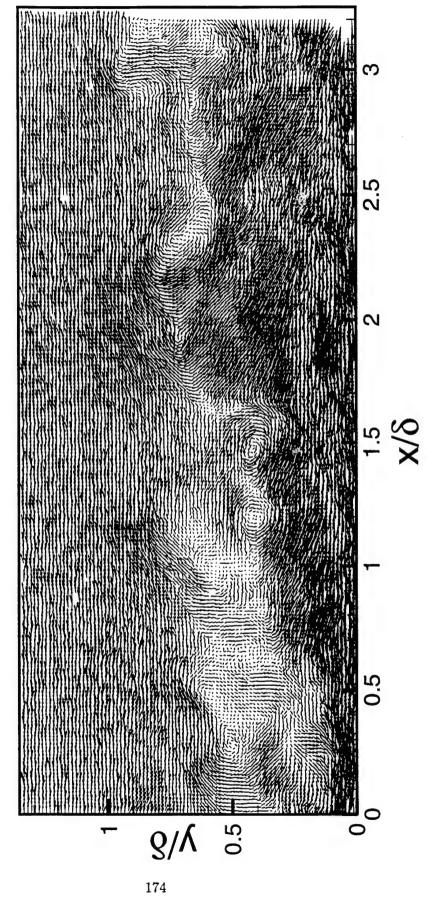
Realization LW-32,  $U_c = 0.65 U_{\odot}$ 



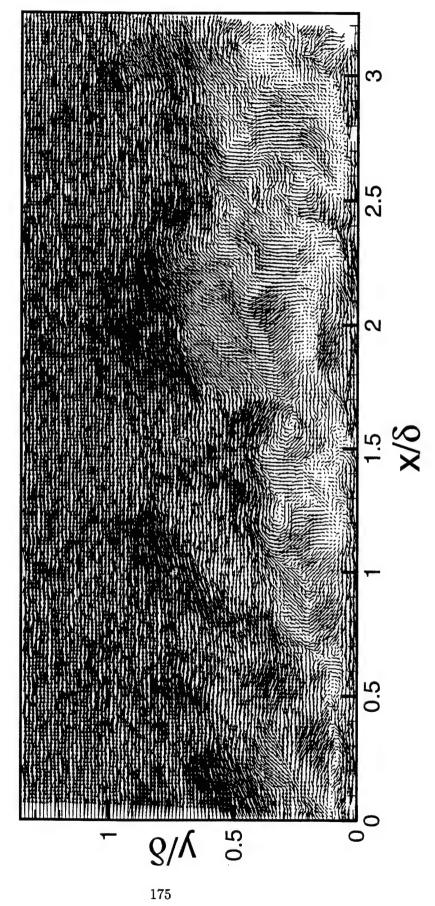
Realization LW-32, Reynolds Fluctuations



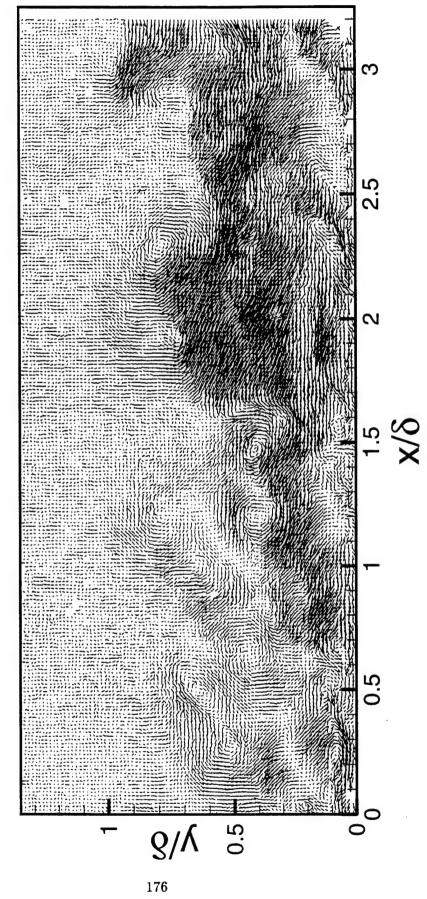
Realization LW-33,  $U_c = 0.85 U_{\odot}$ 



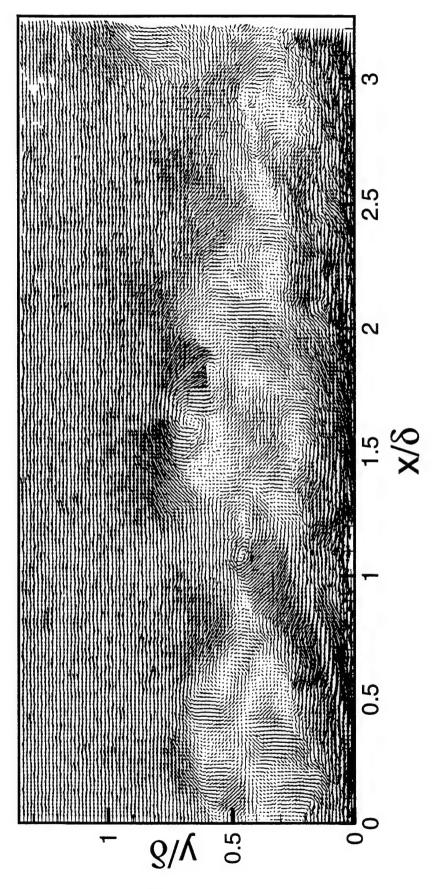
Realization LW-33,  $U_c = 0.65 U_{\odot}$ 



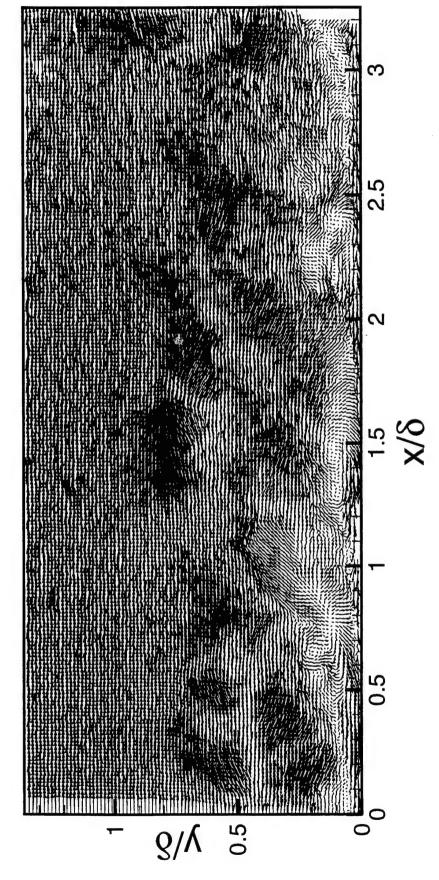
Realization LW-33, Reynolds Fluctuations



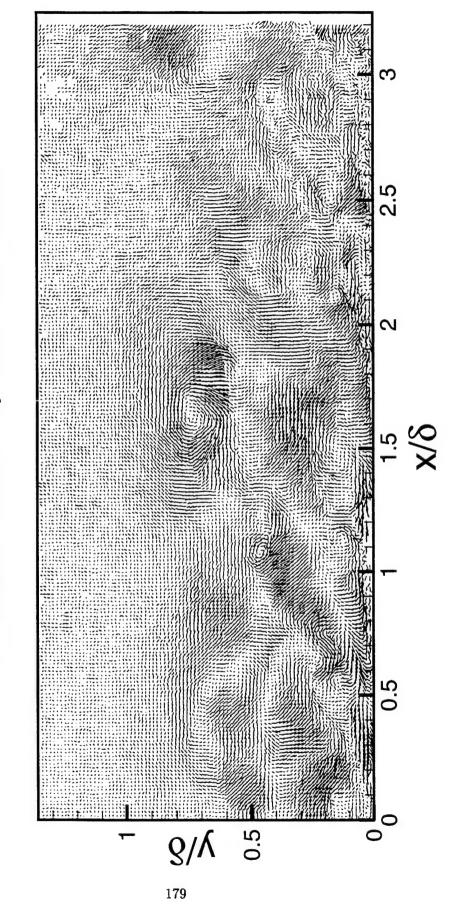
Realization LW-34,  $U_c = 0.85 U_{\odot}$ 



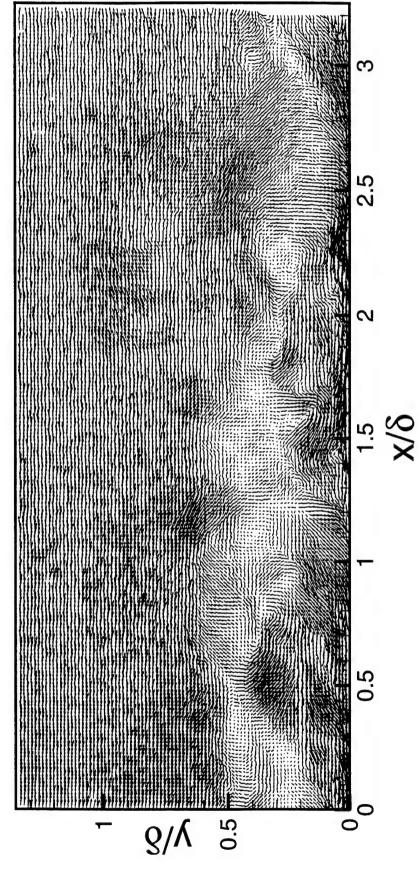
Realization LW-34,  $U_c = 0.65 U_{\odot}$ 



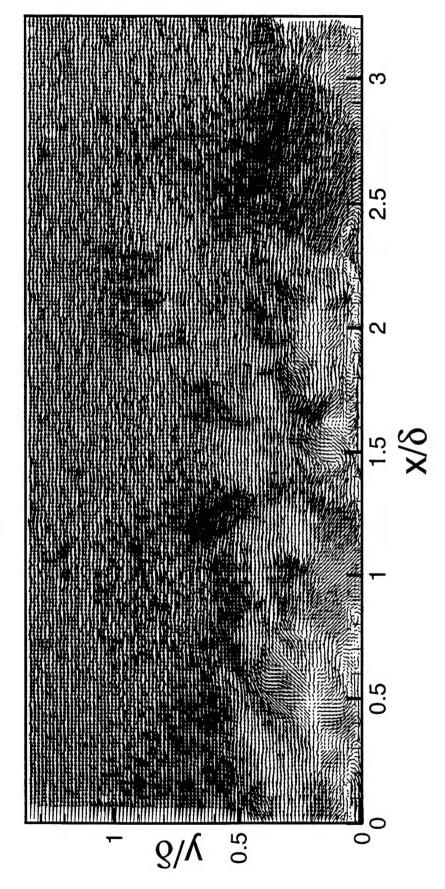
Realization LW-34, Reynolds Fluctuations



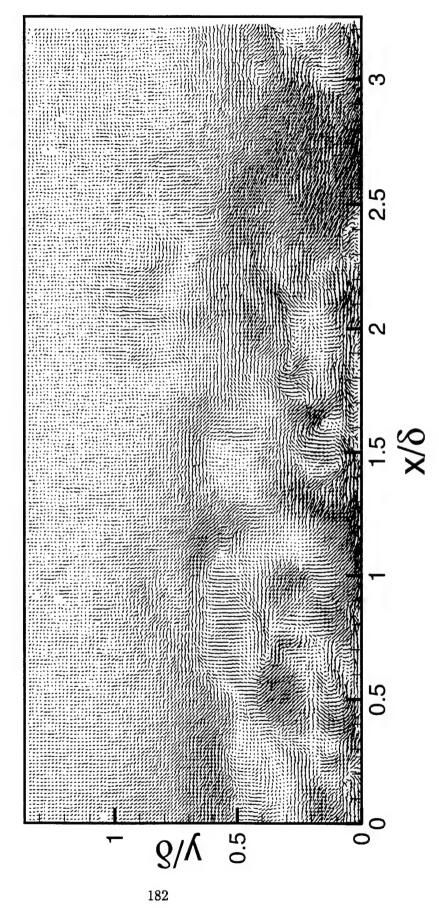
Realization LW-35,  $U_c = 0.85 U_{\odot}$ 



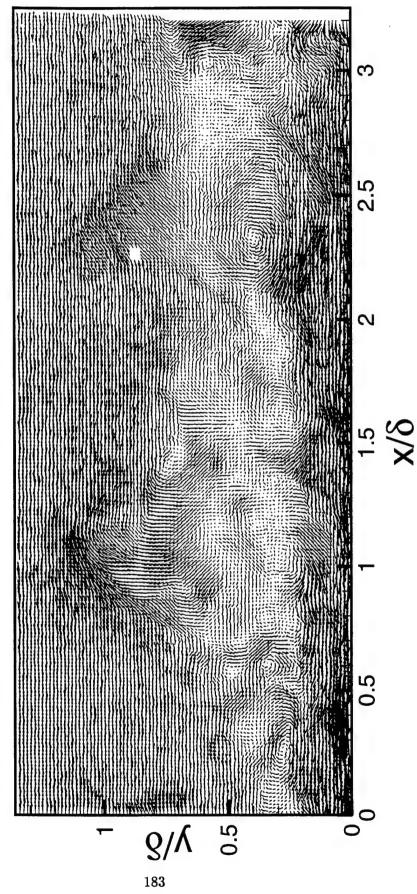
Realization LW-35,  $U_c = 0.65 U_{\odot}$ 



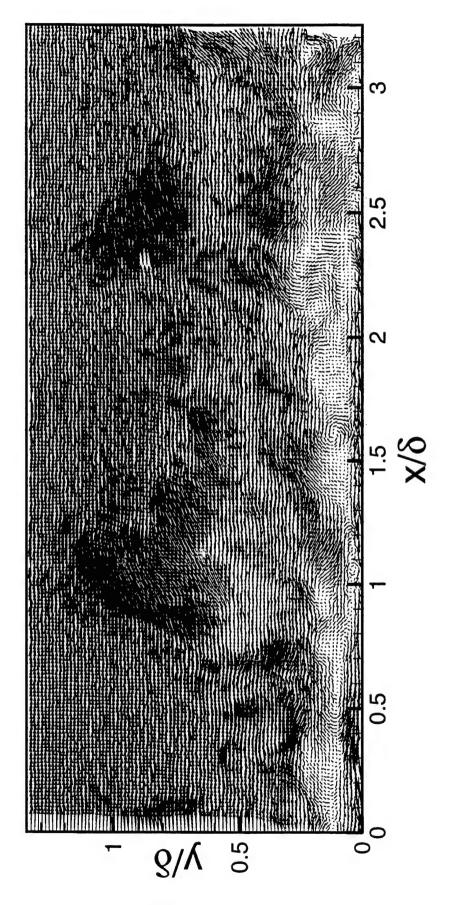
Realization LW-35, Reynolds Fluctuations



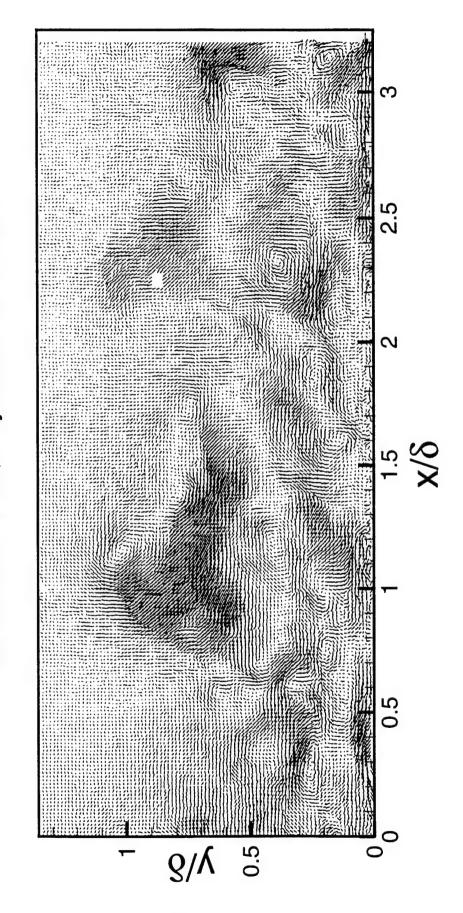
Realization LW-36,  $U_c = 0.85 U_{\odot}$ 



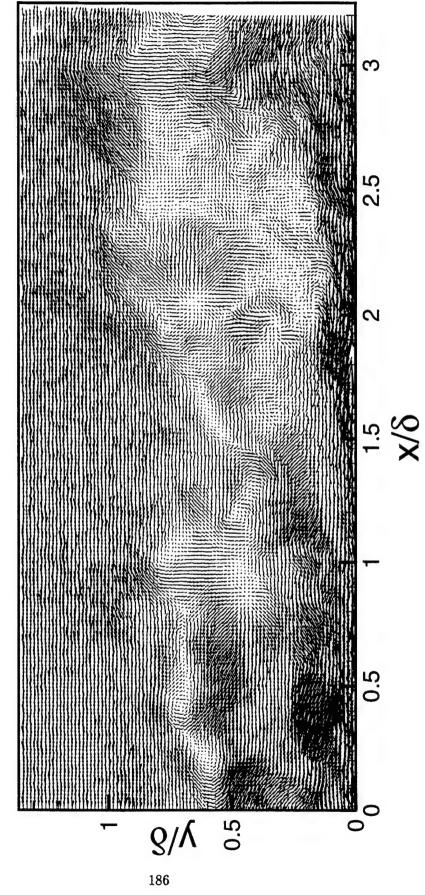
Realization LW-36,  $U_c = 0.65 U_{\odot}$ 



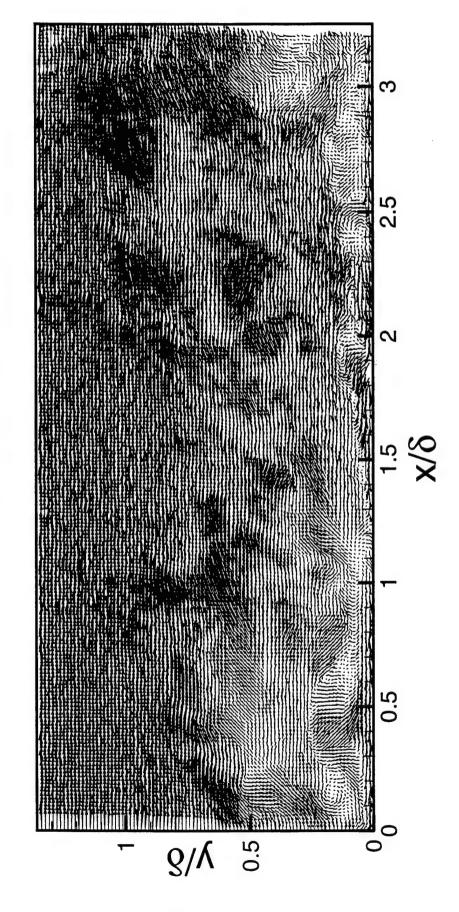
Realization LW-36, Reynolds Fluctuations



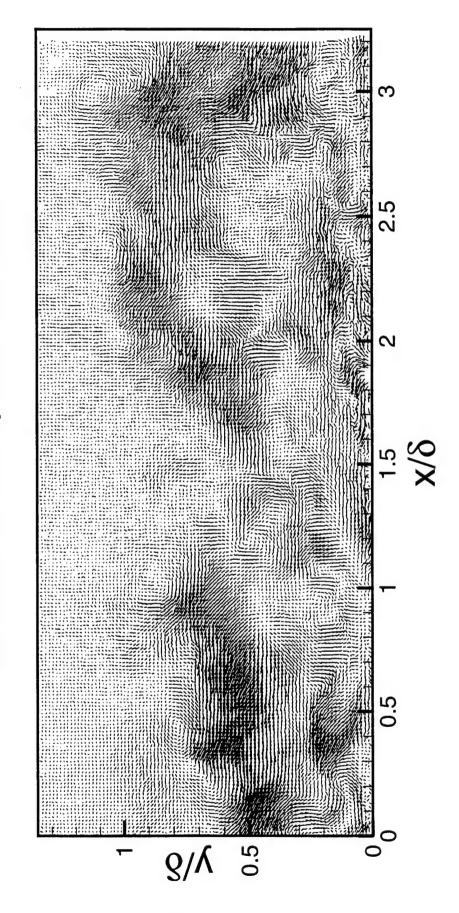
Realization LW-37,  $U_c = 0.85 U_{\odot}$ 



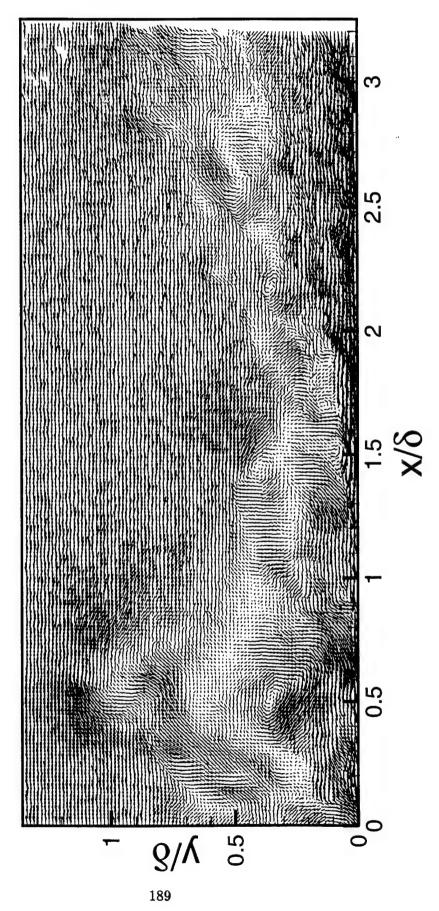
Realization LW-37,  $U_c = 0.65 U_{\odot}$ 



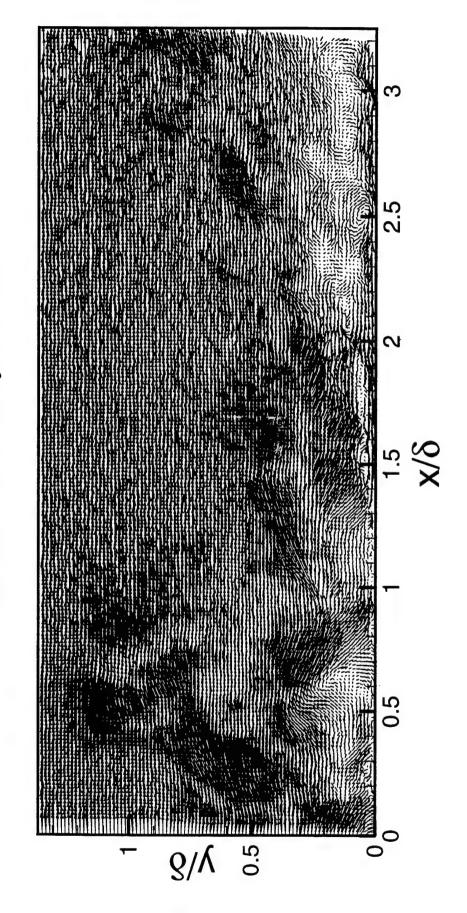
Realization LW-37, Reynolds Fluctuations



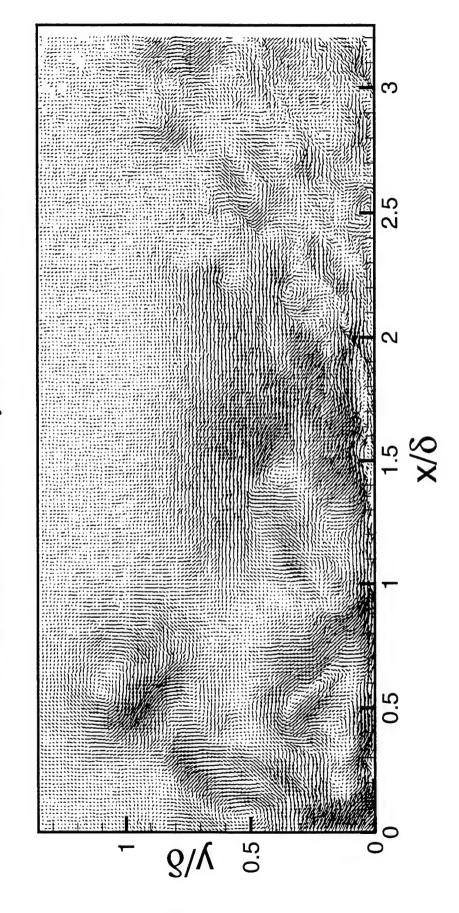
Realization LW-38,  $U_c = 0.85 U_{\odot}$ 



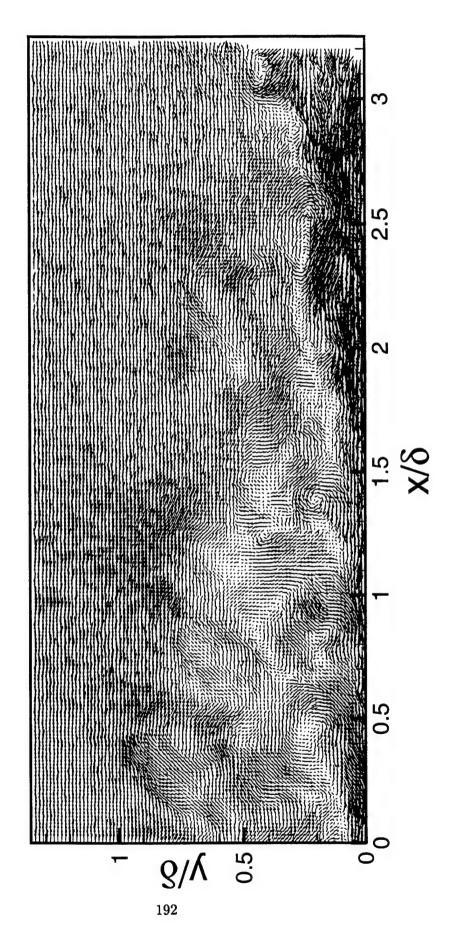
Realization LW-38,  $U_c = 0.65 U_{\odot}$ 



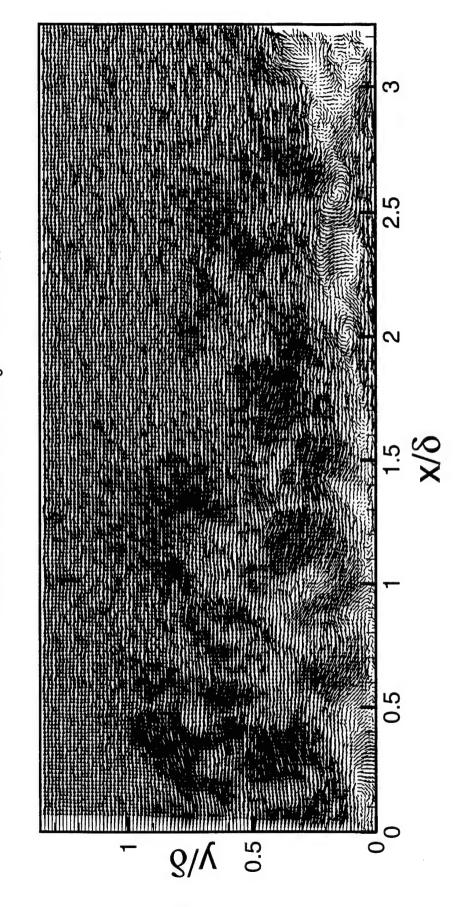
Realization LW-38, Reynolds Fluctuations



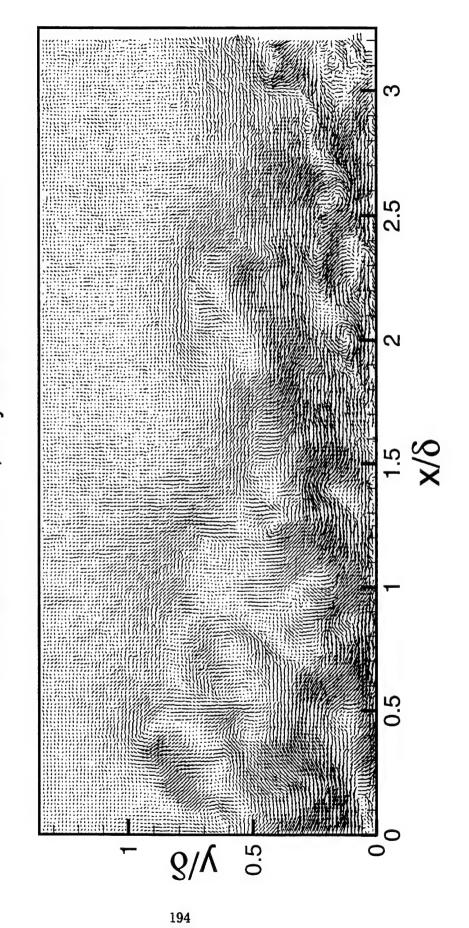
Realization LW-39,  $U_c = 0.85 U_{\odot}$ 



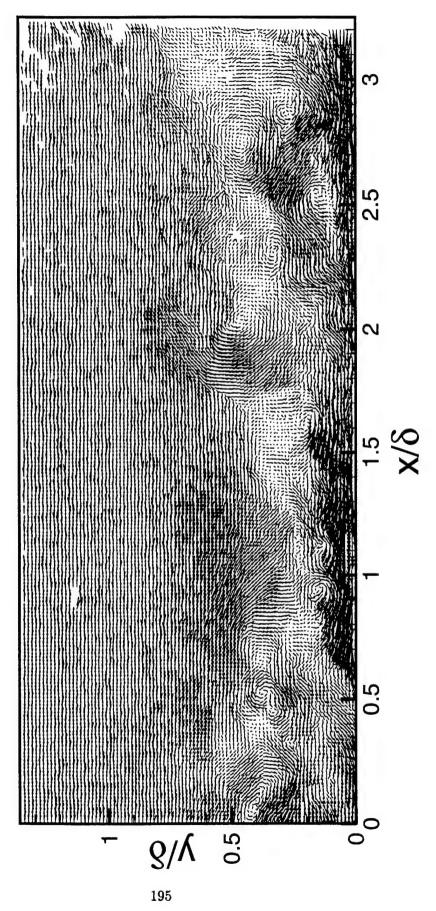
Realization LW-39,  $U_c = 0.65 U_{\odot}$ 



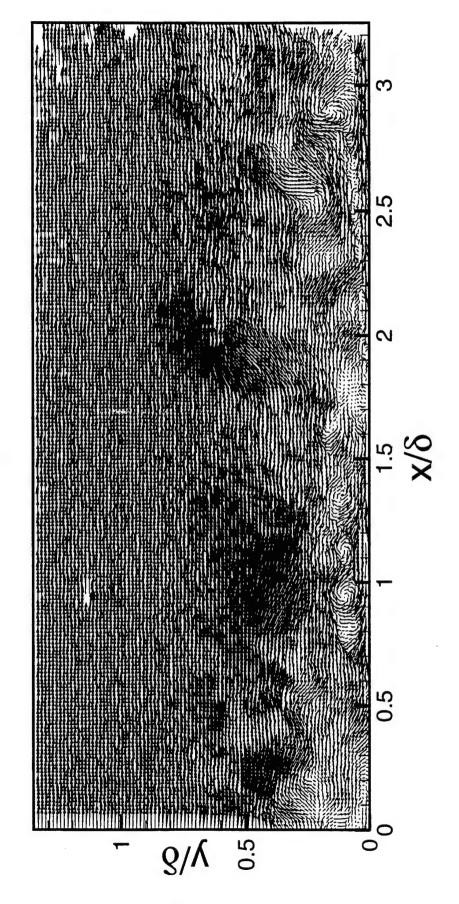
Realization LW-39, Reynolds Fluctuations



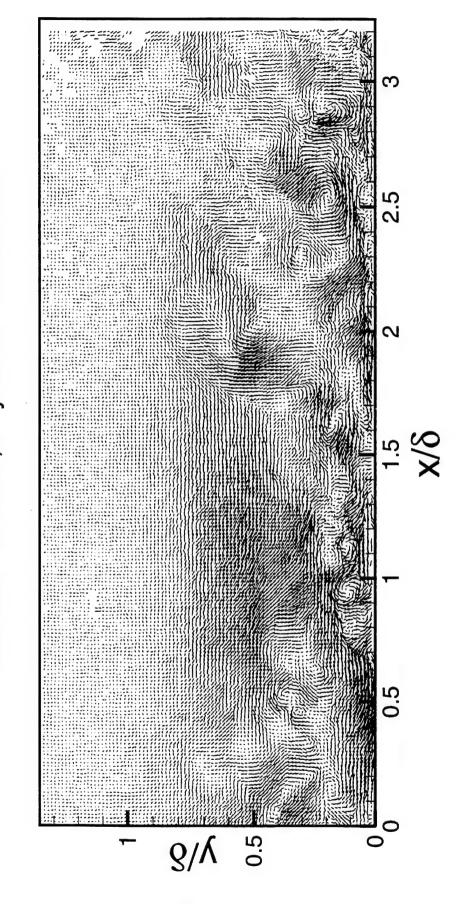
Realization LW-40,  $U_c = 0.85 U_{\odot}$ 



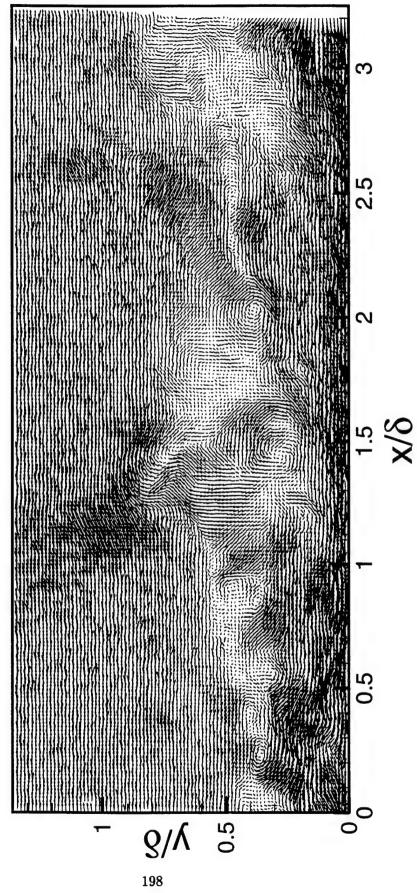
Realization LW-40,  $U_c = 0.65 U_{\odot}$ 



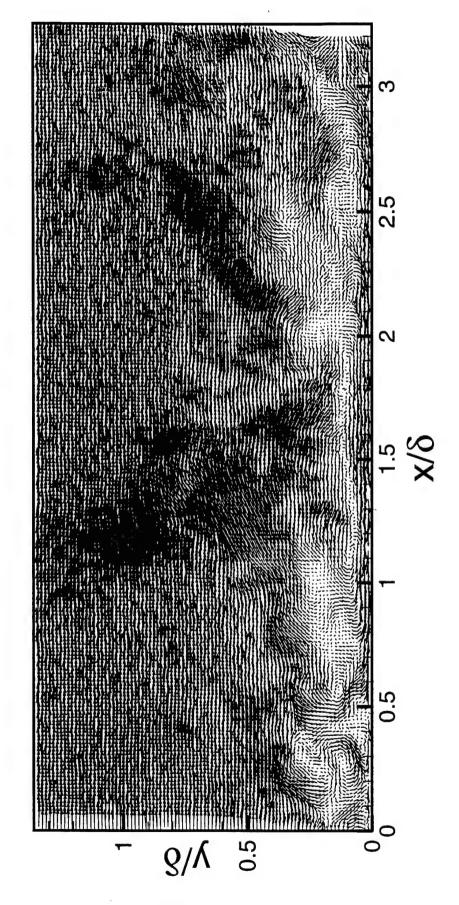
Realization LW-40, Reynolds Fluctuations



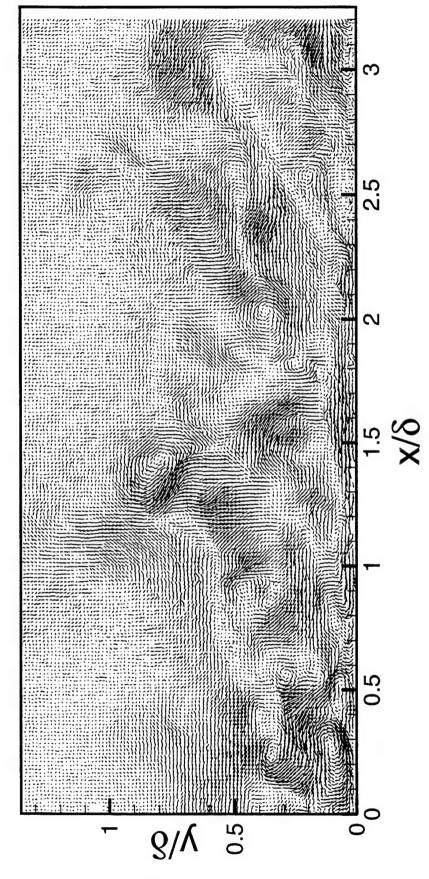
Realization LW-41,  $U_c = 0.85 U_{\odot}$ 



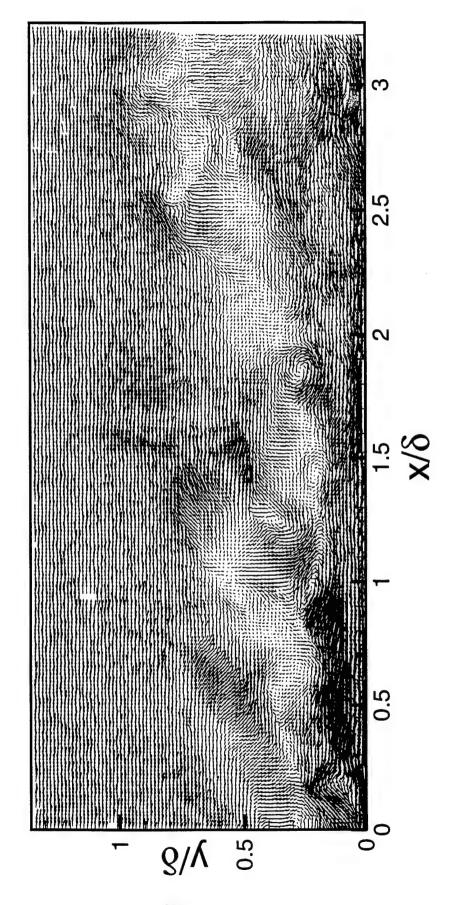
Realization LW-41,  $U_c = 0.65 U_{\odot}$ 



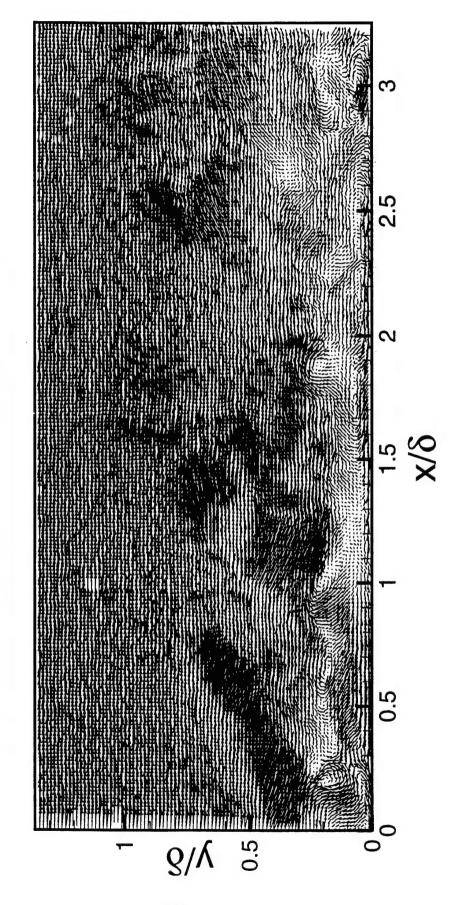
Realization LW-41, Reynolds Fluctuations



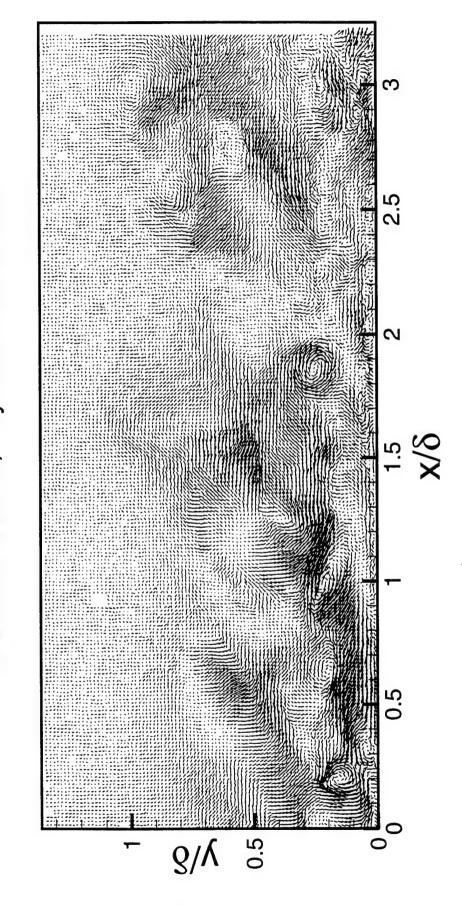
Realization LW-42,  $U_c = 0.85 U_{\odot}$ 



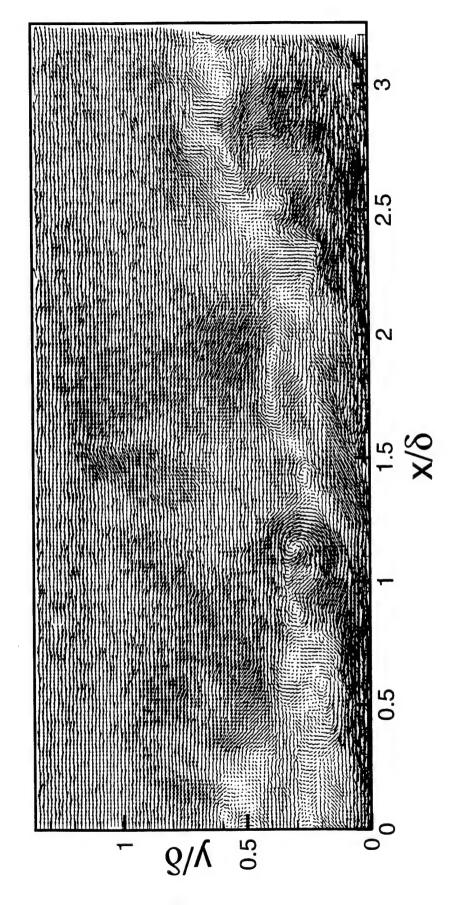
Realization LW-42,  $U_c = 0.65 U_{\odot}$ 



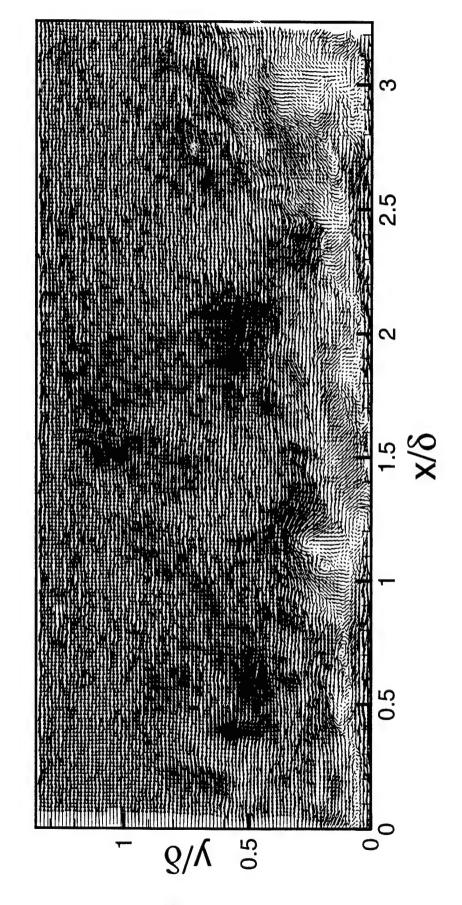
Realization LW-42, Reynolds Fluctuations



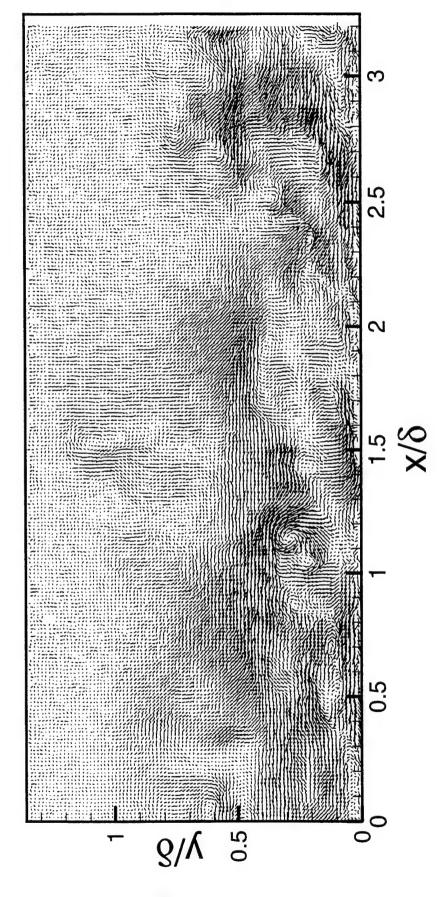
Realization LW-43,  $U_c = 0.85 U_{\odot}$ 



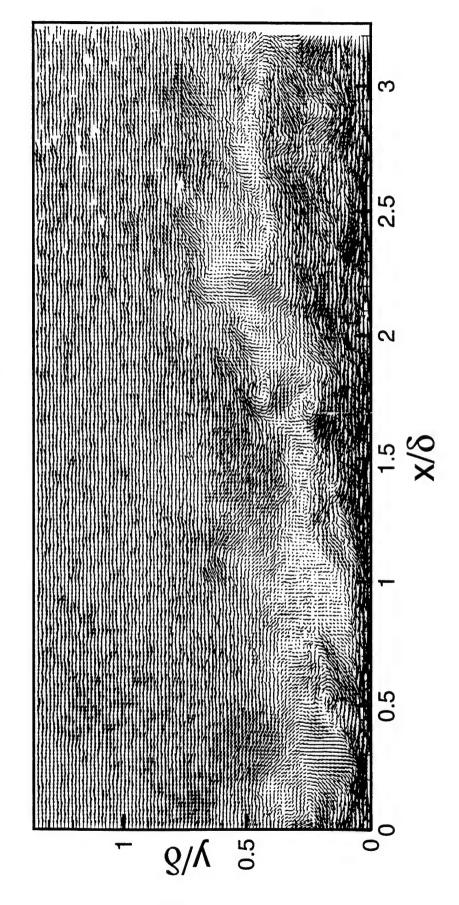
Realization LW-43,  $U_c = 0.65 U_{\odot}$ 



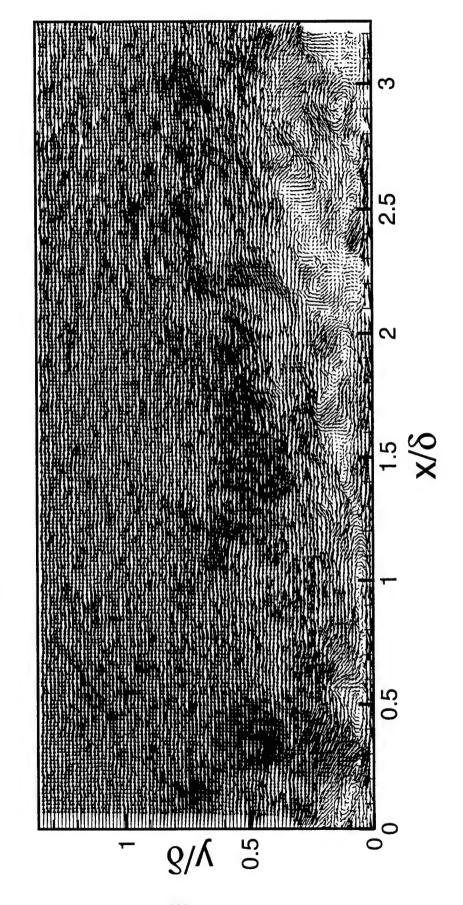
Realization LW-43, Reynolds Fluctuations



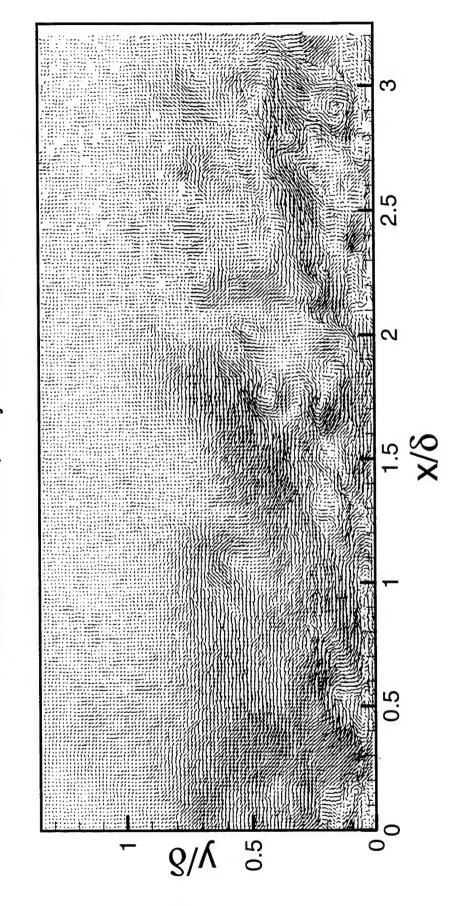
Realization LW-45,  $U_c = 0.85 U_{\odot}$ 



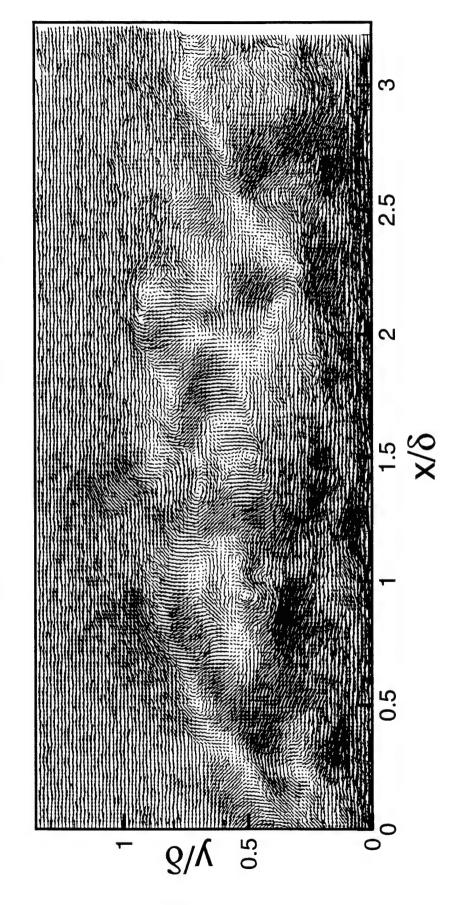
Realization LW-45,  $U_c = 0.65 U_{\odot}$ 



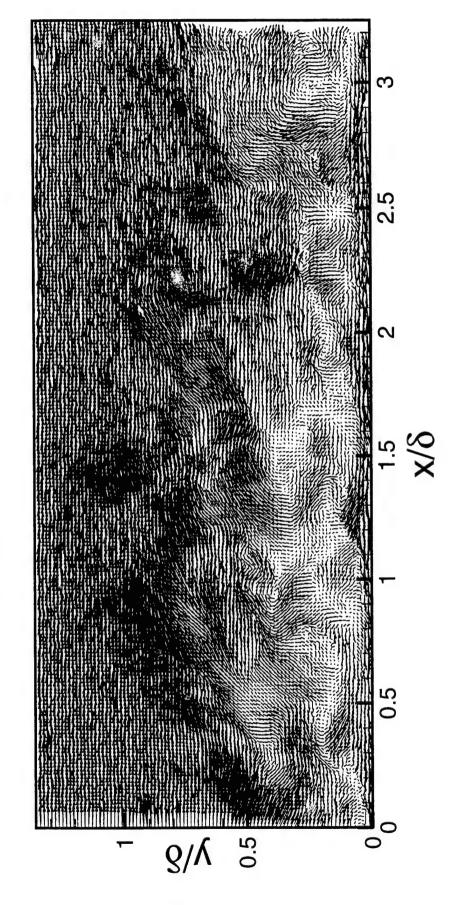
Realization LW-45, Reynolds Fluctuations



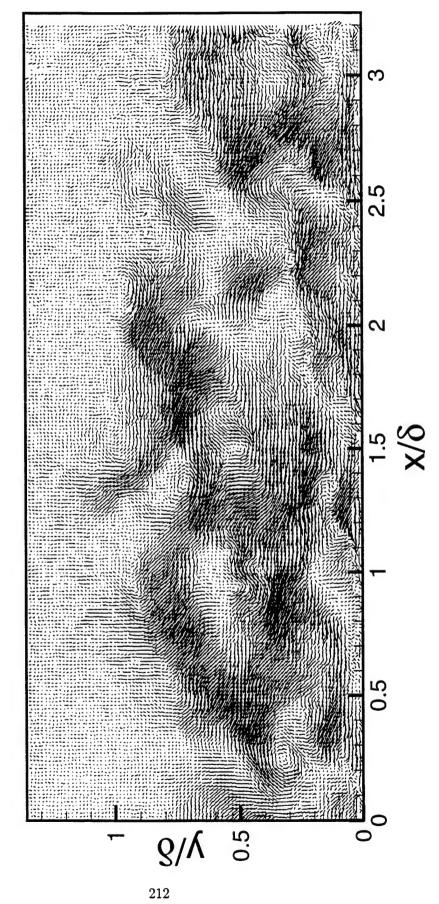
Realization LW-46,  $U_c = 0.85 U_s$ 



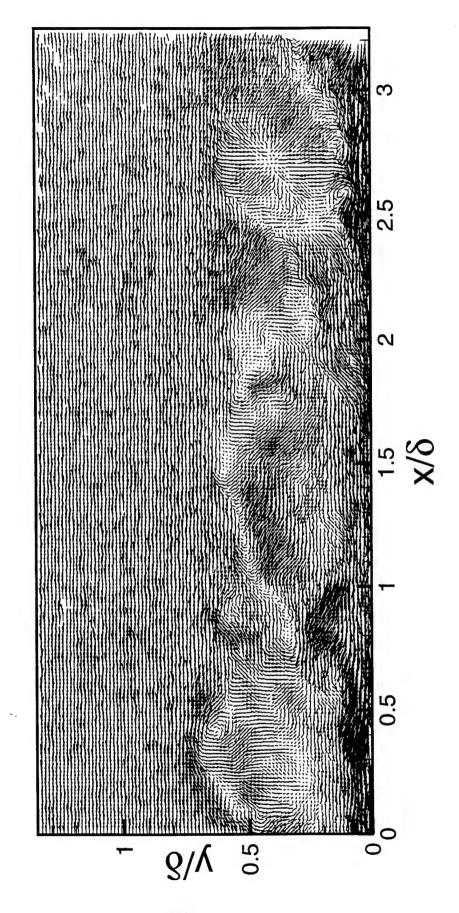
Realization LW-46,  $U_c = 0.65 U_{\odot}$ 



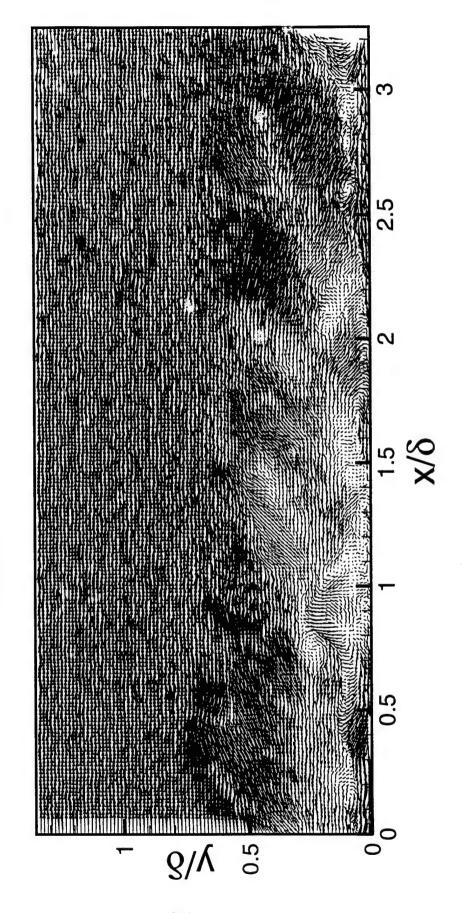
Realization LW-46, Reynolds Fluctuations



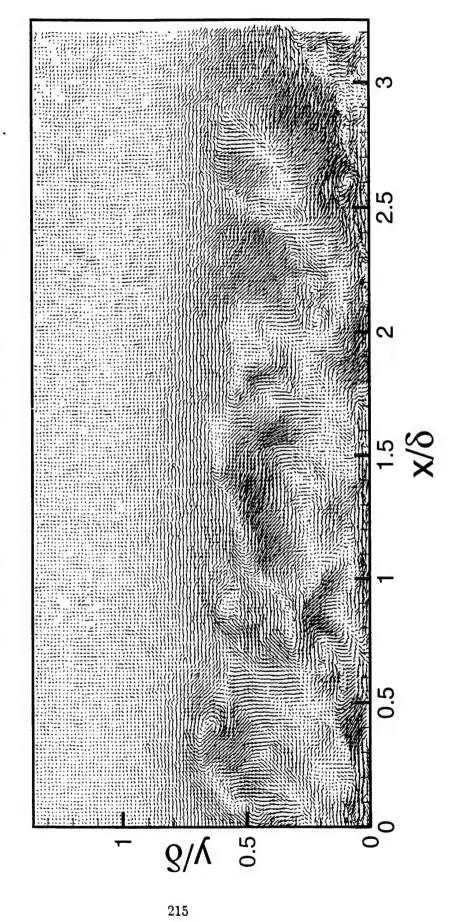
Realization LW-47,  $U_c = 0.85 U_{\odot}$ 



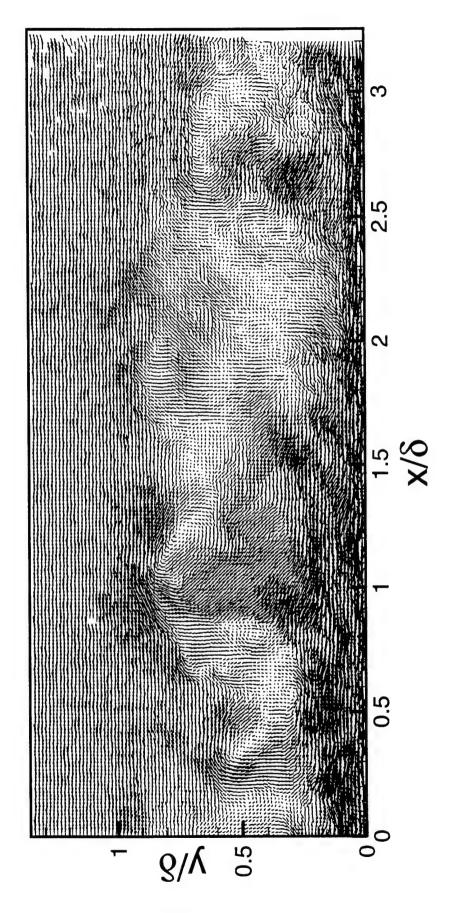
Realization LW-47,  $U_c = 0.65 U_{\odot}$ 



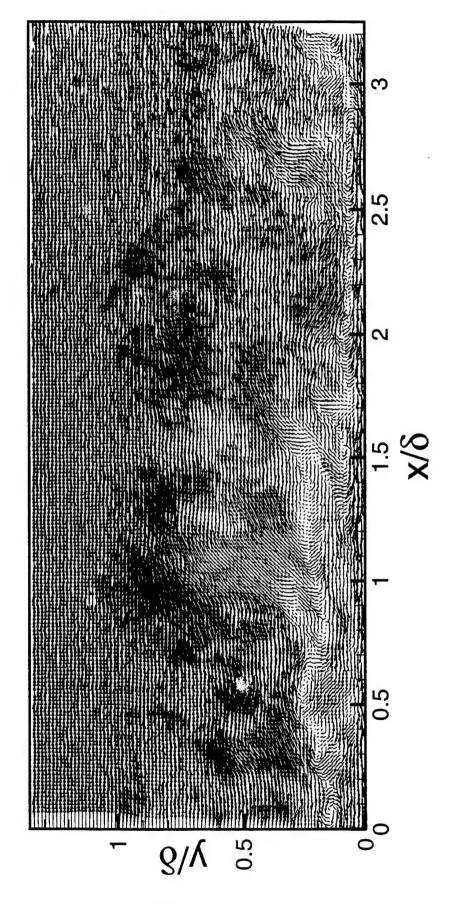
Realization LW-47, Reynolds Fluctuations



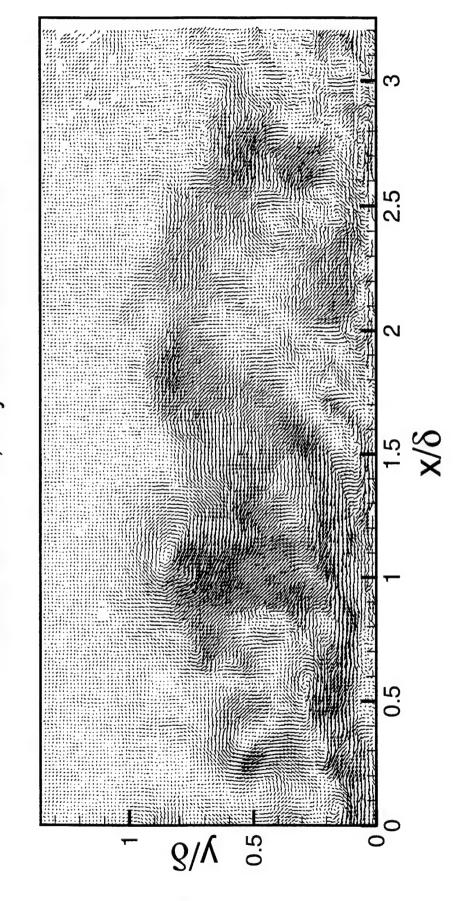
Realization LW-48,  $U_c = 0.85 U_{\odot}$ 



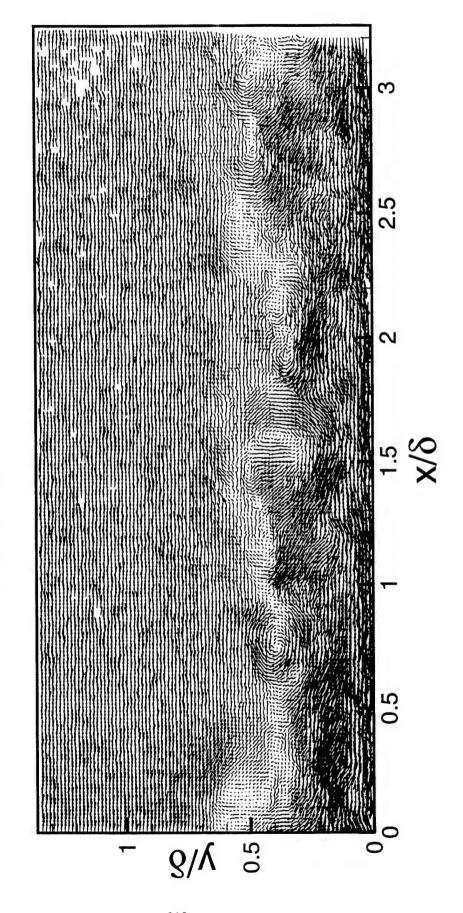
Realization LW-48,  $U_c = 0.65 U_{\odot}$ 



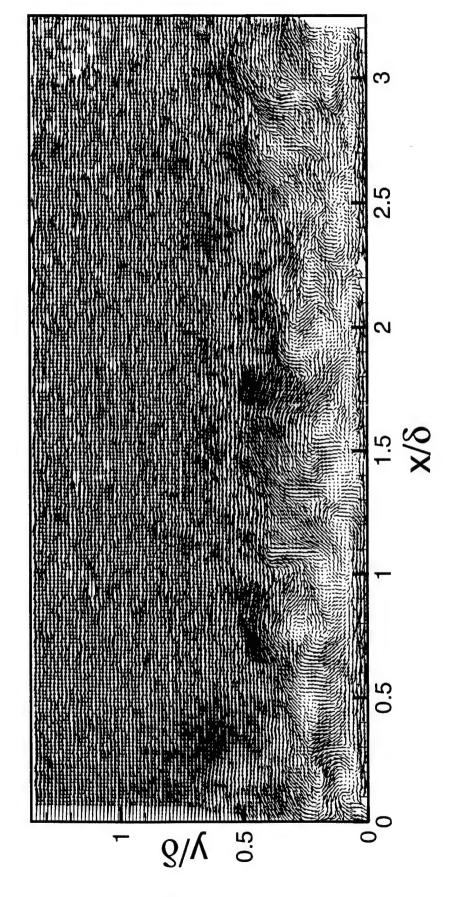
Realization LW-48, Reynolds Fluctuations



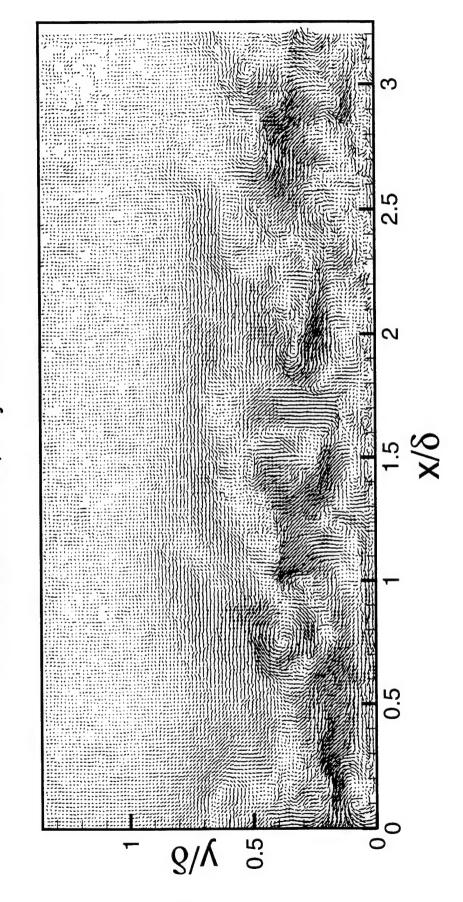
Realization LW-49,  $U_c = 0.85 U_{\odot}$ 



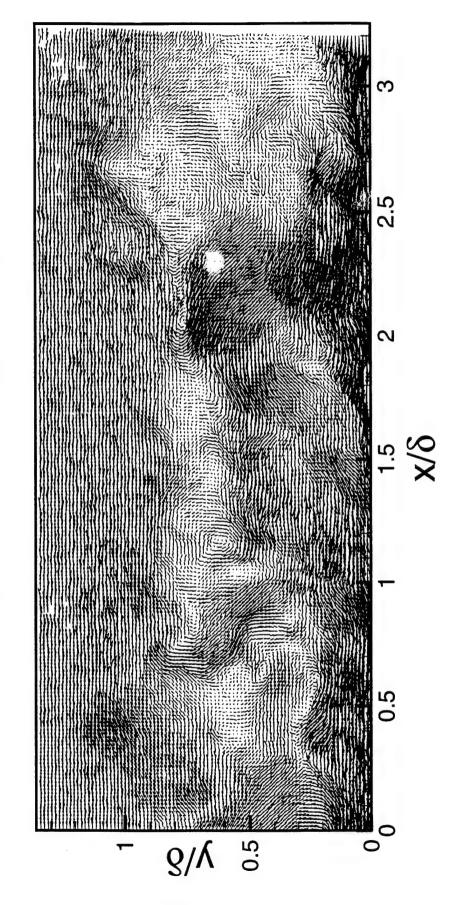
Realization LW-49,  $U_c = 0.65 U_{\odot}$ 



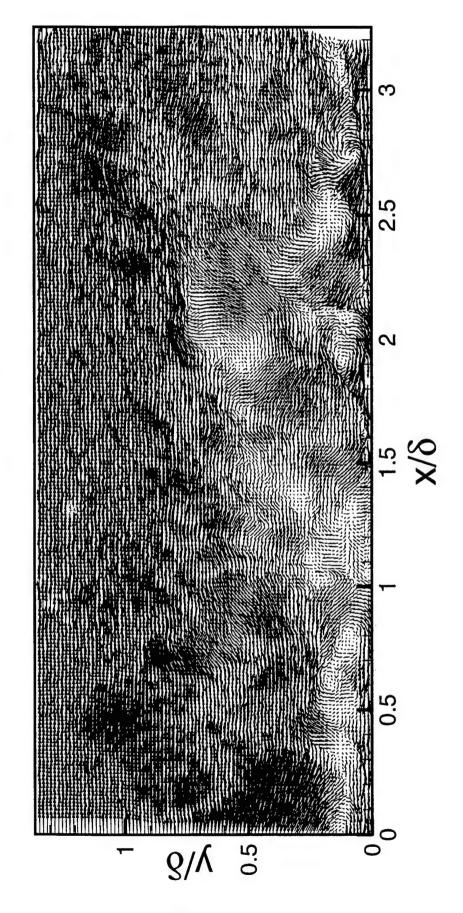
Realization LW-49, Reynolds Fluctuations



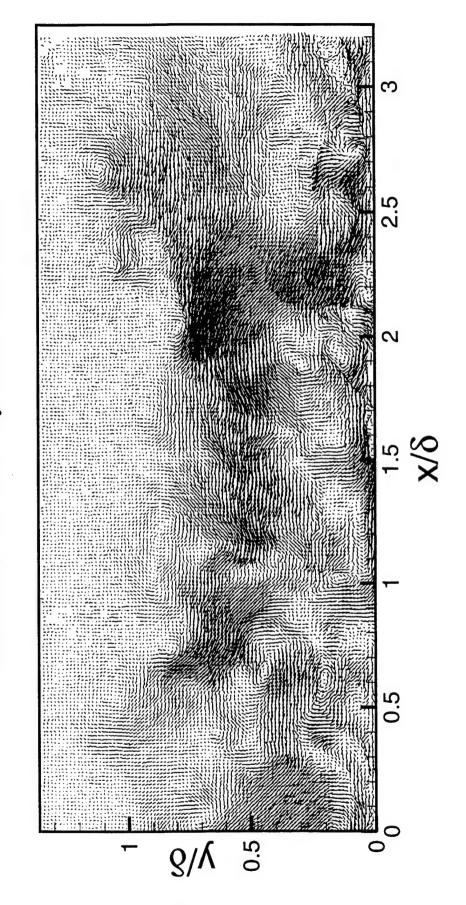
Realization LW-50,  $U_c = 0.85 U_{\odot}$ 



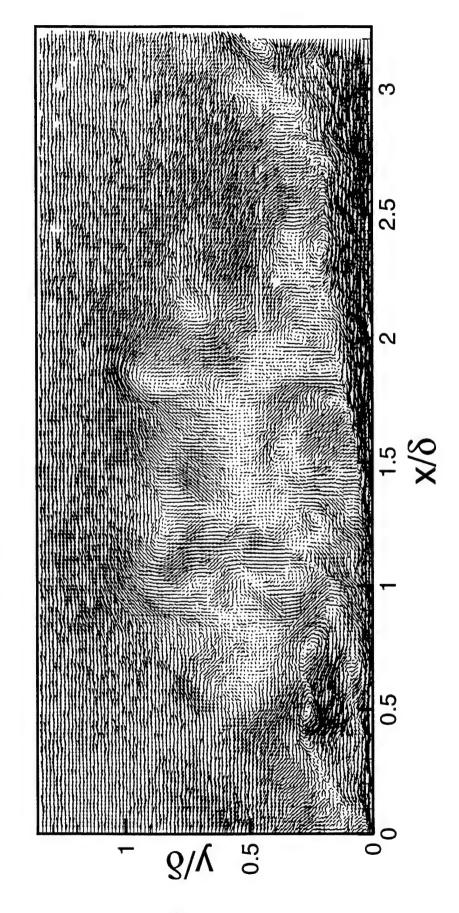
Realization LW-50,  $U_c = 0.65 U_{\odot}$ 



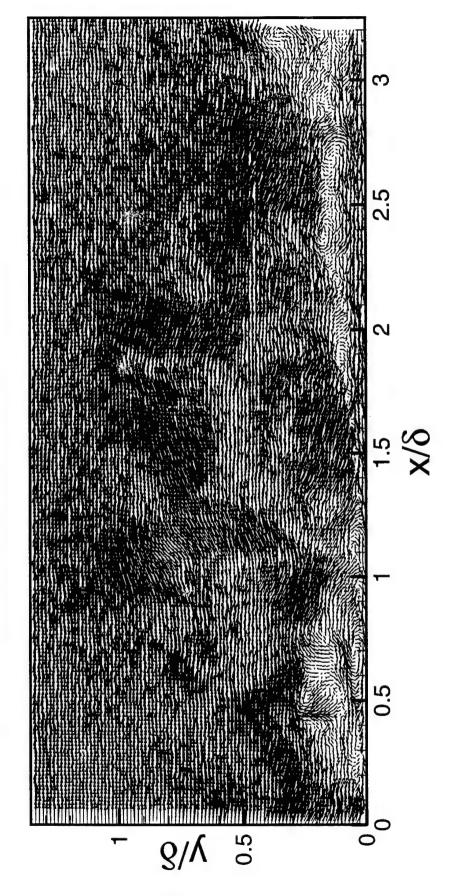
Realization LW-50, Reynolds Fluctuations



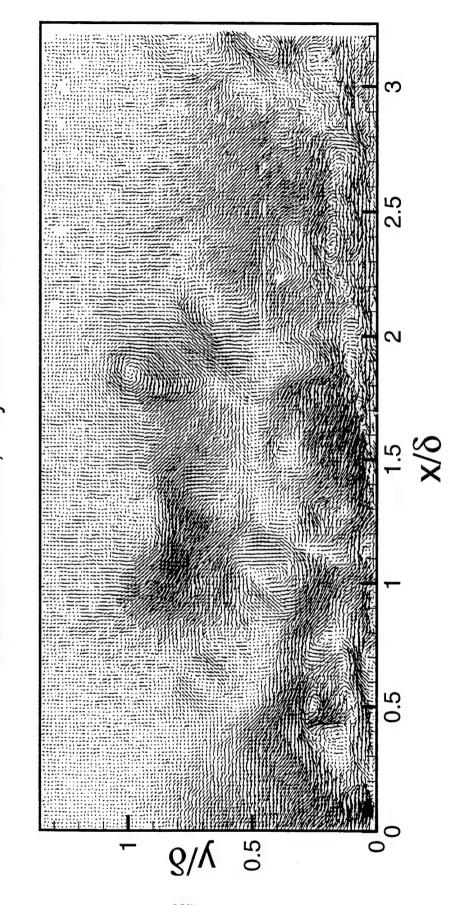
Realization LW-51,  $U_c = 0.85 U_{\odot}$ 



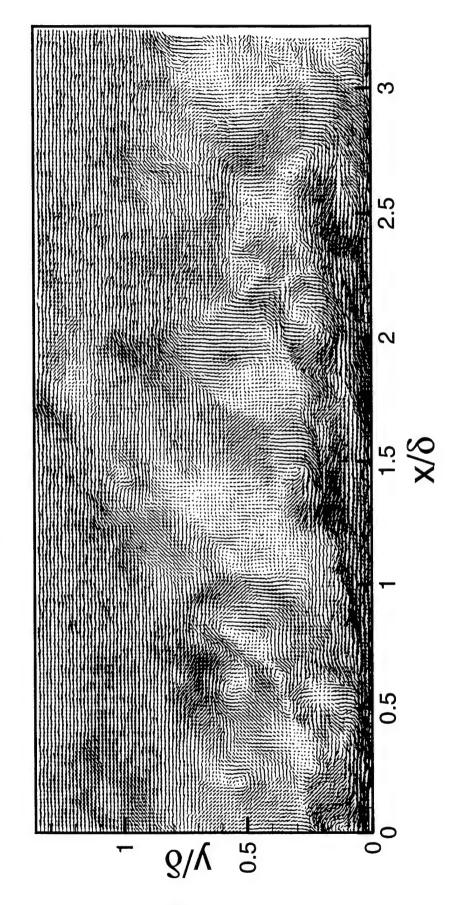
Realization LW-51,  $U_c = 0.65 U_{\odot}$ 



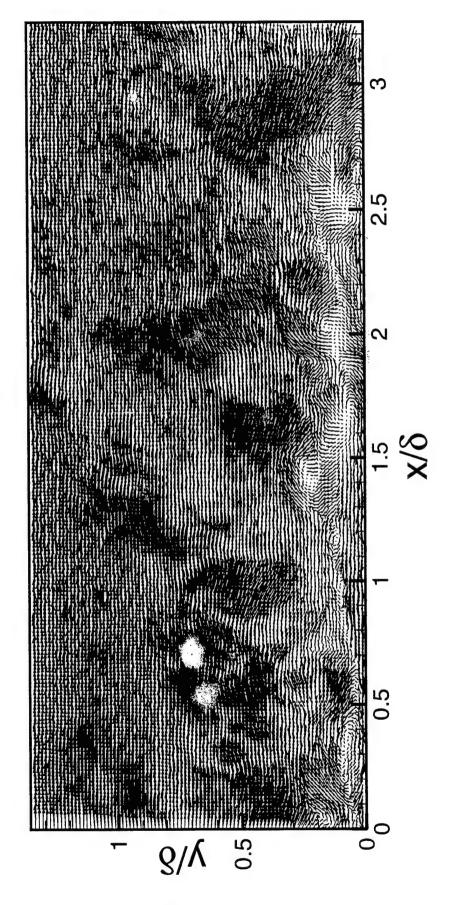
Realization LW-51, Reynolds Fluctuations



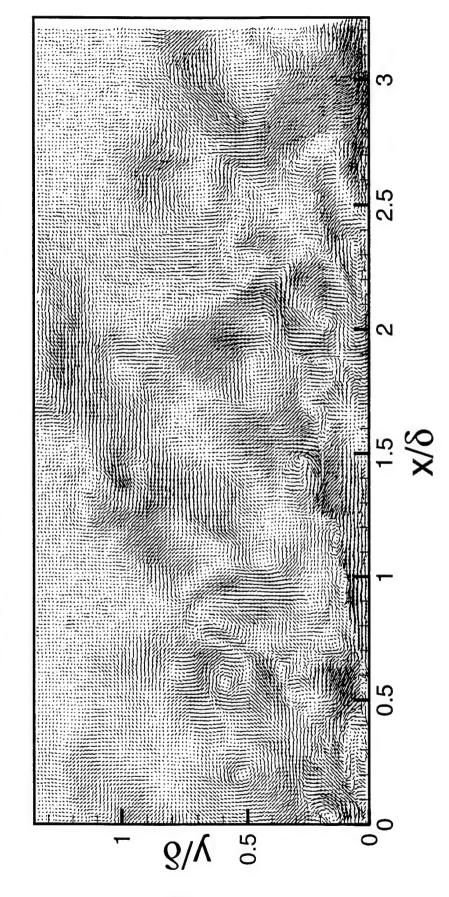
Realization LW-52,  $U_c = 0.85 U_{\odot}$ 



Realization LW-52,  $U_c = 0.65 U_{\odot}$ 

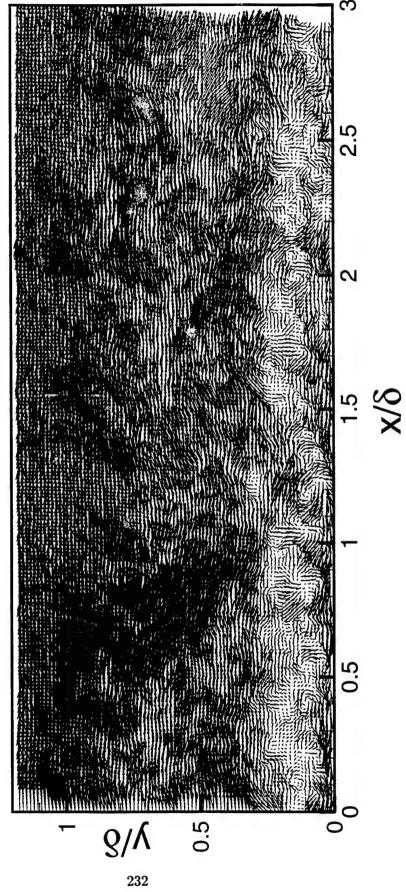


Realization LW-52, Reynolds Fluctuations

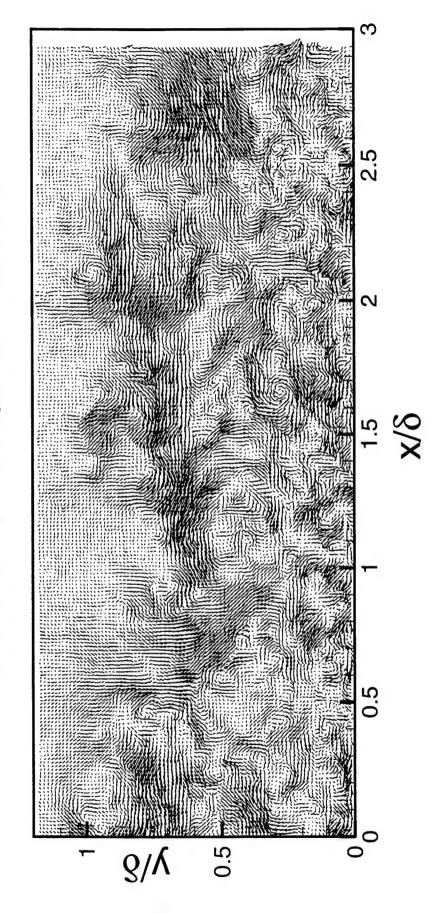


Realization HW-01,  $U_c = 0.85 U_{\odot}$ δ/γ

Realization HW-01,  $U_c = 0.65 U_{\odot}$ 

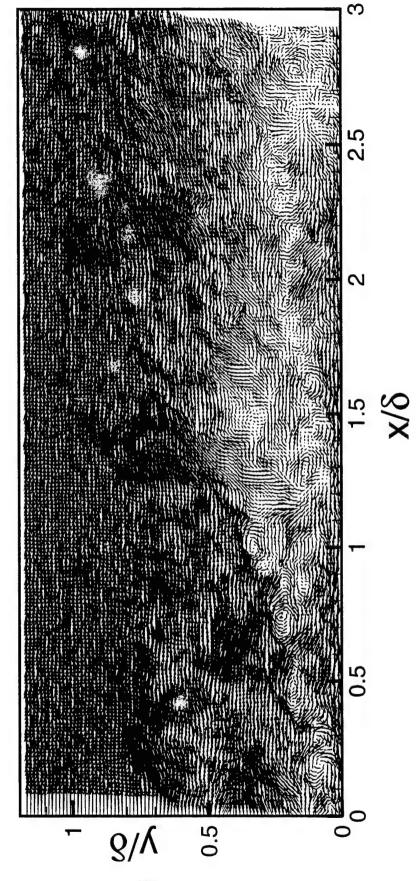


Realization HW-01, Reynolds Fluctuations

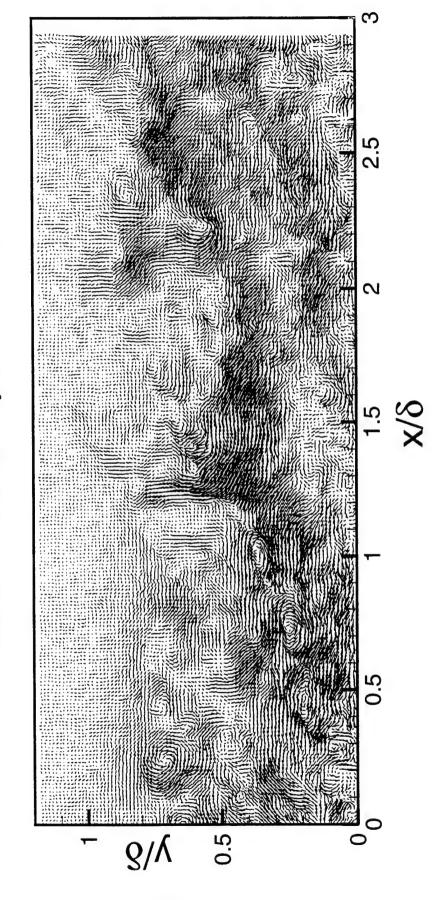


Realization HW-02,  $U_c = 0.85 U_{\odot}$ 0.5 234

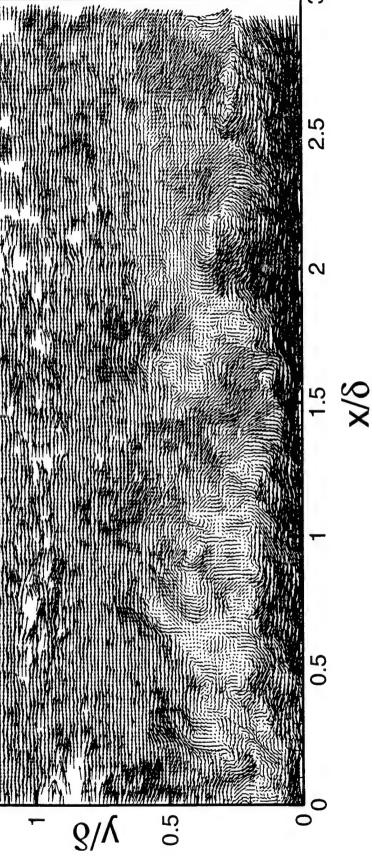
Realization HW-02,  $U_c = 0.65 U_{\odot}$ 



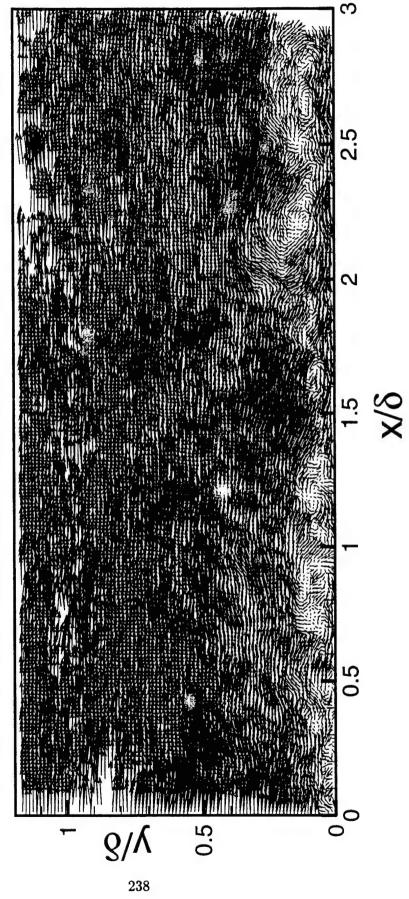
Realization HW-02, Reynolds Fluctuations



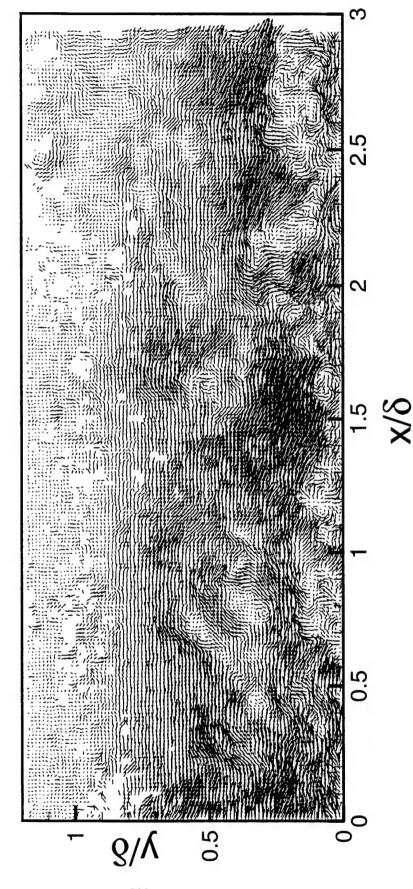
Realization HW-03,  $U_c = 0.85 U_{\odot}$ 



Realization HW-03,  $U_c = 0.65 U_{\odot}$ 



Realization HW-03, Reynolds Fluctuations



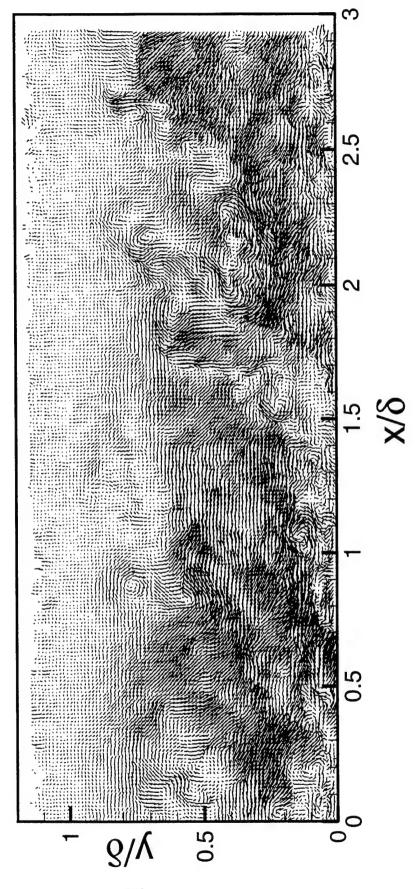
240

Realization HW-04,  $U_c = 0.85 U_{\odot}$ 

0.5 241

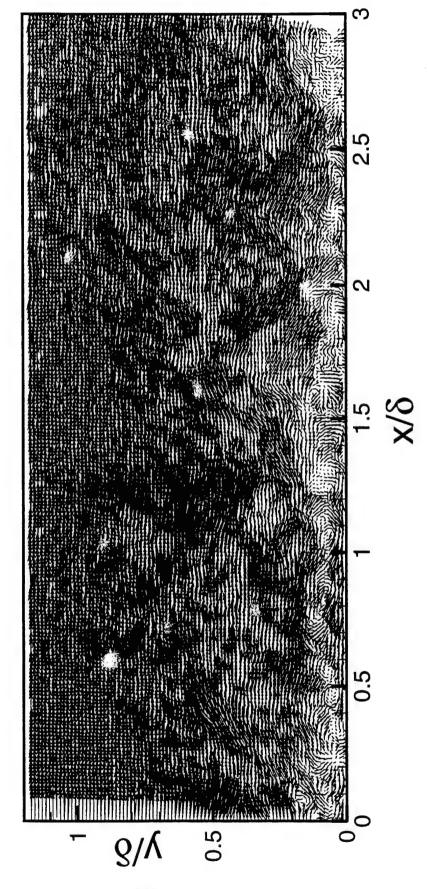
Realization HW-04,  $U_c = 0.65 U_{\odot}$ 

Realization HW-04, Reynolds Fluctuations

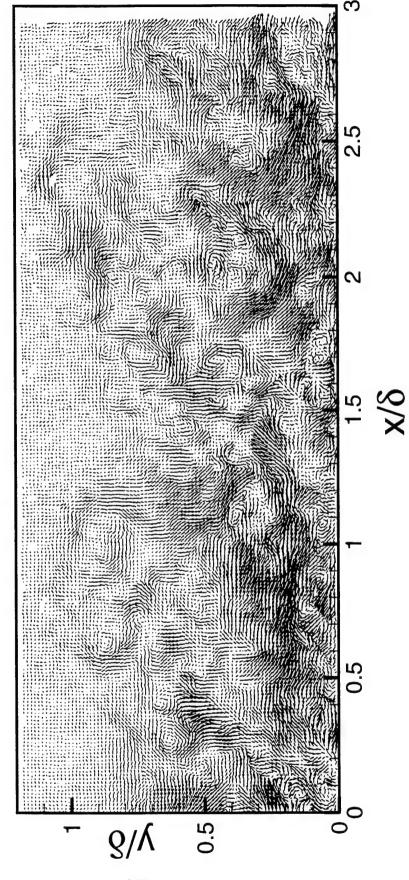


Realization HW-05,  $U_c = 0.85 U_{\odot}$ 0.5 243

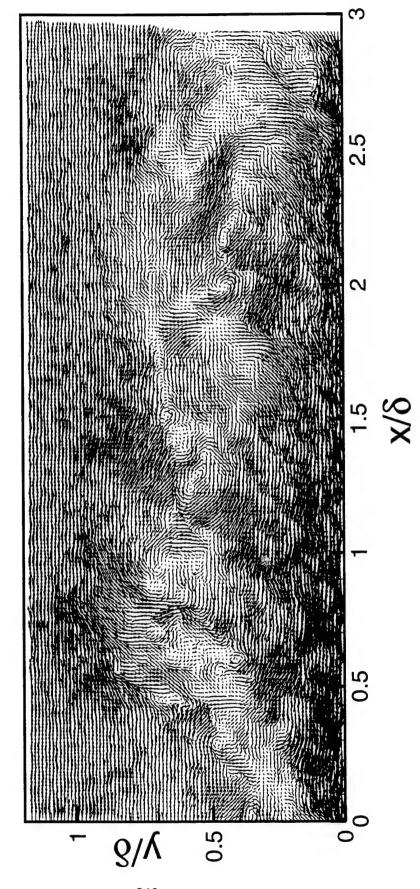
Realization HW-05,  $U_c = 0.65 U_{\odot}$ 



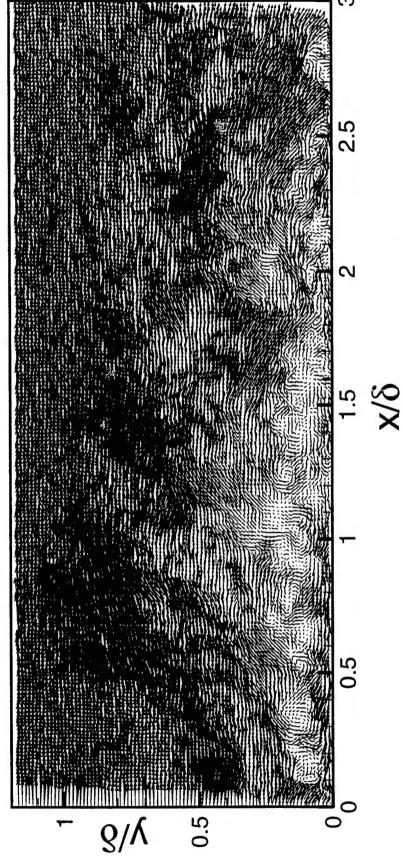
Realization HW-05, Reynolds Fluctuations



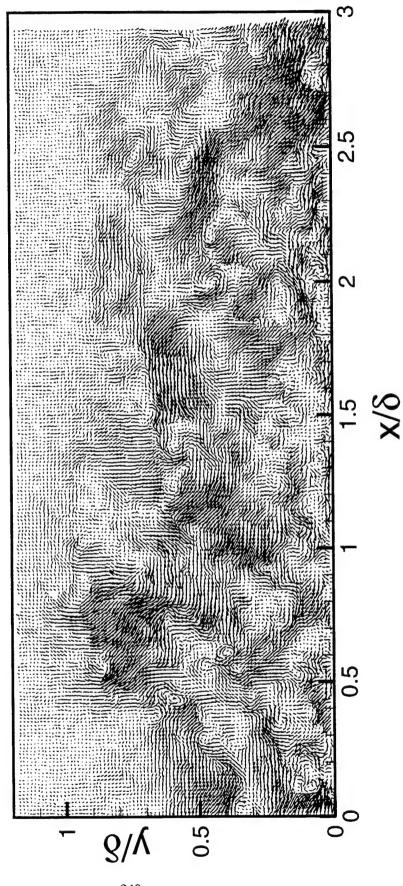
Realization HW-06,  $U_c = 0.85 U_{\odot}$ 



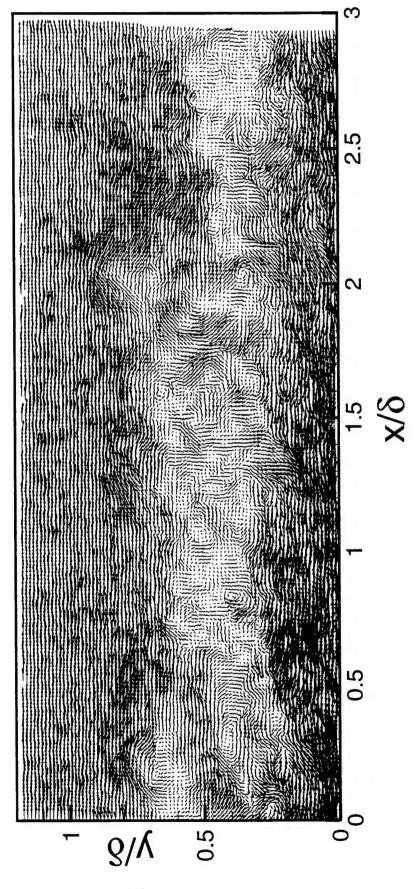
Realization HW-06,  $U_c = 0.65 U_{\odot}$ 



Realization HW-06, Reynolds Fluctuations



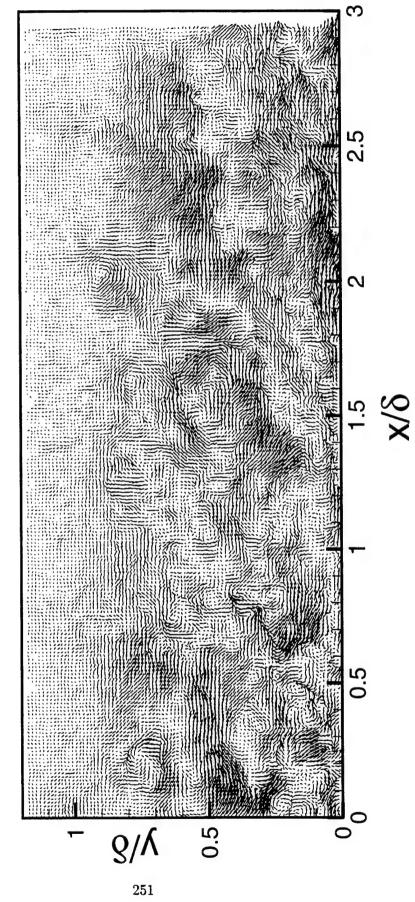
Realization HW-07,  $U_c = 0.85 U_s$ 



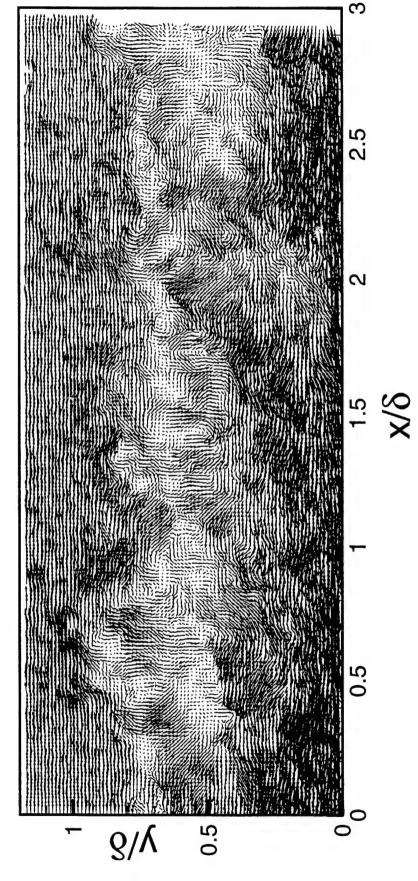
Realization HW-07,  $U_c = 0.65 U_{\odot}$ 

250

Realization HW-07, Reynolds Fluctuations



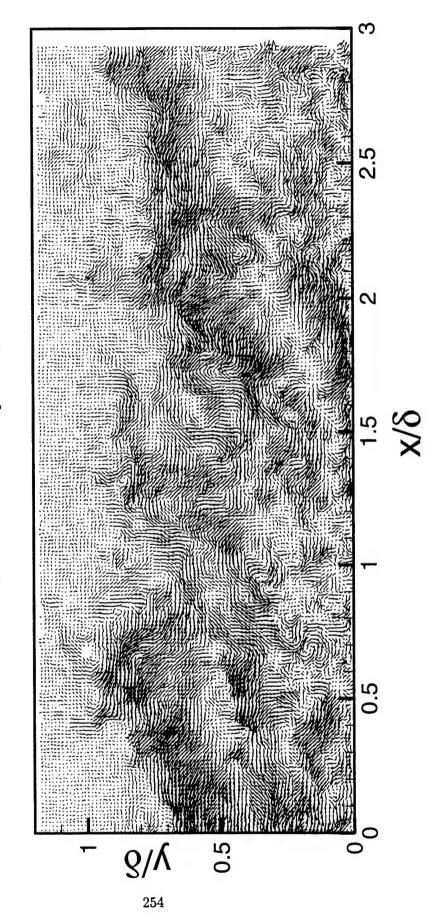
Realization HW-08,  $U_c = 0.85 U_{\odot}$ 



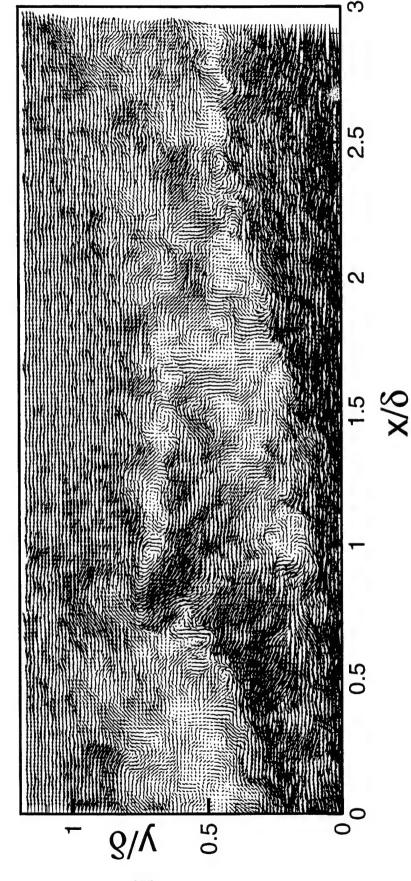
Realization HW-08,  $U_c = 0.65 U_{\odot}$ 

253

Realization HW-08, Reynolds Fluctuations

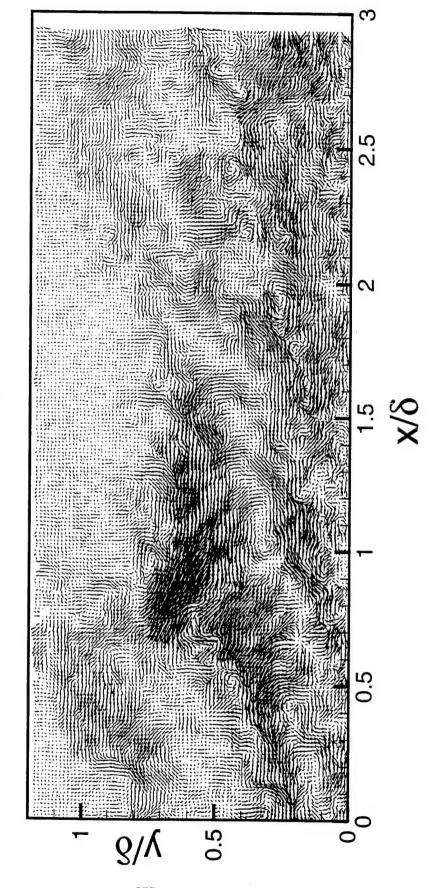


Realization HW-09,  $U_c = 0.85 U_{\odot}$ 



Realization HW-09,  $U_c = 0.65 U_{\odot}$ 

Realization HW-09, Reynolds Fluctuations

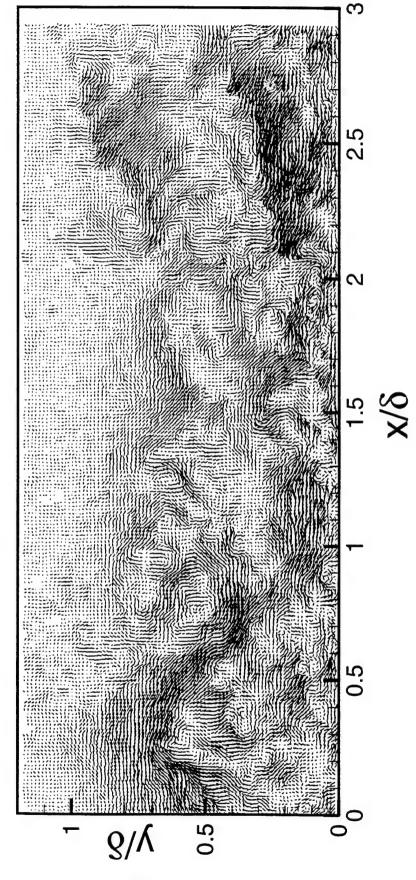


Realization HW-10,  $U_c = 0.85 U_{\odot}$ 0.5

N

Realization HW-10,  $U_c = 0.65 U_{\odot}$ 

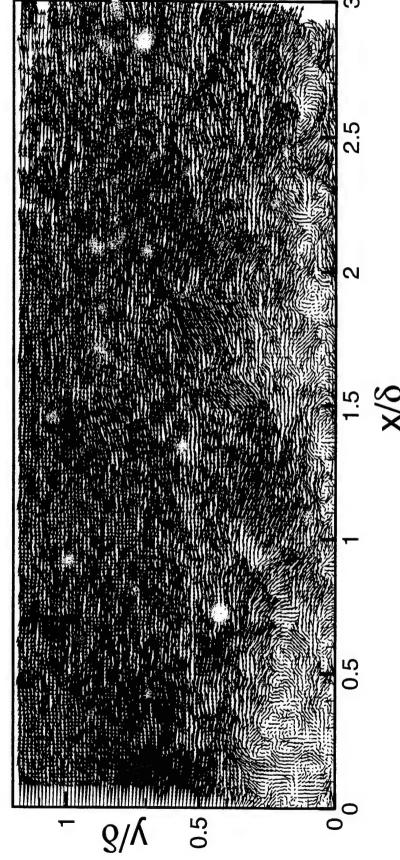
Realization HW-10, Reynolds Fluctuations



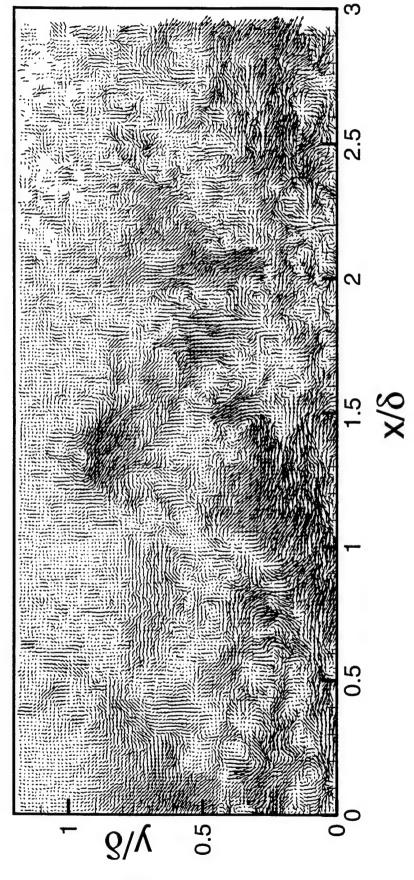
0.5

Realization HW-11,  $U_c = 0.85 U_{\odot}$ 

Realization HW-11,  $U_c = 0.65 U_{\odot}$ 

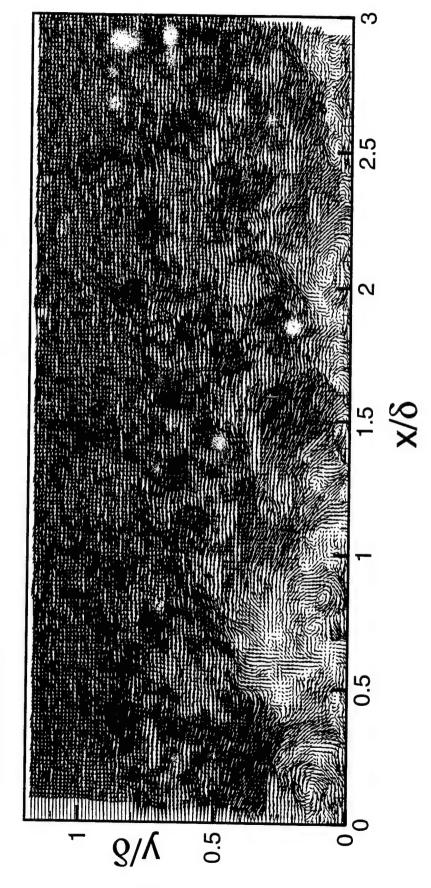


Realization HW-11, Reynolds Fluctuations

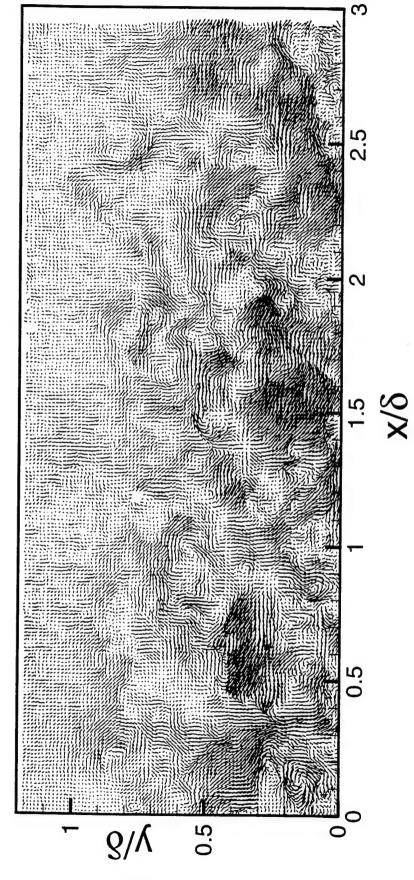


Realization HW-12,  $U_c = 0.85 U_{\odot}$ 

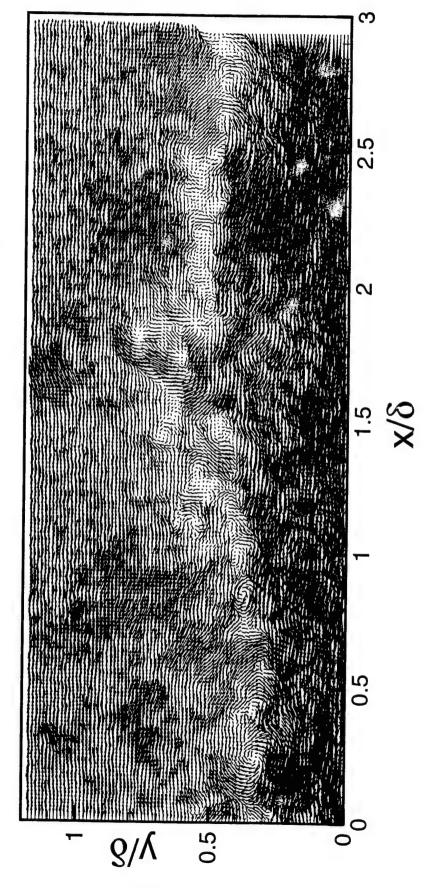
Realization HW-12,  $U_c = 0.65 U_{\odot}$ 



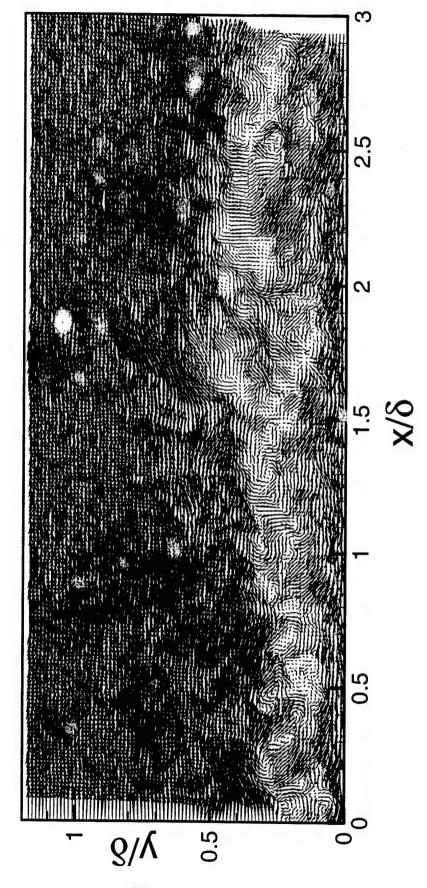
Realization HW-12, Reynolds Fluctuations



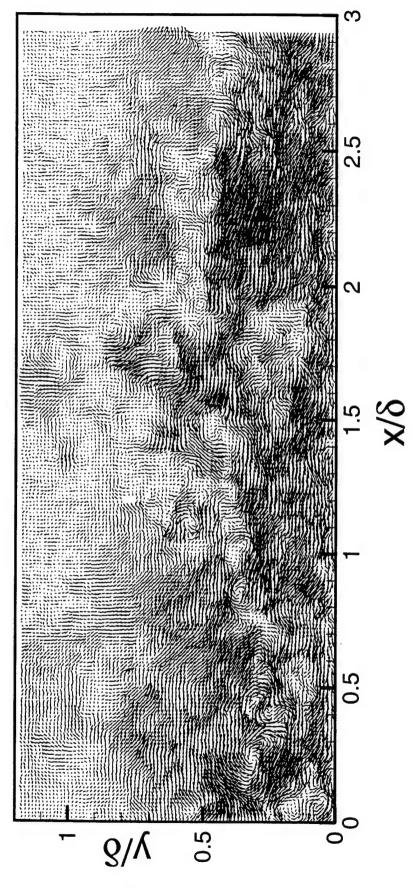
Realization HW-13,  $U_c = 0.85 U_{\odot}$ 



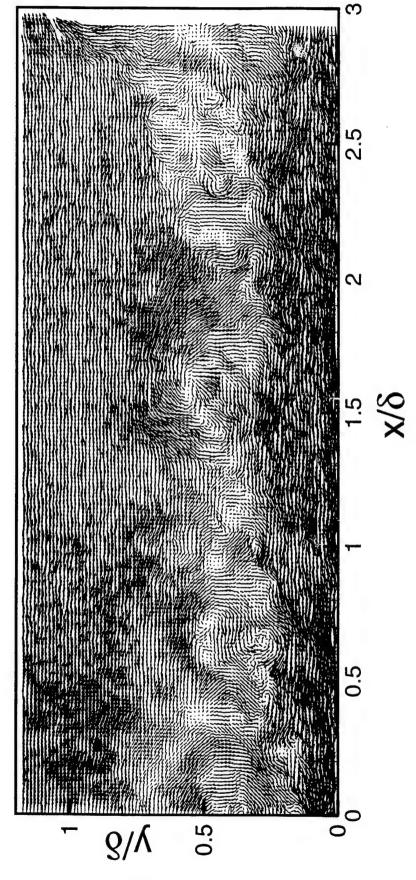
Realization HW-13,  $U_c = 0.65 U_{\odot}$ 



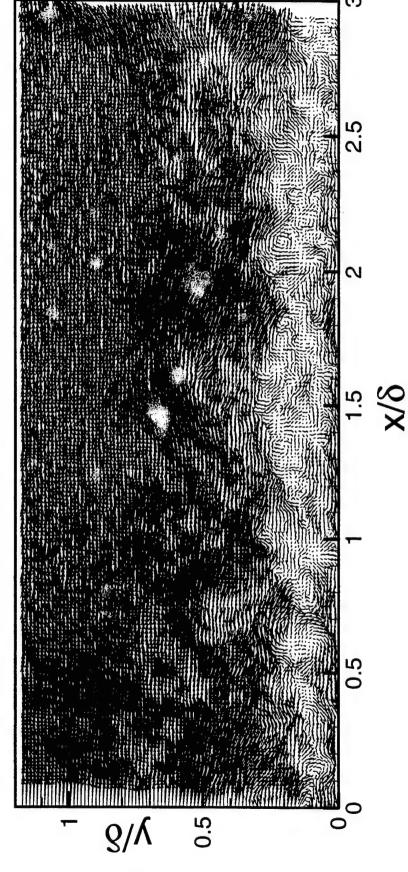
Realization HW-13, Reynolds Fluctuations



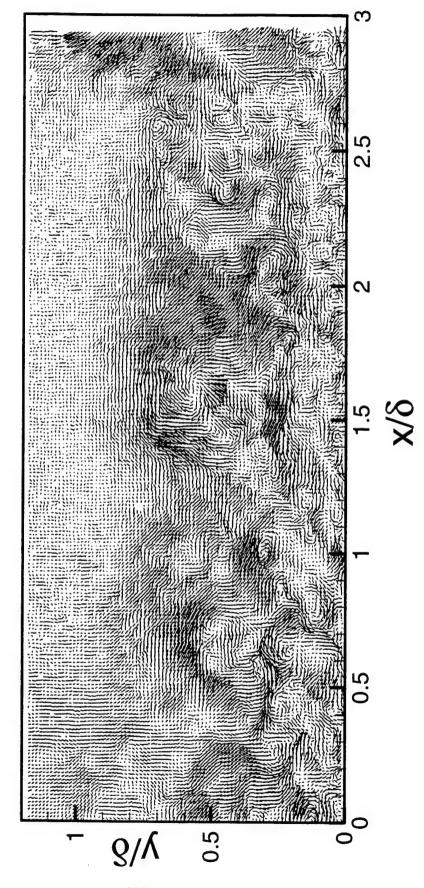
Realization HW-14,  $U_c = 0.85 U_{\odot}$ 



Realization HW-14,  $U_c = 0.65 U_{\odot}$ 



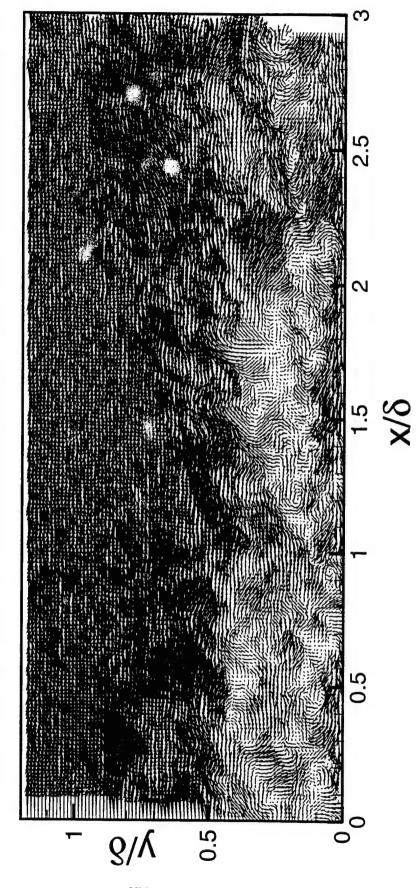
Realization HW-14, Reynolds Fluctuations



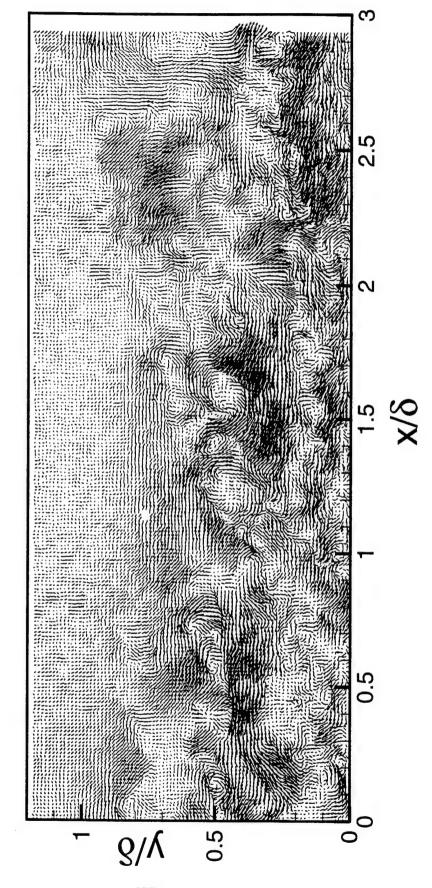
0.5 273

Realization HW-15,  $U_c = 0.85 U_{\odot}$ 

Realization HW-15,  $U_c = 0.65 U_{\odot}$ 

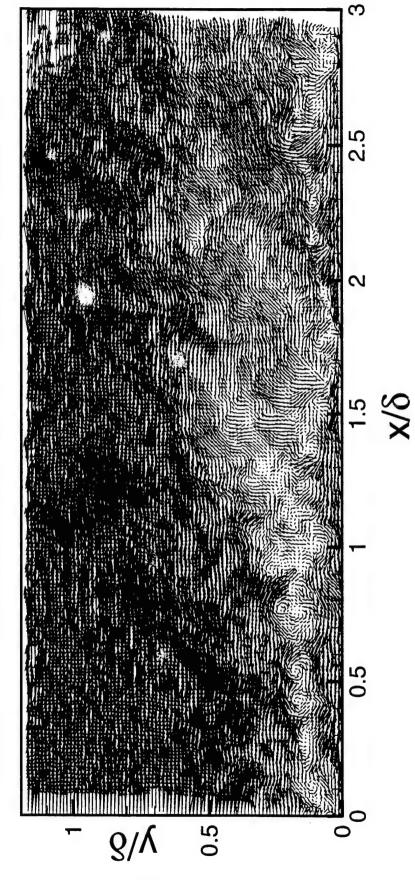


Realization HW-15, Reynolds Fluctuations

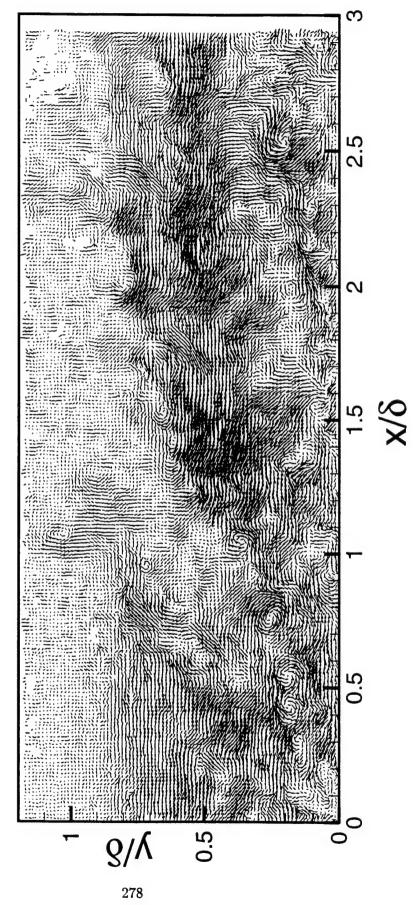


Realization HW-16,  $U_c = 0.85 U_{\odot}$ 

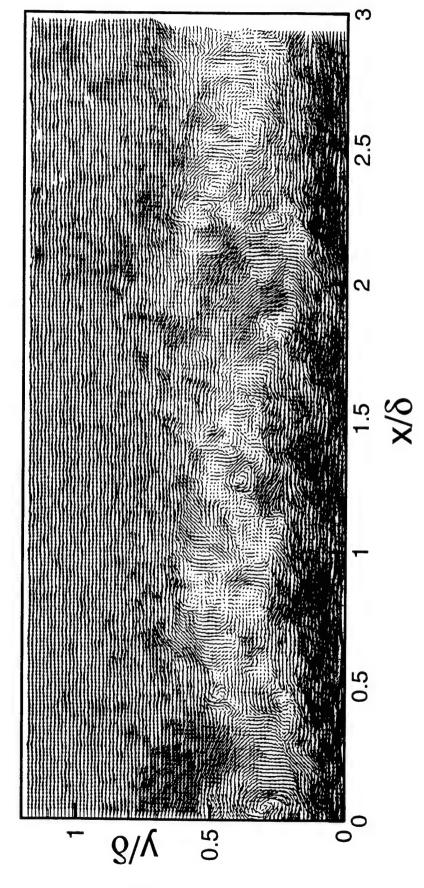
Realization HW-16,  $U_c = 0.65 U_{\odot}$ 



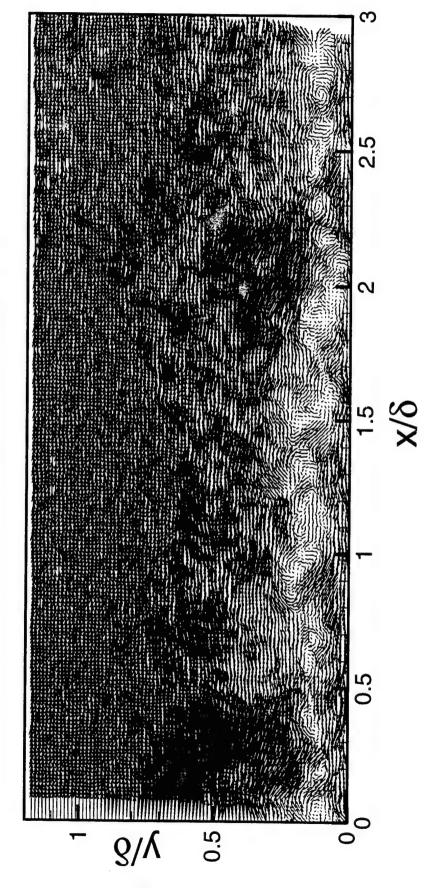
Realization HW-16, Reynolds Fluctuations



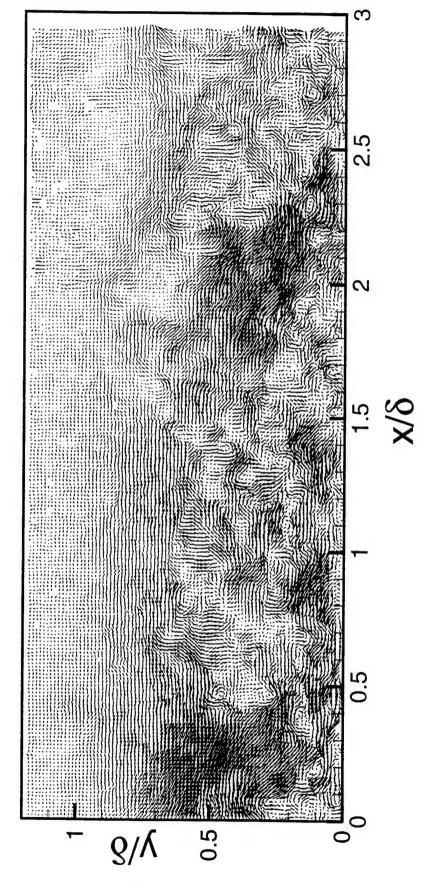
Realization HW-17,  $U_c = 0.85 U_{\odot}$ 



Realization HW-17,  $U_c = 0.65 U_{\odot}$ 



Realization HW-17, Reynolds Fluctuations

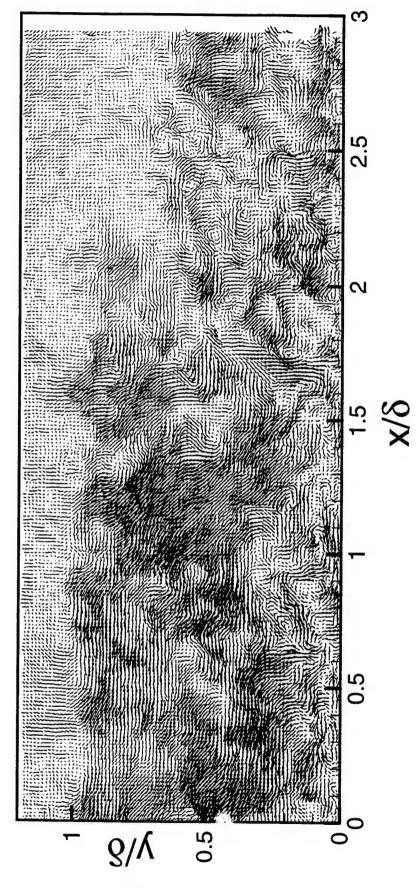


Realization HW-18,  $U_c = 0.85 U_{\odot}$ 

2.5

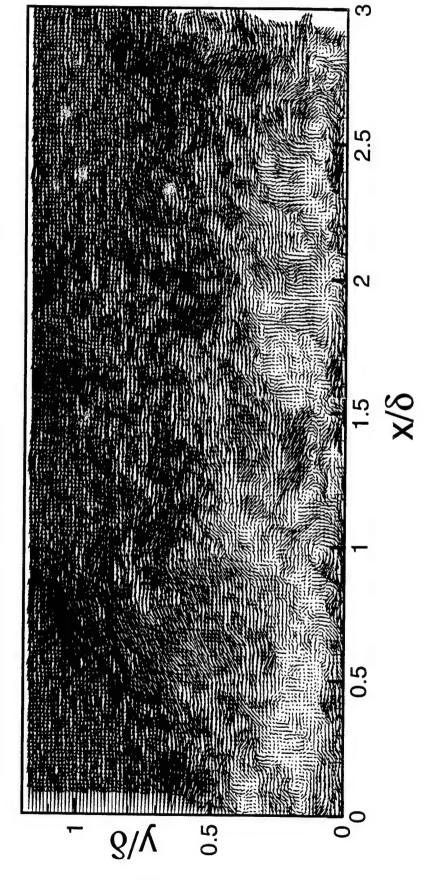
Realization HW-18,  $U_c = 0.65 U_{\odot}$ 

Realization HW-18, Reynolds Fluctuations

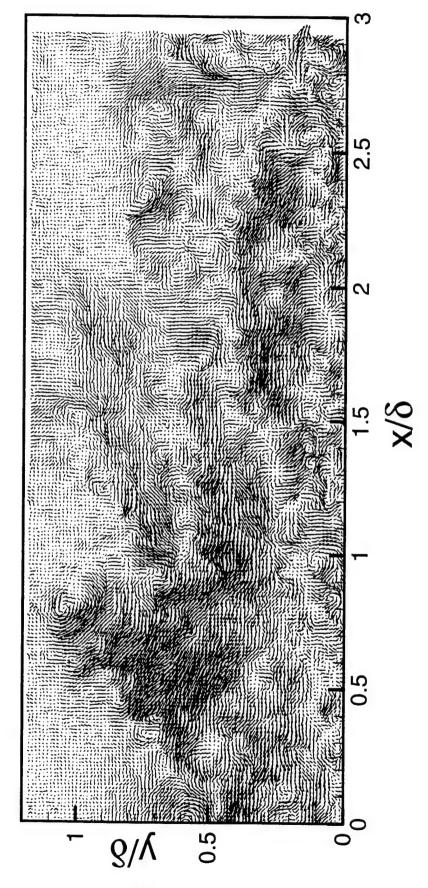


Realization HW-19,  $U_c = 0.85 U_{\odot}$ 

Realization HW-19,  $U_c = 0.65 U_{\odot}$ 

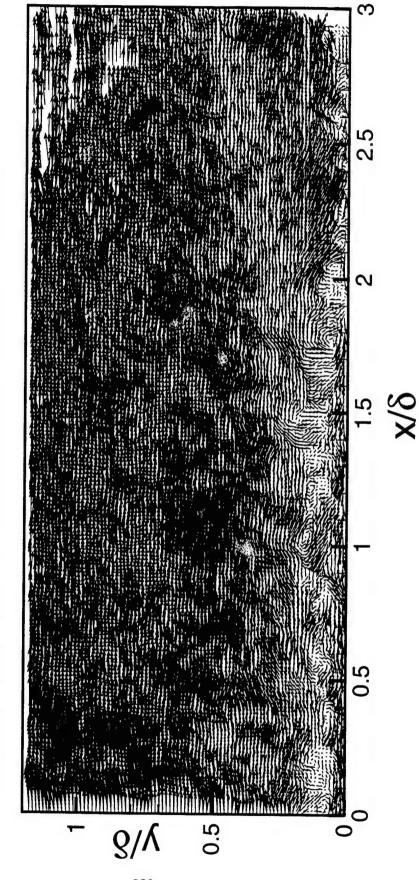


Realization HW-19, Reynolds Fluctuations

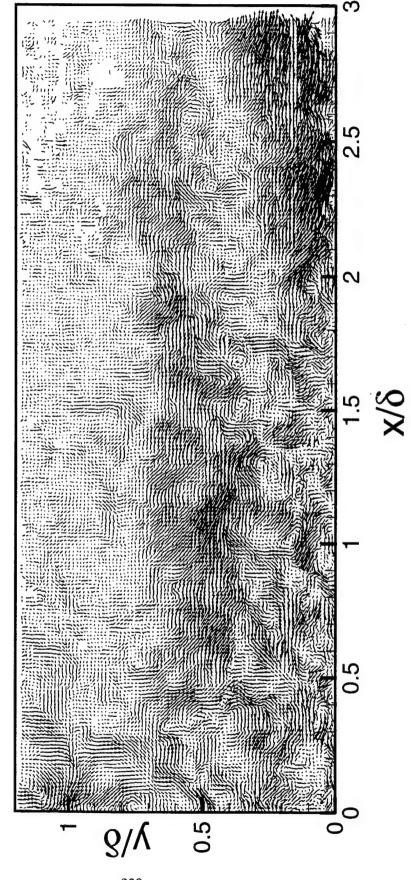


Realization HW-20,  $U_c = 0.85 U_{\odot}$ 

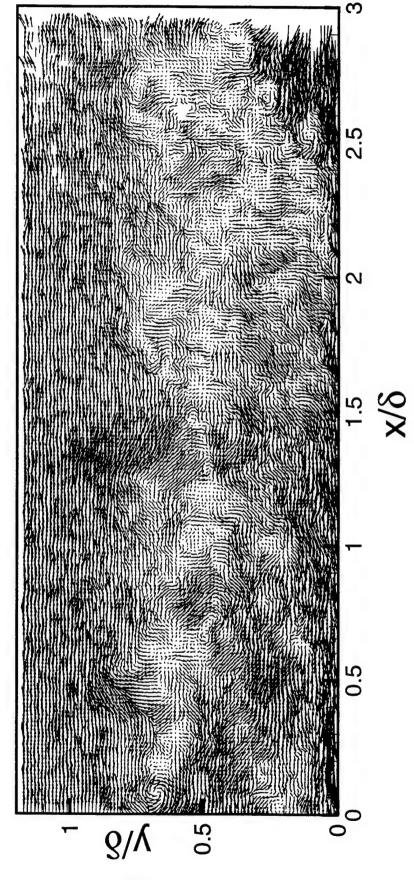
Realization HW-20,  $U_c = 0.65 U_{\odot}$ 



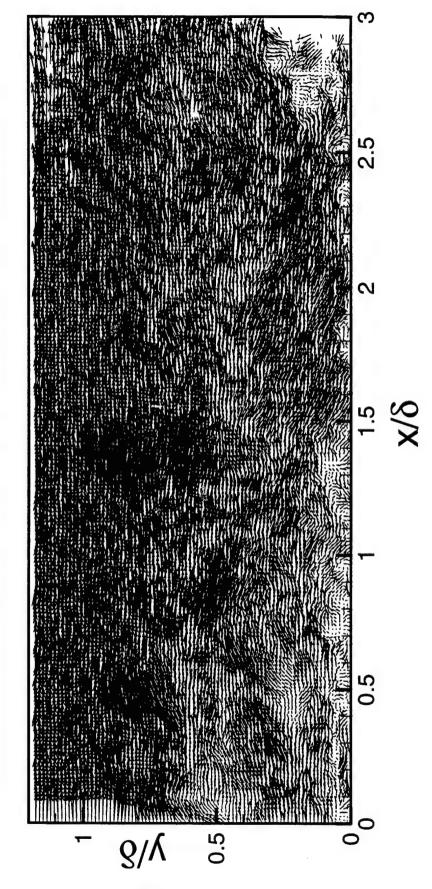
Realization HW-20, Reynolds Fluctuations



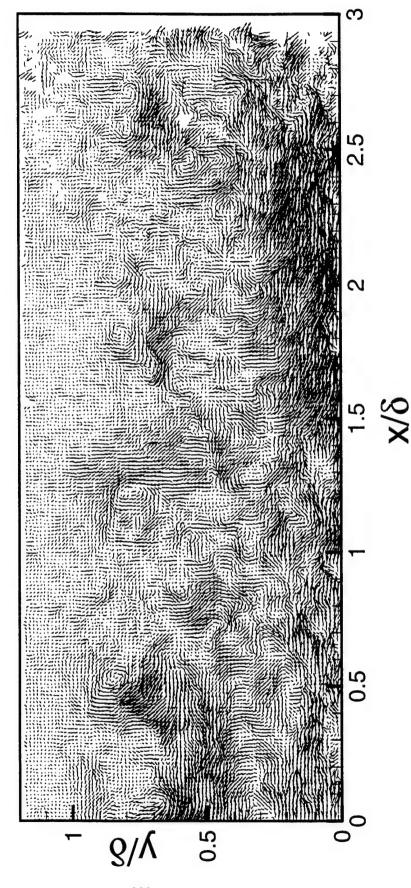
Realization HW-21,  $U_c = 0.85 U_{\odot}$ 

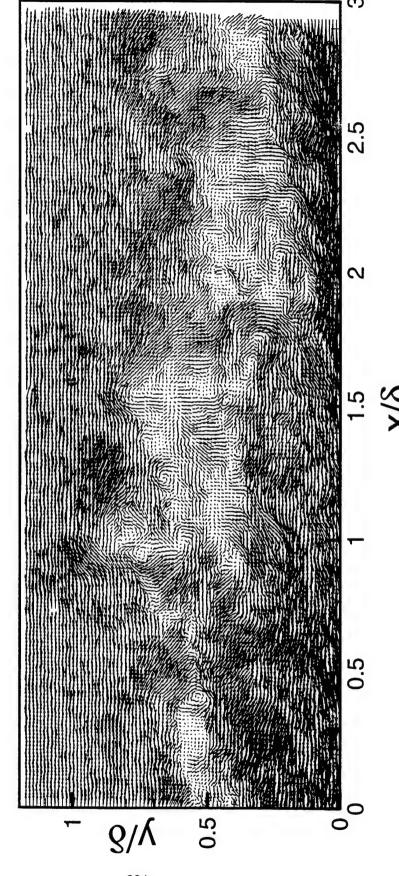


Realization HW-21,  $U_c = 0.65 U_{\odot}$ 



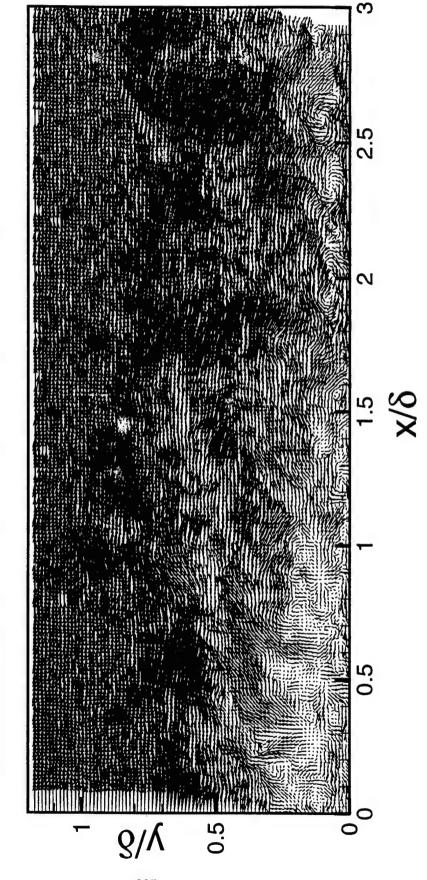
Realization HW-21, Reynolds Fluctuations



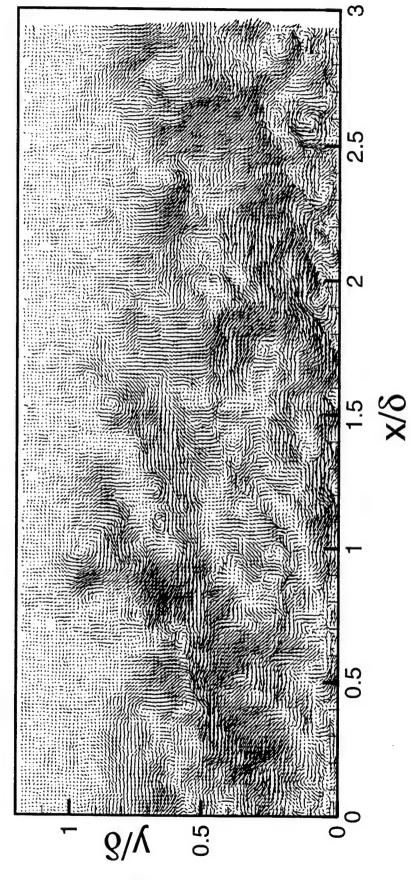


Realization HW-22,  $U_c = 0.85 U_{\odot}$ 

Realization HW-22,  $U_c = 0.65 U_{\odot}$ 



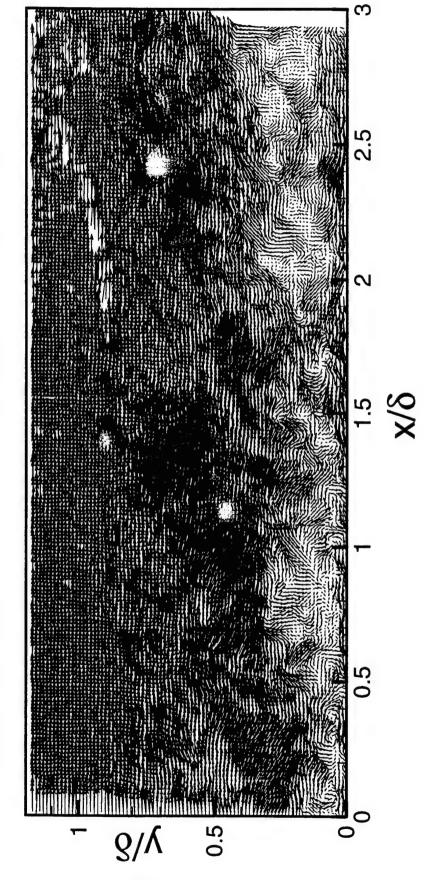
Realization HW-22, Reynolds Fluctuations



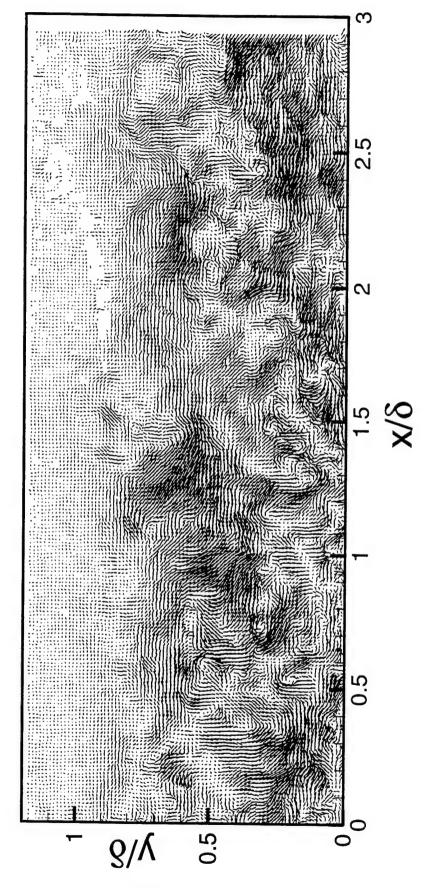
297

Realization HW-23,  $U_c = 0.85 U_{\odot}$ 

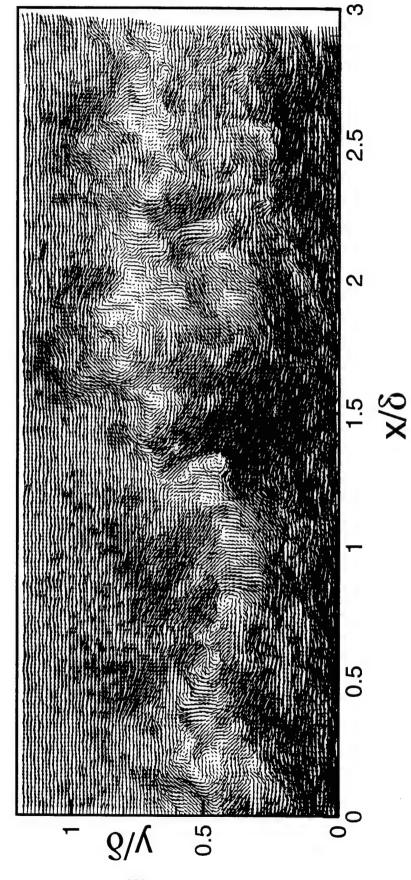
Realization HW-23,  $U_c = 0.65 U_{\odot}$ 



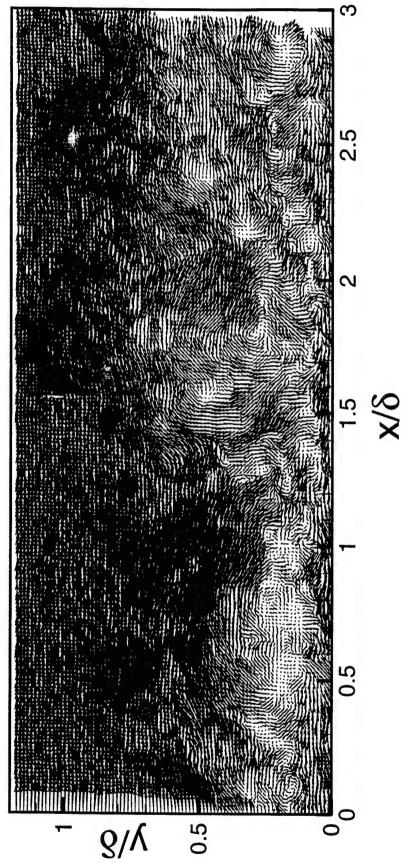
Realization HW-23, Reynolds Fluctuations



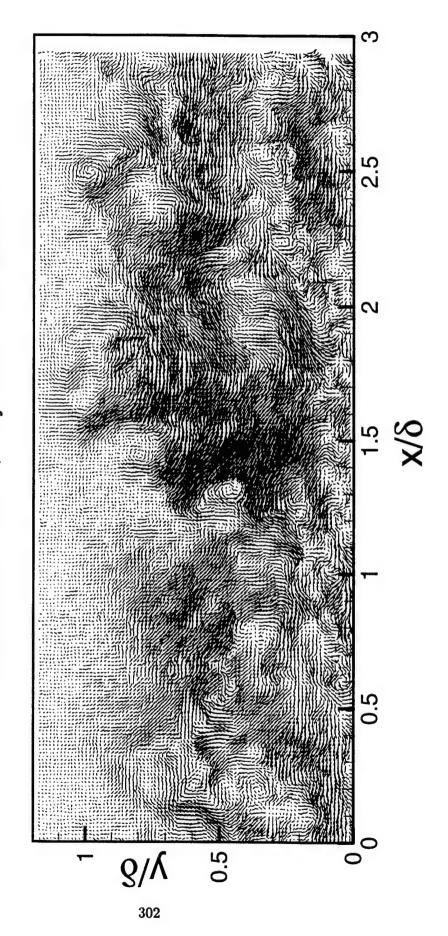
Realization HW-24,  $U_c = 0.85 U_{\odot}$ 



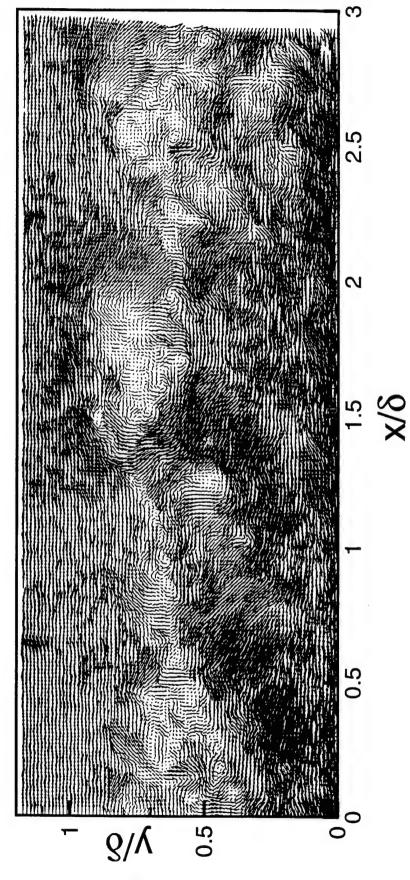
Realization HW-24,  $U_c = 0.65 U_{\odot}$ 



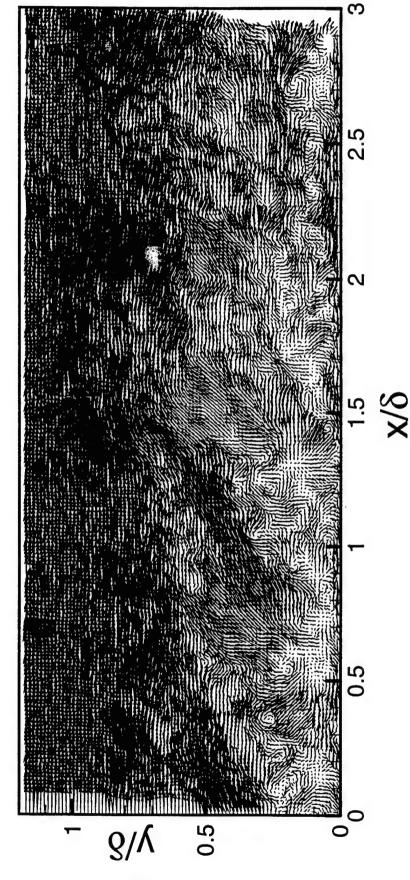
Realization HW-24, Reynolds Fluctuations



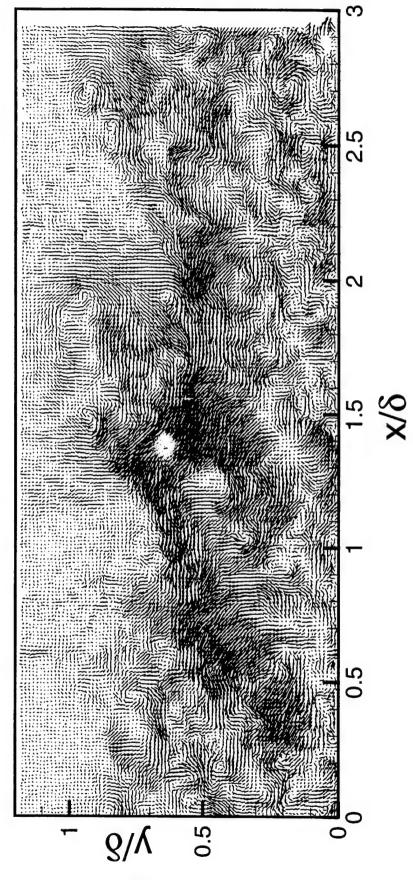
Realization HW-25,  $U_c = 0.85 U_{\odot}$ 



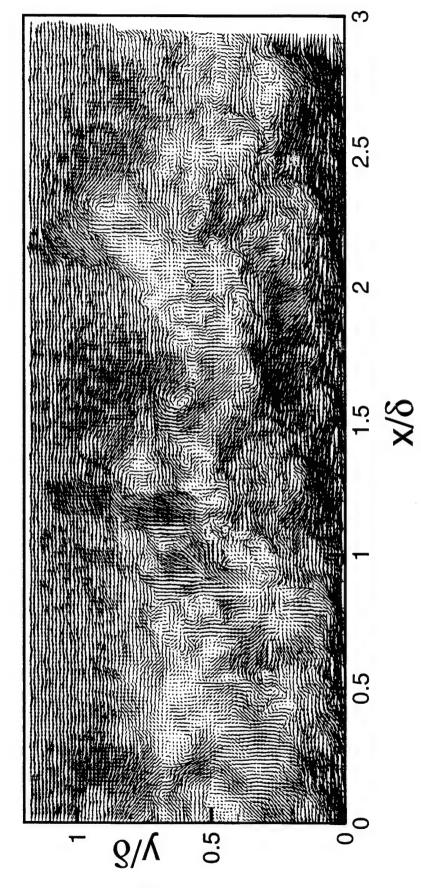
Realization HW-25,  $U_c = 0.65 U_{\odot}$ 



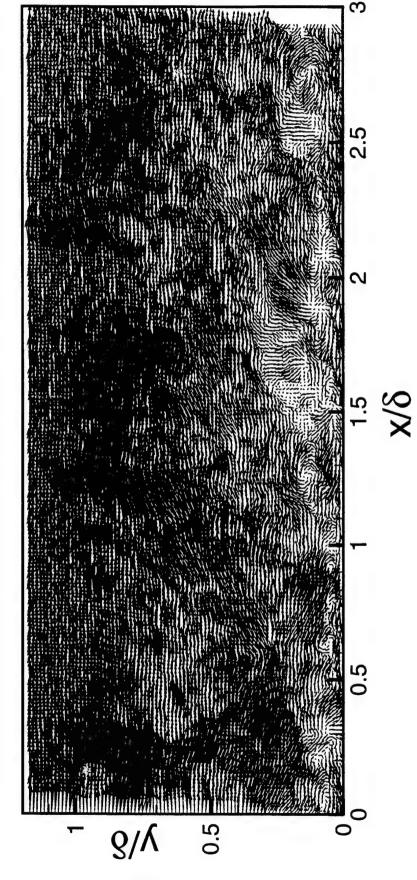
Realization HW-25, Reynolds Fluctuations



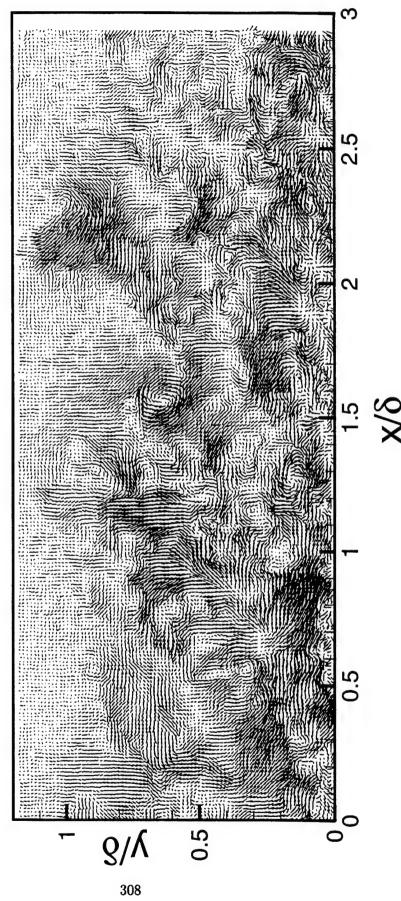
Realization HW-26,  $U_c = 0.85 U_{\odot}$ 



Realization HW-26,  $U_c = 0.65 U_{\odot}$ 

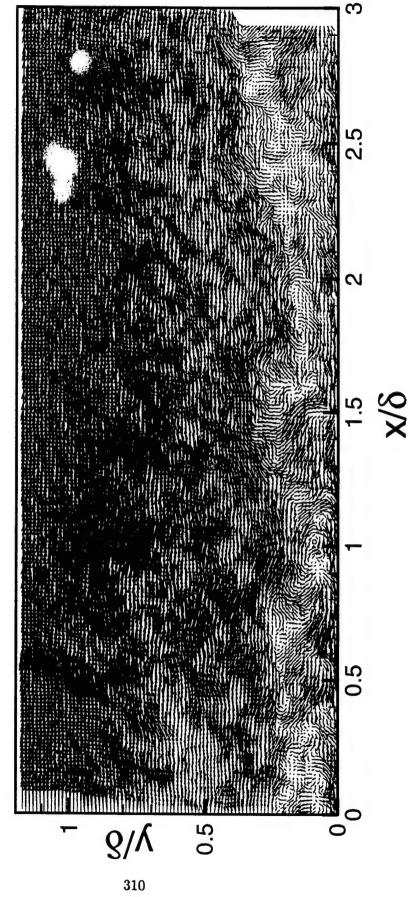


Realization HW-26, Reynolds Fluctuations

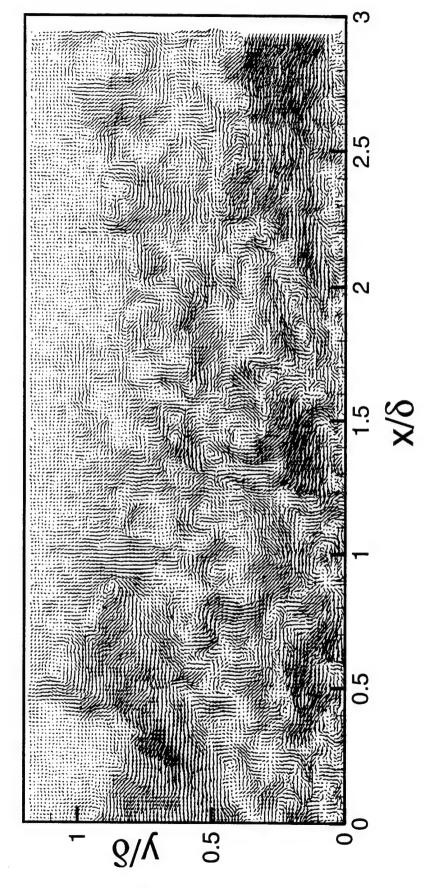


Realization HW-27,  $U_c = 0.85 U_{\odot}$ 

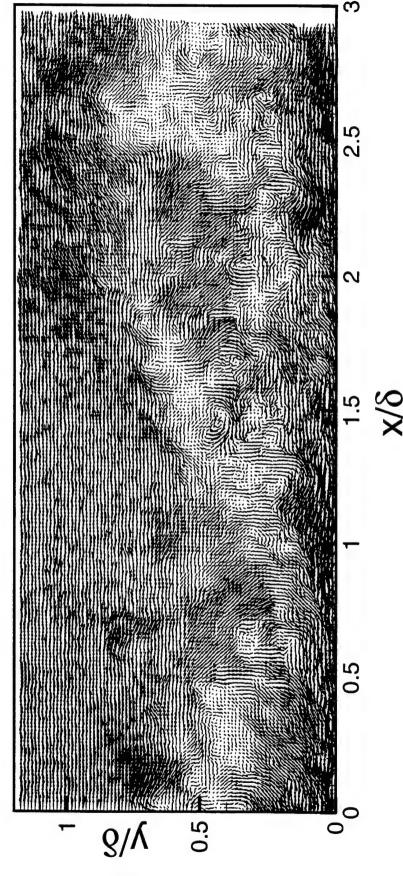
Realization HW-27,  $U_c = 0.65 U_{\odot}$ 



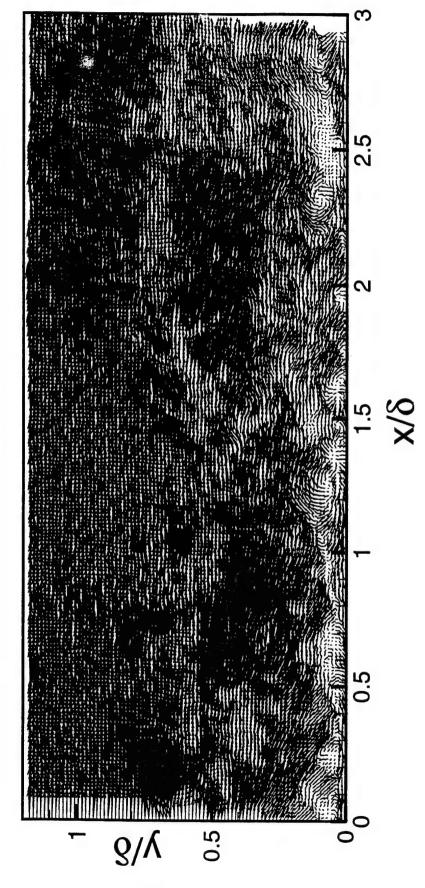
Realization HW-27, Reynolds Fluctuations



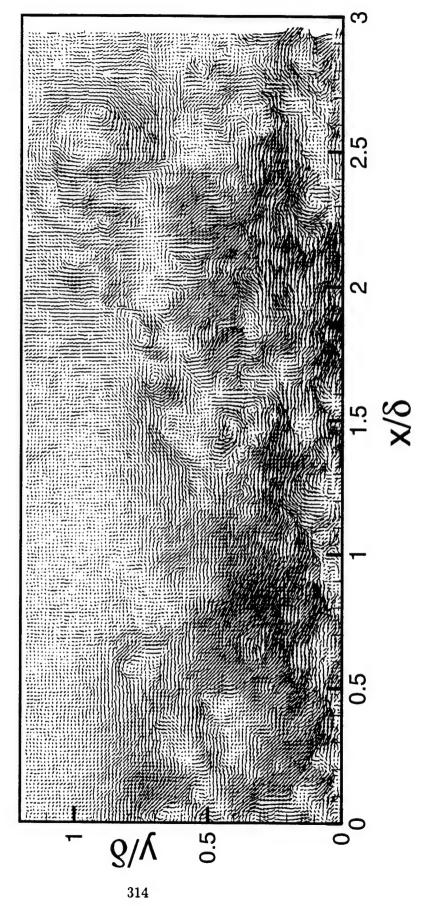
Realization HW-28,  $U_c = 0.85 U_{\odot}$ 



Realization HW-28,  $U_c = 0.65 U_{\odot}$ 

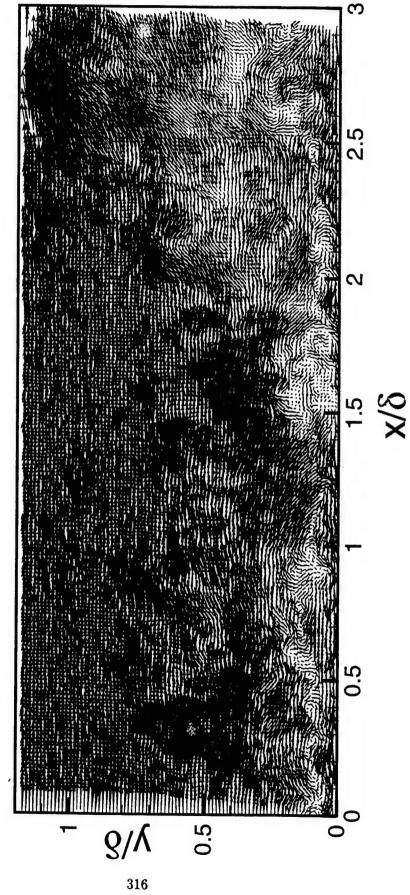


Realization HW-28, Reynolds Fluctuations

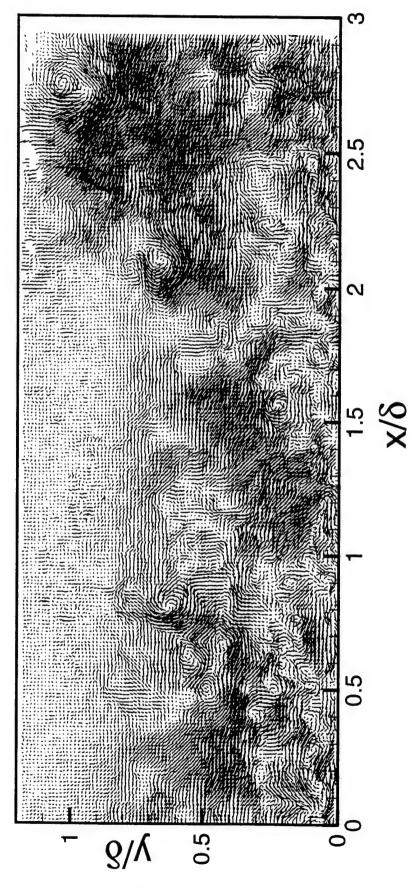


Realization HW-29,  $U_c = 0.85 U_{\odot}$ 

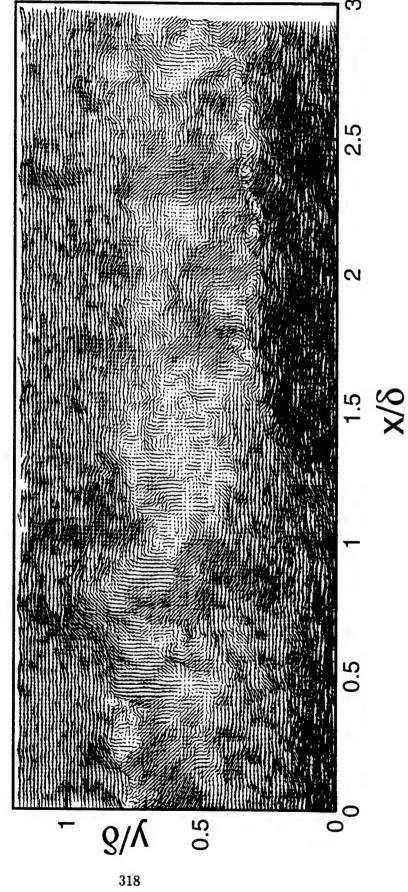
Realization HW-29,  $U_c = 0.65 U_{\odot}$ 



Realization HW-29, Reynolds Fluctuations

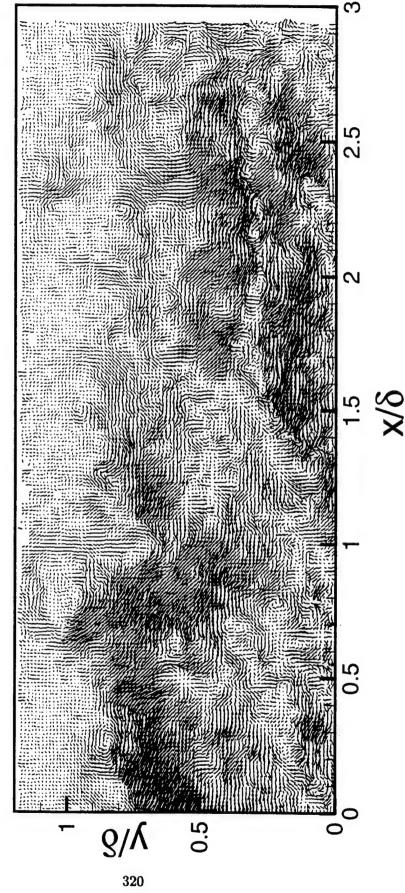


Realization HW-30,  $U_c = 0.85 U_{\odot}$ 



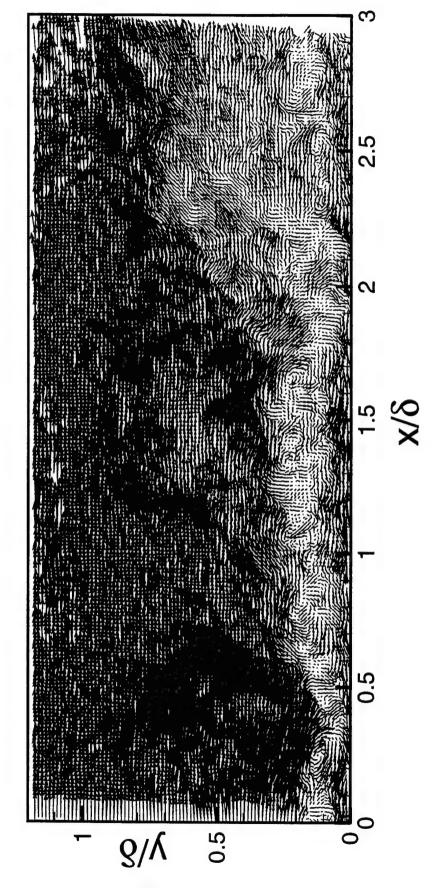
Realization HW-30,  $U_c = 0.65 U_{\odot}$ 

Realization HW-30, Reynolds Fluctuations

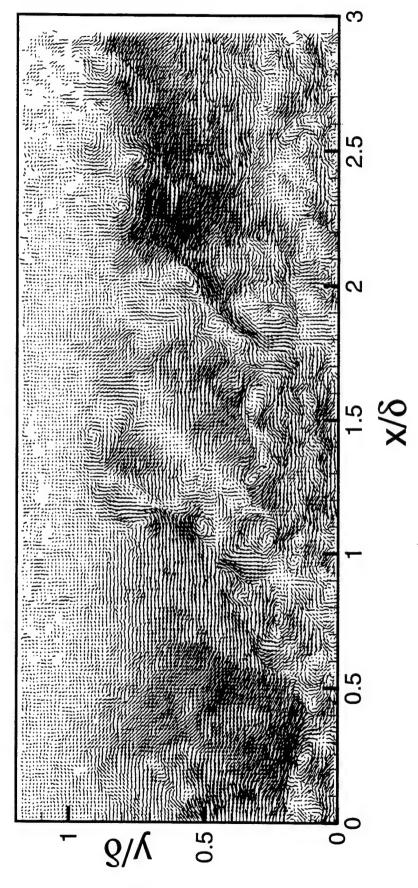


Realization HW-31,  $U_c = 0.85 U_{\odot}$ 

Realization HW-31,  $U_c = 0.65 U_{\odot}$ 



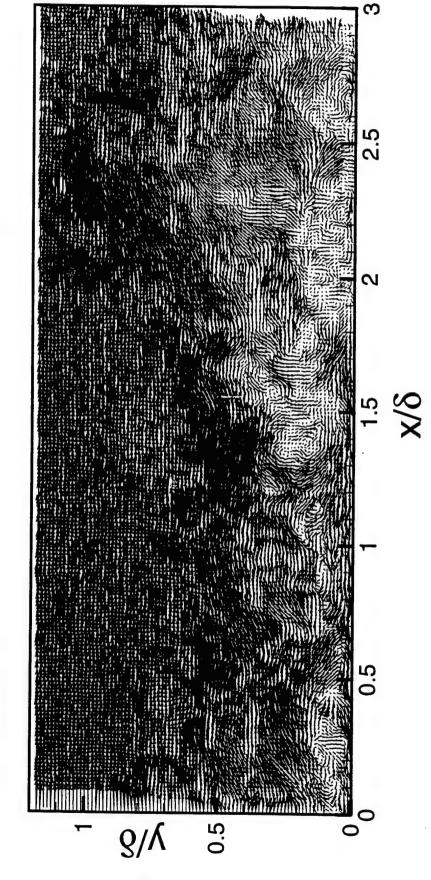
Realization HW-31, Reynolds Fluctuations



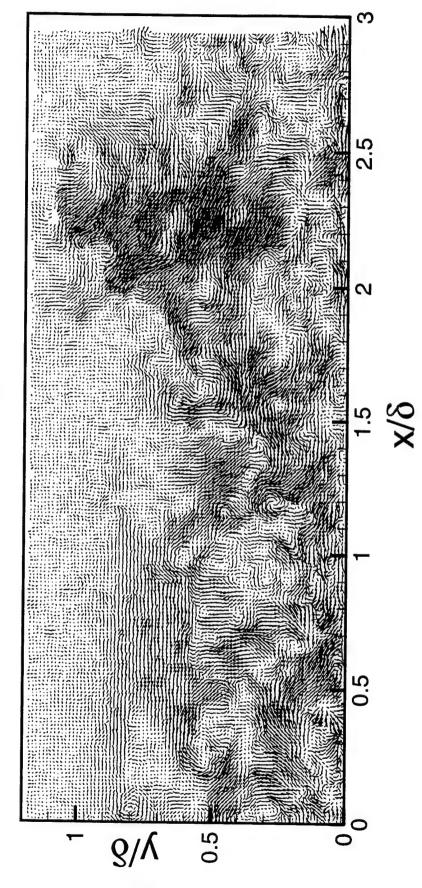
324

Realization HW-32,  $U_c = 0.85 U_{\odot}$ 

Realization HW-32,  $U_c = 0.65 U_{\odot}$ 

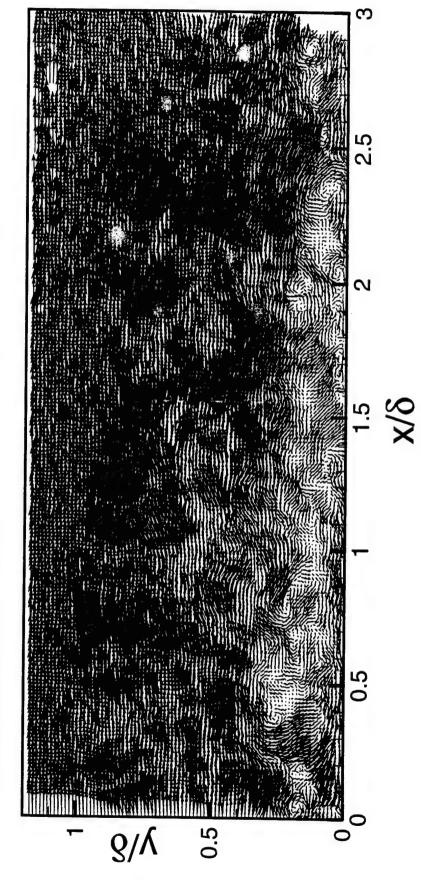


Realization HW-32, Reynolds Fluctuations

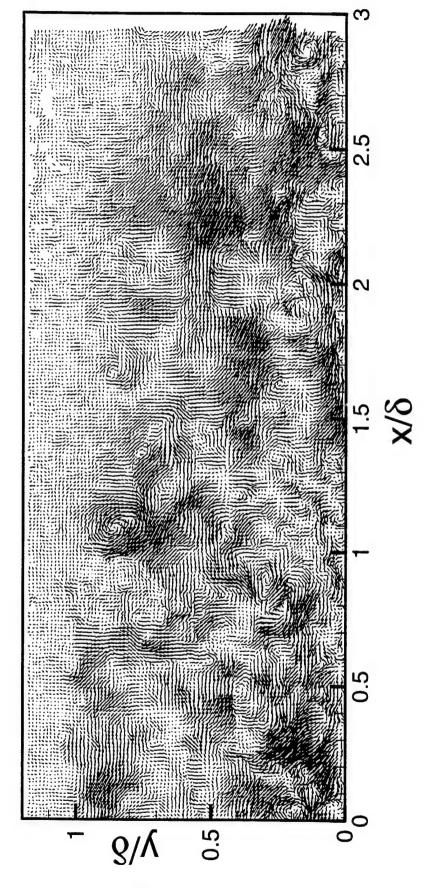


Realization HW-33,  $U_c = 0.85 U_{\odot}$ 

Realization HW-33,  $U_c = 0.65 U_{\odot}$ 

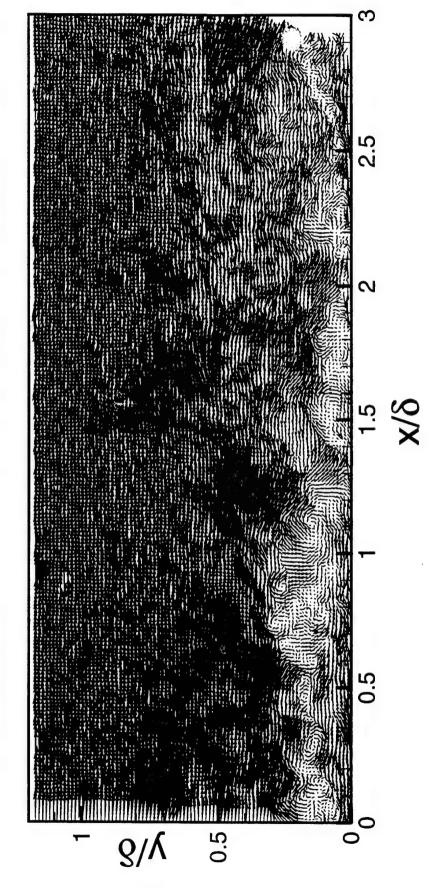


Realization HW-33, Reynolds Fluctuations

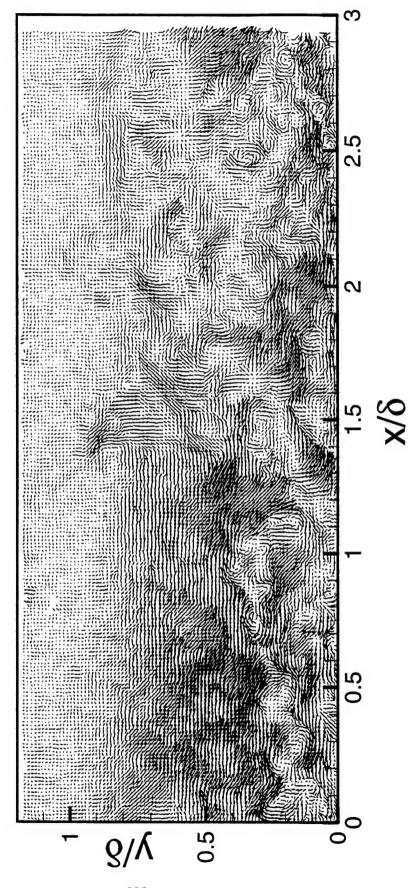


Realization HW-34,  $U_c = 0.85 U_{\odot}$ 

Realization HW-34,  $U_c = 0.65 U_{\odot}$ 



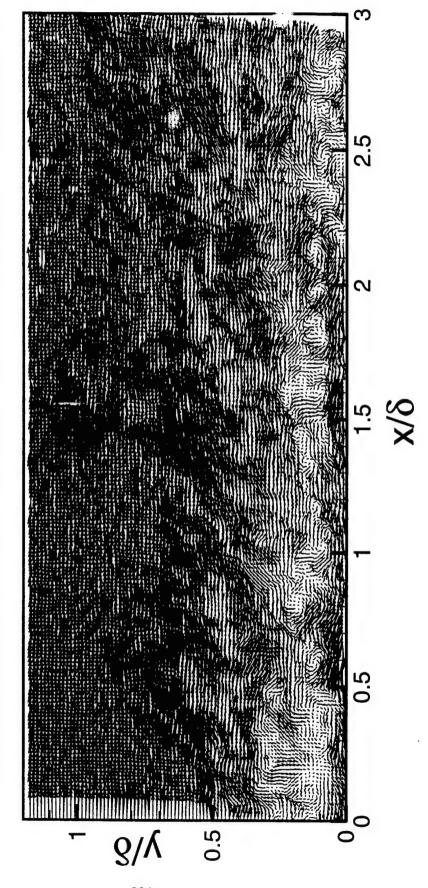
Realization HW-34, Reynolds Fluctuations



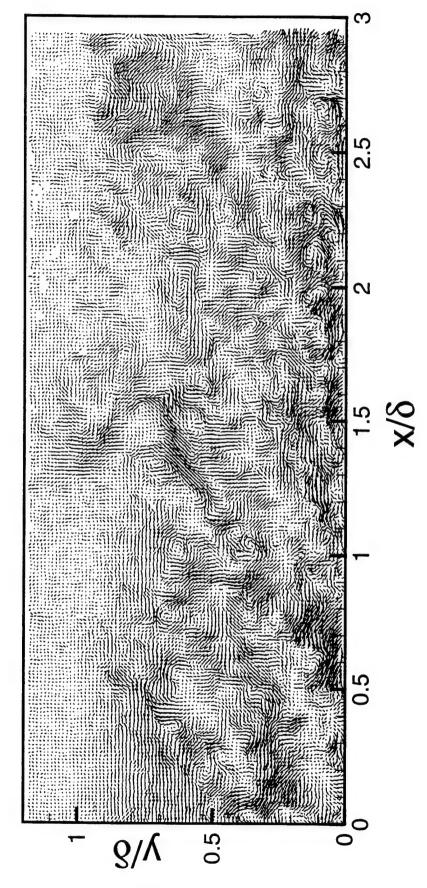
Realization HW-35,  $U_c = 0.85 U_{\odot}$ 

333

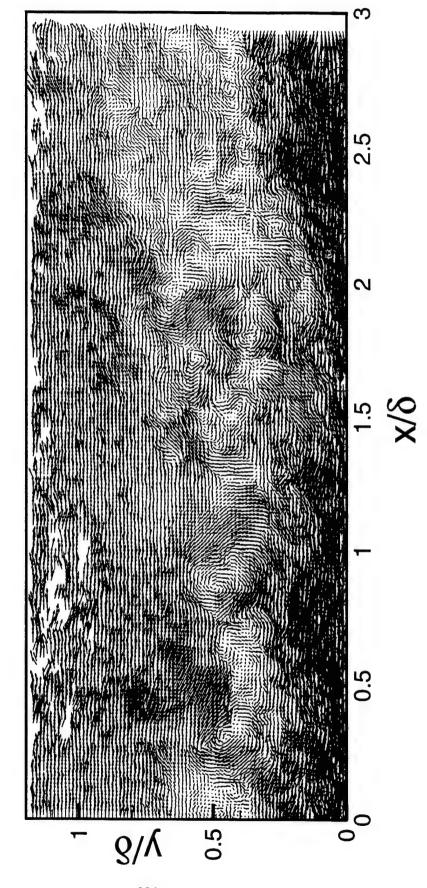
Realization HW-35,  $U_c = 0.65 U_{\odot}$ 



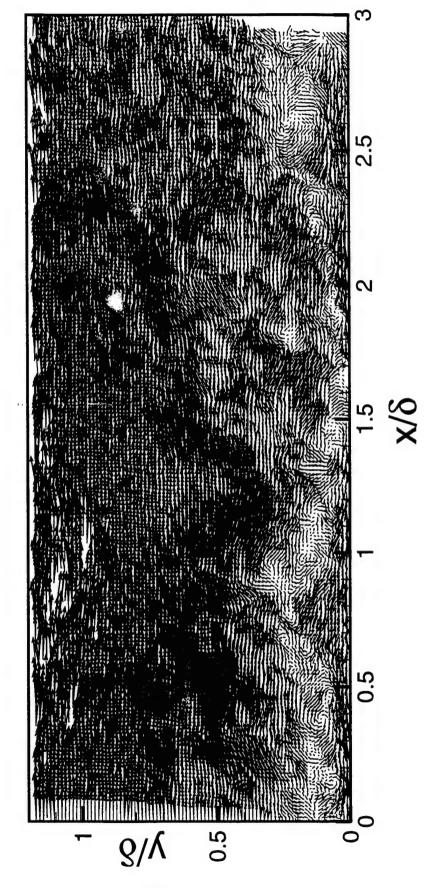
Realization HW-35, Reynolds Fluctuations



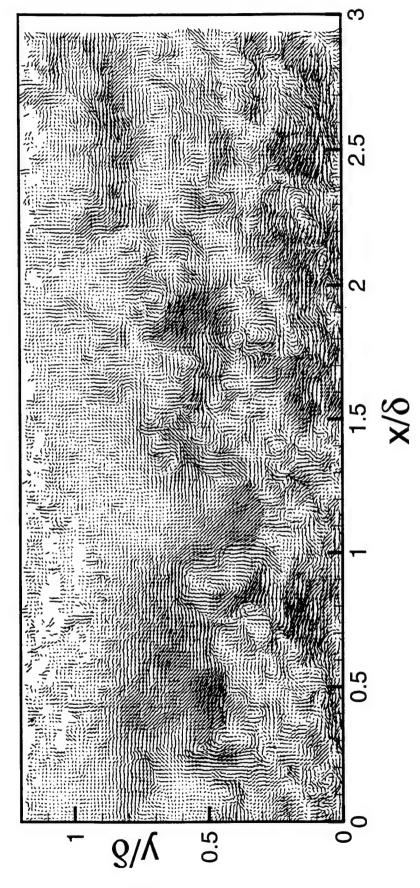
Realization HW-36,  $U_c = 0.85 U_{\odot}$ 



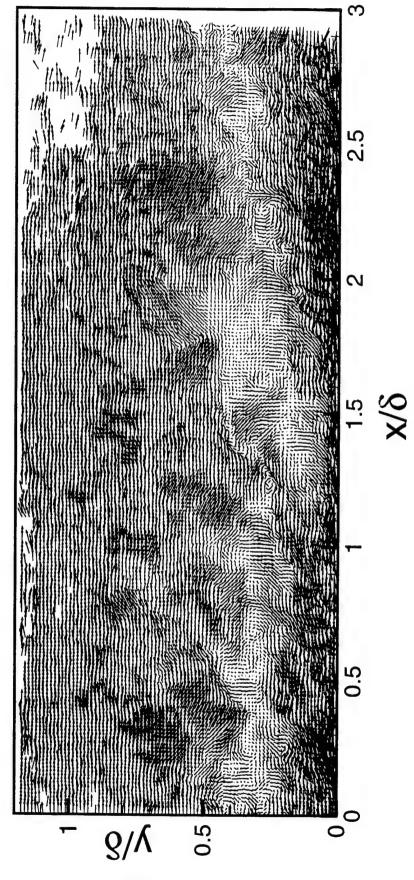
Realization HW-36,  $U_c = 0.65 U_{\odot}$ 



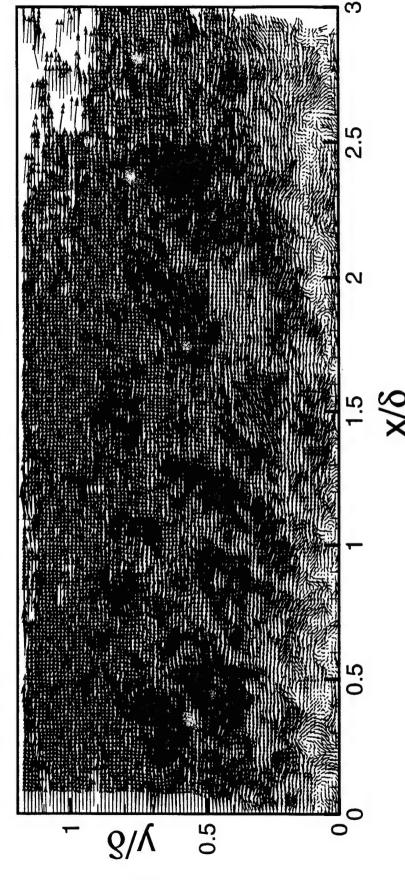
Realization HW-36, Reynolds Fluctuations



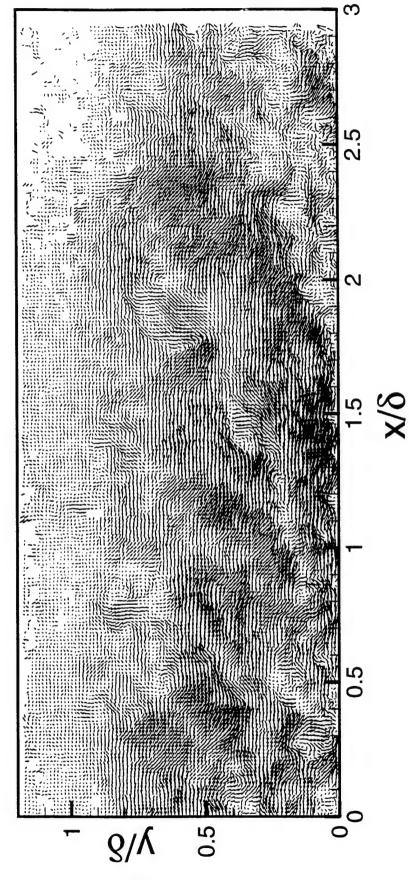
Realization HW-37,  $U_c = 0.85 U_{\odot}$ 



Realization HW-37,  $U_c = 0.65 U_{\odot}$ 

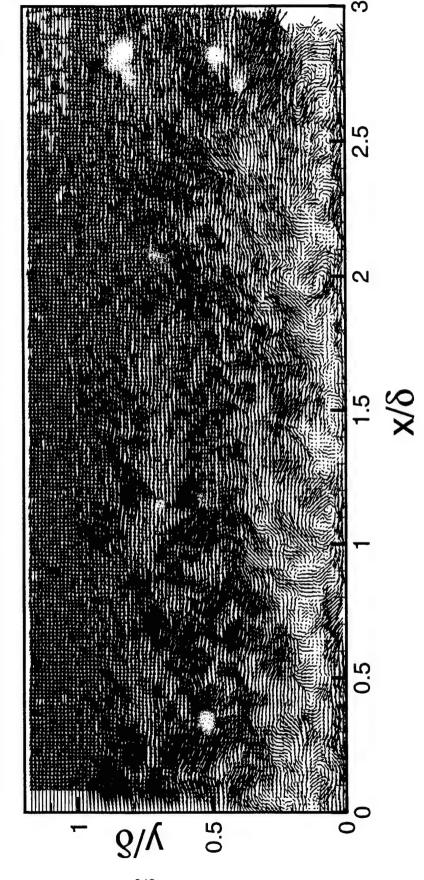


Realization HW-37, Reynolds Fluctuations

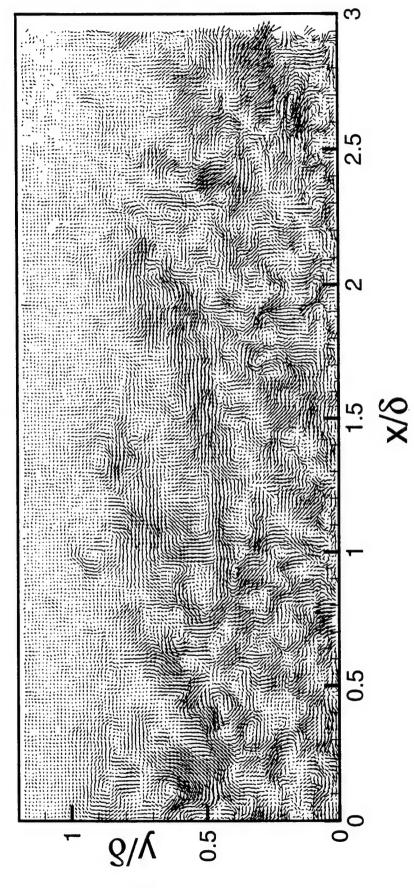


Realization HW-38,  $U_c = 0.85 U_{\odot}$ 0.5

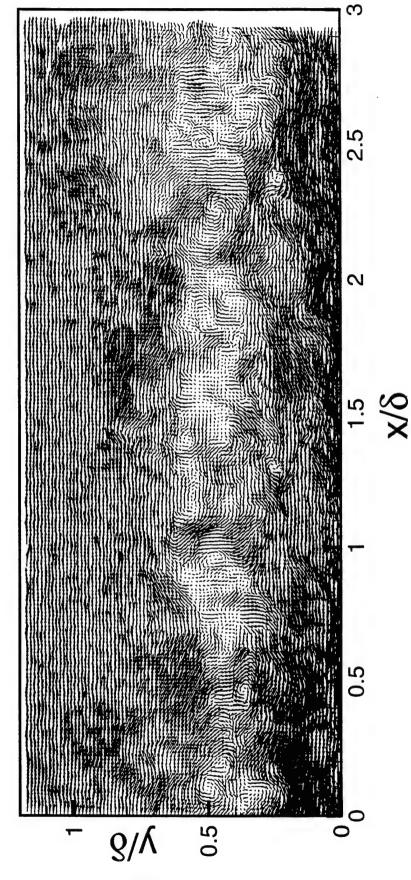
Realization HW-38,  $U_c = 0.65 U_{\odot}$ 



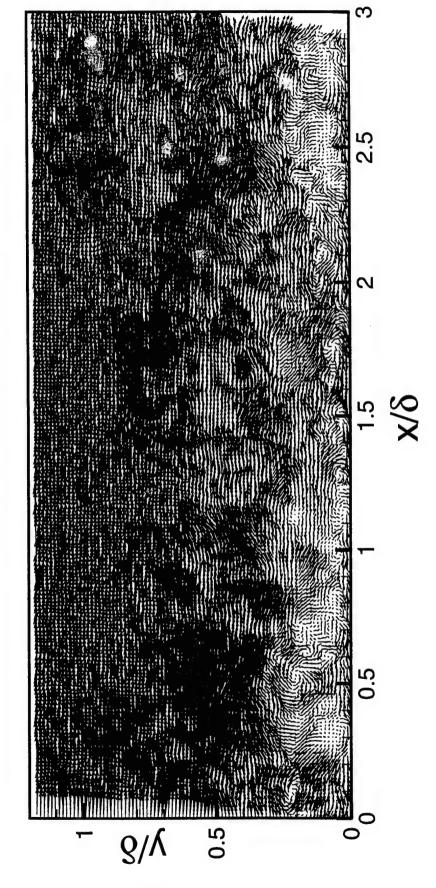
Realization HW-38, Reynolds Fluctuations



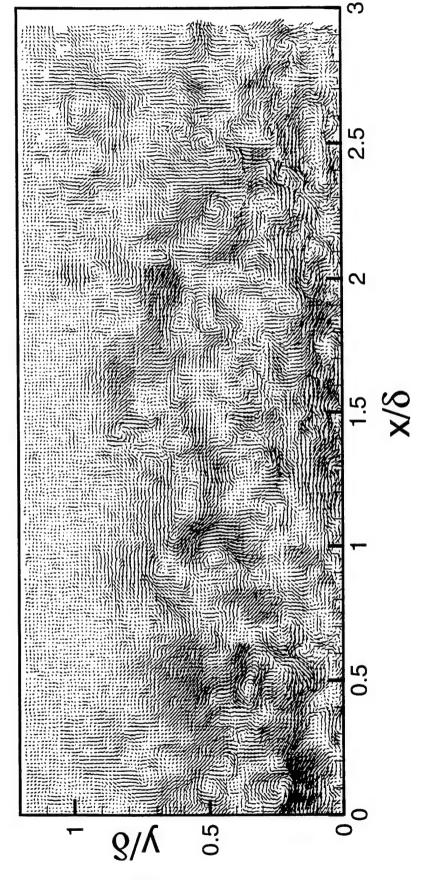
Realization HW-39,  $U_c = 0.85 U_{\odot}$ 



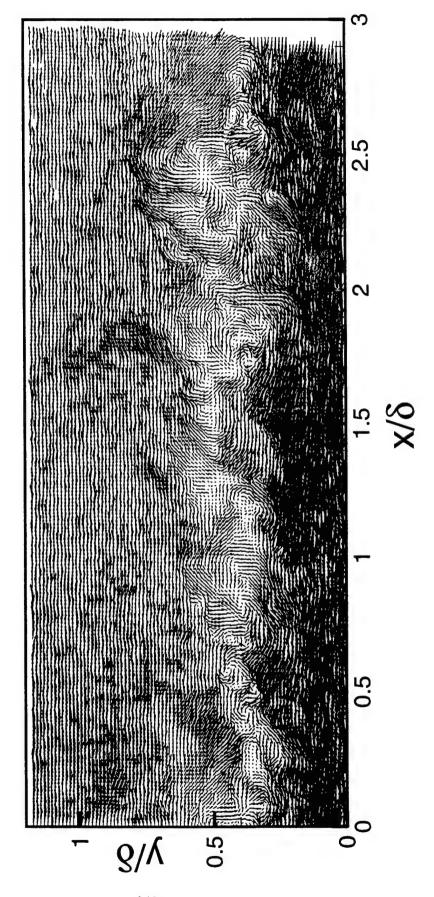
Realization HW-39,  $U_c = 0.65 U_{\odot}$ 



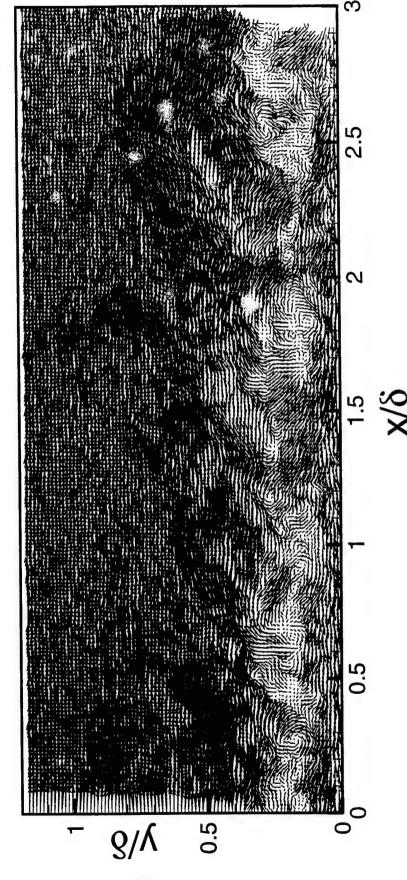
Realization HW-39, Reynolds Fluctuations



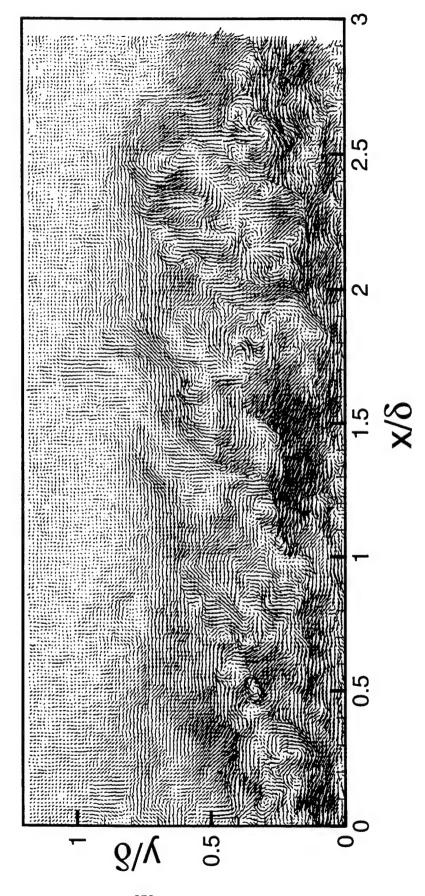
Realization HW-41,  $U_c = 0.85 U_{\odot}$ 



Realization HW-41,  $U_c = 0.65 U_{\odot}$ 

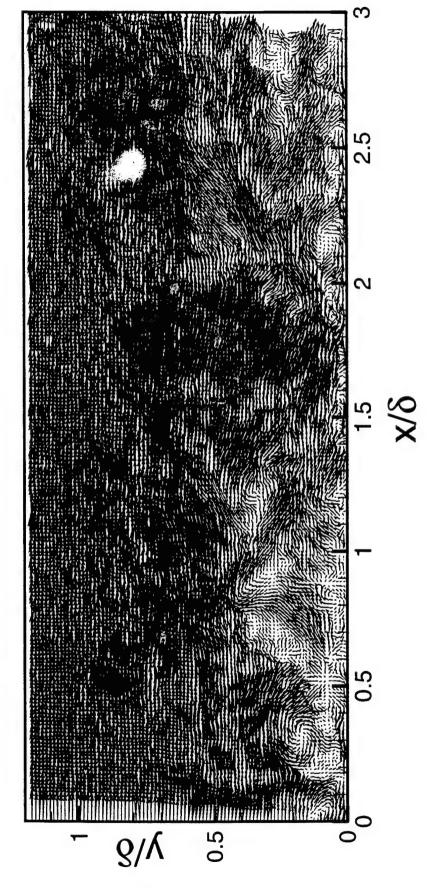


Realization HW-41, Reynolds Fluctuations

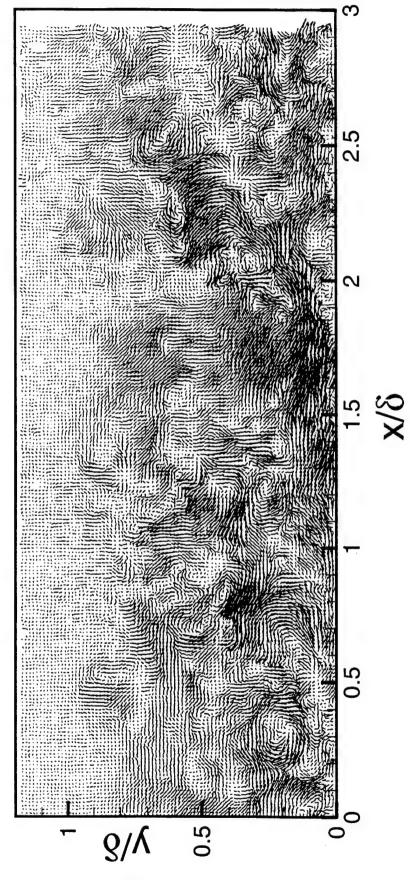


Realization HW-42,  $U_c = 0.85 U_{\odot}$ 

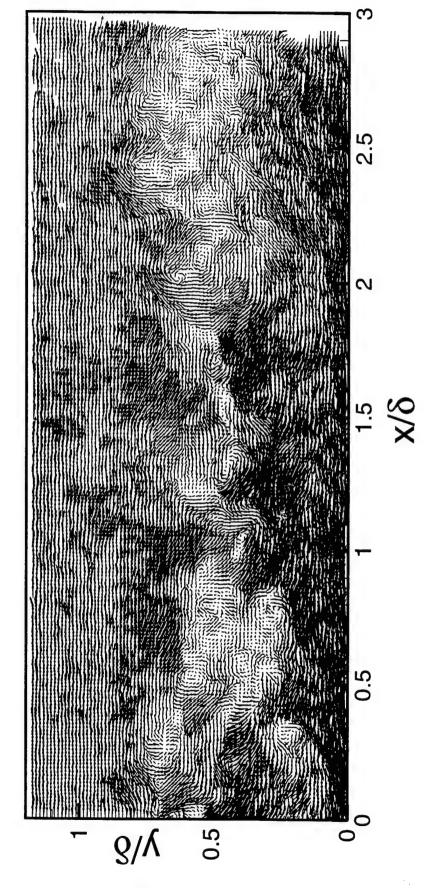
Realization HW-42,  $U_c = 0.65 U_{\odot}$ 



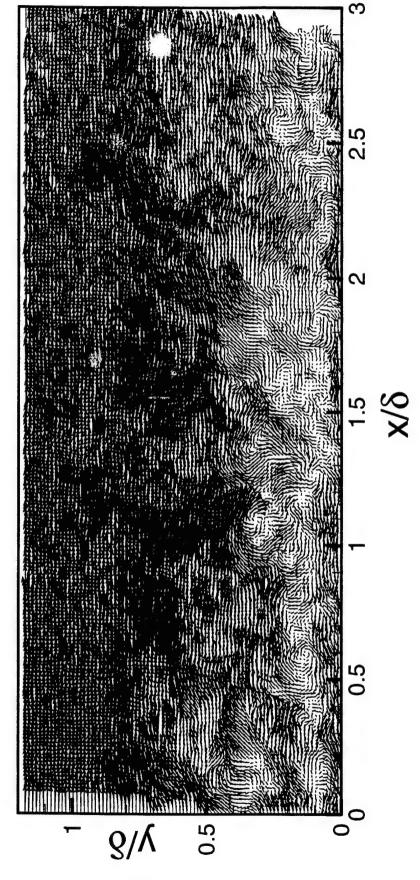
Realization HW-42, Reynolds Fluctuations



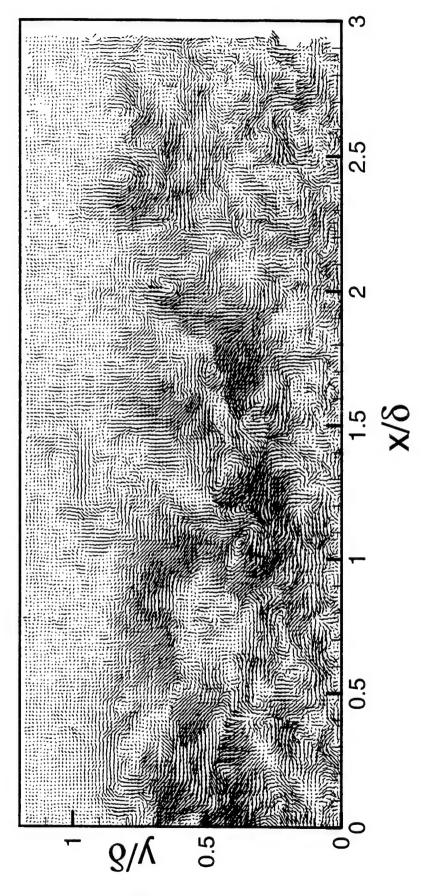
Realization HW-43,  $U_c = 0.85 U_{\odot}$ 



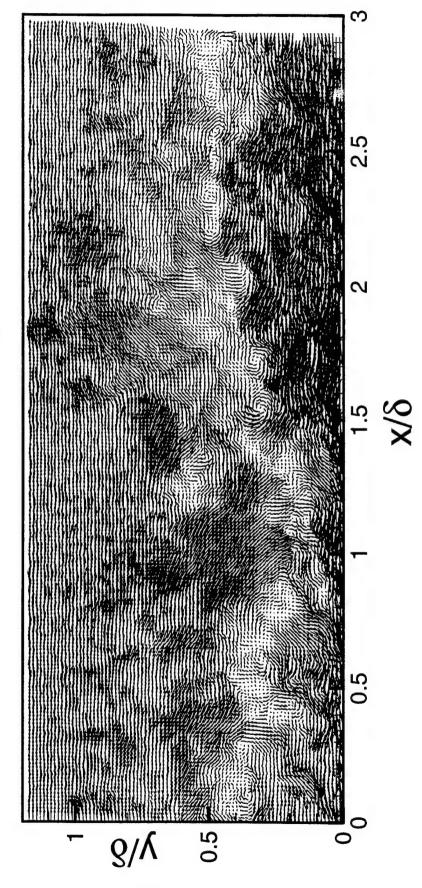
Realization HW-43,  $U_c = 0.65 U_{\odot}$ 



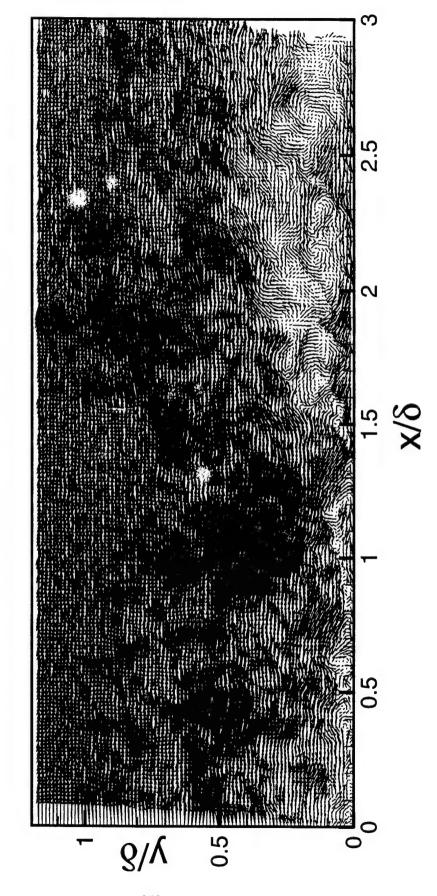
Realization HW-43, Reynolds Fluctuations



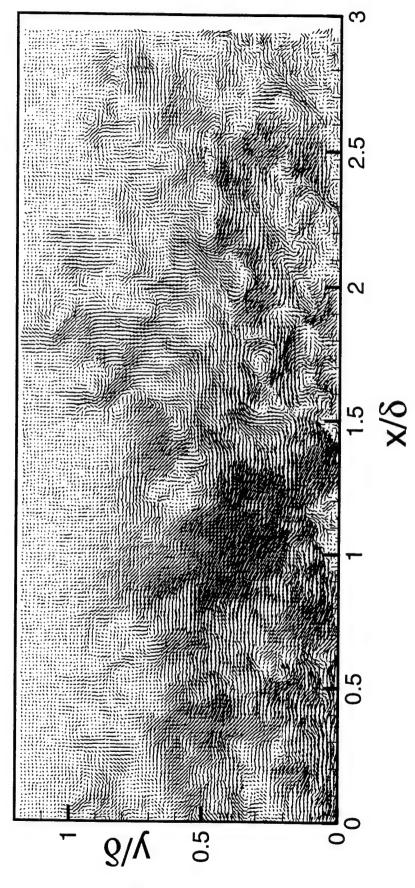
Realization HW-44,  $U_c = 0.85 U_{\odot}$ 



Realization HW-44,  $U_c = 0.65 U_{\odot}$ 

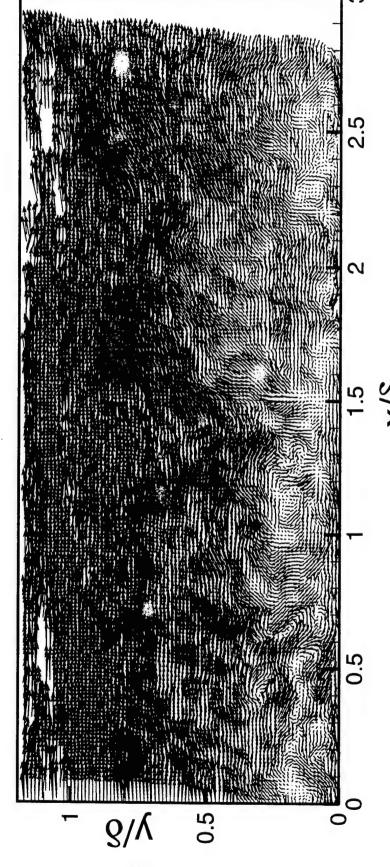


Realization HW-44, Reynolds Fluctuations



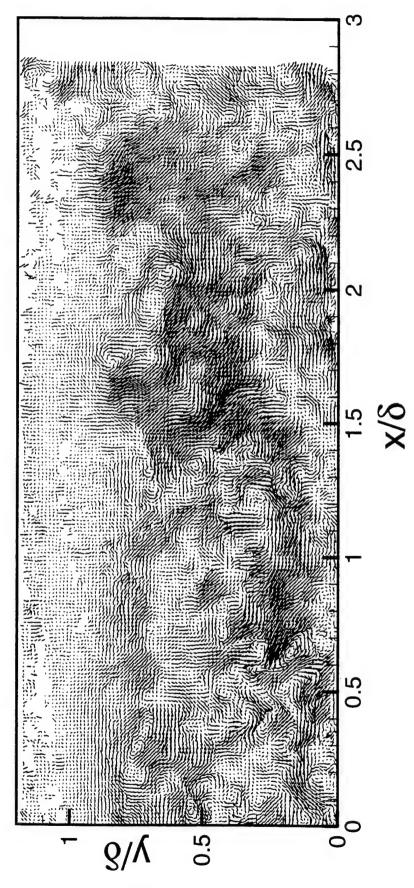
2 0.5 360

Realization HW-45,  $U_c = 0.85 U_{\odot}$ 



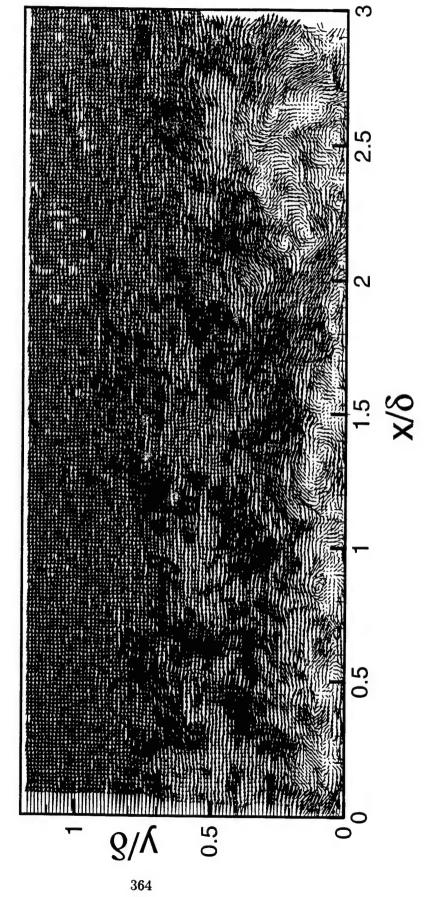
Realization HW-45,  $U_c = 0.65 U_{\odot}$ 

Realization HW-45, Reynolds Fluctuations

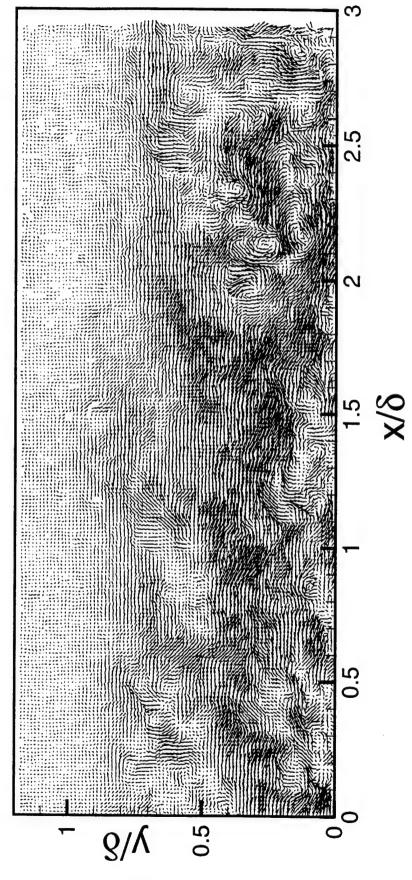


Realization HW-46,  $U_c = 0.85 U_{\odot}$ 

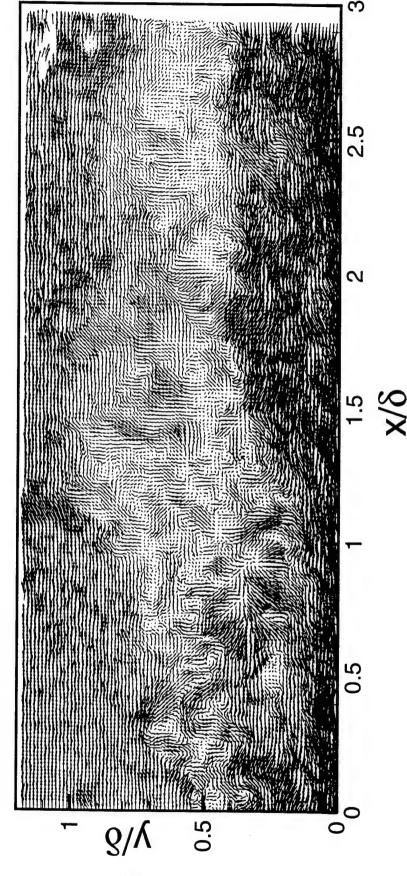
Realization HW-46,  $U_c = 0.65 U_{\odot}$ 



Realization HW-46, Reynolds Fluctuations

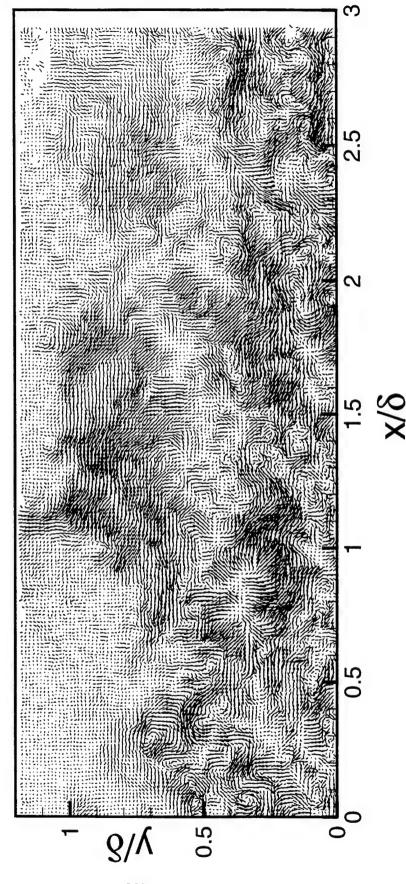


Realization HW-47,  $U_c = 0.85 U_{\odot}$ 



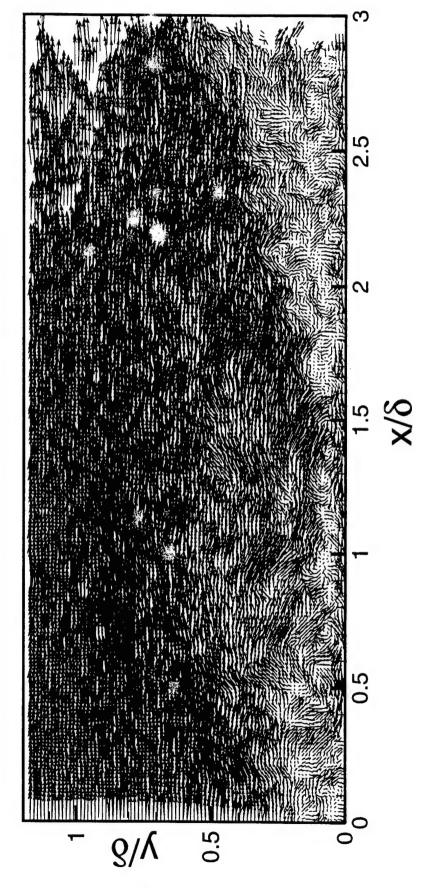
Realization HW-47,  $U_c = 0.65 U_{\odot}$ 

Realization HW-47, Reynolds Fluctuations

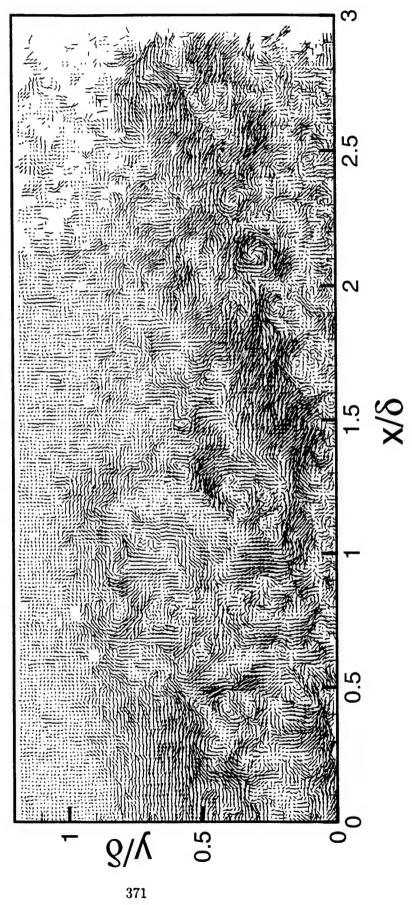


Realization HW-48,  $U_c = 0.85 U_{\odot}$ 

Realization HW-48,  $U_c = 0.65 U_{\odot}$ 



Realization HW-48, Reynolds Fluctuations



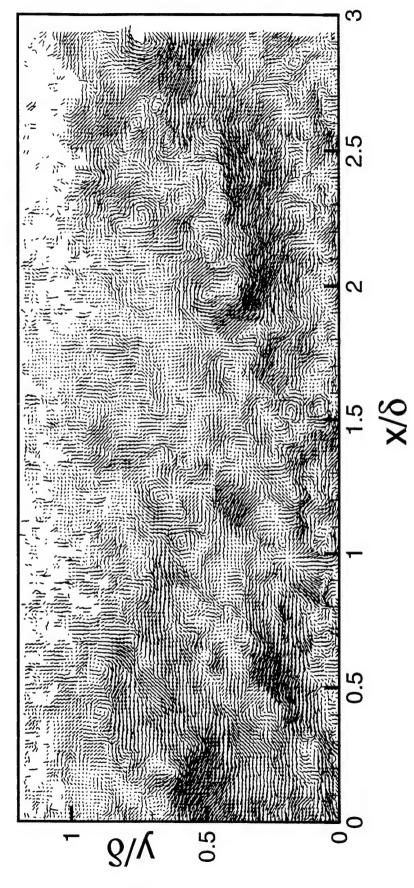
0.5

Realization HW-49,  $U_c = 0.85 U_{\odot}$ 

2.5 N

Realization HW-49,  $U_c = 0.65 U_{\odot}$ 

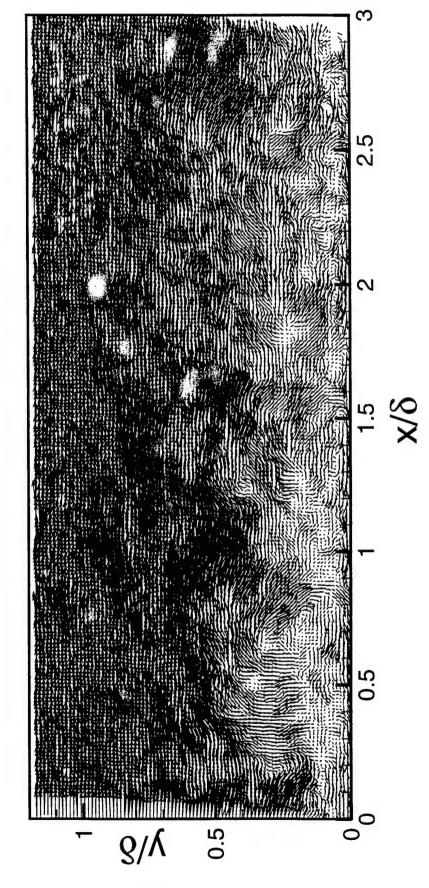
Realization HW-49, Reynolds Fluctuations



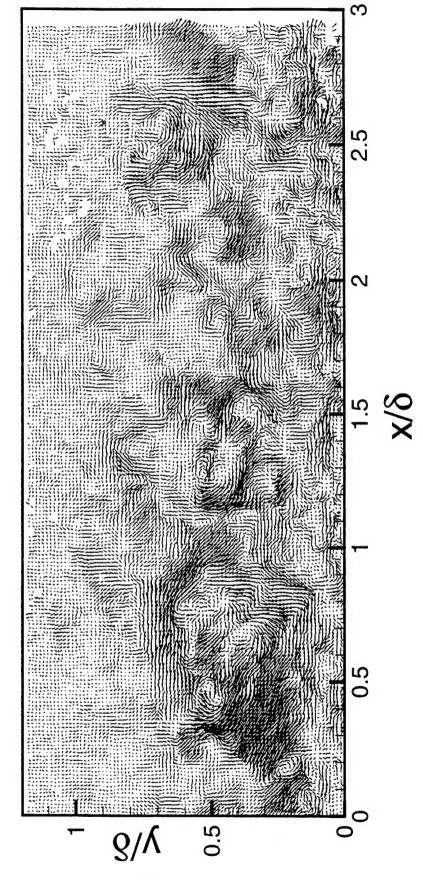
0.5

Realization HW-50,  $U_c = 0.85 U_{\odot}$ 

Realization HW-50,  $U_c = 0.65 U_{\odot}$ 

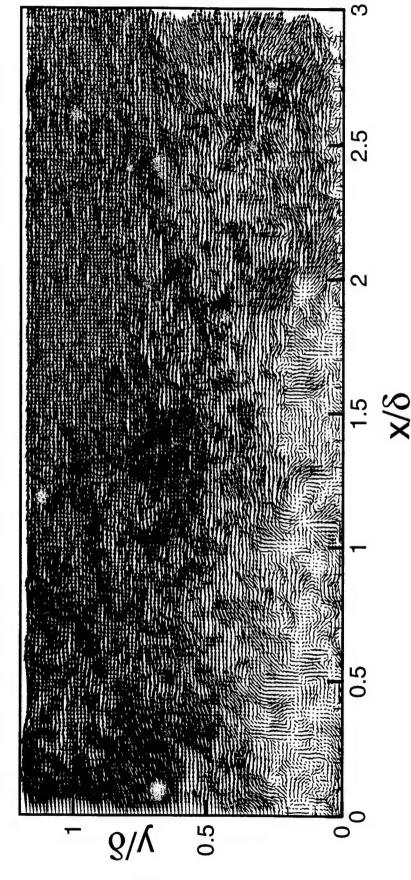


Realization HW-50, Reynolds Fluctuations

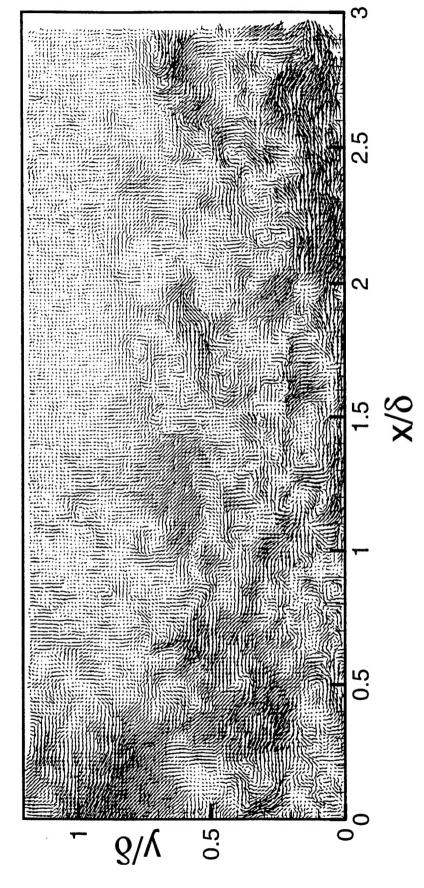


Realization HW-51,  $U_c = 0.85 U_{\odot}$ 0.5 δ/γ

Realization HW-51,  $U_c = 0.65 U_{\odot}$ 



Realization HW-51, Reynolds Fluctuations



## REFERENCES

- [1] M. S. Acarlar and C. R. Smith. A study of hairpin vortices in a laminar boundary layer. part 1. hairpin vortices generated by a hemisphere protuberance. J. Fluid Mech., 175:1-41, 1987.
- [2] R. J. Adrian. On the role of conditional averages in turbulence theory. In J. Zakin and G. Patterson, editors, *Turbulence in Liquids*, pages 323-332. Science Press, 1977.
- [3] R. J. Adrian. Multi-point optical measurements of simultaneous vectors in unsteady flow—a review. Intl. J. Heat and Fluid Flow, 7:127-145, 1986.
- [4] R. J. Adrian. Statistical properties of particle image velocimetry measurement in turbulent flow. In Laser Anemometry in Fluid Mechanics—III, pages 115-129. Ladoan-Inst. Super. Tec., 1988.
- [5] R. J. Adrian. Particle imaging techniques for experimental fluids. In Ann. Rev. Fluid Mech., number 23, pages 261-304, 1991.
- [6] R. J. Adrian and C.-S. Yao. Pulsed laser technique application to liquid and gaseous flows and the scattering power of seed materials. Appl. Opt., 24(1):44-52, 1985.
- [7] R. A. Antonia, D. K. Bisset, and L. W. B. Browne. Effect of reynolds number on the topology of the organized motion in a turbulent boundary layer. *J. Fluid Mech.*, 213:267-286, 1990.
- [8] R. F. Blackwelder and R. E. Kaplan. On the wall structure of the turbulent boundary layer. J. Fluid Mech., 76:89-112, 1976.
- [9] G. L. Brown and A. S. W. Thomas. Large structure in a turbulent boundary layer. *Phys. Fluids*, 20, October 1977.
- [10] C-H.P. Chen and R. F. Blackwelder. Large-scale motion in a turbulent boundary layer: a study using temperature contamination. J. Fluid Mech., 89:1-31, 1978.
- [11] F. Clauser. The turbulent boundary layer. Advances in Applied Mechanics, 4:1-51, 1956.
- [12] E. R. Corino and R. S. Brodkey. A visual investigation of the wall region in turbulent flow. J. Fluid Mech., 37:1-30, 1969.
- [13] S. Corrsin and A. L. Kistler. The freestream boundaries of turbulent flows. Technical report, NACA TN-3133, 1954.
- [14] R. E. Falco. Coherent motions in the outer region of turbulent boundary layers. *Phys. Fluids*, 20, October 1977.
- [15] J. W. Goodman. Introduction to Fourier Optics. McGraw-Hill, 1968.
- [16] H. L. Grant. The large eddies of turbulent motion. J. Fluid Mech., 4:149-190, 1958.
- [17] Y. G. Guezennec. Stochastic estimation of coherent structures in turbulent boundary layers. *Phys. Fluids*, 1, June 1989.
- [18] M. R. Head and P. Bandyopadhyay. New aspects of turbulent boundary-layer structure. J. Fluid Mech., 107:297-338, 1981.

- [19] E. Hecht. Optics. Addison-Wesley. 2nd edition, 1987.
- [20] T. B. Hedley and J. F. Keffer. Some turbulent/non-turbulent properties of the outer region of a boundary layer. J. Fluid Mech., 64:645-678, 1974.
- [21] R. D. Keane and R. J. Adrian. Optimization of particle image velocimeters. part i: Double pulsed systems. *Meas. Sci. Tech.*, 1:1202-1215, 1990.
- [22] H. T. Kim, S. J. Kline, and W. C. Reynolds. The production of turbulence near a smooth wall in a turbulent boundary layer. *J. Fluid Mech.*, 50:133-160, 1971.
- [23] P. S. Klebanoff. Characteristics of turbulence in a boundary layer with zero pressure gradient. Technical report, NACA TN-3178, 1954.
- [24] S. J. Kline, W. C. Reynolds, F. A. Schraub, and P. W. Runstadler. The structure of turbulent boundary layers. J. Fluid Mech., 30:741-773, 1967.
- [25] L. S. G. Kovasznay, V. Kibens, and R. F. Blackwelder. large-scale motion in the intermittent region of a turbulent boundary layer. J. Fluid Mech., 41:283-325, 1970.
- [26] T. S. Luchik and W. G. Tiederman. Timescale and structure of ejections and bursts in turbulent channel flows. J. Fluid Mech., 174:529-552, 1987.
- [27] C. D. Meinhart. Investigation of turbulent boundary layer structure using particle-image velocimetry. Ph. d. dissertation, University of Illinois, 1994.
- [28] C. D. Meinhart and R. J. Adrian. On the existence of uniform momentum zones in a turbulent boundary layer. *Phys. Fluids*, 7, April 1995.
- [29] C. D. Meinhart and R. J. Adrian. Untitled- hpv in tbl. Submitted to J. Fluid Mech., 1997.
- [30] J. Murlis, H. M. Tsai, and P. Bradshaw. The structure of turbulent boundary layers at low reynolds number. J. Fluid Mech., 122:13-56, 1982.
- [31] S. G. Nychas, H. C. Hershey, and R. S. Brodkey. A visual study of turbulent shear flow. J. Fluid Mech., 61:513-540, 1973.
- [32] P. W. Offutt. A study of turbulent thermal convection using particle-image velocimetry. Ph. d. dissertation, University of Illinois, 1995.
- [33] A. E. Perry and M. S. Chong. On the mechanism of wall turbulence. J. Fluid Mech., 119:173-217, 1982.
- [34] A. E. Perry, S. Henbest, and M. S. Chong. A theoretical and experimental study of wall turbulence. J. Fluid Mech., 165:163-199, 1986.
- [35] A. E. Perry and I. Marusic. A wall-wake model for the turbulence structure of boundary layers. part 1. extension of the attached eddy hypothesis. J. Fluid Mech., 298:361-388, 1995.
- [36] A. K. Prasad, R. J. Adrian, C. C. Landreth, and P. W. Offutt. Effect of resolution on the speed and accuracy of particle image velocimetry interrogation. *Exp. Fluids*, 13:105–116, 1992.
- [37] A. K. Praturi and R. S. Brodkey. A stereoscopic visual study of coherent structures in turbulent shear flow. J. Fluid Mech., 89:251-272, 1978.
- [38] S. K. Robinson. Coherent motions in the turbulent boundary layer. In Ann. Rev. Fluid Mech., number 23, pages 601-639, 1991.
- [39] P. R. Spalart. Direct simulation of a turbulent boundary layer up to  $r_{\theta} = 1410$ . J. Fluid Mech., 187:61-98, 1988.
- [40] T. Theodorson. Mechanism of turbulence. In Proceeding from the Second Midwestern Conference of Fluid Mechanics, page 123, 1952.

- [41] A. A. Townsend. Entrainment and the structure of turbulent flow. J. Fluid Mech., 41:13-46, 1970.
- [42] T. Urushihara, C. D. Meinhart, and R. J. Adrian. Investigation of the logarithmic layer in pipe flow using particle image velocimetry. In C. G. Speziale R. M. C. So and B. E. Launder, editors. Near-wall turbulent flows, pages 433-446. Elsevier Science Publishers, 1993.
- [43] J. M. Wallace, R. S. Brodkey, and H. Eckelmann. Pattern-recognized structures in bounded turbulent shear flows. J. Fluid Mech., 83:673-693, 1977.
- [44] J. M. Wallace, H. Eckelmann, and R. S. Brodkey. The wall region in turbulent shear flow. J. Fluid Mech., 54:39-48, 1972.
- [45] J. Zhou, R. J. Adrian, and S. Balachandar. Formation of hairpin vortex packets by autogeneration. Submitted to Phys. Fluids, 1997.